

1                   **Alpacas in Space - An Autobiography**  
2

3                   By  
4

5                   JOSEPH LEVINE  
6                   DISSERTATION  
7

8                   Submitted in partial satisfaction of the requirements for the degree of  
9  
10                   DOCTOR OF PHILOSOPHY

11                   in  
12

13                   Physics  
14

15                   in the  
16

17                   OFFICE OF GRADUATE STUDIES  
18  
19                   of the  
20

21                   UNIVERSITY OF CALIFORNIA  
22

23                   DAVIS  
24

25                   Approved:  
26

---

27                   J. Anthony Tyson, Chair  
28

---

30                   S. Mani Tripathi  
31

---

33                   Brian Kolner  
34

36                   Committee in Charge  
37

38                   2025

39 

# Abstract

40 comment: This is my qual write up and is here only as a place holder. Don't edit this  
41 yet It is believed that a large majority of the mass in the universe comes from an as yet  
42 undetermined source. This claim stems originally from work performed in 1933 by Fritz  
43 Zwicky who noticed a discrepancy between measured velocities of galaxies within the Coma  
44 Cluster and velocities predicted by applying the virial theorem. He wrote

45 *If this [experimental result] would be confirmed we would get the surprising result  
46 that dark matter is present in much greater amount than luminous matter [1].*

47 Vera Rubin furthered this work by measuring velocities of stars rotating in the M31 galaxy  
48 and concluded there must be additional non-luminous mass (originally published in [2],  
49 and shown in Fig.0.1). Studies of other phenomena, such as lensing (see [**lensing2**]) have  
50 confirmed the existence of this dark matter, and it is currently one of the major mysteries  
51 in modern physics.

52 Since the 1980's, the leading theories have consisted of an unknown species of elementary  
53 particle. The search for weakly interacting massive particles (WIMPs) have dominated  
54 the budgets and schedules of the dark matter search effort but have yet to provide any  
55 experimental evidence.

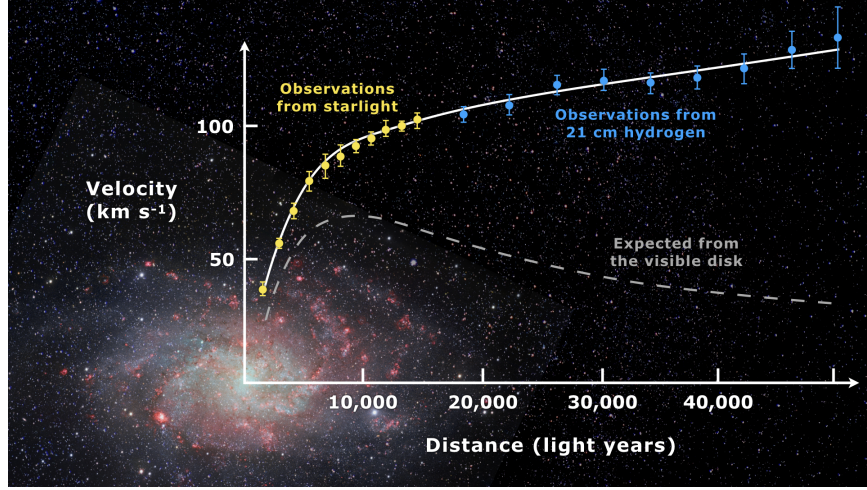


Figure 0.1: Expected vs observed velocity distributions of M33

56 In light of this, the 2017 community report on dark matter [3] highlights a need for a multi-  
 57 experiment program in which many small scale experiments (< \$10M) split up to cover the  
 58 vast landscape of potential dark matter candidates (see Fig. 0.2). Since very little is known  
 59 about the dark matter, it is a playground for theoretical physicists to invent candidates.  
 60 This overwhelming search should be narrowed down.

61 The enormous mass range splits nicely into two regimes; waves and particles. At a mass of  
 62 order 1eV the inter-particle spacing  $\approx$  wavelength. Lighter than this it is more convenient  
 63 to think of dark matter as a wave. Alternatively, dark matter candidates heavier than this  
 64 are more conveniently modeled as exhibiting particle-like behavior. The Dark E-Field Radio  
 65 experiment searches for dark photons in the nano- to milli-eV mass range where dark matter  
 66 is best described as a wave. This property means one would search for a dark photon using  
 67 wave-like detectors, e.g. antennas.

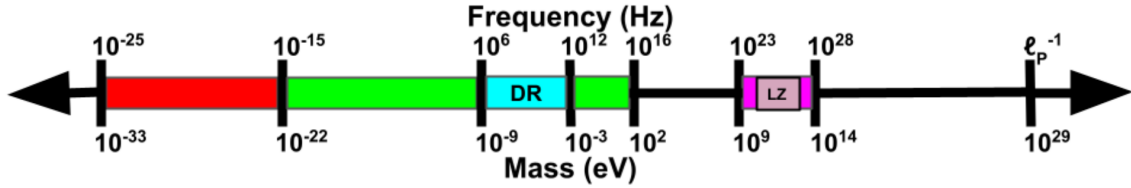


Figure 0.2: Cartoon depicting the mass scales over which dark matter may be found. Corresponding frequencies shown above. At heavy mass scales  $> \mathcal{O}(1\text{ eV})$  the dark matter would behave like a particle, while on the lighter end it would behave like a wave. The Dark Radio Experiment searches at radio/microwave frequencies (blue) for a hidden photon using an antenna and spectrum analyzer. LUX-ZEPLIN Experiment (LZ) also shown.

68 comment: Discussion from paper. Good to pull from

69 This experiment extends the earlier results of our pilot experiment [4], which was designed to  
 70 demonstrate feasibility of the Dark E-field Radio technique. The pilot experiment was run  
 71 over the same frequency range as the experiment reported here, but did not make use of the  
 72 calibration techniques to approximate statistical uniformity, nor did it fully account for the  
 73 resonant enhancement of the cavity. In this paper we describe how we randomize antenna  
 74 positions by moving it many times during the run. In addition, we detail EM simulations  
 75 which give the average relation between the E-field at the antenna and the voltage into  
 76 the LNA, accounting for resonant enhancement of the cavity. A  $2^{24}$ -point FFT produces a  
 77 spectrum dominated by background thermal noise which varies gradually with frequency.

78 We then searched over the full 50-300 MHz frequency span for any narrow-band dark photon  
 79 signal of at least 5% global significance. Optimally filtering the resulting spectrum, we detect  
 80 a single candidate which we are able to identify as interference, likely from our electronics.

81 Rejecting this candidate, we obtain a null result for any signal which could be attributed  
82 to the dark photon in our frequency range. The resulting 95% exclusion limit for the dark  
83 photon kinetic coupling  $\epsilon$  is then obtained over this mass range of 0.2-1.2  $\mu\text{eV}$ . Our null result  
84 is a factor of  $\approx 100$  more sensitive than current astrophysical limits.

85 Ultimately, we can apply this detection technique at higher frequencies, ultimately going up  
86 to the sub-THz band. This will require new antennas and microwave electronics. Cryogenic  
87 cavities and LNAs could improve our sensitivity by an order of magnitude.

# 88 **Contents**

89	<b>Contents</b>	vi
90	<b>List of Figures</b>	x
91	<b>List of Tables</b>	xiv
92	<b>1 The Dark Matter Story</b>	1
93	1.1 The History of Dark Matter . . . . .	2
94	1.1.1 Early ideas in dark matter . . . . .	2
95	1.1.2 Into the modern era . . . . .	3
96	1.1.2.1 Galactic rotation curves . . . . .	7
97	1.1.3 Local dark matter density measurements . . . . .	7
98	1.2 From “History” to “Current Events” . . . . .	7
99	1.2.1 Modern evidence and observations of dark matter . . . . .	8
100	1.2.1.1 The cosmic microwave background . . . . .	8
101	1.2.1.2 Gravitational lensing . . . . .	8
102	1.2.1.3 MOND and the bullet cluster . . . . .	8
103	1.3 MACHOs, WIMPs and WISPs, oh my! . . . . .	9
104	1.4 Dark Photon Physics . . . . .	9
105	1.5 Detection Strategy: a Resource Allocation Problem . . . . .	10
106	<b>2 Experiment Overview and Design</b>	11
107	2.1 Sources of Power in Measured Spectrum . . . . .	14
108	2.1.1 Thermal Noise . . . . .	14
109	2.1.1.1 Blackbody Electric Field Density . . . . .	14
110	2.1.1.2 Antenna Noise . . . . .	17
111	2.1.1.3 Dicke radiometer equation . . . . .	20
112	2.1.2 Dark Photon Signal . . . . .	25
113	2.1.3 Radio Frequency Interference . . . . .	27
114	2.1.4 Amplifier Chain Noise . . . . .	28
115	2.1.5 ADC effects . . . . .	32
116	2.1.5.1 Spurious signals . . . . .	33
117	2.1.5.2 ADC noise . . . . .	33

118	2.2	Toy Analysis . . . . .	34
119	2.2.1	Signal significance . . . . .	36
120	2.2.1.1	Computing an exclusion limit . . . . .	38
121	2.2.2	Predicted time to detection . . . . .	42
122	2.3	Thermal Noise in A Cavity: Thermal Wiggles . . . . .	44
123	2.3.1	Theory of thermal radiation in a cavity . . . . .	44
124	2.3.2	Inspection of thermal noise spectra . . . . .	48
125	2.3.3	A simple resonator: shorted coax cable . . . . .	49
126	2.3.3.1	RF circulators . . . . .	52
127	2.3.4	A simpler resonator: shorted coax cable and circulator . . . . .	55
128	2.3.5	A more complex resonator: antenna in room . . . . .	57
129	2.3.6	Effective temperature of amplifier . . . . .	59
130	2.3.7	Intentional breaking of thermal equilibrium . . . . .	62
131	2.3.8	Relation of antenna $S_{11}$ to thermal noise without a circulator . . . . .	69
132	2.3.9	Discussion of Thermal Wiggles . . . . .	72
133	2.4	Reverberation Chambers and Statistical Uniformity . . . . .	73
134	2.4.1	Deterministic solutions to electromagnetic waves in cavities . . . . .	75
135	2.4.2	Statistical approach to electromagnetic waves in cavities . . . . .	79
136	2.5	System Design . . . . .	80
137	2.5.1	Shielded room . . . . .	83
138	2.5.2	Antenna . . . . .	84
139	2.5.3	Terminator and fiber-optic switch control . . . . .	88
140	2.5.4	Signal conditioning . . . . .	88
141	2.5.4.1	Low noise amplifier . . . . .	89
142	2.5.4.2	Secondary amplifier . . . . .	89
143	2.5.4.3	Band pass filter . . . . .	90
144	2.5.4.4	Putting together a signal conditioning chain . . . . .	91
145	2.5.5	Veto antenna . . . . .	94
146	2.5.6	12 V power system . . . . .	95
147	2.5.7	GPU-Based Real-Time Spectrum Analyzer . . . . .	98
148	<b>3</b>	<b>System Characterization and Data Acquisition System</b>	<b>102</b>
149	3.1	Measurement of Amplifier Chain Performance . . . . .	103
150	3.1.1	Y-factor method . . . . .	103
151	3.1.2	Confirming gain with tracking generator measurement . . . . .	111
152	3.1.3	System stability over a run period . . . . .	112
153	3.2	Measurement of shielding effectiveness and radio frequency interference . . . . .	116
154	3.3	Spectrum Analyzer Characterization . . . . .	122
155	3.3.1	Spectrum analyzer calibration . . . . .	122
156	3.3.2	Spurious signal performance of the ADC . . . . .	123
157	3.3.3	ADC clock performance . . . . .	125
158	3.3.4	Real-time data collection efficiency . . . . .	126

159	<b>4 Data Acquisition, Data Analysis and Calibration</b>	<b>128</b>
160	4.1 Data Acquisition . . . . .	130
161	4.1.1 Raw data, $S_o$ . . . . .	131
162	4.2 Data Analysis . . . . .	134
163	4.2.1 Fit background, $\hat{B}(\nu)$ . . . . .	136
164	4.2.2 Normalized spectrum, $S_o^{\text{norm}}$ . . . . .	138
165	4.2.3 Signal-matched filter . . . . .	139
166	4.2.4 Monte Carlo: pseudo experiments . . . . .	142
167	4.2.5 Rejection of a single candidate . . . . .	147
168	4.3 Calibration . . . . .	148
169	4.3.1 Average effective aperture, $\langle A_e(\nu) \rangle$ . . . . .	149
170	4.3.2 Simulation of $\langle \tilde{Q} A_e \rangle$ . . . . .	150
171	4.3.3 Correction and uncertainty of $\langle \tilde{Q} A_e \rangle$ . . . . .	153
172	4.4 Hardware Injection Test . . . . .	156
173	4.4.1 Injection test prerequisites . . . . .	157
174	4.4.1.1 Determination of required injected power . . . . .	157
175	4.4.1.2 Proxy dark photon signal injection . . . . .	160
176	4.4.2 Performing the injection test . . . . .	162
177	4.4.3 Inspection of Data . . . . .	166
178	<b>5 Results</b>	<b>170</b>
179	5.1 Discussion of uncertainties . . . . .	171
180	5.2 Exclusion Limit <sup>1</sup> . . . . .	172
181	<b>6 Beyond 300 MHz</b>	<b>175</b>
182	6.1 A first attempt at Run 1B <sup>2</sup> . . . . .	178
183	6.1.1 Run 1B upgrades . . . . .	178
184	6.1.1.1 Run 1B spectrum analyzer . . . . .	178
185	6.1.1.2 Vivalid antenna stand . . . . .	179
186	6.1.1.3 Mode stirrer and statistical uniformity . . . . .	179
187	6.1.2 Run 1B data run and analysis . . . . .	181
188	6.2 Mixer System: Run 2 . . . . .	185
189	6.2.1 Frequency mixing . . . . .	185
190	6.2.1.1 The superheterodyne receiver . . . . .	188
191	6.2.2 A mixer system for DER . . . . .	190
192	6.3 Possible Future Upgrades . . . . .	192
193	<b>A Overview of RTSA code base</b>	<b>194</b>
194	A Tips for using the RTSA system . . . . .	196

<sup>1</sup>Code for this section can be found at: <https://github.com/josephmlev/darkRadio/tree/master/Computelimit>

<sup>2</sup>Code for this section can be found at: <https://github.com/josephmlev/darkRadio/tree/master/daqAnalysisAndExperiments/run1B/analysis>

195	B	Data structure and processing . . . . .	197
196		B.1 Writing data . . . . .	197
197		B.2 Reading and averaging data . . . . .	201
198	<b>Bibliography</b>		<b>204</b>

# <sup>199</sup> List of Figures

200	0.1	Expected vs observed velocity distributions of M33 . . . . .	iii
201	0.2	Dark matter mass regimes . . . . .	iv
202	2.1	Overview of the Dark E-field Radio experiment . . . . .	13
203	2.2	Blackbody electric field spectral density from radio to UV frequencies . . . . .	16
204	2.3	An antenna and matched resistor in cavities which are in thermal equilibrium.	19
205	2.4	Simulated antenna noise voltage at room temperature in the time domain . . . . .	21
206	2.5	Simulated antenna noise power spectral density at room temperature in the frequency domain . . . . .	22
207	2.6	Effect of averaging on simulated antenna noise power spectral density at room temperature in the frequency domain . . . . .	24
209	2.7	Schematic of LNA adding input referred noise . . . . .	28
210	2.8	Schematic of cascade of amplifiers and their added noise . . . . .	30
212	2.9	Cascaded noise temperature for system with two amplifiers . . . . .	31
213	2.10	Input-referred power spectral density from simplified simulation . . . . .	36
214	2.11	Noise spectrum containing sub-detection-threshold signal . . . . .	40
215	2.12	Noise spectrum containing sub-detection-threshold signal, various number of averages . . . . .	41
217	2.13	Predicted time to detection for the toy analysis spectra . . . . .	43
218	2.14	Two cavities in thermal equilibrium of arbitrary shape, material and physical contents contain equivalent radiation fields . . . . .	45
220	2.15	A cavity with a small hole behaves like a black body as long as the probability of absorption << 1. The probability of absorption at each reflection is given by the emissivity, so the total probability of <i>reflection</i> is the emissivity raised to the power of the average number of bounces. Figure from Wikipedia. . . . .	47
224	2.16	Output-referred Vivaldi antenna and terminator spectra as measured through Run 1A amplifier chain . . . . .	49
226	2.17	A coax cable with a short on the end and a matched measurement device on the other behaves like a “closed-open” resonator. Replacing the short termination with an open (not shown here) produces a similar resonator, though with a 180-degree phase shift. . . . .	51
230	2.18	Power spectrum of short and open terminations at the end of 1.85 m of RG400 coax cable . . . . .	51
232	2.19	Schematic symbol of a circulator . . . . .	52

233	2.20 Photo of Teledyne C-0S03A-3M RF circulator . . . . .	53
234	2.21 3-port, frequency-dependent S-parameter data for Teledyne C-0S03A-3M circulator	54
235	2.22 A coax cable with a short on one end and a circulator isolating the system from the amplifier. . . . .	56
237	2.23 Power spectrum of 185 cm coax resonator as measured through circulator. . . . .	56
238	2.24 Schematic of experimental set-up using circulator to isolate antenna from ampli- fier effects . . . . .	58
240	2.25 Normalized power spectrum for Vivaldi antenna in the room with and without circulator . . . . .	58
242	2.26 Schematic of set-up to measure the noise emerging <i>out</i> of an amplifiers input . .	61
243	2.27 Power spectrum of noise emerging <i>out</i> of the input of an amplifier's input . . .	61
244	2.28 Setup to create hot and cold terminator . . . . .	63
245	2.29 Spectra resulting from the antenna and circulator set up at a variety of temper- atures above room temperature . . . . .	65
247	2.30 Spectra resulting from the antenna and circulator set up with the terminator 210 K above and below room temperature . . . . .	67
249	2.31 Sum of normalized spectra shown in Fig. 2.30 . . . . .	68
250	2.32 $1 -  S_{11} ^2$ and the normalized antenna spectrum over plotted . . . . .	70
251	2.33 Correlation of $1 -  S_{11} ^2$ and the normalized antenna spectrum . . . . .	71
252	2.34 Modal density for an electromagnetic cavity with dimensions of the shielding room	77
253	2.35 Pictures of conductor configurations in shielded room . . . . .	78
254	2.36 Measured $S_{11}$ with different conductors in shielded room . . . . .	78
255	2.37 Schematic of the RF receiver system . . . . .	81
256	2.38 Photo of dark radio lab . . . . .	82
257	2.39 AB-900A biconical antenna free space effective aperture, simulated, measured and theoretical . . . . .	86
259	2.40 simulated AB-900A biconical antenna free space complex input impedance, vs measured biconical data . . . . .	87
261	2.41 Through gain ( $S_{21}$ ) of bandpass filter . . . . .	93
262	2.42 Schematic of Run 1A Amplifier chain . . . . .	94
263	2.43 Schematic of Interlock board . . . . .	96
264	2.44 Photo of lead-acid battery and slow turn on circuit . . . . .	97
265	2.45 Real time DAQ data stream. . . . .	100
266	3.1 Cartoon showing Y-factor data . . . . .	104
267	3.2 Raw output power spectra used to compute the gain and noise temperature for the Run 1.4 amplifier chain using the Y-factor method . . . . .	106
269	3.3 Y-factor data from Run 1.4 amplifier chain at a single frequency (625 MHz) . .	107
270	3.4 Frequency dependent noise temperature of Run 1.4 amplifier chain, measured using the Y-factor method . . . . .	108
272	3.5 Frequency-dependent gain of the Run 1.4 amplifier chain, measured using the Y-factor method . . . . .	109
274	3.6 Run 1.4 terminator, input-referred power spectral density . . . . .	110

275	3.7	Gain vs. frequency of Run 1.4 amplifier chain . . . . .	111
276	3.8	Gain vs. LNA voltage of Run 1.4 amplifier chain . . . . .	113
277	3.9	Voltage at LNA vs. time . . . . .	114
278	3.10	Frequency-averaged power spectral density vs. time of the terminator from Run 279       1.4 . . . . .	115
280	3.11	Photo of setup to measure Shielding effectiveness of shielded room . . . . .	118
281	3.12	Shielding effectiveness of shielded room, 50-300 MHz . . . . .	119
282	3.13	Shielding effectiveness of shielded room, 125-3000 MHz . . . . .	120
283	3.14	Spectrum from veto antenna during 300 MHz data run . . . . .	121
284	3.15	Scan of terminated input of Teledyne spectrum analyzer system to measure spur 285       performance . . . . .	124
286	3.16	Acquisition efficiency for GPU-based Real-time spectrum analyzer . . . . .	127
287	4.1	Run 1A averaged, output-referred antenna power spectrum $S_o$ . . . . .	132
288	4.2	Logarithmic scaled Run 1A averaged, output-referred, antenna and terminator 289       power spectra . . . . .	133
290	4.3	Flow chart outlining the logic of signal processing in the detection algorithm of 291       sections 4.2.1 through 4.2.3 . . . . .	135
292	4.4	Fitting background $\hat{B}$ in the presence of a synthetic signal . . . . .	138
293	4.5	Normalized, output-referred power spectrum $S_o^{\text{norm}}$ . . . . .	140
294	4.6	$S_o^{\text{norm}}$ after it has been passed through a matched filter . . . . .	142
295	4.7	Result of Monte Carlo pseudo experiments on signal detection . . . . .	145
296	4.8	Limit on output-referred total integrated signal power, $P_o^{\text{lim}}$ . . . . .	146
297	4.9	Screenshot of COMSOL simulation GUI for two-antenna validation . . . . .	152
298	4.10	Simulated vs measured $\langle S_{21} \rangle$ . . . . .	153
299	4.11	Corrected average effective aperture . . . . .	155
300	4.12	Schematic of hardware injection test . . . . .	158
301	4.13	Average S-parameters of hardware injection test . . . . .	159
302	4.14	Histogram of frequencies used for hardware injection test . . . . .	162
303	4.15	Output-referred power spectral density from the hardware injection test . . . . .	164
304	4.16	Standard deviation of output-referred power spectral density from the hardware 305       injection test, computed with median absolute deviation . . . . .	165
306	4.17	Output-referred power spectrum from hardware injection test, various levels of 307       zoom . . . . .	167
308	4.18	Normalized, output-referred power spectrum from hardware injection test, various 309       levels of zoom . . . . .	168
310	4.19	Matched filtered, output-referred power spectrum from hardware injection test, 311       various levels of zoom . . . . .	169
312	5.1	Zoom of 95 % exclusion limit on $\epsilon$ from Dark E-field Radio run 1A . . . . .	173
313	5.2	Dark photon limits of various experiments with this work shown in red . . . . .	174

314	6.1	Picture of modified COMPOWER antenna stand holding Vivaldi antenna for Run 1B . . . . .	179
315			
316	6.2	Closeup picture of modified COMPOWER antenna stand holding Vivaldi antenna for Run 1B . . . . .	180
317			
318	6.3	Run 1B averaged, output-referred antenna power spectrum $S_o$ . . . . .	182
319	6.4	Run 1B $S_o^{\text{norm}}$ after it has been passed through a matched filter. . . . .	183
320	6.5	9-day averaged veto spectrum and Run 1B $S_o^{\text{norm}}$ after it has been passed through a matched filter . . . . .	184
321	6.6	Overview of basic mixer operation in both upconversion and downconversion mode	187
322			
323	6.7	Illustration of the problem of images in frequency mixing . . . . .	188
324	6.8	Schematic of a basic superheterodyne receiver system . . . . .	189
325	6.9	XXXX . . . . .	190
326	6.10	Block diagram of the mixer system to be used in Run 2 . . . . .	191
327	A.1	Real-time heads up window for data acquisition. . . . .	200

# <sup>328</sup> List of Tables

329    2.1	Statistics of simple Monte Carlo simulation for probability of signal detection in the toy analysis . . . . .	42
331    2.2	Direction, coordinate, and length measurements of the shielded room in lab 314. Note that Fig. 2.38 is looking south, so x is right-left, and z is into the page. Note that these are the mean values of several measurements. The room was found to be about 5 mm out of square, so these should be interpreted as $\pm 5$ mm. . . . .	84
335    2.3	Specifications for the Pasternack PE15A1012-E. The voltage is regulated internally, so the exact voltage supplied is not critical, though there is a slight gain dependence on voltage since a higher voltage causes the amp to run warmer, see Fig 3.8. . . . .	89
339    2.4	Specifications for the Mini-Circuits ZKL-1R5+ as measured with 9.05 V bias. There is no internal regulator, so the voltage is set using an external regulator (built around a TI LM317 [64]). . . . .	90
342    2.5	Specifications for the custom, real-time spectrum analyzer used for run 1A. . . . .	99
343    4.1	Run 1.4 Details. Many specifications are related and can be computed from each other but are listed for reference. The efficiency differs from that calculated in Fig. 3.16 mainly because of switching to a terminator and brief daily pauses to move the antenna. . . . .	130
347    4.2	Threshold parameters that are part of the detection algorithm and Monte Carlo. X is the significance of the analysis. It is a parameter passed to the detection algorithm which specifies the significance threshold. The quantity $100\% - Y$ is the statistical power of the analysis. It is a parameter in the MC, which specifies a threshold on signal power where a given signal is detected in $100\% - Y$ of the MC iterations. We choose both X and Y = 5%. . . . .	144
353    6.1	Overview of future runs including hardware (antenna, LNA, mixer), status, how/if statistical uniformity will be ensured, and any comments . . . . .	177
355    A.1	Example database file. . . . .	198

356

## Acknowledgments

357 Thank you to: Ben

358      Dave Hemmer

359      Nathan IT

360      Monda

361      emiljia

362      Bill Tuck

363      Buchholtz/Ayars/Nelson/Kagan/Clare/Patrova/Rick Danner/pechkis

364      parents

365      janet/joel

366      baba/papa

367      Belva

368      chatGPT

369      Mr Keye

370      Bill Nye

371      pechkis

372      hepcat

373      paul

374      Self plagiarism statement <https://journals.aps.org/copyrightFAQ.html>

375      As the author of an APS-published article, may I include my article or a portion  
376      of my article in my thesis or dissertation? Yes, the author has the right to use  
377      the article or a portion of the article in a thesis or dissertation without requesting  
378      permission from APS, provided the bibliographic citation and the APS copyright  
379      credit line are given on the appropriate pages.

380    <https://grad.ucdavis.edu/preparing-filing-your-thesis-or-dissertation>

381      Published or publishing pending material may be used with permission from the  
382      copyright owner, if not you, and the Graduate Chair, if you are not the first-  
383      author. See the Copyright FAQ for information about permissions when using  
384      published material.

385      Material you have authored, and which has been previously published or is pend-  
386      ing publishing, may be used in its published format with three exceptions: 1)  
387      Margins - You must maintain 1" margins on all sides throughout the paper. 2)  
388      Pagination - page numbers must follow the UC Davis standards. 3) The title  
389      page must follow UC Davis standards and you must include an overall abstract.

390      comment: Need to add note about github and where code comes from

<sup>391</sup> Chapter 1

<sup>392</sup> The Dark Matter Story

393

If we start making a list of things that aren't here, we could be here all night. You know, pens for instance. Let's stick with things we can see.

---

Wheatley

394 While there are many ways to begin a thesis on a dark matter search (of which many  
395 hundreds are written every year), I have opted to prioritize narrative over completeness. I  
396 will aim to answer the following questions:

- 397 • Why do we believe there to be some mysterious “dark matter” which we can’t even  
398 see?
- 399 • Can we back up this prediction?
- 400 • What is the best way to balance answering this question with the economic reality of  
401 finite money?

402 There will be a few digressions along the way, however the goal of this chapter is simply  
403 to motivate what brought society to the point of paying young scientists to put antennas in  
404 metal boxes and measure noise.

## 405 **1.1 The History of Dark Matter**

### 406 **1.1.1 Early ideas in dark matter**

407 The fundamental idea that things exist which can not be easily observed by human senses is  
408 not a new one. Following a long history of discovery of previously unobserved phenomena,  
409 the study of dark matter began to take shape around the end of the 19th century with the  
410 discovery of dark regions among areas with a high density of stars [5]. It was Lord Kelvin  
411 who began a dynamical study of the motions of stars in order to tease out the weight of

412 the luminiferous aether (who's "existence is a fact that can not be questioned" as stated  
413 in his 1901 lecture which is transcribed on page 260 of [6]). Eventually the theory of the  
414 aether would give way to special relativity, which ruled out a potential candidate for the  
415 dark regions. This proposing of dark matter candidates and their rejection is a cycle that  
416 continues to this day, and is the topic of this thesis.

### 417 1.1.2 Into the modern era

418 1905, known as Einstein's miracle year, ushered in a new era of "modern physics". The  
419 aether that Lord Kelvin was trying to weigh was accepted as non-existent, but that didn't  
420 answer the questions of galactic dynamics which were posed by those who believed in it.  
421 Fritz Zwicky is credited with the first discovery of dark matter in 1933 [1], though it was  
422 not widely accepted at this time. This lack of acceptance was in part due to his technique  
423 of "morphological analysis" which is similar to arranging refrigerator magnets to arrive at  
424 creative solutions<sup>1</sup>. The many "creative" solutions are simultaneously to the benefit and  
425 detriment of this technique. To quote Stephen Maurer[7],

426 *When researchers talk about neutron stars, dark matter, and gravitational lenses,*  
427 *they all start the same way: "Zwicky noticed this problem in the 1930s. Back then,*  
428 *nobody listened..."*.

429 It even seems if Zwicky himself didn't believe his own result[1],

---

<sup>1</sup>This analogy is from a class I took from Andrew Wetzel at U.C. Davis. In researching it for this thesis, it is surprisingly accurate

430        *If this [experimental result] would be confirmed we would get the surprising result*  
431        *that dark matter is present in much greater amount than luminous matter [1].*

432        comment: Tony summarizes virial therm this in his '97 physics today article, p. 1 [8] In  
433        retrospect however, this idea is seemingly on firm theoretical footing. The viral theorem is a  
434        well known from statistical mechanics. It was formalized 1870 by Rudolf Clausius (English  
435        translation can be found here [9]). The name *virial* was coined by Clausius. Kinetic energy  
436        was, at the time, referred to as *vis viva* latin for “living force”. The plural of vis is virias,  
437        and since the theorem is concerned with many particles each with their own vis vita the  
438        name *virial* theorem was chosen. The theorem is derived briefly here (following chapter 3 of  
439        Goldstein[10]) since it is informative, however the reader can skip to Eq. 1.6 for the result  
440        as it applies to galacite dynamics.

441        The “virial” the system is defined as

$$G \equiv \sum_{i=1}^N \mathbf{r}_i \cdot \mathbf{p}_i \quad (1.1)$$

442        Where  $\mathbf{r}_i$  is the position of the ith particle and  $\mathbf{p}_i$  is it's momentum,  $m_i \mathbf{v}_i$ .

443        By the product rule, the time derivative of G is

$$\dot{G} = \sum_{i=1}^N (\dot{\mathbf{r}}_i \cdot \mathbf{p}_i + \mathbf{r}_i \cdot \dot{\mathbf{p}}_i) . \quad (1.2)$$

444        Since the first term is really  $m_i \mathbf{v}_i \cdot \mathbf{v}_i$  it can be seen as twice the kinetic energy,  $2T$ . The  
445        second term can be simplified by Newton's second law,  $\mathbf{F} = \dot{\mathbf{p}}$ . So,

$$\dot{G} = 2T + \sum_{i=1}^N (\mathbf{r}_i \cdot \mathbf{F}_i) . \quad (1.3)$$

Solving for the time-averaged, time-derivative of  $G$ ,

$$\begin{aligned}\bar{\dot{G}} &= \frac{1}{T} \int_0^\tau dt \dot{G} \\ &= \frac{G(\tau) - G(0)}{\tau}\end{aligned}$$

446 Where  $T$  is the period the average is taken over, not to be confused with the Kinetic energy.

447 In the case that the system is bound together (i.e.  $\mathbf{r}_i, \mathbf{p}_i > \infty$ ),  $G$  is finite and as  $\tau$   
448 approaches  $\infty$ ,  $\bar{\dot{G}}$  approaches 0

449 Returning to Eq. 1.2, we can now say

$$\overline{T} = -\frac{1}{2} \overline{\sum_{i=1}^N (\mathbf{r}_i \cdot \mathbf{F}_i)}, \quad (1.4)$$

450 A familiar statement of the virial theorem, where the term on the right hand side is  
451 known as *the virial of Clausius*.

452 While incredibly general (one can pull the ideal gas law out of this in just a few steps,  
453 see again Ch. 3 of Goldstein [10]), we are concerned not with a jar filled with gas in some  
454 lab, but with “gas” of stars (among which all labs are contained!).

455 To specify the equation to that of galactic dynamics, recognize for a conservative central  
456 force,  $\mathbf{F} = -\nabla U$  and  $\mathbf{r} \cdot \mathbf{F} = rF$ . If  $U$  is in a power law, i.e. of the form  $k r^{n+1}$ , it can quickly  
457 be seen that the virial of Clausius of Eq. 1.4 can be written  $\frac{n+1}{2} \overline{U}$ .

458 For a problem involving an inverse square force as we are concerned with,  $n = -2$ , and we  
459 arrive at the well known result which is usually just called “the virial theorem”, though as we  
460 have seen, it reaches much deeper than a simple statement of kinetic vs potential energies  
461 for galaxies:

$$\overline{T} = -\frac{1}{2}\overline{U}. \quad (1.5)$$

462 Finally following Edington's 1916 paper [11] we can form a useful formula which ul-  
 463 timately gave a clue to the existence of dark matter. By setting  $T = 1/2M\overline{v^2}$  and  $U =$   
 464  $GM^2/2R$  where M is the total mass of a cluster or galaxy, v is it's velocity, and R is it's  
 465 radius, we arrive at

$$M \approx \frac{2R\overline{v^2}}{G} \quad (1.6)$$

466 As pointed out by Bertone [12], one of the earliest "clean" arguments for the existence  
 467 of dark matter is known as the timing argument. It was derived by Kahn and Woltjer [13].  
 468 The basic idea is given the negative red-shift (i.e. blue-shift) of the Andromeda galaxy, they  
 469 are approaching (at 125 km/s), an indication that they are bound system. Given that the  
 470 period of this system must be less than the age of the universe (assumed to be  $10^{10}$  yr), a  
 471 lower bound can be set on the reduced mass of the system (since orbital period T is inversely  
 472 proportional to the reduced mass).

473 In the years following these arguments, WWII brought unprecedeted destruction, the  
 474 reconstruction of which slowed the progress of all science that was not essential to the war  
 475 effort, especially in Europe. The focus of astronomy and astrophysics largely shifted to  
 476 stellar structure and evolution, in large part due to the work and understanding of nuclear  
 477 reactions around this time. The war also brought with it advances in radar technology. At  
 478 the end of the war, the German occupation forces left large amounts of radar equipment

479 strewn about Europe. This included a large number of 7.5 m Würzburg antennas designed  
480 to 54 cm aircraft radar, but were also sensitive to the famous Hydrogen 21[cm] line [14]. This  
481 would play a major role in what was to come.

482 **1.1.2.1 Galactic rotation curves**

483 **1.1.3 Local dark matter density measurements**

484 **comment: Add plots of local dark matter density estimate.**

485 Good figure 2 of historical DM density through 2014 by Read [15]. Also Figure 1 explains  
486 the difference between local and global density of DM

487 Read is also an author on [16], which has a nice figure 1 showing a continuation of this  
488 out to 2021

489 This is questionable (not peer-reviewed, 2 citations) but has a good overview of Gaia,  
490 and gets DM density using data release 3 [17]

491 **1.2 From “History” to “Current Events”**

492 As pointed out by Trimble, “Practicing scientists will normally put the cut between history  
493 and current events at the time when they started reading the literature for themselves,  
494 probably early in graduate school.” [18]. While that puts my personal cut-off around 2020,  
495 the cut-off of the Dark E-field Radio group is closer to the mid-1960’s, a fruitful time for  
496 research into dark matter.

497 A characteristic shift in the dark matter problem occurs in this era of current events.  
498 Instead of asking “is there dark matter (and if so how much)”, we ask “what is this stuff?!”.  
499 To be sure, the first question is still relevant today and the ever more precise answer was  
500 outlined in Sec. 1.1.3. This section is concerned with more modern evidence for dark matter,  
501 which tend to point to the modern non-baryonic particle models, which the Dark E-Field  
502 Radio Experiment is searching for.

503 **1.2.1 Modern evidence and observations of dark matter**

504 **1.2.1.1 The cosmic microwave background**

505 Billy and Ben’s thesis

506 **1.2.1.2 Gravitational lensing**

507 -ben thesis

508 -tony 92 article// -J. A. Tyson, G. P. Kochanski, and I. P. Dell’Antonio, Detailed mass map  
509 of CL0024+1654 from strong lensing

510 **1.2.1.3 MOND and the bullet cluster**

511 -history of dark matter bertone

512 - billy and ben

513 - D. Clowe, M. Bradac, A. H. Gonzalez, M. Markevitch, S. W. Randall, et al., A direct  
514 empirical proof of the existence of dark matter,

515 **1.3 MACHOs, WIMPs and WISPs, oh my!**

516 -Billy thesis sec 1.2

517 - G. Bertone, D. Hooper, and J. Silk, Particle dark matter: Evidence, candidates and con-  
518 straints

519 **1.4 Dark Photon Physics**

520 - Ben's thesis

521

$$|\mathbf{E}_{\text{ant}}| \approx \epsilon \sqrt{\frac{2}{\varepsilon_0} \rho_{\text{DM}}}, \quad (1.7)$$

522 Tony says 9/23/25– Production mechanisms: fluctuation occurs early in inflation or mis-  
523 alignment mechanism.

524

525 two scales cross, peter graham Point out that DP doesn't have a thermal origin like a  
526 WIMP does

<sup>527</sup> **1.5 Detection Strategy: a Resource Allocation**

<sup>528</sup> **Problem**

<sup>529</sup> - US Cosmic Visions 2017

<sup>530</sup>

<sup>531</sup> Chapter 2

<sup>532</sup> Experiment Overview and Design

A month in the laboratory can often save an

<sup>533</sup> hour in the library.

---

Frank Westheimer

534 Veljko Radeka said of detectors, “One would imagine that in each particular case the  
535 best solution is arrived at by 1) the detector design to maximize the significant signal, 2)  
536 reduction of noise at its physical source, and 3) optimum filtering of signal and noise.” [19].  
537 While he was referring to position-sensitive particle detectors, the same three principles  
538 apply to this experiment. Put more directly, the goal is to maximize the signal-to-noise  
539 ratio. The detector, in this case, is a low-noise, wide-band radio receiver system searching  
540 not for discrete instances of particle-like interactions but for coherent waves that are constant  
541 over long periods. The signal is a small RF-power excess received by an antenna in a cavity.  
542 The dominant noise is due to the thermal background of the 300 K cavity walls. This noise  
543 is nearly white, with small variations. See Sec. 2.1.1 for an overview and Sec. 2.3 for more  
544 detail. An overview of the entire experiment is shown in Fig. 2.1.

545 This chapter begins with Sec. 2.1, devoted to exploring the sources of power in the mea-  
546 sured spectrum. It walks through several back-of-the-envelope calculations to follow the  
547 signals and noises as they progress from fields in free space through a simplified detector.  
548 Section 2.2 takes the next step. It simulates these signals and noises and shows a framework  
549 for statistical data analysis. These two sections serve to build up intuition about the experi-  
550 ment which will explain design choices discussed in later chapters. Furthermore, this section  
551 is useful because the actual experiment will report a null result, i.e. a lack of detection of a  
552 signal. By following a signal *forward* through the system and toy data analysis, it will be  
553 clearer how to infer an exclusion limit from a power spectrum and working *backward* through  
554 the experiment. In the following two sections, 2.3 and 2.4, effects will be introduced that  
555 were not apparent from the simplistic analysis of the first section. The final section, 2.5,

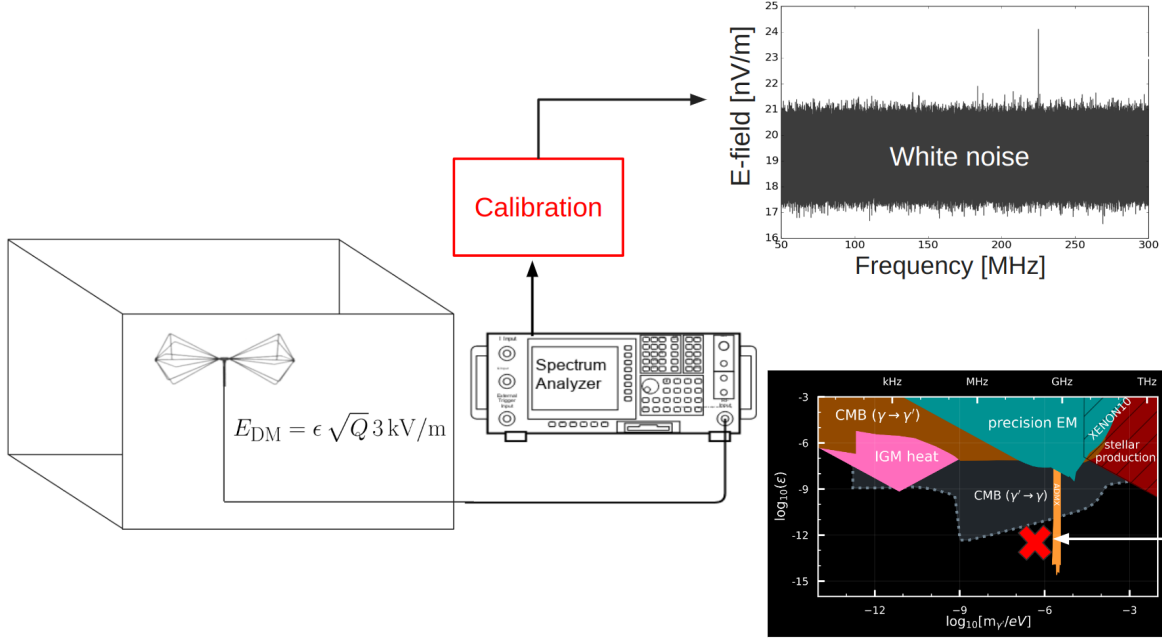


Figure 2.1: Overview of Dark E-field Radio experiment. The free space electric field strength was calculated in Sec. 1.4, and will be modified to include the  $Q$  of the cavity in Sec. 2.1.2. The design of the system is outlined in this chapter, while its performance is measured in Ch. 3. The use of the system, its calibration, and setting a limit are all discussed in Ch. 4. **comment: Remake this. Change  $E_{DM}$  to  $E_{ant}$ , 3kV to 4.5kV, change limit plot. Image from google slide called "schematic"**

556 details each piece of the system. Measurements of system performance are put off until Ch.  
 557 3).

558 A note on experiment “run numbers”. Run 1A is the 50-300 MHz run. There have been  
 559 four attempts at collecting run 1A data. The final, published data run was collected between  
 560 May 10 and May 19, 2023, and is called run 1.4 or run 1p4 throughout my power points and  
 561 file names. I will refer to this run interchangeably as run 1A or run 1.4. Strictly speaking,  
 562 it should be run 1A.4, but if I change it now it will be inconsistent with file names.

563 **2.1 Sources of Power in Measured Spectrum**

564 This section will break down each term in the following equation for the input-referred power

$$P_i = \text{Thermal Noise} + \text{Dark Photon Signal} + \text{RFI} + \text{Amp Chain Noise} + \text{ADC Effects}/G, \quad (2.1)$$

565 where  $G$  is a gain factor. While convenient, this word equation is not rigorous and relies

566 on the following subsections 2.1.1 - 2.1.5 for definition.

567 **2.1.1 Thermal Noise**

568 **2.1.1.1 Blackbody Electric Field Density**

569 This subsection estimates the noise-like<sup>1</sup> electric field in free space due to black body ra-  
570 diation. It assumes to be in *some* enclosure in that the ambient temperature is known to  
571 be 300 K and not, for example, the 3.6 K of the sky. The enclosure considered is assumed  
572 to be "black" in that all radiation impinging on its surface is absorbed. This assumption is  
573 introduced in Sec. 2.1.1.2 and investigated further in Sec. 2.3.

574 Planck's law gives the black body spectral energy density as

$$u_\nu(\nu, T) d\nu = \frac{8\pi h\nu^3}{c^3} \frac{1}{e^{h\nu/kT} - 1} d\nu \quad \left[ \frac{J}{m^3} \right]. \quad (2.2)$$

575 This is frequently written in terms of spectral radiance,

---

<sup>1</sup>"Noise-like" simply means that the power contained in a signal is proportional to the bandwidth measured. Noise-like signals are more conveniently described as a power spectral density (PSD) which we will describe with the symbol  $S$ . As we will see, coherent signals that have finite width in frequency space  $\Delta\nu_{\text{sig}}$  can share this property if the measurement bandwidth  $\Delta\nu_{\text{RF}} \lesssim \Delta\nu_{\text{sig}}$ , even though one wouldn't think of a coherent signal as being "noise-like"

$$B_\nu(\nu, T) d\nu = \frac{2h\nu^3}{c^2} \frac{1}{e^{h\nu/kT} - 1} d\nu d\Omega \quad \left[ \frac{W}{m^2} \right]. \quad (2.3)$$

576 Integrating this isotropic radiance over a solid angle  $4\pi$  sr as well as a small frequency  
 577 band  $\Delta\nu$  gives the flux density  $|\mathbf{S}|$  (AKA, the magnitude of the Poynting vector),

$$\begin{aligned} |\mathbf{S}| &= \int_0^{4\pi} \int_{\nu}^{\nu+\Delta\nu} B_\nu(\nu, T) d\nu d\Omega \\ &= \int_0^{4\pi} \int_{\nu}^{\nu+\Delta\nu} \frac{2h\nu^3}{c^2} \frac{1}{e^{h\nu/kT} - 1} d\nu d\Omega \quad \left[ \frac{W}{m^2} \right]. \\ &\approx \frac{8\pi h\nu^3}{c^2} \frac{1}{e^{h\nu/kT} - 1} \Delta\nu \end{aligned} \quad (2.4)$$

578 Poynting's theorem relates this flux density to the RMS electric field

$$|\mathbf{S}| = \frac{|E_{rms}|^2}{\eta} \quad \left[ \frac{W}{m^2} \right], \quad (2.5)$$

579 where  $\eta$  is the impedance of free space. Equating Eqs. 2.4 and 2.5 and solving for the  
 580 electric field gives

$$\frac{|E_{rms}|}{\sqrt{\Delta\nu}} = \sqrt{\eta \frac{8\pi h\nu^3}{c^2} \frac{1}{e^{h\nu/kT} - 1}} \quad \left[ \frac{V}{m \cdot \sqrt{Hz}} \right], \quad (2.6)$$

581 and is plotted in Fig. 2.2.

582 Eq. 2.6 breaks up nicely into two regimes,

$$\frac{|E_{rms}|}{\sqrt{\Delta\nu}} = \begin{cases} \sqrt{\eta \frac{8\pi kT\nu^2}{c^2}} & \text{Rayleigh-Jeans regime } (h\nu \ll kT) \\ \sqrt{\eta \frac{8\pi h\nu^3}{c^2} e^{-h\nu/kT}} & \text{Wien approximation } (h\nu \gg kT) \end{cases} \quad \left[ \frac{V}{m \cdot \sqrt{Hz}} \right]. \quad (2.7)$$

583 At frequencies and temperatures where the experiment is operated ( $< 300$  MHz and  
 584 300 K),  $h\nu/kT \lesssim 5 \times 10^{-5}$  suggesting the Rayleigh-Jeans approximation is valid. At 300 K,

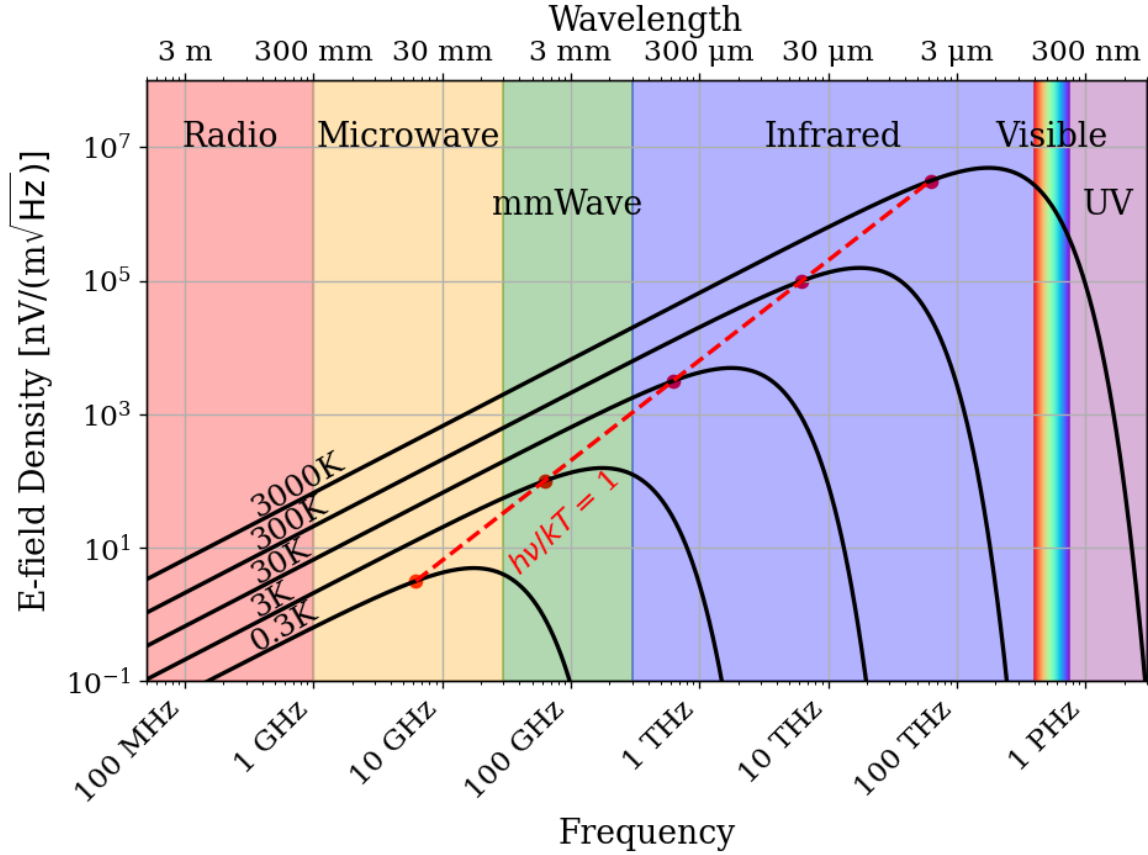


Figure 2.2: Blackbody electric field spectral density from radio to UV frequencies. A variety of temperatures are shown in black. The dashed red curve and red points indicate where along the black curves  $h\nu = kT$ , i.e. where Eq. 2.7 breaks up between the Rayleigh-Jeans regime to the Wien approximation. Note that these points are only a function of  $\nu$  and  $T$ ; their vertical placement is chosen to lie on their respective curve but has no physical significance. The dark radio experiment is firmly in the Rayleigh-Jeans regime.

585 this yields electric field spectral densities of 1 and 6 nV/(m $\sqrt{\text{Hz}}$ ) at 50 and 300 MHz respec-

586 tively.

587 It is interesting to note, however, that for cryogenic experiments operating at a few GHz

588 and in the sub K range (A common technique; see, for example, [20–22] ),  $h\nu/kT \approx 1$  and

589 the full form of Eq. 2.6 must be used. This is shown at frequencies and temperatures to the

590 right of the red dashed line in Fig. 2.2.

591 **2.1.1.2 Antenna Noise**

592 An antenna's effective aperture,  $A_e$  [ $\text{m}^2$ ], represents the effective area that it has to collect  
593 power density or irradiance [ $\text{W}/\text{m}^2$ ] from an incident Poynting vector,

$$P_A = |\mathbf{S}|A_e, \quad (2.8)$$

594 Where  $|\mathbf{S}|$  is the magnitude of the incident Poynting vector, and  $P_r$  is the power received at  
595 the antenna, which is available at its terminals.

596  $A_e$  is a directional quantity that varies with the antenna's directivity  $D(\Omega)$ , where  $\Omega$   
597 represents the solid angle around the antenna. It varies with frequency  $\nu$ , though it is  
598 generally discussed in terms of wavelength  $\lambda$ . Three matching parameters are introduced to  
599 describe how much actual power the antenna is able to deliver to a transmission line;  $p$  the  
600 polarization match of the wave to the antenna,  $m$  the impedance match of the antenna to  
601 the transmission line and  $\eta_a$  the efficiency of the antenna which represents how much power  
602 is absorbed compared to that lost to Joule heating of the antenna.  $p$ ,  $m$  and  $\eta_a$  are all real,  
603 dimensionless and vary between 0 and 1.

$$A_e \equiv \frac{\lambda^2}{4\pi} D(\Omega) p m \eta_a. \quad (2.9)$$

604 This definition follows [23], though some authors do not include  $p$  in the definition [24,  
605 25].

606 A simple derivation of the direction-averaged effective aperture based on thermodynamics  
 607 will provide intuition. An isotropic antenna placed in a cavity at temperature T will be  
 608 illuminated by randomly polarized, isotropic radiation of the form given by the Rayleigh-  
 609 Jeans limit of Eq. 2.4,  $|\mathbf{S}| = 8\pi kT\Delta\nu\nu^2/c^2$ . The power received by the antenna can be found  
 610 by Eq. 2.8,

$$\begin{aligned}
 P_A &= \langle A_e \rangle \frac{1}{2} |\mathbf{S}| \\
 &= \langle A_e \rangle \frac{4\pi kT\nu^2}{c^2} \Delta\nu,
 \end{aligned} \tag{2.10}$$

611 Where the factor of 1/2 is introduced to account for the random polarization and the  $\langle \rangle$   
 612 indicate an average aperture over all angles around the antenna. If a resistor is placed in a  
 613 second cavity, also at temperature T, it will deliver its Johnson-Nyquist noise power [26, 27]

$$P_R = kT\Delta\nu \tag{2.11}$$

614 into a matched transmission line. This is shown in Fig. 2.3. The second law of thermo-  
 615 dynamics makes a very powerful statement here: the net power flow between the antenna  
 616 and terminator must equal 0 if the two temperatures are indeed equivalent. This means  
 617  $P_R = P_A$  or Eq. 2.10 = Eq. 2.12,

$$\langle A_e \rangle \frac{4\pi kT\nu^2}{c^2} \Delta\nu = kT\Delta\nu \tag{2.12}$$

618 or,

$$\begin{aligned}
 \langle A_e \rangle &= \frac{c^2}{4\pi\nu^2} \quad [\text{m}^2] \\
 &= \frac{\lambda^2}{4\pi}
 \end{aligned} \tag{2.13}$$

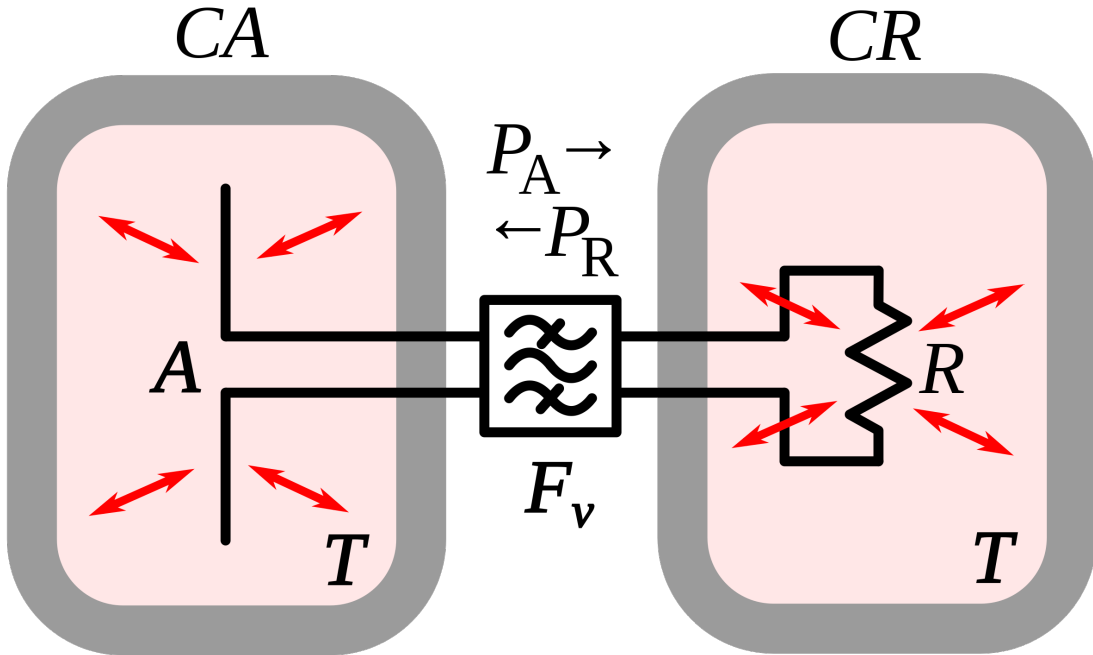


Figure 2.3: An antenna and matched resistor in cavities that are in thermal equilibrium. They are connected by a narrow filter permitting a narrow frequency band  $\Delta\nu$ . Image from Wikipedia, and is similar to the thought experiment proposed by Dicke [28].

619 This allows us to conclude that the power spectral density  $S_{\text{ant}}$  received by an antenna  
 620 surrounded by an isotropic temperature is simply  $kT\Delta\nu$  in the Rayleigh-Jeans limit of room  
 621 temperatures and standard electronic frequencies. This result is independent of frequency,  
 622 which can be understood by the reciprocal frequency dependence of the blackbody radiation  
 623 (Eq. 2.4) and the average effective aperture (Eq. 2.13). The result is an antenna power which  
 624 is equivalent to the well-known result for a resistor at 290 K,

$$S_{\text{ant}} = 3.9 \times 10^{-22} [\text{W/Hz}] = -174 [\text{dBm/Hz}]. \quad (2.14)$$

625 Note that  $S_{\text{ant}}$  indicates power spectral density and should not be confused with  $S$  which

626 indicates a Poynting vector.

627 **2.1.1.3 Dicke radiometer equation**

628 Equation 2.14 gave the mean of a power spectrum that is inherently noisy. We will now  
629 show the origin of this spectrum.

630 An enclosure whose electrically-lossy walls contain free charge carriers at a finite tem-  
631 perature will radiate incoherently by the fluctuation-dissipation theorem. This theorem is  
632 the underlying principle of phenomena such as Brownian motion [29] and Johnson-Nyquist  
633 noise [26, 27], but was not generally proven until 1951 by Callen and Welton [30]. The  
634 random thermal fluctuation of the charge carriers will radiate a black-body spectrum. Ob-  
635 serving the electric field in the time domain, one can imagine the radiation arriving at a  
636 detector at a wide variety of random frequencies and phases. This is incoherent noise in that  
637 at each time domain sample is independent of the one proceeding it <sup>2</sup>. The detector will  
638 produce a voltage that can be modeled as Gaussian with zero mean and standard deviation  
639  $\sigma = \sqrt{S_{\text{ant}} \Delta \nu_{\text{RF}} |Z|}$  where  $Z$  is the system impedance (here  $50 \Omega$ ). This is shown for a room  
640 temperature antenna (or equivalently a room temperature resistor, see Fig. 2.3) in Fig. 2.4.

---

<sup>2</sup>The hidden assumption here is that blackbody radiation is totally incoherent. It actually has a coherence time  $\tau_c \approx 2 \times 10^{-14} \text{ s}$  at 300 K [31]. For this statement to hold, the sample time  $\tau_s \gg \tau_c$ . For run 1A,  $\tau_s = 1/800 \text{ MHz} = 1.25^{-9} \text{ s}$ , 5 orders of magnitude more than  $\tau_c$

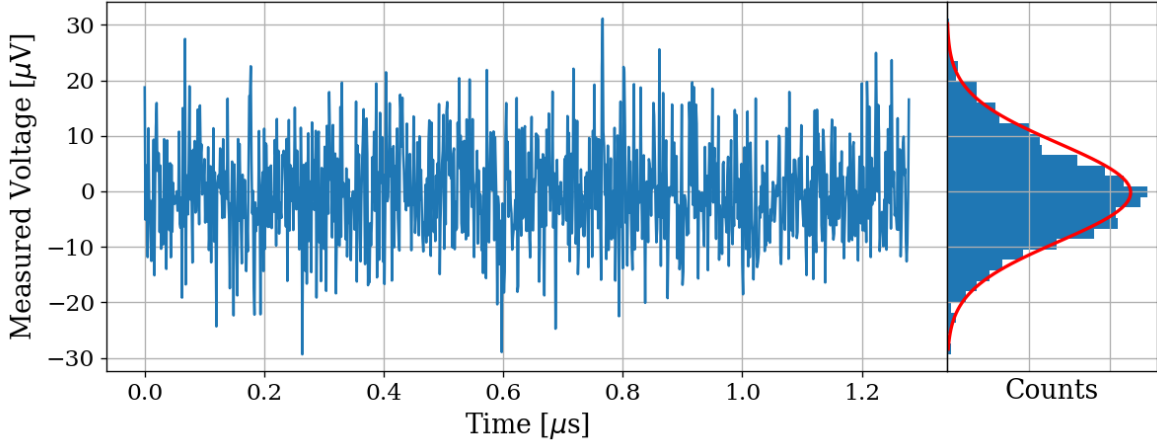


Figure 2.4: Simulated antenna noise voltage at room temperature in the time domain. Sample rate  $\nu_s = 800\text{MHz}$  and number of samples  $N = 2^{10} = 1024$ . Bin width  $\Delta\nu_{\text{RF}} = \nu_s/N \approx 800\text{ kHz}$ . Data are binned and plotted as a histogram to the right. The best fit Gaussian is shown on the histogram in red with  $\mu = -0.199\text{ }\mu\text{V}$  and  $\sigma = 8.86\text{ }\mu\text{V}$ . Counts have been normalized such that the bins add up to unity.

641 The next step is converting this time-domain voltage signal to a frequency-domain power  
 642 spectral density (PSD). The first step is taking a discrete Fourier transform. This is usually  
 643 implemented with an algorithm known as a fast Fourier transform (FFT), so that  $\tilde{V} =$   
 644  $\text{FFT}(V)$ . In order to convert to a power spectrum, a non-trivial normalization prefactor  
 645 must be included;

$$S = \frac{2}{N^2 |Z|} |\Re(\tilde{V})[:N//2]|^2, \quad (2.15)$$

646 where N is the number of samples, Z is the system impedance, and [:N//2] is Python notation  
 647 for the second half of the samples contained in the  $\tilde{V}$  array. Performing this operation on  
 648 the data in Fig. 2.4 yields the data in Fig. 2.5

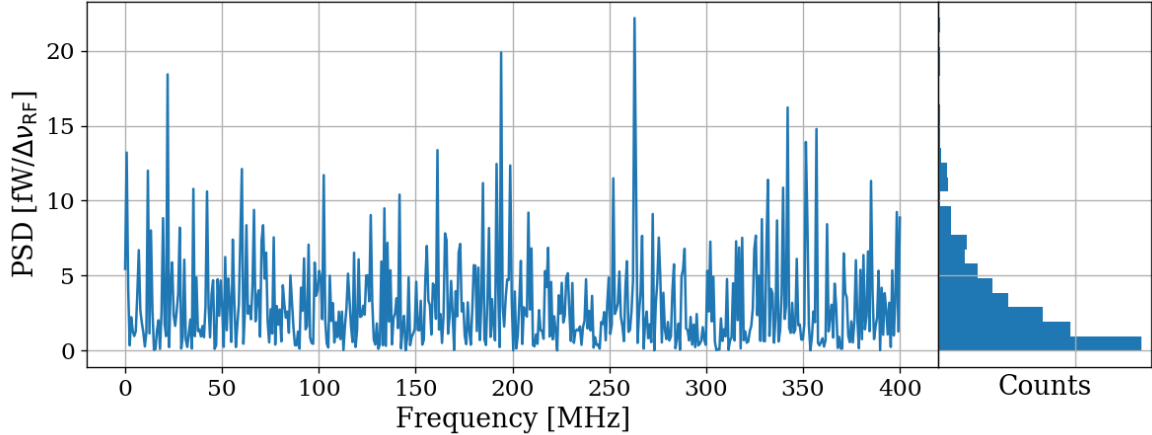


Figure 2.5: Simulated antenna noise power spectral density (PSD) at room temperature in the frequency domain. Sample rate  $\nu_s = 800\text{MHz}$  and number of samples  $N = 2^{10} = 1024$ . Bin width  $\Delta\nu_{\text{RF}} = \nu_s/N \approx 800\text{ kHz}$ . Data are binned and plotted as a histogram to the right. Counts have been normalized such that the bins add up to unity.

649     The peculiar PDF of the histogram shown in Fig. 2.5 is known as a  $\chi^2$  distribution with  
 650     1 degree of freedom and comes about because power is a positive-definite quantity and the  
 651     standard deviation of the PSD is greater than it's mean.

652     However, by averaging many of these power spectra together, the central limit theorem  
 653     dictates that we can expect the resulting PDF to be Gaussian. The transition from  $\chi^2$  to  
 654     Gaussian distributed spectra is shown in Fig. 2.6.

655     Finally, this averaged power spectrum can be modeled with the Dicke radiometer equa-  
 656     tion. The measured power (assuming only thermal noise) is given by

$$P_{\text{ant}} = kT\Delta\nu \left( 1 \pm \frac{1}{\sqrt{\Delta\nu\tau}} \right) \quad [\text{W}]. \quad (2.16)$$

657     Here  $\tau$  is the total acquisition time, and so  $\Delta\nu\tau$  is equivalent to the number of spectra

658 that are averaged together. This can be nondimensionalized and written

$$\frac{P_{\text{ant}}}{kT\Delta\nu_{\text{RF}}} = 1 \pm \frac{1}{\sqrt{N}} \quad [\text{None}], \quad (2.17)$$

659 which will become important during data analysis which is the topic of Sec. 4.2.

660 For the remainder of this thesis, unless otherwise stated, it will be assumed enough  
661 spectra have been averaged together that a PSD is Gaussian and scales with the square root  
662 of total acquisition time according to Eq. 2.16.

663 Thus far the analysis has focused only on thermal noise, however there are other sources  
664 of noise and interfering signals which must be considered, not to mention the actual dark  
665 photon signal.

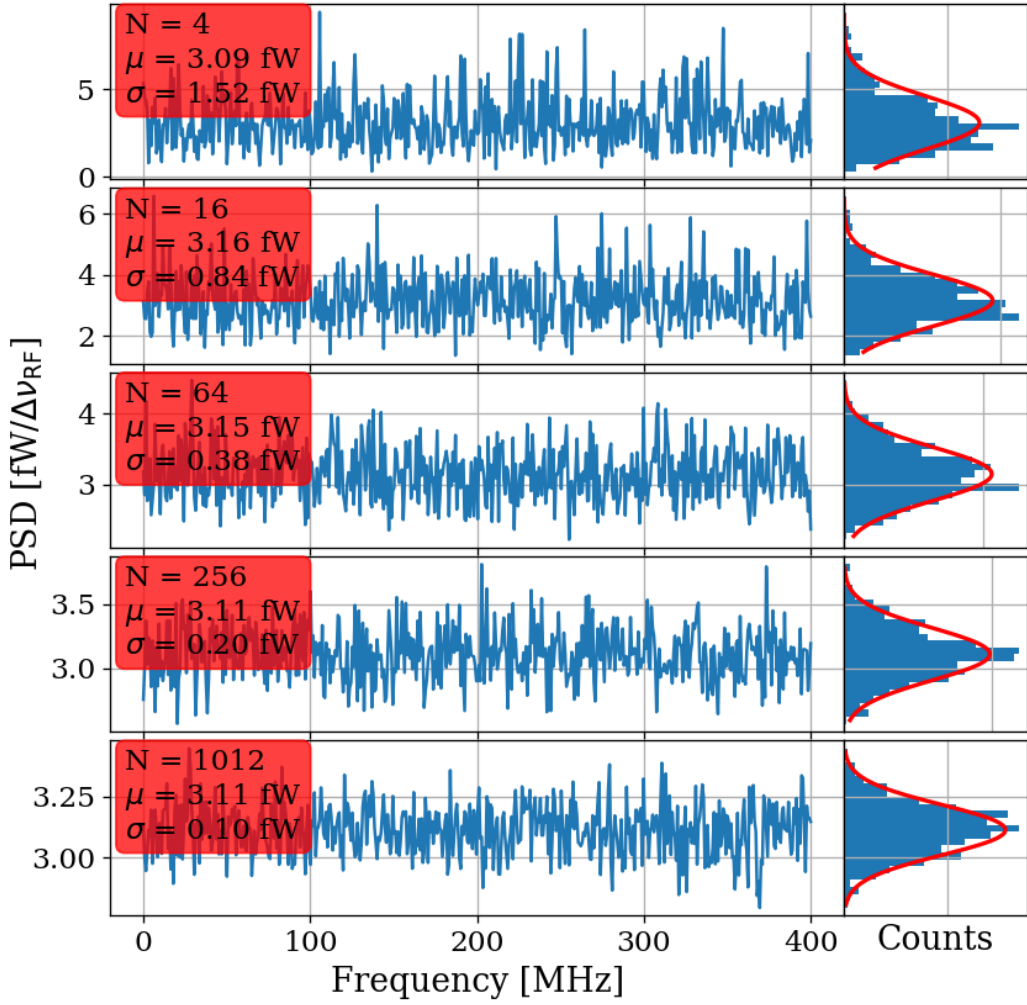


Figure 2.6: Effect of averaging on simulated antenna noise power spectral density (PSD) at room temperature in the frequency domain. Subplots show different numbers of averaged power spectra from  $N = 4$  to 1024. Each subplot shows a factor of 4 times more averaging than the previous one. The Dicke radiometer equation predicts the standard deviation  $\sigma$  will scale like  $N^{-1/2}$  once a large number of averages have been taken such that  $\sigma \ll \mu$ . Sample rate  $\nu_s = 800\text{MHz}$  and number of samples  $N = 2^{10} = 1024$ . Bin width  $\Delta\nu_{\text{RF}} = \nu_s/N \approx 800 \text{ kHz}$ . Data are binned and plotted as a histogram to the right with a best-fit Gaussian shown in red. Counts have been normalized such that the bins add up to unity. Note that the Y-axis scale changes between subplots to show the improvement of the Gaussian fit. The standard deviation is indeed decreasing between plots.

666 **2.1.2 Dark Photon Signal**

667 The electric field of a kinetically mixed dark photon in free space  $\mathbf{E}_{\text{ant}}^{\text{free space}}$  was shown in  
668 Eq. 1.7. In a cavity, the E-field will be enhanced by the quality factor  $Q$  of the cavity. This  
669  $Q$  must be measured or simulated, but for this toy analysis, we will assume it to be known  
670 <sup>3</sup>. The E-field inside the cavity then is

$$\mathbf{E}_{\text{ant}} = \mathbf{E}_{\text{ant}}^{\text{free space}} \sqrt{Q}, \quad (2.18)$$

671 since  $Q$  is proportional to power, i.e.  $\mathbf{E}^2$ . This E-field will then need to be converted from  
672 a wave in the cavity to a wave in a  $50\Omega$  transmission line by an antenna. Similar to the  
673 thermal noise of the previous section, this electric field will be converted via the effective  
674 aperture of the antenna. Similar to  $Q$ , the aperture will be assumed to be known.

675 The total received power from a coherent signal inside the room then is

$$P = \frac{\mathbf{E}_{\text{ant}}^{\text{free space}^2}}{\eta} Q < A_e >, \quad (2.19)$$

676 where  $\eta$  is the impedance of free space.

677 The observed spread of the frequencies of the dark photon is an important effect that  
678 determines system design. In the following paragraphs of this section, several sections of  
679 Gramolin et al. [33] are summarized. Also note that the original calculation for the predicted  
680 line shape appears to be Michael Turner in 1990 [34].

681 A simple model of the dark photon line assumes it is monochromatic, i.e. its line shape  
682 is a delta function in the frequency-domain,

$$\nu_{\text{obs}} = \delta(\nu - \nu_{\text{DP}}). \quad (2.20)$$

---

<sup>3</sup>Typical values are in the ballpark of 100. Some experiments have ultra-high  $Q$  cavities  $\approx 10^{10}$  [32]

683 This is consistent with its production add reference: misalignment mechanism/ch 1.

684 However, when observed in a frame other than its rest frame, the frequency of a (single)

685 dark photon will shift by an amount proportional to its kinetic energy

$$\nu_{\text{obs}} = \left(1 + \frac{v_n^2}{2c^2}\right) \nu_{\text{DP}}, \quad (2.21)$$

686 where  $\nu_{\text{obs}}$  is the observed frequency of the  $n$ th dark photon,  $v_n$  is its velocity,  $c$  is the speed

687 of light, and  $\nu_{\text{DP}}$  is its rest frequency. The end result will be a signal that has some spread

688 in frequency,  $\nu_{\text{DP}}/(\Delta\nu) \equiv Q_{\text{DP}} \approx 10^6$ , with a line shape given by 2.24.

689 By summing over an infinity of dark photons of random phases and velocities (sampled

690 from the relative velocity of the dark matter halo), each with a frequency given by Eq. 2.21,

691 one can construct a PSD of the dark photon signal as measured on earth,  $S$  [W/Hz].

692 When performing a measurement, one records the voltage  $V$  emerging from a detector

693 for a period of time greater than the coherence of the dark photon  $\tau_{\text{FFT}} \gg \tau_c$ . The Fourier

694 transform of  $V(t)$  is denoted  $\tilde{V}(\nu)$

695 The signal will have a total power

$$P_0 = \frac{1}{\tau_{\text{FFT}}} \int_0^{\tau_{\text{FFT}}} \frac{V(t)^2}{|Z|} dt = \int_0^{1/\tau_{\text{FFT}}} S(\nu)^2 d\nu, \quad (2.22)$$

696 which is a statement of Parseval's theorem.

697 The normalized line shape is defined by dividing by  $P_0$ ;  $\lambda(\nu) \equiv S(\nu)/P_0$ . This has the

698 property of being normalized to unity,

$$\int_0^\infty \lambda(\nu) d\nu = 1. \quad (2.23)$$

699 Finally, the result for this normalized line shape is

$$\lambda(\nu) = \frac{2 c^2}{\sqrt{\pi} v_0 v_{\text{lab}} \nu_{\text{DP}}} \exp \left( -\frac{\beta^2 v_0^2}{4 v_{\text{lab}}^2} - \frac{v_{\text{lab}}^2}{v_0^2} \right) \sinh \beta \quad \left[ \frac{1}{\text{Hz}} \right], \quad (2.24)$$

700 where  $|v_0| \approx 220$  km/s is the circular rotation speed of the Galaxy at the radius of the sun  
701 (approximately 8 kpc),  $v_{\text{lab}} \approx 233$  km/s is the relative velocity of the Sun to the rest frame  
702 of the Galaxy and

$$\beta \equiv \frac{2 c v_{\text{lab}}}{v_0^2} \sqrt{\frac{2 (\nu - \nu_{\text{DP}})}{\nu_{\text{DP}}}}.$$

703 Equation 2.24 is used to generate Fig. 4.14. Note the quality factor  $Q_{\text{DP}} \approx 10^6$  as  
704 mentioned above.

### 705 2.1.3 Radio Frequency Interference

706 Radio Frequency Interference (RFI) includes any coherent interfering signals which can be  
707 detected by the experiment. While noise is better described as a power spectral *density*  
708 [W/Hz] or electric field *density* [V/(m  $\sqrt{\text{Hz}}$ )], RFI is made up of more narrow lines and is  
709 discussed in terms of power [W] or electric field [V/m]. In this experiment, RFI is mitigated  
710 through the shielding effectiveness (SE) of the cavity. SE measurements and more details  
711 about local RFI are discussed further in Sec. 2.5.1 and Sec. 3.2, and a plot of the local RFI  
712 spectrum is shown in Fig. 3.14.

713 The peak RFI spike is at 186 MHz and approximately 100  $\mu\text{V}/\text{m}$ , an energy density  
714 of roughly  $10^{-11}$  W/m<sup>2</sup>. This will be reduced by the SE of the room (roughly 120 dB at  
715 200MHz, see Fig. 3.11), but just like a coherent dark photon, it will be enhanced by the

716 Q/effective aperture. This will be right on the edge of detection, but in the actual data run,  
 717 it was not detected.

718 **2.1.4 Amplifier Chain Noise<sup>4</sup>**

719 Any amplifier will have some noise which it adds to an incoming signal which will degrade  
 720 the signal-to-noise ratio (SNR) of the measurement <sup>5</sup>. A low noise amplifier (LNA) is an  
 721 amplifier that has been specifically designed to minimize the noise contribution. This process  
 722 is shown schematically in Fig. 2.7.

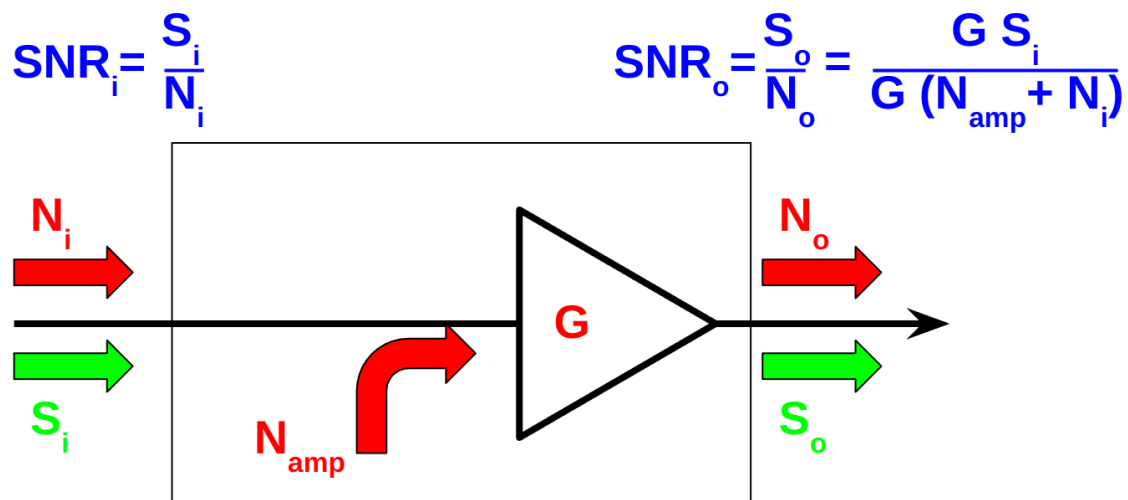


Figure 2.7: Schematic of LNA (with power gain G) adding input referred noise  $N_{amp}$ . Since  $N_{amp}$  is referred to the input, it can be directly added to the input noise which is itself input-referred. The ideal, noiseless amplifier is represented by the triangle, while the physical amplifier, including noise, is contained in the rectangle.

---

<sup>4</sup>Code for this section can be found at: <https://github.com/josephmlev/darkRadio/tree/master/thesis/ch2/CH2.ipynb>

<sup>5</sup>A great lecture on the subject by Prof. Greg Durgin can be found at [35]

723        The performance of an LNA is generally evaluated by its noise factor ( $F$ ).  $F$  is defined  
 724   to be the ratio of the SNR at the input of an LNA to that at its output.

$$\begin{aligned}
 F &\equiv \frac{\text{SNR}_i}{\text{SNR}_o} \\
 &= \frac{S/N}{[S G]/[(N + N_{\text{amp}})G]} \\
 &= \frac{1}{1/[1 + N_{\text{amp}}/N]} \\
 &= 1 + \frac{N_{\text{amp}}}{N},
 \end{aligned} \tag{2.25}$$

725   where  $S$  and  $N$  are the signal and noise [W] presented to the LNA respectively,  $N_{\text{amp}}$  is  
 726   the input-referred noise added by the LNA, and  $G$  is the power gain. By factoring out the  
 727   implicit  $k \Delta\nu$  from  $N = kT\Delta\nu$ , we find

$$F = 1 + \frac{T_e}{T_0}, \tag{2.26}$$

728        where  $T_e$  is the noise temperature of a device and  $T_0$  is the temperature of the system  
 729   being measured by the LNA.

730        Note that following the same derivation as Eq. 2.25, it is simple to show that the noise  
 731   figure of an attenuator at temperature  $T$  with loss  $L$  is given by

$$F_{\text{att}} = 1 + \frac{(L - 1)T}{T_0}, \tag{2.27}$$

732        where  $T_0$  is the reference temperature defined above. If  $T = T_0$ , Eq. 2.27 simplifies to  
 733    $F_{\text{att}} = L$

734 In order to standardize device specifications for across system applications, it is common  
 735 to choose a reference temperature  $T_0$  of 290K. If not specified, it is generally safe to assume  
 736 this has been done.

737 Noise factor is simply defined in terms of noise figure,

$$\text{NF} \equiv 10\log_{10}(F). \quad (2.28)$$

738 When working with LNAs, all three measurements ( $T_e$ ,  $F$  and NF) are frequently used,  
 739 and one must use Eqs. 2.26 and 2.28 to convert between them.

740 One important generalization is that of a cascaded series of amplifiers, shown schemati-  
 741 cally in Fig. 2.8.

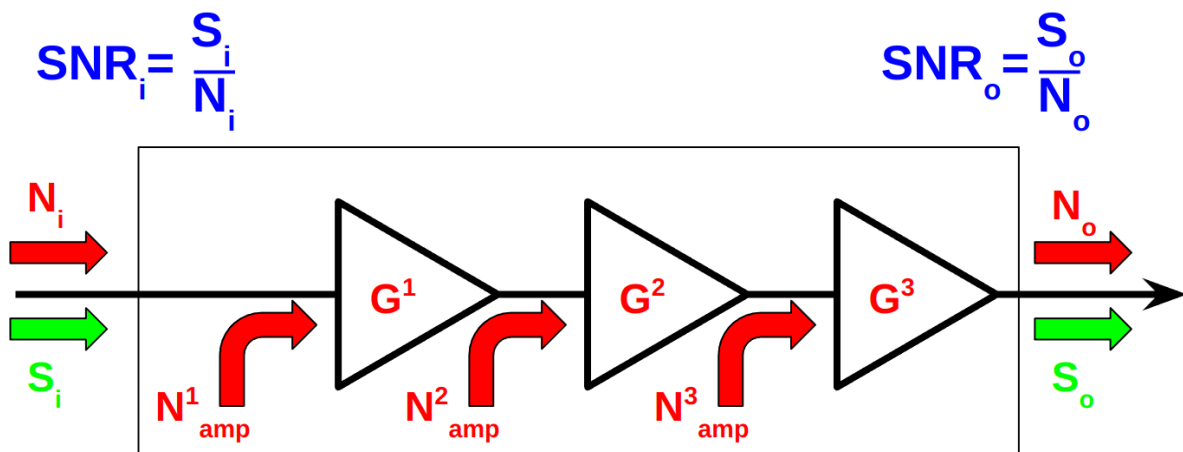


Figure 2.8: Schematic of cascade of  $n = 3$  amplifiers and their added noise  $N_{\text{amp}}^n$ . Each amplifier has a gain of  $G^n$ . The SNR at the output is derived in Eq. 2.29. Note that superscripts in the figure and caption refer to the index of each component and are not exponents.

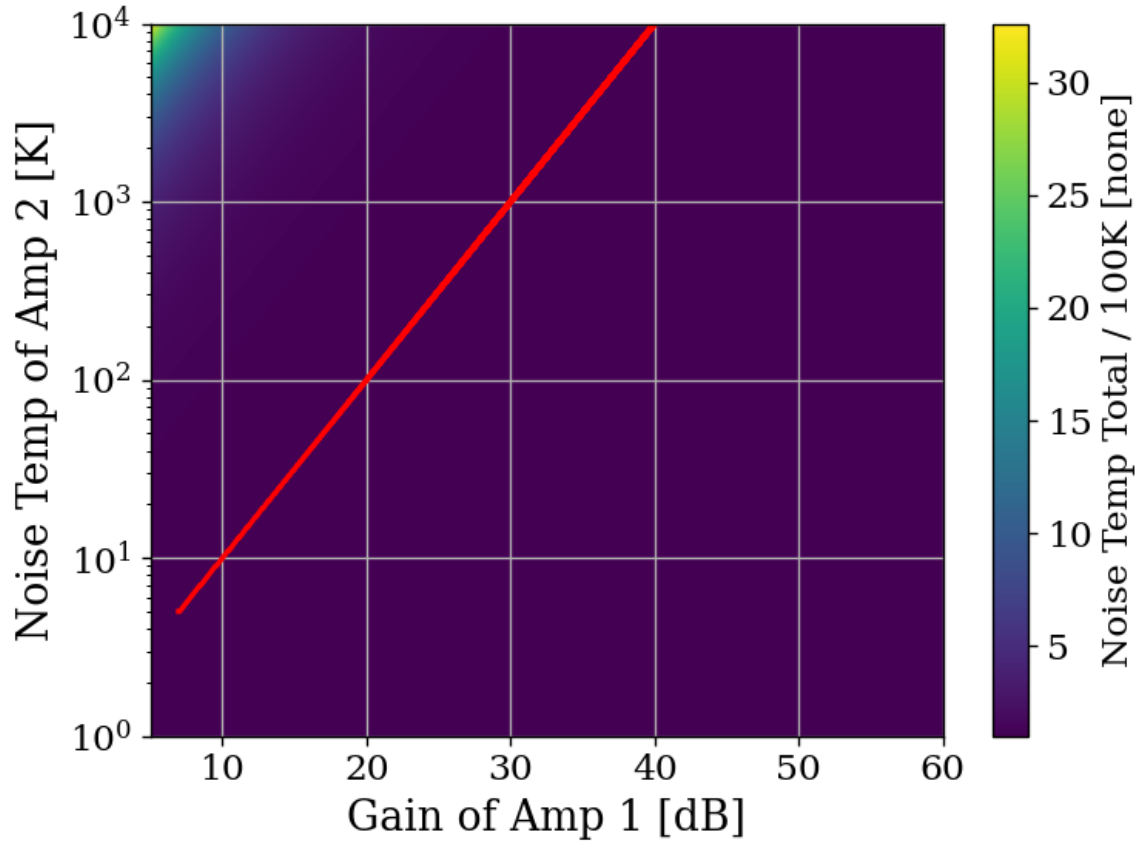


Figure 2.9: Cascaded noise temperature for a system with  $n = 2$  amplifiers, normalized to noise temperature of amplifier 1 (the so-called LNA) = 100 K. Shown schematically (for  $n = 3$ ) in Fig. 2.8. The first amplifier's noise temperature and gain (40 dB and 100 K, respectively) are roughly equivalent to the LNA used in phase 1A of the experiment[36]. The red curve shows where the system's noise temperature is 1% higher than LNA noise temperature. This shows that for a 40 dB, 100 K LNA, in order to change the system noise temperature by 1 K, a second-stage amplifier with a noise temperature of  $10^4$  would be required. Secondary amplifiers with noise temperatures closer to 500 K are realistic and inexpensive. Note that the red curve should continue but is cut off as a plotting artifact.

742 Here the total noise figure of  $n$  amplifiers can be shown to be

$$F_{\text{total}} = F_1 + \frac{F_2 - 1}{G_1} + \frac{F_3 - 1}{G_1 G_2} + \cdots + \frac{F_n - 1}{G_1 G_2 \cdots G_{n-1}}, \quad (2.29)$$

743 following the same derivation as Eq. 2.25. Since the noise temperature of a system depends

744 on the noise temperature a given amplifier divided by he gain which precedes it, a front-end  
745 LNA with modest gain ensures the total noise figure of the the system is equal to it's noise  
746 figure to very good approximation. This is shown in Fig. 2.9. We will use this approximation  
747 and assert

$$\text{Amp Chain Noise} = \text{LNA Noise}, \quad (2.30)$$

748 Where LNA here is taken to mean the first gain stage in the amplifier chain  
749 Noise figures are typically frequency dependent, though they vary slowly over frequency  
750 and can be approximated as constant over narrow frequency bands. Noise figures are typically  
751 given on the data sheet of the LNA [36], but can also be measured. Measurement of LNA  
752 noise is covered in Sec. 3.1.1 and is shown in Fig. 3.4 (which is in good agreement with the  
753 LNA's data sheet [36]).

754 The power contributed by the LNA's noise is simply given by

$$P_{\text{LNA}} = kT_e\Delta\nu \quad (2.31)$$

755 This is again the mean of a fluctuating power, just as 2.16.

### 756 2.1.5 ADC effects

757 “ADC effects” is a catch-all term that refers to power introduced by an analog-to-digital  
758 converter. It contains are a three components, listed in order of importance;

$$\text{ADC Effects} = \text{Spurious Signals} + \text{ADC Noise Floor} \quad (2.32)$$

759       Equation 2.29 shows that (power) gain  $G$  introduced before a noisy element in the RF  
760   chain will reduce the relative contribution of that noise (power) by a factor of  $G$ . The same  
761   idea applies to ADC effects, though one must be careful with the language used to describe  
762   this; spurious *signals* are not noise, and the experiment's output *is* mostly noise.

763   **2.1.5.1 Spurious signals**

764   Spurious signals (also known as spurs) are coherent signals that are introduced into the signal  
765   path at the ADC<sup>6</sup>. They are likely caused by candidates caused by RFI due to various clocks  
766   in the PC in close proximity to the ADC. The coherence of spurs means they will pop up  
767   above the noise with more averaging. Spurs don't degrade the SNR of the experiment in  
768   the same way a noisy amplifier chain would; instead, they produce false positive candidates,  
769   which must be excluded, similar to RFI discussed in Sec. 2.1.3. Similar to ADC noise,  
770   they can be measured easily by terminating the input of the ADC and scanning. They are  
771   investigated in Sec. 3.3.2 and shown in Fig. 3.15, where they are shown to be nearly negligible,  
772   having been mitigated by the gain of the system. There is a single spur detected after a few  
773   days (see Sec. 4.2.5), but for this simple analysis, we will assume spurs are negligible.

774   **2.1.5.2 ADC noise**

775   ADC noise can simply be measured by terminating the input and taking a scan. This is the  
776   same procedure used to measure spurs and can be seen in Fig. 3.15. The result is that ADC

---

<sup>6</sup>Note that these spurs described here are not the same as the spurs that are described by the ADC specification *spur free dynamic range* (SFDR). SFDR is measured in dBc, i.e. *relative* to a carrier. Since our "carrier" is broadband noise, each bin produces some spurs, which are -66 dBc [37] relative to itself. The aggregate of these spurs is also broadband and averages down with the experiment's noise. The SFDR spurs are negligible for an experiment that looks at a noise-like background.

777 noise is  $\approx -130\text{dBm}/47.7\text{Hz}$ ; a factor of  $10^5$  lower than the thermal noise of the experiment  
 778  $\approx -81\text{dBm}/47.7\text{Hz}$ , both output-referred<sup>7</sup>, which agrees with the ADC's data sheet [37].  
 779 Since ADC noise follows the same scaling as the experiment's thermal noise (Eq. 2.16), this  
 780 factor of  $10^5$  is independent of averaging, and ADC noise is totally negligible.

## 781 2.2 Toy Analysis<sup>8</sup>

782 With each of the terms of Eq. 2.1 defined in the previous section, we will now perform and  
 783 view several simulations of a simplified dark photon signal on a simplified background. This  
 784 section should provide intuition about the process of detecting a weak, narrow signal on a  
 785 background PSD of thermal noise. It is assumed the noise has been averaged a sufficient  
 786 number of times such that its PDF is Gaussian (discussed in Sec. 2.1.1.3). Furthermore,  
 787 following the discussion of Sec. 2.1, Eq. 2.1 can be simplified by setting RFI and ADC  
 788 Effects to zero and combining Thermal Noise (300 K) with Amp Chain Noise (100 K) into a  
 789 single term which represents the total of the noise in the whole system,  $S_{\text{sys}} = P_{\text{sys}}/\Delta\nu_{\text{RF}} =$   
 790  $k(T_{\text{ant}} + T_{\text{LNA}})$ . With these simplifications, the input-referred measured power of Eq. 2.1  
 791 reduces to

$$P_i = P_{\text{DP}} + kT_{\text{sys}}\Delta\nu_{\text{RF}} \left[ 1 \pm \frac{1}{\sqrt{N}} \right], \quad (2.33)$$

792 where  $T_{\text{sys}} \equiv 400$  K, realistic for the experiment that is being simulated. Also, note that this  
 793 equation assumes the dark photon's line shape is much more narrow than  $\Delta\nu_{\text{RF}}$  such that the

---

<sup>7</sup>Technically it doesn't matter where they are referred since they are taken in ratio. As long as they are referred to the same point!

<sup>8</sup>Code for this section can be found at: <https://github.com/josephmlev/darkRadio/tree/master/thesis/ch2/toyAnalysis.ipynb>

794 measured input-referred dark photon power is independent of  $\Delta\nu_{\text{RF}}$ . In the simulations, the  
795 line shape will be modeled as a delta function as in Eq. 2.20. The signal will be introduced  
796 simply by adding some power in a single bin to a Gaussian background in the frequency-  
797 domain. Performing an FFT on a perfect (discretized) sine wave can cause it's power to  
798 be split among adjacent bins depending on the ratio of the sample rate to the sine wave's  
799 frequency. This can be minimized by windowing the time-domain data as is discussed in  
800 Ch. 2 Sec. 2 of Ben Godfrey's thesis [38]. This effect is avoided by working in the frequency  
801 domain and adding power to a single bin which is the method used here. A reminder that  
802 throughout this thesis, code is available at github and is linked in the footnote of each section  
803 title.

804 With a simple simulation framework in place, we can now begin to generate signal-  
805 containing-spectra. Figure 2.10 qualitatively shows the 400 K system noise (input-referred  
806 antenna plus LNA) averaging down, leaving a small signal visible. Further subsections in  
807 this section will quantify this.

808 With a basic conceptual framework in place, it is now simpler to quantify signal detection  
809 and the uncertainty on how many averages are required to detect a signal and have that  
810 detection be significant in that it isn't a random fluctuation (false positive).

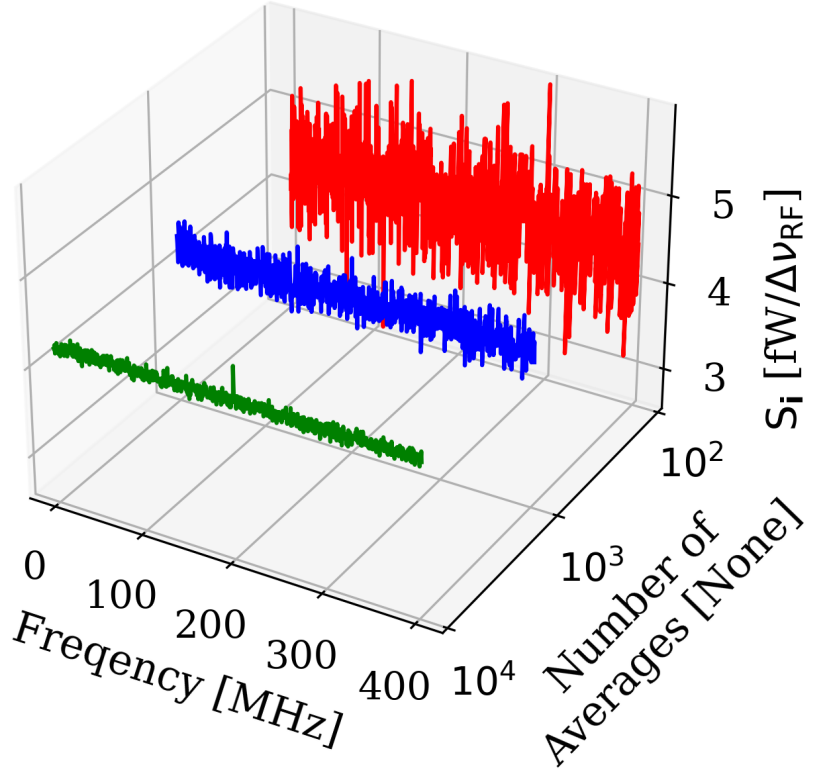


Figure 2.10: Input-referred power spectral density from simplified simulation illustrating noise averaging down to reveal a persistent, software-injected, dark photon proxy signal. The red, blue and green spectra represent 100, 1,000 and 10,000 averages, respectively. The power of the signal  $P_{DP}$  is set to 0.4 fW and it only occupies a single bin. The mean of the noise is  $\approx 4.3 \text{ fW}/\Delta\nu_{RF}$  where  $\Delta\nu_{RF} \approx 0.78 \text{ MHz}$ . The standard deviation ranges between  $0.41 \text{ fW}/\Delta\nu_{RF}$  and  $0.041 \text{ fW}/\Delta\nu_{RF}$  for 100 and 10,000 averages respectively. Note that this factor of 10 reduction in noise is predicted by the Dicke radiometer equation Eq. 2.16 for a factor of 100 times more averaging, as is shown in the red and green curves. Noise represents a 300 K antenna into a 100 K LNA for a total system temperature of 400 K. Signal is in a single bin at 200 MHz with a delta function line shape, defined in Eq. 2.20.

### 811 2.2.1 Signal significance

812 The problem of the extraction of signal from noise is fundamentally a statistical one since,  
 813 in general, both the signal and noise are random variables. A method for computing a

814 *significance threshold* (ST) must be established, such that any bin containing more power  
815 than this threshold is X % significant. In this way, it is possible to have some known  
816 confidence a given signal was not just a random fluctuation.

817 The probability that all N bins are less than  $z$  standard deviations  $z\sigma$  for a standard  
818 Gaussian distribution is given by

$$P(\max < z\sigma) = \left\{ \frac{1}{2} \left[ 1 + \operatorname{erf} \left( \frac{z}{\sqrt{2}} \right) \right] \right\}^N, \quad (2.34)$$

819 where  $P$  is the probability,  $\operatorname{erf}(z)$  is the standard error function and  $z$  is real. Setting  
820 this equal to 100%–X (where X is the *significance* or the desired probability a fluctua-  
821 tion crosses the  $z\sigma$  threshold assuming no signal), and inverting  $\operatorname{erf}(z)$  yields a significance  
822 threshold (ST). A convenient significance that was used in [39] is X = 5% corresponding to  
823 a 5% probability that an observed fluctuation above this ST is due to chance rather than a  
824 significant effect (i.e., a signal). A 5% ST for  $2^{10}/2 = 512$  frequency bins<sup>9</sup> works out to  $3.9\sigma$ .

825 It should be noted that it is common in physics to discuss “ $5\sigma$  significance”. This means  
826 that a given experiment has a  $1 - \operatorname{erf}(5/\sqrt{2})$  probability (about 1 in  $3 \times 10^6$ ) of a false positive.  
827 The analysis of these normal spectra involves testing many independent frequency bins to see  
828 if any one of them exceeds some threshold. It is helpful to view these bins as “independent  
829 experiments”, each involving a random draw from the same parent Gaussian distribution.  
830 In this context, we discuss global significance (all of the bins) in contrast to local significance  
831 (a single bin). Setting a global 5% significance threshold is equivalent to setting a local

---

<sup>9</sup>Note that a real FFT produces half the number of frequency bins as an output compared to the time domain sample it received, hence the factor of 2 established in Fig. 2.4

832 threshold of  $3.9\sigma$  given 512 bins.

833 One concept that can assist in choosing the significance is known as the *cost* of a decision.

834 If an experiment requires a facility that charges by the hour and where the schedule is  
835 set years in advance, a false positive is quite expensive since it will lead to publicity and,  
836 ultimately, humiliation. A follow-up experiment will have to take out more expensive time  
837 to verify the results, and until that happens, theorists will spend their time rewriting physics  
838 to explain the result of a random fluctuation. In this case, the global significance should  
839 be quite low to avoid these high-cost outcomes, hence the  $5\sigma$  discussed in the previous  
840 paragraph.

841 In the case of the dark radio experiment, a false positive is quite inexpensive. If a signal  
842 is detected, just repeat the experiment. For run 1A, this is 9 days of averaging which is  
843 mostly passive and is little more than an annoyance. If a signal is detected at the same  
844 frequency, things become interesting. This concept of cost is discussed formally in Appendix  
845 1 of Extraction of Signals From Noise by Wainstein and Zubakov [40].

846 For this reason, a significance of 5 % (i.e. 5 % chance of a false positive) is acceptable  
847 for this experiment, where it is certainly not acceptable at the LHC.

#### 848 2.2.1.1 Computing an exclusion limit

849 With the significance threshold (ST) defined for a spectrum containing a signal in the previ-  
850 ous subsection, we turn briefly to the concept of an exclusion limit. In the actual experiment,  
851 no signals were detected. In this case, the null result must be translated into an exclusion  
852 limit, as in Fig. 5.2. While this section on toy analysis looks at small signals riding on noise

853 spectra, it can be easy to lose sight of the fact that no signal was observed.

854 It is tempting to draw a line above the spectrum, claim no signals were observed above  
855 it, and cite that as the exclusion limit. This is the red dashed line in Fig. 2.11. However,  
856 this line is riding on the thermal background and is actually significantly higher than the  
857 true exclusion limit, which is shown in dashed green. The mean  $\mu$  must be subtracted from  
858 this upper (red) line to compute the exclusion limit. In Fig. 2.12, the exclusion limit is  
859 pushed down with additional averaging, resulting in the detection of a small signal shown as  
860 an orange dot. The frequency-dependent exclusion limit from the actual run 1A data run is  
861 shown in Fig. 4.8.

862 With the derivation of the significance threshold complete, the next subsection will focus  
863 on predicting the amount of time.

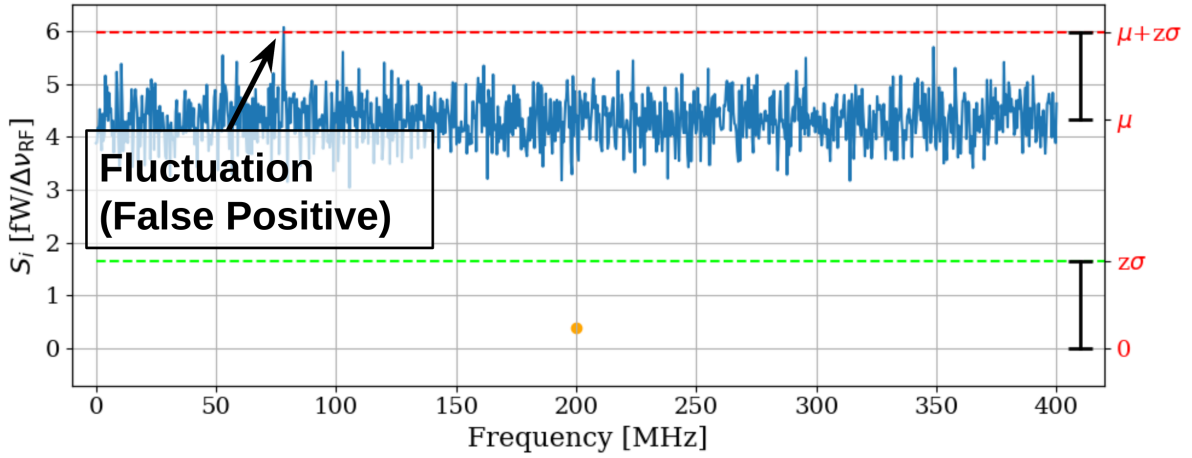


Figure 2.11: Simulated, input-referred noise spectrum containing small signal at 200MHz. The signal power = 0.4 fW, system temperature = 400 K and  $N_{avg} = 100$ ; the same as is shown in the red spectrum of Fig. 2.10. The 0.4 fW signal is shown as an orange point. This power is added to the random background, so the measured power in the bin at 200 MHz is a Gaussian random variable given by Eq. 2.33; the mean is shifted up by the power contained in the signal. The dashed red line shows  $\mu + z\sigma$ , where  $z$  was derived in section 2.2.1. The detection threshold (dashed green line) is the red line minus the mean,  $(\mu + z\sigma) - \mu = z\sigma$ . This shows that the detection threshold is set by *fluctuations* of the measured power spectrum and not its mean. Note the detection at approximately 75 MHz; this is a random fluctuation and is expected to occur in 5 out of 100 simulations of these spectra since the significance used to calculate the ST was set at 5%.

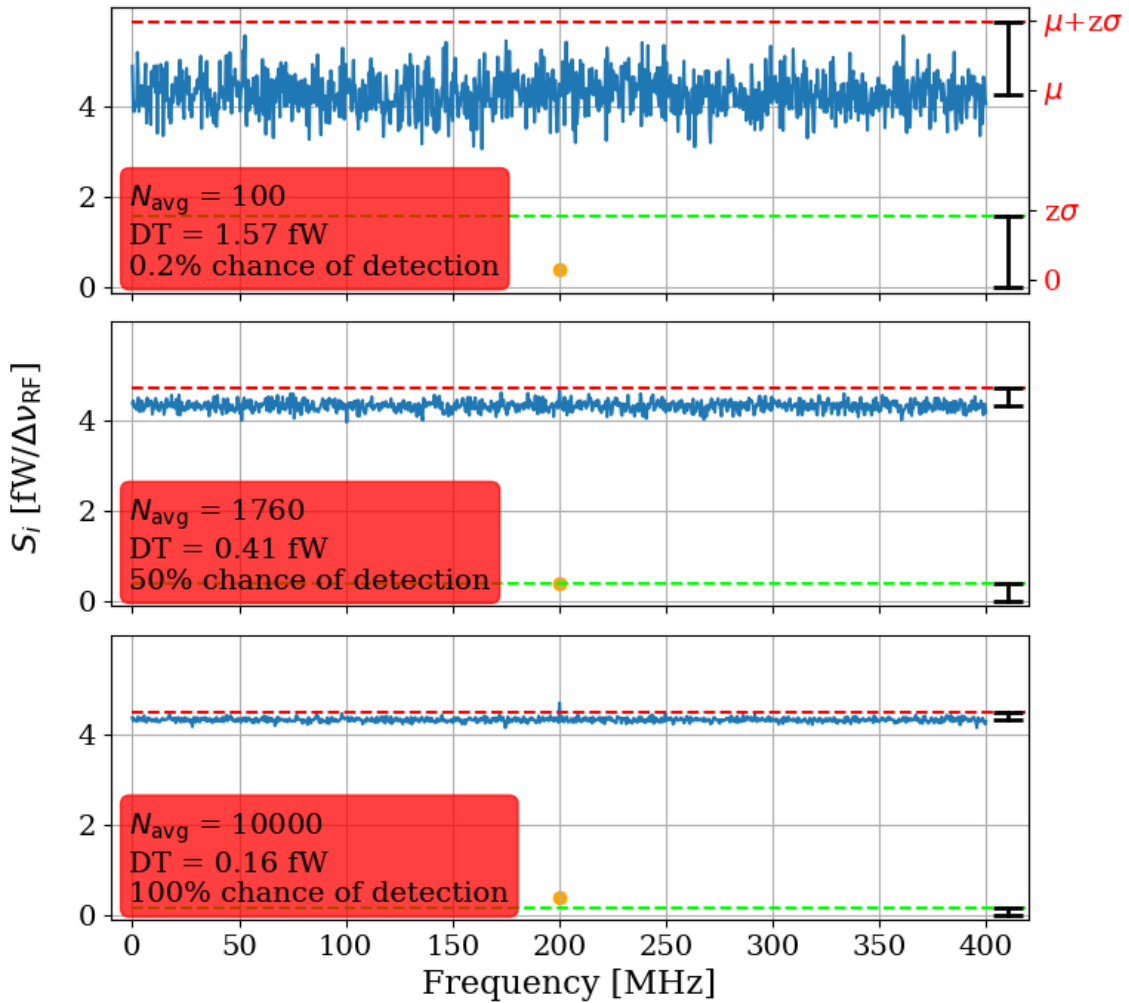


Figure 2.12: Simulated, input-referred noise spectrum containing small signal at 200MHz. The signal power = 0.4 fW, system temperature = 400 K and  $N_{avg}$  = 100, 1,760 and 10,000; the first and last are shown as the red and green spectra respectively in Fig. 2.10. The 0.4 fW signal is shown as an orange point. The chance of detection is computed via a simple Montie Carlo where 100,000 similar spectra containing noise and signal are generated, and the number of times the measured power at 200 MHz is greater than  $\mu + z\sigma$  (red dashed line). The full set of statistics from this Montie Carlo is shown in Table 2.1. The detection threshold (DT, dashed green line) is  $(\mu + z\sigma) - \mu = z\sigma$ . Note that red labels on the right Y-axis are suppressed for the second and third subplots to prevent clutter, but they are the same as the first subplot

864 **2.2.2 Predicted time to detection**

865 To conclude this subsection, Fig. 2.13 fills in the gaps between the three sub-plots shown  
866 in Fig. 2.12. The continuous detection threshold is shown to decrease following  $1/\sqrt{N}$   
867 shape given by Eq. 2.16. The intersections with this curve and the  $1-\sigma$  uncertainty of the  
868 background give the  $1-\sigma$  uncertainty on the number of averages required for a known signal  
869 and background. Table 2.1 summarizes the statistics for the probability of detection for a  
870 few numbers of averages.

Number of Averages	True Pos. [%]	False Neg. [%]	False Pos. [%]	True Neg. [%]
100	0.2	99.8	5.7	94.3
971	16.3	83.7	5.5	94.5
1,760	49.8	50.2	5.7	94.3
2,782	83.8	16.2	5.7	94.3
10,000	100.0	0.0	5.6	94.4

Table 2.1: Statistics of simple Monte Carlo simulation for the probability of signal detection in the toy analysis. Number of averages chosen based on Fig. 2.13. 100 and 10,000 averages show extreme cases, 1760 is a 50% chance of detection, and the two remaining values show the  $\pm 1\sigma$  uncertainty band (shaded red region in Fig. 2.13).

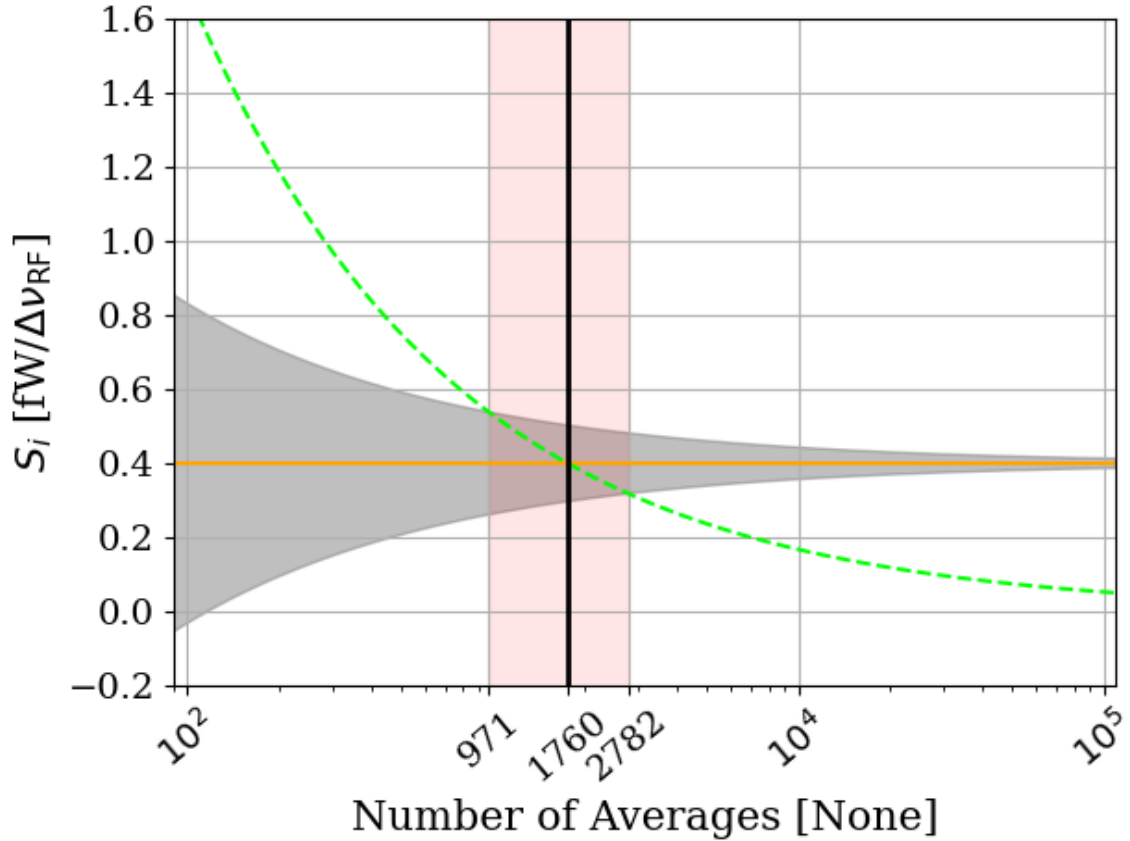


Figure 2.13: Predicted time to detection for the toy analysis spectra shown throughout this section. This is a companion to Fig. 2.12 and shows all numbers of averages between the three subplots shown in that figure, though only at a single frequency bin; 200 MHz in the case of the previous figures in this section. Orange line represents the known, injected signal, shown as orange points in Fig. 2.12. Gray shaded region shows the standard deviation of the noise  $\sigma$ , which is equivalent to the uncertainty on the measured power. It is given by Eq. 2.16, and scales with the square root of time. Dashed green curve is the exclusion limit defined in Sec. 2.2.1.1. It is also shown as a dashed green line in Fig. 2.12. Finally, the red shaded region shows the intersection of the exclusion limit (dashed green) with measurement uncertainty (shaded gray), which gives the  $\pm 1\sigma$  uncertainty on the number of averages required to detect the signal. The detection statistics from a simple Monte Carlo simulation at a few points from this plot are shown in Tab. 2.1. This figure is a recreation of Fig. 3 in [4].

## 871 2.3 Thermal Noise in a Cavity: Thermal Wiggles

872 This section is concerned with the topic of variations of thermal noise emerging from a cavity;  
873 “Thermal Wiggles”. Throughout this experiment, this was a challenging concept since the  
874 theory outlined in Sec. 2.3 predicts the experiment will measure a frequency-independent  
875 noise spectrum, and it doesn’t. This theory will be expanded upon, the data that seem  
876 not to conform to this theory will be presented, the reasons for this disagreement will be  
877 discussed, and finally, an experiment that tests this understanding will be presented.

### 878 2.3.1 Theory of thermal radiation in a cavity

879 In his 1946 paper The Measurement of Thermal Radiation at Microwave Frequencies [28],  
880 Robert Dickie presented a thought experiment to derive the aperture of a matched antenna  
881 from thermodynamic arguments. This was previously discussed in Sec. 2.1.1.2.

882 To recap the argument; if an antenna (in a black cavity) and matched load are matched  
883 to a transmission line and in thermal equilibrium (the situation presented in Fig. 2.3), the  
884 net power flow in the line must be zero by the second law of thermodynamics. If there was  
885 a power flow, one of the environments would warm up, resulting in spontaneous pumping of  
886 heat. An interesting way to model this situation is by treating the antenna as an aperture  
887 in the cavity, as pointed out in [41].

888 A simpler model removes the antenna and load altogether. Although removal of the  
889 antenna also removes the ability to perform the measurement, this is a useful thought exper-  
890 iment. In Fundamentals of Statistical and Thermal Physics [42], F. Reif uses four examples

891 to explore the radiation field  $f_\alpha(\kappa, \mathbf{r})$  (wave vector  $\kappa$  at position  $\mathbf{r}$  with polarization  $\alpha$ )  
 892 within cavities connected by an aperture (see Fig. 2.14). All cavities and materiel contained  
 893 within them are presumed to be in thermal equilibrium. As we shall see, this function is  
 894 independent of position, direction, polarization and specifics of the cavity. It can be written  
 895 simply as  $f(|\kappa|)$ , where the dependence on wave number is simply given by Eq. 2.6.

$$f_\alpha^{(1)}(\kappa) = f_\alpha^{(2)}(\kappa)$$

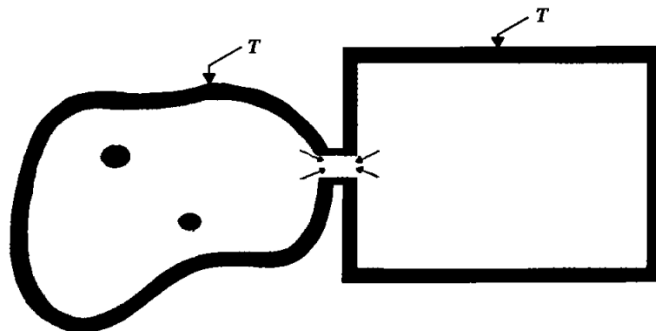


Figure 2.14: Two cavities in thermal equilibrium of arbitrary shape, material and physical contents contain equivalent radiation fields  $f_\alpha(\kappa, \mathbf{r})$ . Figure from Reif [42].

896 1. **Independence of Position:** The radiation field inside an enclosure is homogeneous,  
 897 meaning  $f_\alpha(\kappa, \mathbf{r}) = f_\alpha(\kappa)$ , independent of position  $\mathbf{r}$ . If the radiation field depended  
 898 on position, two identical bodies at temperature  $T$  placed at different points in the  
 899 enclosure would absorb different amounts of radiation, leading to a temperature dif-  
 900 ference.  
 901 2. **Independence of Direction:** The radiation field is isotropic, meaning it depends  
 902 only on  $|\kappa|$  and not its direction. If this were not true, then bodies placed in the  
 903 enclosure would absorb different amounts of energy based on orientation.

904     3. **Independence of Polarization:** The radiation field is unpolarized, meaning  $f(|\kappa|)$   
905       is independent of the polarization index  $\alpha$ . If it depended on polarization, bodies  
906       surrounded by polarizing filters would absorb different amounts of radiation depending  
907       on the orientation, leading to temperature differences.

908     4. **Independence of Enclosure Shape and Contents:** The function  $f(|\kappa|)$  is inde-  
909       pendent of the shape, volume, and material of the enclosure, as well as the bodies  
910       contained within. The argument is that if  $f^{(1)}(|\kappa|)$  and  $f^{(2)}(|\kappa|)$  were different for two  
911       enclosures at the same temperature  $T$ , then connecting them would result in unequal  
912       radiation transfer. Therefore,  $f(|\kappa|)$  must be the same across different enclosures.

913       To further flush out argument four, picture a photon entering a metallic cavity (emissivity  
914        $< 1$ ) through a small hole as in Fig. 2.15. At each bounce, the photon has a probability of  
915       absorption given by the emissivity (a photon hitting a perfect black body has a 100% chance  
916       of being absorbed). As long as the geometries of the cavity and aperture allow a photon to  
917       bounce many times before it escapes, even a highly reflective cavity will behave like a black  
918       body. This is because when a photon enters, it is likely to be absorbed and a new photon will  
919       be emitted with a random wavelength drawn from the blackbody spectrum corresponding  
920       to the temperature of the walls. (Fig. 2.2).

921       The conclusion is rather surprising; a cavity with a small aperture will behave as a  
922       black body, and the spectrum emanating from a black body is a universal function that is  
923       independent of the cavity and its modes. Therefore, **a well-matched antenna in a cavity**  
924       **will not measure the modal structure of the cavity.** This seems to defy intuition.

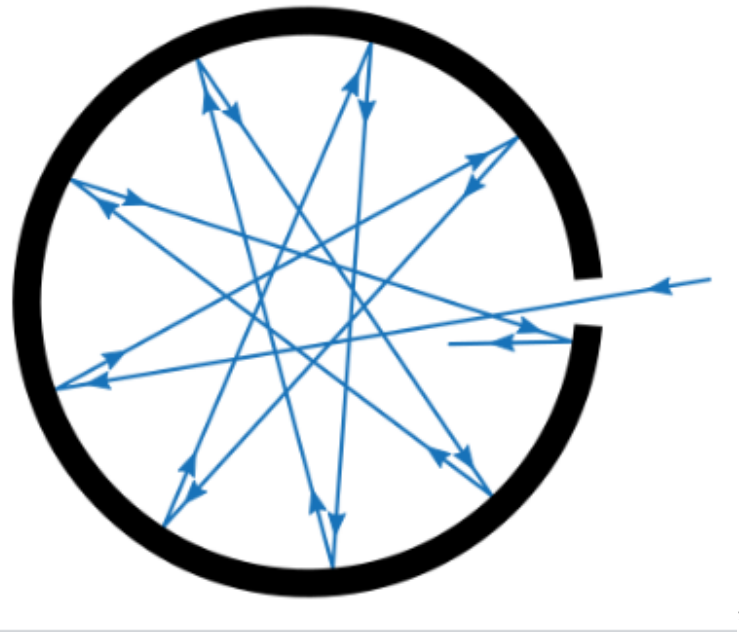


Figure 2.15: A cavity with a small hole behaves like a black body as long as the probability of absorption  $\ll 1$ . The probability of absorption at each reflection is given by the emissivity, so the total probability of *reflection* is the emissivity raised to the power of the average number of bounces. Figure from Wikipedia.

925 Cavities are resonators, and resonators... resonate?

926 The resolution to the seeming discrepancy is that this intuition only holds outside of  
927 equilibrium, a situation that is nearly ubiquitous in engineering contexts. A resonant cavity  
928 has the resonance it does because photons are being pumped in faster than they can be  
929 absorbed by the walls and remitted with a thermal distribution. In this out-of-equilibrium  
930 case, the photons interfere in such a way as to excite cavity modes. Turn the amplitude of the  
931 source down to  $\approx kT$  and the modes vanish. This case, among others, will be investigated  
932 in the following subsections.

933 **2.3.2 Inspection of thermal noise spectra**<sup>10</sup>

934 The theory outlined above predicts the (input-referred) spectrum of an antenna in a cavity  
935 should not vary with frequency if there is thermal equilibrium between the cavity and the  
936 receiver system<sup>11</sup>. A real measurement will take place after an amplifier (in other words,  
937 will be output-referred), and will vary due to the gain and noise figure of the amplifier. A  
938 simple way to correct for the amplifier is to compare the spectrum between an antenna and  
939 a terminator since both will have identical gain and amplifier noise contributions. Since we  
940 are more focused on the qualitative *shape* of the spectrum and not absolute input referred  
941 power, this method is acceptable. A comparison of antenna and terminator data from an  
942 identical amplifier chain is shown in Fig. 2.16.

943 The variations are unexpected in light of the theory presented in the previous subsection.

944 In the following subsection, the thermal spectrum emerging from a simple resonator will be  
945 presented.

---

<sup>10</sup>Code for this section can be found at: [https://github.com/josephmlev/darkRadio/tree/master/daqAnalysisAndExperiments/run1p4/thermalNoiseVsH/thermalWiggles\\_writeup.ipynb](https://github.com/josephmlev/darkRadio/tree/master/daqAnalysisAndExperiments/run1p4/thermalNoiseVsH/thermalWiggles_writeup.ipynb)

<sup>11</sup>this assumes  $h\nu \ll kT$ (Rayleigh-Jeans limit), an ideal antenna aperture  $\propto \lambda^2$ , and an impedance match between the antenna and amplifier. The final assumption will be relaxed in Sec. 2.3.8.

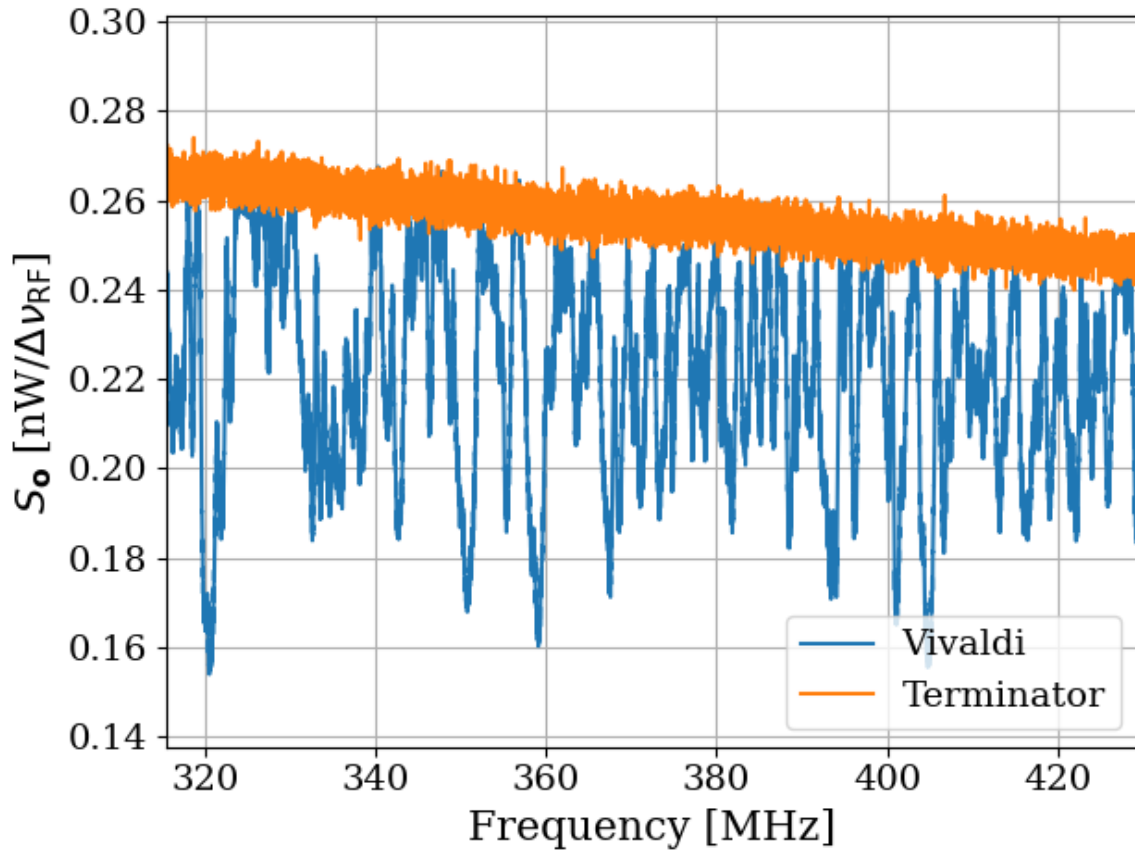


Figure 2.16: Output-referred Vivaldi antenna and terminator thermal spectra as measured through an amplifier chain ( $G \sim 68$  dB, noise temperature  $\sim 120$  K). The Vivaldi is inside the shielded room. Both spectra represent about 1 second of data, with  $\Delta\nu_{RF} = 9.5$  kHz. The Vivaldi antenna is in a single position throughout all averaging, in contrast to the technique where it moves, outlined in later chapters.

### 946 2.3.3 A simple resonator: shorted coax cable

947 A coax cable that is shorted on one end and matched to a measurement device <sup>12</sup> on the other

948 is a simple resonator. The short provides a boundary condition demanding the voltage goes

949 to zero<sup>13</sup> while the measurement device, being matched, absorbs the wave. A “closed-open”

---

<sup>12</sup>In the entirety of this section, a Pasternack PE15A-1012 will be used as the front end amplifier.

<sup>13</sup>Similarly, an open termination will force the *current* to zero, resulting in a similar resonator, though with a 180-degree phase shift.

950 resonator such as this will resonate with frequency

$$\nu = \frac{v(2n - 1)}{4L}, \quad (2.35)$$

951 for integer  $n > 0$ , where  $v$  is the wave speed in the cable and  $L$  is the length. For a

952 185 cm cable with velocity factor = 69.5% (i.e.  $v = 0.695 c$ ), this works out to a first mode

953 at 28.2 MHz and following modes every 56.4 MHz. A schematic of the setup is shown in

954 Fig. 2.17, and the output power spectrum is shown in ratio to a terminator in Fig. 2.18.

955 Also shown in Fig. 2.18 is an open termination at the end of the cable in place of the short.

956 Fitting the peaks <sup>14</sup> reveals the average spacing between peaks is  $55.2 \pm 2.4$  MHz, in good

957 agreement with the prediction of 56.4 MHz of Eq. 2.35.

958 By the fluctuation-dissipation theorem, the loss of the cable will dissipate some thermal

959 noise into the system, which can excite the cable. As discussed in Sec 2.3.1, if the resonator

960 (cable) is in thermal equilibrium with the measurement device, a frequency-independent

961 power spectrum is expected. The deviation from this expectation is surprising because the

962 data seem to be in contradiction with thermodynamics. Now, a cable is not a particularly

963 good resonator ( $Q \lesssim 10$ ), so the effects are rather small here, but the simplicity of the system

964 makes it one that is worth exploring.

965 One assumption which is critical to the above logic is that of equilibrium. The amplifier

966 is a likely culprit for breaking this equilibrium, so a test that can remove the amplifier's

967 ability to interact with the resonator is worth pursuing. Fortunately, such a test is quite

968 simple to implement using a circulator <sup>15</sup>.

---

<sup>14</sup>Code for this section can be found at: [https://github.com/josephmlev/darkRadio/tree/master/daqAnalysisAndExperiments/run1p4/thermalNoiseVsH/thermalWiggles\\_writeup.ipynb](https://github.com/josephmlev/darkRadio/tree/master/daqAnalysisAndExperiments/run1p4/thermalNoiseVsH/thermalWiggles_writeup.ipynb)

<sup>15</sup>I got one for \$36 on Ebay!



Figure 2.17: A coax cable with a short on the end and a matched measurement device on the other behaves like a “closed-open” resonator. Replacing the short termination with an open (not shown here) produces a similar resonator, though with a 180-degree phase shift.

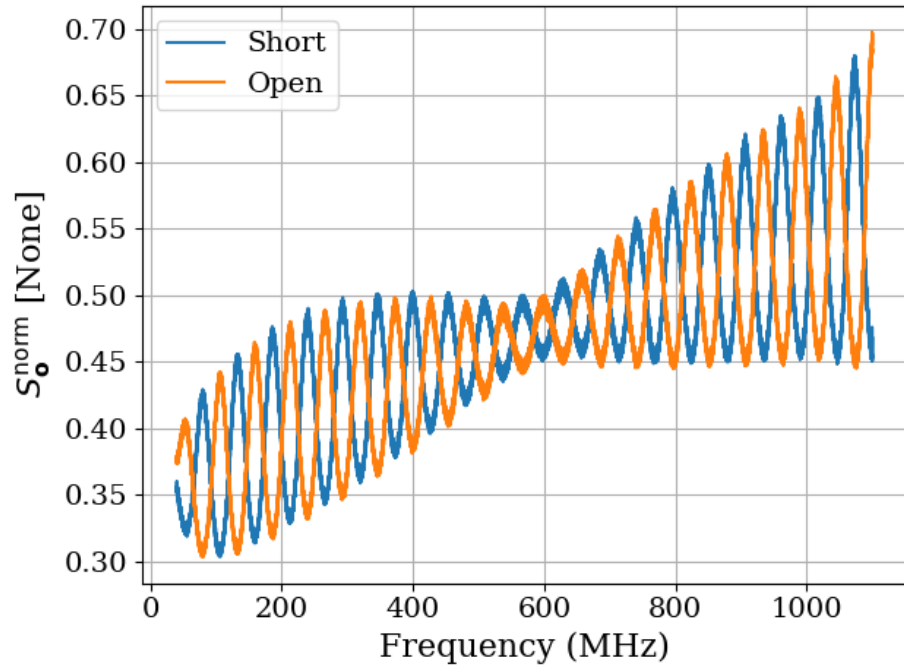


Figure 2.18: Power spectra of short (blue) and open (orange) terminations at the end of 1.85 m of RG400 coax cable (velocity factor = 69.5%). Schematic of this set-up is shown in Fig. 2.17. These spectra are normalized to the spectrum of a terminator, which was measured through the same amplifier chain. For example, when  $S_o^{\text{norm}} = 0.5$ , the power measured in this setup is half of the power measured by a terminator through the same amplifier chain. The average spacing between peaks is  $55.2 \pm 2.4$  MHz, in good agreement with the prediction of 56.4 MHz of Eq. 2.35.

969 **2.3.3.1 RF circulators**<sup>16</sup>

970 A circulator is a three-port, non-reciprocal device that allows power to flow only in specific

971 ways between its ports<sup>17</sup>. A schematic symbol is shown in Fig. 2.19.

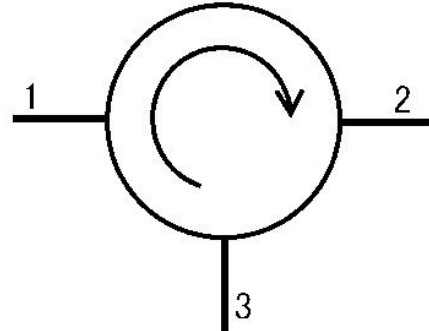


Figure 2.19: Schematic symbol of a circulator. Power can only flow from ports 1 to 2, 2 to 3 and 3 to 1. Image from Wikipedia.

972 The (linear) S-parameters [43, 44] of an ideal circulator are given by the matrix

$$S = \begin{pmatrix} 0 & 0 & 1 \\ 1 & 0 & 0 \\ 0 & 1 & 0 \end{pmatrix}. \quad (2.36)$$

973 In other words, in an ideal circulator,  $S_{12} = 0$ , so power can not flow from port 2 to port

974 1, while  $S_{21} = 1$ , so power can flow from 1 to 2. Also of note, the diagonal elements  $S_{ii} = 0$ ,

975 meaning ports do not reflect power.

976 A Teledyne C-0S03A-3M RF circulator has an approximate bandwidth from 490-510 MHz

977 and was available inexpensively on eBay, so it is used for testing. A photo of it is shown in

<sup>16</sup>Code for this section can be found at: [https://github.com/josephmlev/darkRadio/tree/master/thesis/ch2/circulatorData/SParameter\\_circulator/calc3portSPParam.ipynb](https://github.com/josephmlev/darkRadio/tree/master/thesis/ch2/circulatorData/SParameter_circulator/calc3portSPParam.ipynb)

<sup>17</sup>See Ch. 9 of Pozar's *Microwave Engineering* for a detailed reference.

978 Fig. 2.20, and its S-parameter data are shown in Fig. 2.21. Note that a circulator with one  
979 port terminated is sometimes known as an “isolator”, but I will refrain from using this term.



Figure 2.20: Photo of Teledyne C-0S03A-3M RF circulator. Lines in the background are collage-ruled lined paper ( $\approx$  7mm spacing) for scale.

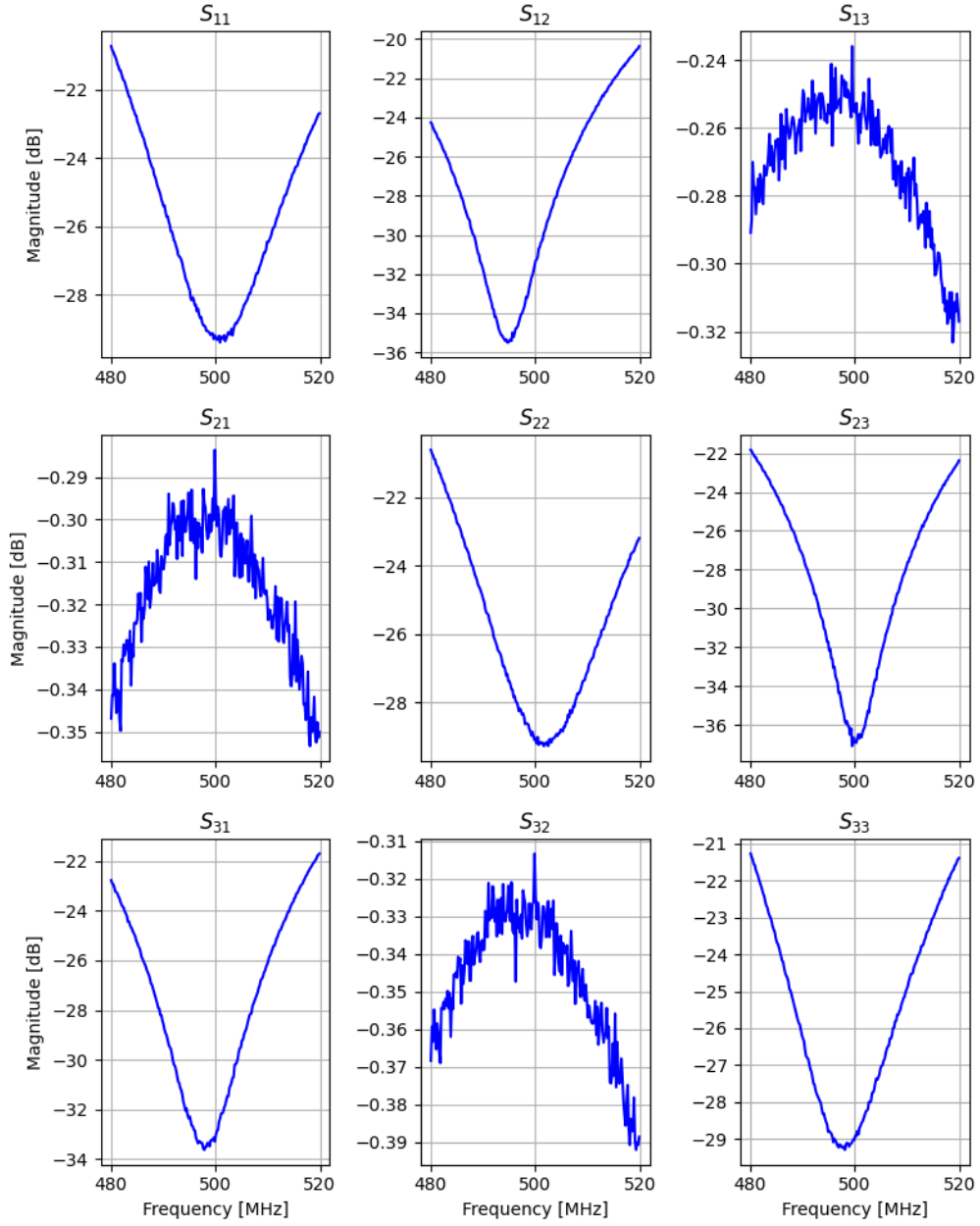


Figure 2.21: 3-port, frequency-dependent S-parameter data for Teledyne C-0S03A-3M circulator. Data taken by Ben Godfrey and Andrea Lopez Arguello with 2-port VNA with the circulator's unused port terminated. Circulator is rated for use between 490 and 510 MHz. These data show good agreement with Eq. 2.36. Note that magnitude is in dB, so these data are proportional to power, i.e. the square of linear S-parameters.

980 **2.3.4 A simpler resonator: shorted coax cable and circulator**

981 In light of the variations observed in Fig. 2.18, a similar measurement was made using  
982 a circulator in order to isolate the coax resonator from any effects of the amplifier. The  
983 schematic of this setup is shown in Fig. 2.22, and resulting the spectrum is shown in Fig. 2.23.  
984 This is an interesting measurement because any net power flow from the amplifier will be  
985 absorbed by the terminator on port three since it presents a good impedance match. This  
986 net power flow has the potential to cause a temperature change in the terminator; however,  
987 it is in a thermally-conductive metal can that is exposed to the air, which serves as a heat  
988 bath and holds it very close to room temperature. The coax resonator will just see the  
989 Johnson noise of the room temperature terminator in equilibrium with the Johnson noise  
990 caused by its internal loss. The overall effect is a resonator that is in thermal equilibrium  
991 yet is able to be measured by an extremely sensitive spectrum analyzer.

992 The result of introducing the circulator and matched load on port 3 is the removal of the  
993 variations that were seen without the circulator (Fig. 2.23).

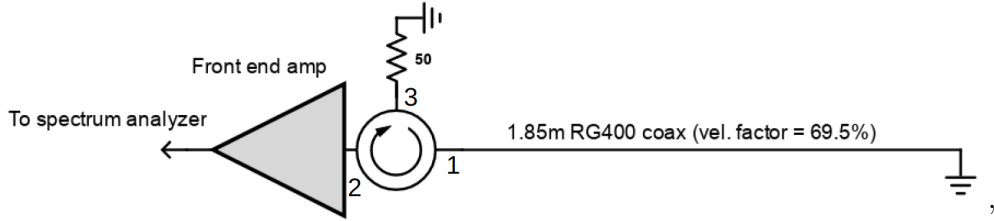


Figure 2.22: A coax cable with a short on one end and a circulator isolating the system from the amplifier.

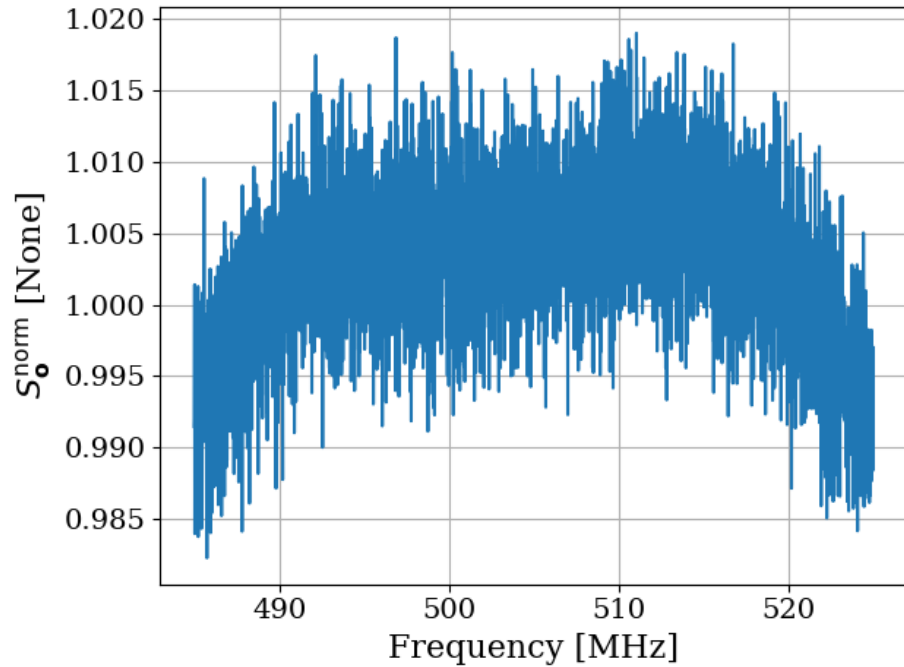


Figure 2.23: Power spectrum of 185 cm coax resonator as measured through a circulator. Short termination at the end of the cable as depicted in Fig. 2.22. The amplitude of the variations in this spectrum is on the order of half a percent and hardly visible under the noise. They are much smaller than those at the  $\sim 15\%$  level without a circulator (Fig. 2.18). Also, note this spectrum is normalized to a terminator through the same amplifier chain and very close to 1. The normalized spectrum without the circulator shown in Fig. 2.18 was significantly lower, around 0.5. Note that the peak-to-peak frequency variations of the cable without a circulator (Fig. 2.18) are  $\approx 55\text{ MHz}$ , and would be visible in the  $\approx 30\text{ MHz}$  span shown here. This span is limited by the circulator.

994 **2.3.5 A more complex resonator: antenna in room**

995 Similar to the coax resonator shown in Fig. 2.17, the antenna data presented in Fig. 2.16  
996 are of a resonator (antenna-room system) which is being measured by an amplifier. The  
997 experiment in the previous section suggests that the amplifier seems to have an effect on  
998 the delicate thermal equilibrium, which can be mitigated by including a circulator. The  
999 experimental set-up for the antenna in the room is shown in Fig. 2.24, and the data from  
1000 this setup is shown in Fig. 2.25.

1001 The result is striking. The theory outlined early in the chapter predicted the noise  
1002 power spectrum of an antenna in a cavity will look the same as a matched terminator;  
1003  $-174$  dBm/Hz, independent of frequency. The Dark E-Field Radio Experiment measures  
1004 just such a spectrum, but comparing a terminator and antenna in Fig. 2.16, they are remark-  
1005 ably different; the Vivaldi has large variations. However, introducing a circulator to the set  
1006 up such as in Fig. 2.24 removes these variations. Compare blue/orange curves in Fig. 2.25.

1007 A nice test case would be to measure the thermal noise of an extremely high  $Q$  cavity  
1008 after carefully ensuring the radiation that is allowed to enter has a black body spectrum of  
1009 the same temperature of the cavity. This is nicely demonstrated in a few places, notably by  
1010 Cervantes et. al with a cavity of  $Q = 10^{10}$  (!!!) [32]. When care is taken to create equilibrium  
1011 here, the resulting spectrum is flat, even on a frequency span that includes the resonance  
1012 (Fig. 2). When this equilibrium condition is broken, the cavity resonance becomes visible  
1013 (Fig. 10).

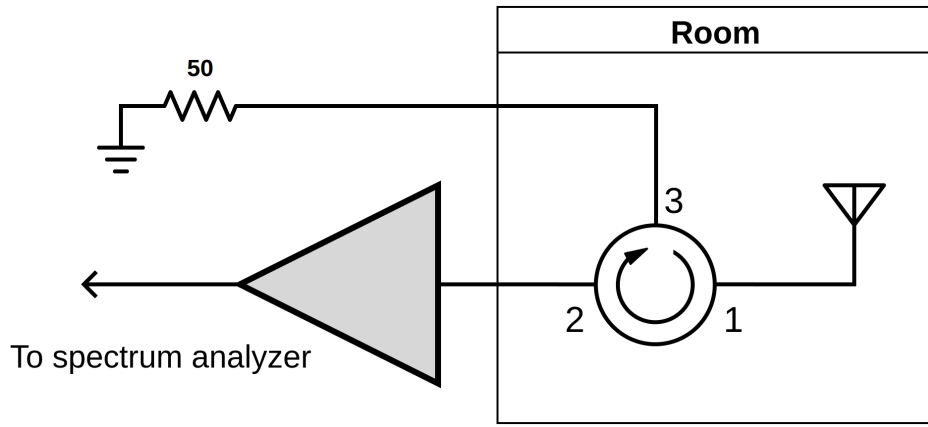


Figure 2.24: Schematic of experimental set-up using circulator to isolate the antenna from amplifier effects.

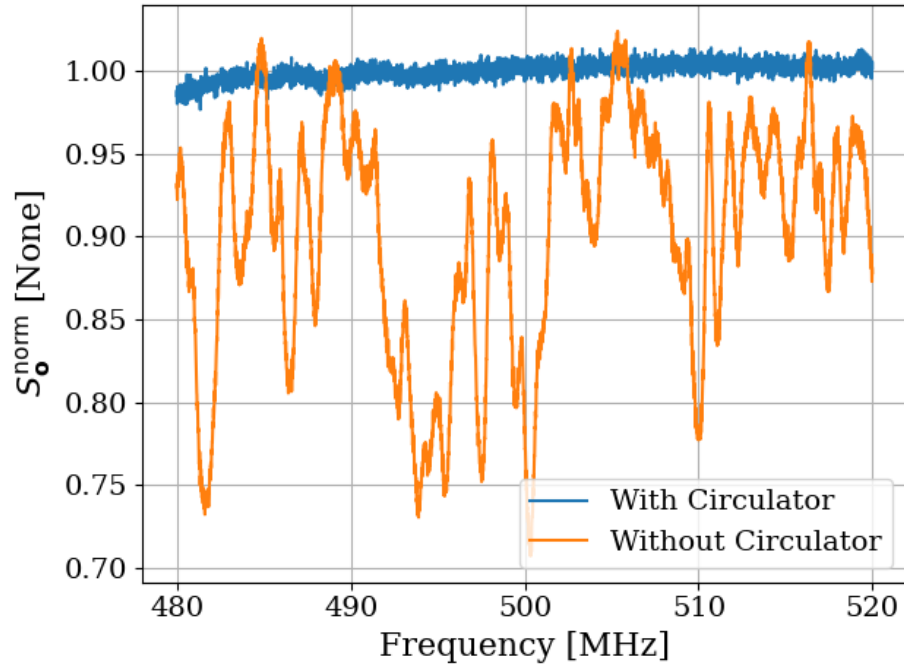


Figure 2.25: Normalized power spectrum for Vivaldi antenna in the room with/without circulator (blue/orange). This setup is shown schematically in Fig. 2.24. The normalized spectrum of the same antenna in the same position is shown with the circulator removed in orange for reference. This orange spectrum is the same as that shown in Fig. 2.16, but here it has been normalized to a terminator measured through the same amplifier chain. The terminator's spectrum is also shown in Fig. 2.16.

1014 **2.3.6 Effective temperature of amplifier**

1015 At this point, the seemingly obvious explanation is that the amplifier, being warm, is sourcing  
1016 more power than it's absorbing. To test this theory, two amplifiers can be placed input-to-  
1017 input as shown in Fig. 2.26. The noise power emerging *out* of the amp-under-test's input will  
1018 be measured by the front-end amplifier. This amplifier has a noise temperature  $\sim 100\text{ K}$ , so  
1019 it should be sensitive to very small variations in power. The data from the set-up is shown  
1020 in Fig. 2.27. Also shown in this figure are the spectra of the amp-under-test replaced by  
1021 both short and open terminations for reference.

1022 An important number to keep in mind is the noise floor of this detector and what it looks  
1023 like in the dimensionless units shown. This is set by the noise temperature of the front end  
1024 amp,  $\sim 100\text{ K}$ . If the load-under-test were at  $0\text{ K}$ , the power measured  $S_{0\text{K}}^{\text{meas}}$  would be only  
1025 that of the front end amp. Taken in ratio to a  $300\text{ K}$  matched terminator measured by the  
1026 same amp chain,

$$\frac{S_{0\text{K}}^{\text{meas}}}{S_{300\text{K}}^{\text{meas}}} \approx \frac{0 + 100\text{ K}}{300 + 100\text{ K}} \quad (2.37)$$

$$= 0.25, \quad (2.38)$$

1027 where the factors of Boltzman's constant  $k$  and the measurement bandwidth  $\Delta\nu_{\text{RF}}$  were  
1028 suppressed since they cancel immediately.

1029 Thus, anything with an apparent noise temperature  $\ll 100\text{ K}$  will appear with a dimen-  
1030 sionless power spectral density of  $\sim 0.25$  in Fig. 2.27.

1031        This phenomenon actually has been discussed in the literature[19].<sup>18</sup>, which I will provide  
1032      a brief summary of.

1033        In this case, two amplifiers are placed back to back on either side of a transmission  
1034      line. When a particle interacts with the transmission line, a pulse is detected at each of the  
1035      amplifiers, and the difference in time provides a means to work out the position the particle  
1036      came in along the line. It is advantageous in this case to minimize the noise emanating out  
1037      of the inputs of these amplifiers. By tuning the reactance of the input of these amplifiers,  
1038      they can absorb a net power, putting them at an “effective temperature” lower than their  
1039      physical temperature.

1040        In the case of off-the-shelf Pasternack RF amplifiers, this was likely not an intentional  
1041      effect. However, the data presented here seem to agree with the idea that the amplifiers have  
1042      an effective temperature  $\ll 100\text{ K}$ .

1043        In the next subsection, I will demonstrate that by changing the temperature of the  
1044      matched load outside the shielded room (shown in Fig. 2.24), the amplitude of the thermal  
1045      wiggles can be controlled.

---

<sup>18</sup>I am very grateful to Greg Wright for pointing this out.

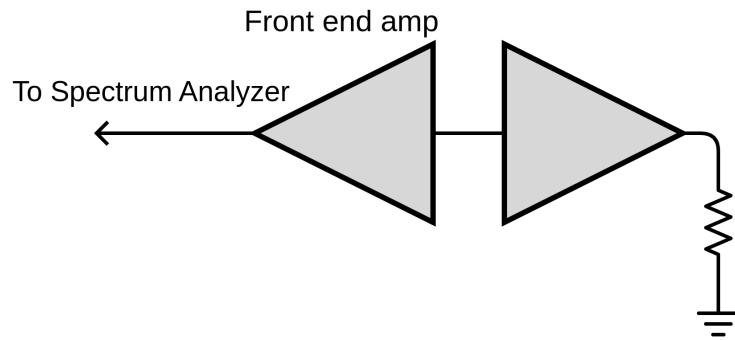


Figure 2.26: Schematic of set-up to measure the noise emerging *out* of an amplifier's input.

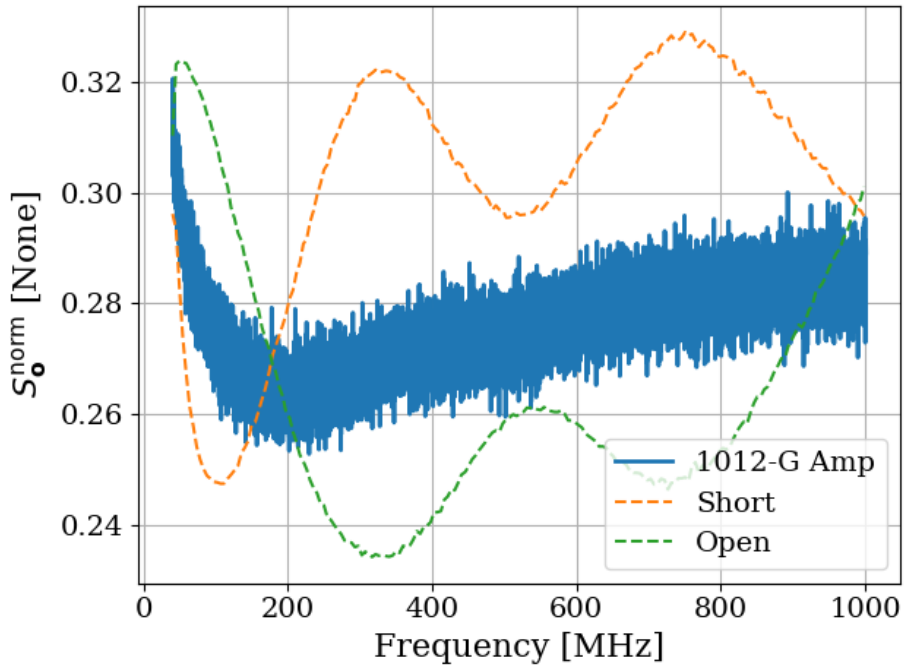


Figure 2.27: Power spectrum of noise emerging *out* of the input of an amplifier's (Paster-nack PE15A-1012-G) input, see Fig. 2.26. Normalized to a matched  $50\Omega$  terminator. Also shown as dashed curves are the spectra of a short and open termination. These spectra have a median fit applied to reduce visual clutter. Low-frequency behavior is due to the high noise figure of the amplifier at these frequencies; see Eq. 2.37.

### 1046 2.3.7 Intentional breaking of thermal equilibrium

1047 At this point, it has been demonstrated that an amplifier absorbs more thermal noise than  
1048 it emits, likely due to the electronic cooling effect described by Radeka [19]. This causes the  
1049 spectrum of a resonator, which is measured with such an amplifier, to exhibit wiggles, which  
1050 disappear when a circulator is used to isolate the system from the amplifier. An interesting  
1051 question naturally arises; what happens when the the thermal equilibrium is disturbed by  
1052 varying the temperature of the  $50\Omega$  terminator on port 3 of the circulator (Fig. 2.24)? Since  
1053 the terminator is outside the room, it is simple to conduct a highly controlled experiment  
1054 where the terminator's temperature is varied without entering the room and disturbing  
1055 sensitive boundary conditions.

1056 The hot terminator is created by using a noise source (red device in the left panel of  
1057 Fig. 2.28). The noise source has an effective noise ratio (ENR) of approximately 16.1 dB  
1058 according to its calibration sheet. Noise temperature is related to ENR by the formula[45]

$$T_n = (10^{\text{ENR}/10} \times 290 K) + 290 K, \quad (2.39)$$

1059 where ENR is measured in dB and a reference temperature of 290 K has been assumed.  
1060 Therefore, the noise source has a noise temperature of around 12,100 K <sup>19</sup>.  
1061 The cold terminator is a standard Pasternack  $50\Omega$  (with the blue rubber case removed),  
1062 and the cable is semi-rigid and rated for cryogenic temperatures. This assembly is shown  
1063 immersed in liquid nitrogen in the right panel of Fig. 2.28.

---

<sup>19</sup>This testing was performed before the Y-factor measurements of Sec. 3.1.1. The noise source worked correctly here but failed before the Y-factor measurements.

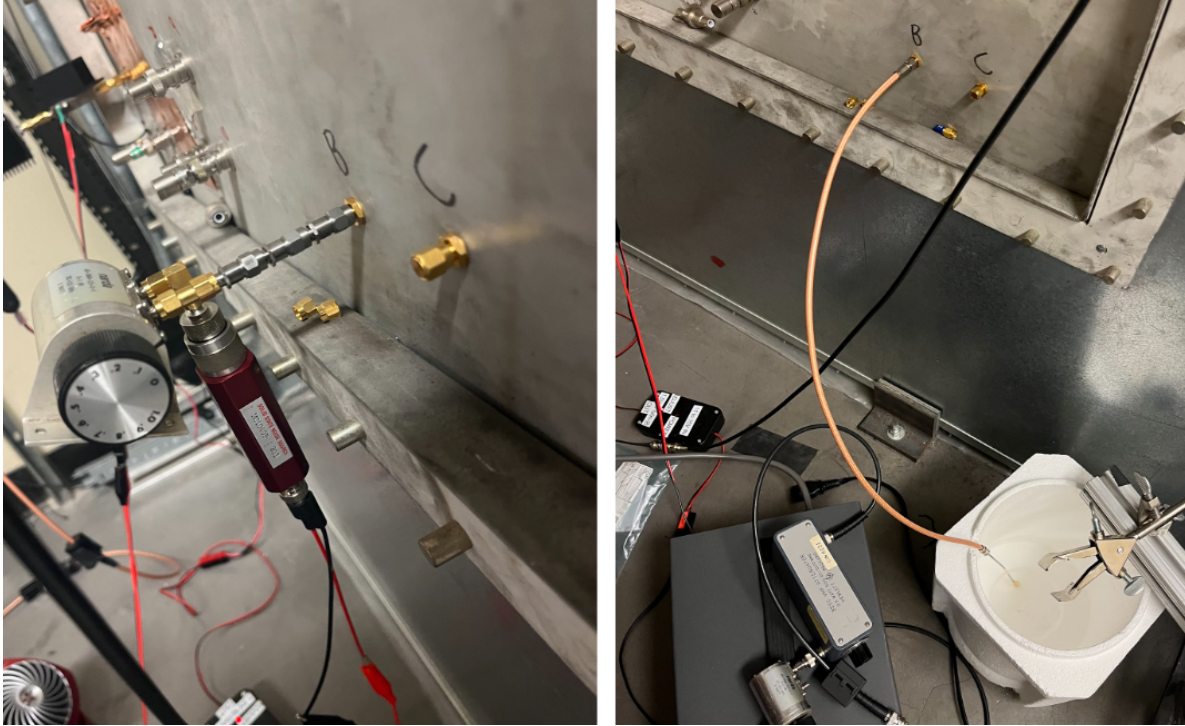


Figure 2.28: Setup to create hot and cold terminator. The hot/cold load is connected to port 3 of the circulator (as shown in Fig. 2.24). The circulator is in the room and not visible in this photo. The left panel shows the noise source ( $16.1 \text{ dB ENR} \approx 12,000 \text{ K}$  noise temperature) and attenuators allowing the specific control of the hot temperature, see Eq. 2.40. Course attenuation is controlled by adding fixed attenuators, while fine control ( $0.1 \text{ dB steps}$ ) is provided by the step attenuator. Right panel shows the semi-rigid cryogenic-capable cable in liquid nitrogen to create a cold load.

1064 In both the hot and cold measurements, the loads were shown to have a good impedance  
 1065 match to the  $50\Omega$  line using a VNA. The noise source is designed to have a good match,  
 1066 but the terminator is not rated for cryogenic temperatures, so this is an important test.  
 1067 The cryogenic test load (semi-rigid cable plus terminator) was measured to have  $S_{11} <$   
 1068  $-35 \text{ dB}$  at both room temperature and at  $77 \text{ K}$  (by submerging in liquid nitrogen), confirming  
 1069 performance at cryogenic temperatures.

1070 The noise source looks like a terminator, which is a factor of  $\sim 40$  times hotter than room

1071 temperature, while the cryogenic terminator is a factor of  $\sim 4$  colder than room tempera-  
1072 ture. To account for this, room temperature attenuators can be added to bring the effective  
1073 temperature of the noise source down closer to room temperature. Therefore, the total noise  
1074 temperature  $T_{\text{out}}$  of a terminator at physical temperature  $T_{\text{in}}$  in series with an attenuator at  
1075 physical temperature  $T_{\text{att}}$  with (linear) loss  $L$  is a useful quantity. For brevity, the derivation  
1076 outlined in the white paper by Whitham D. Reeve [46] is skipped, and the result is provided;

$$T_{\text{out}} = \frac{T_{\text{in}}}{L} + T_{\text{att}}\left(1 - \frac{1}{L}\right). \quad (2.40)$$

1077 Returning to the set-up in Fig. 2.24, replacing the terminator on port 3 with either a  
1078 noise source (including an attenuator chain) or a terminator in liquid nitrogen provides a  
1079 means to break thermal equilibrium in both the hot and cold direction by applying a matched  
1080 load at a very precise temperature to port 3 of the circulator. Equation 2.40 converts the  
1081 attenuation and noise source temperature into an output temperature.

1082 Figure 2.29 shows the resulting spectra from the set-up shown in Fig. 2.24 using a noise  
1083 source/attenuator chain shown in the left panel of Fig. 2.28. The two panels show the spectra  
1084 from the same set-up, but for different ranges and resolutions of  $T_{\text{out}}$  as defined by Eq. 2.40.

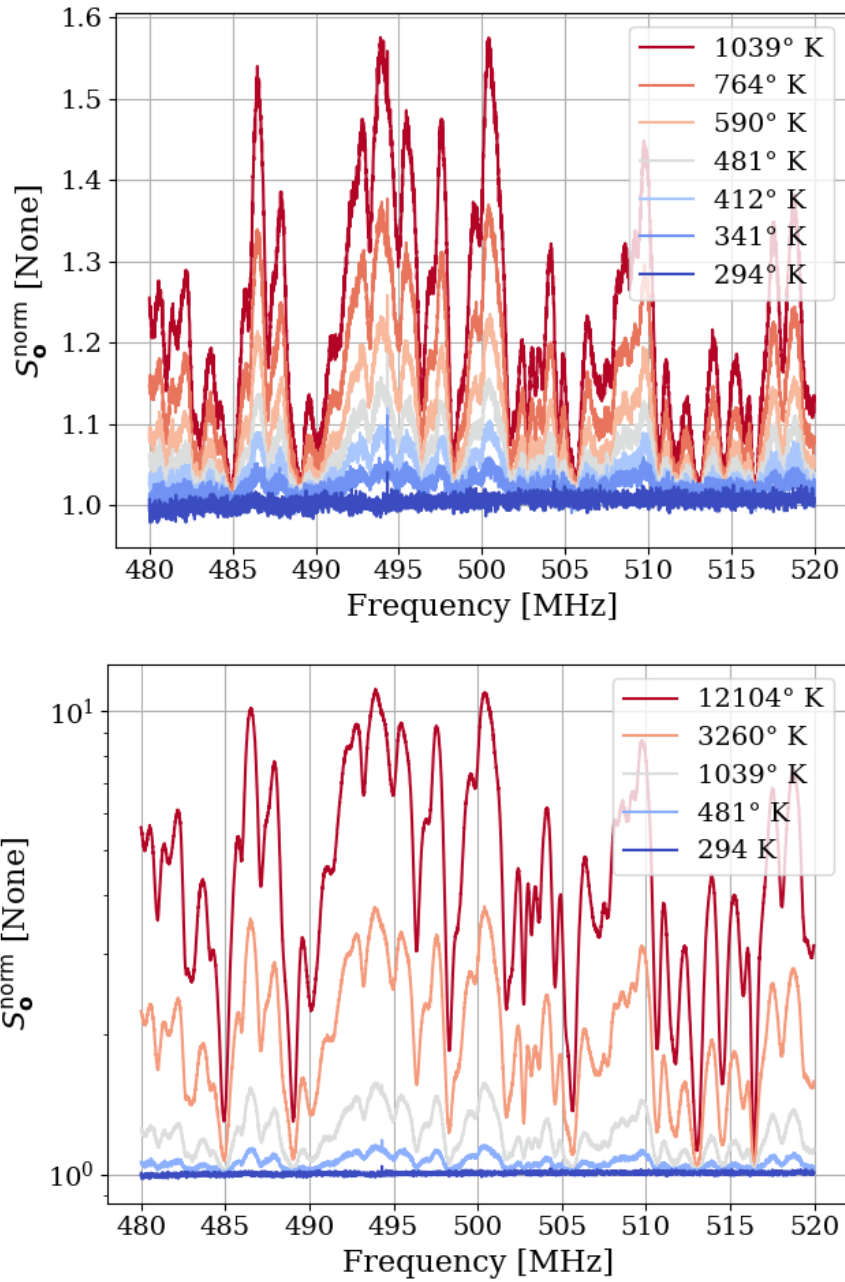


Figure 2.29: Spectra resulting from the antenna and circulator set up of Fig. 2.24 with the terminator on port 3 of the circulator at a variety of temperatures, as calculated by Eq. 2.40. Spectra are all normalized to a terminator through the same amplifier chain. The two panels show different ranges and resolutions of temperatures for clarity, but are the same setup.

1085       Figure 2.29 showed spectra from the set-up shown in Fig. 2.24 for a hot terminator, but  
1086   a cold terminator can also be used by dunking a terminator into liquid nitrogen (Fig. 2.28).  
1087   Neglecting the small attenuation of the cable, the noise temperature is simply 77 K. An  
1088   interesting test case is to set the hot temperature such room temperature is halfway between  
1089    $T_{\text{hot}}$  and  $T_{\text{cold}}$ . In other words, let

$$T_{\text{hot}} = (T_{\text{room}} - T_{\text{cold}}) + T_{\text{room}} \quad (2.41)$$

$$\approx 511 \text{ K}. \quad (2.42)$$

1090       For  $T_{\text{hot}} = 12, 100 \text{ K}$ ,  $T_{\text{att}} = 294 \text{ K}$  and  $T_{\text{out}} = 511 \text{ K}$ , inverting Eq. 2.40 we expect  $L$  to  
1091   be  $\sim 54.4$  or  $17.4 \text{ dB}$ .

1092       The two spectra with the terminator at 504 K (the closest temperature accessible with the  
1093   0.1dB step attenuator) and 77 K are shown in Fig. 2.30. Again, they have been normalized  
1094   to the spectrum of a room-temperature terminator.

1095       The two spectra shown in Fig. 2.30 appear to be mirrored about  $S_0^{\text{norm}} = 1$ . In a test of  
1096   this reflection, these spectra are added, and the resulting sum spectrum is flat to about 1%  
1097   with another 1.5% offset from the expected value of 2. This is shown in Fig. 2.31. The offset  
1098   is likely due to the amplifier gain or ambient temperature drift between measurements.

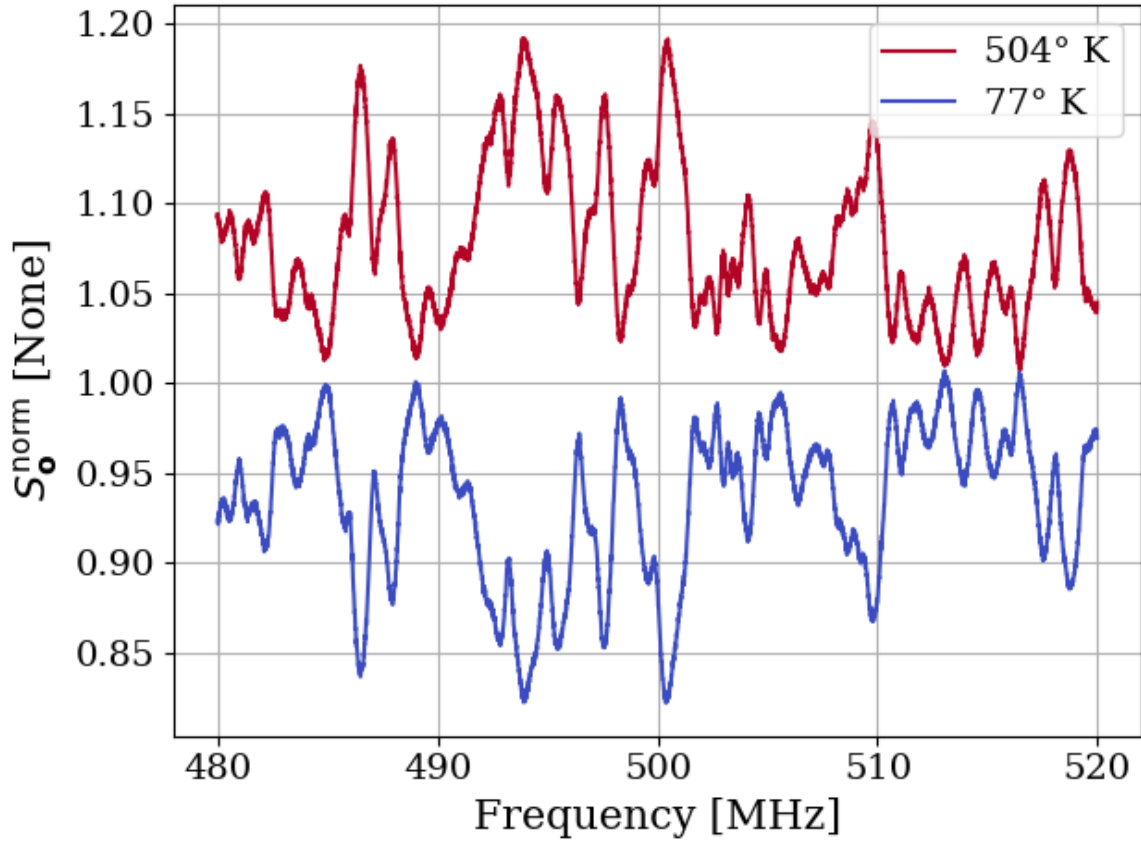


Figure 2.30: Spectra resulting from the antenna and circulator set up of Fig. 2.24 with the terminator on port 3 of the circulator  $\approx 210\text{ K}$  above and below room temperature, as calculated by Eq. 2.40. Spectra are both normalized to a terminator through the same amplifier chain.

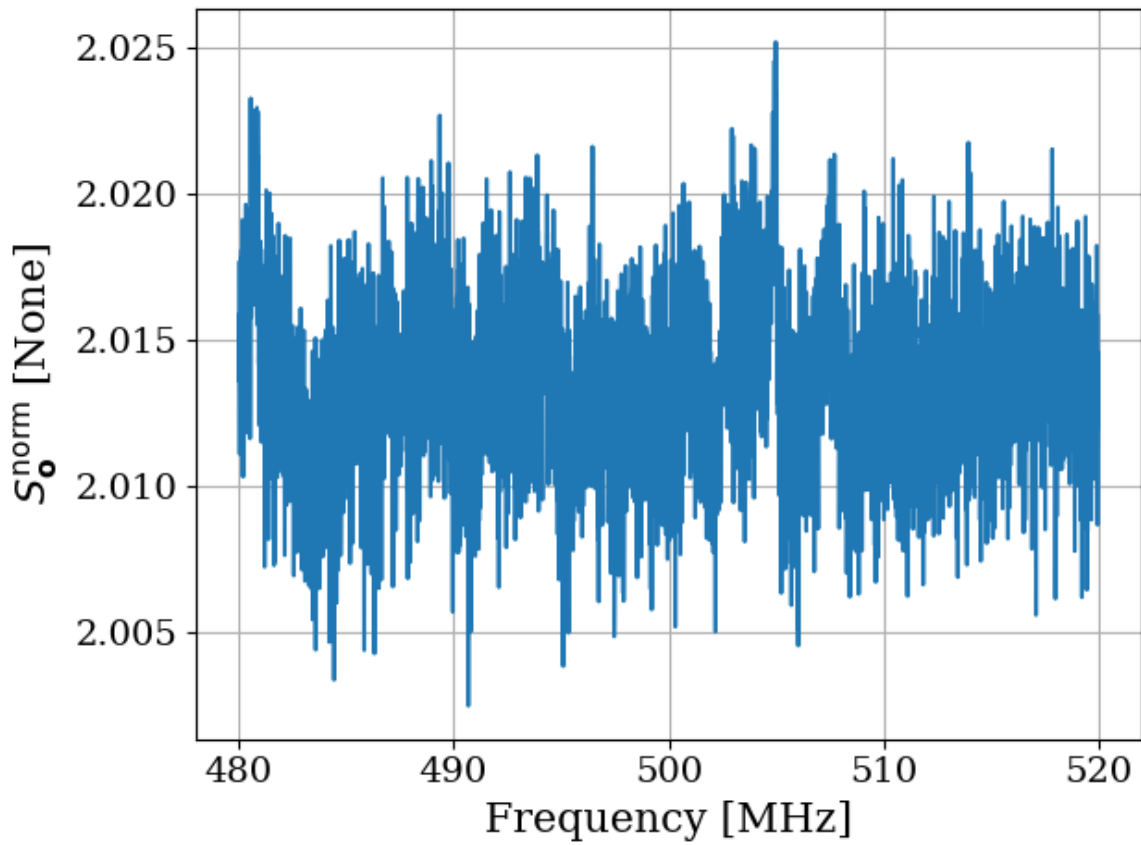


Figure 2.31: Sum of normalized spectra shown in Fig. 2.30. If the two normalized spectra in that figure were perfect reflections about 1, their sum would be a constant 2 in this figure. That is close to what is observed.

1099 **2.3.8 Relation of antenna  $S_{11}$  to thermal noise without a**

1100 **circulator**

1101 As pointed out in [41], the antenna impedance determines how much power is transferred  
1102 from the cavity's electric field noise into the transmission line, and therefore what is mea-  
1103 sured by the amplifier<sup>20</sup>. Indeed, impedance is a useful tool in understanding the situation  
1104 outside equilibrium. However, viewing from this perspective misses a subtle point when con-  
1105 sidering equilibrium; while an impedance mismatch will prevent the antenna's noise power  
1106 from entering the transmission line, it will also prevent the noise in the line from leaving!  
1107 This power will reflect off of the mismatch at the antenna and be absorbed by the matched  
1108 amplifier, resulting in a flat spectrum. This can be seen in the coax resonator when mea-  
1109 sured with the circulator in Sec. 2.3.4, specifically Figs. 2.22 and 2.23. Figure 2.32 shows a  
1110 comparison of  $1 - |S_{11}|^2$  and the noise spectrum of an antenna measured with a Pasternack  
1111 low noise amplifier (LNA). There is no circulator in the setup, so variations are observed.  
1112 Figure 2.33 shows the strong correlation between the curves in Fig. 2.32.

---

<sup>20</sup>The amplifier has a small impedance mismatch as well ( $S_{11} \lesssim -15$  dB), but this is a small effect and is neglected.

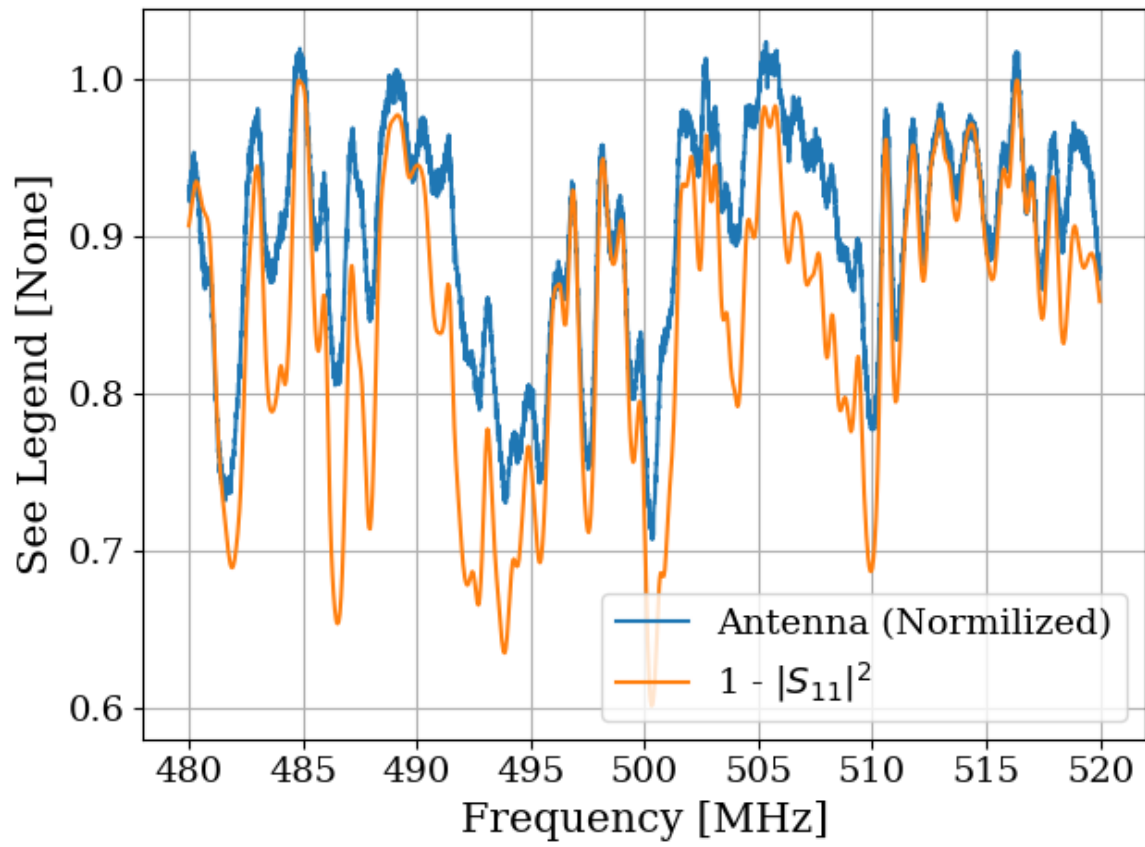


Figure 2.32:  $1 - |S_{11}|^2$  and the normalized antenna spectrum without circulator. Shown at significant zoom to show detail. A much wider span is used to generate the correlation shown in Fig. 2.33.

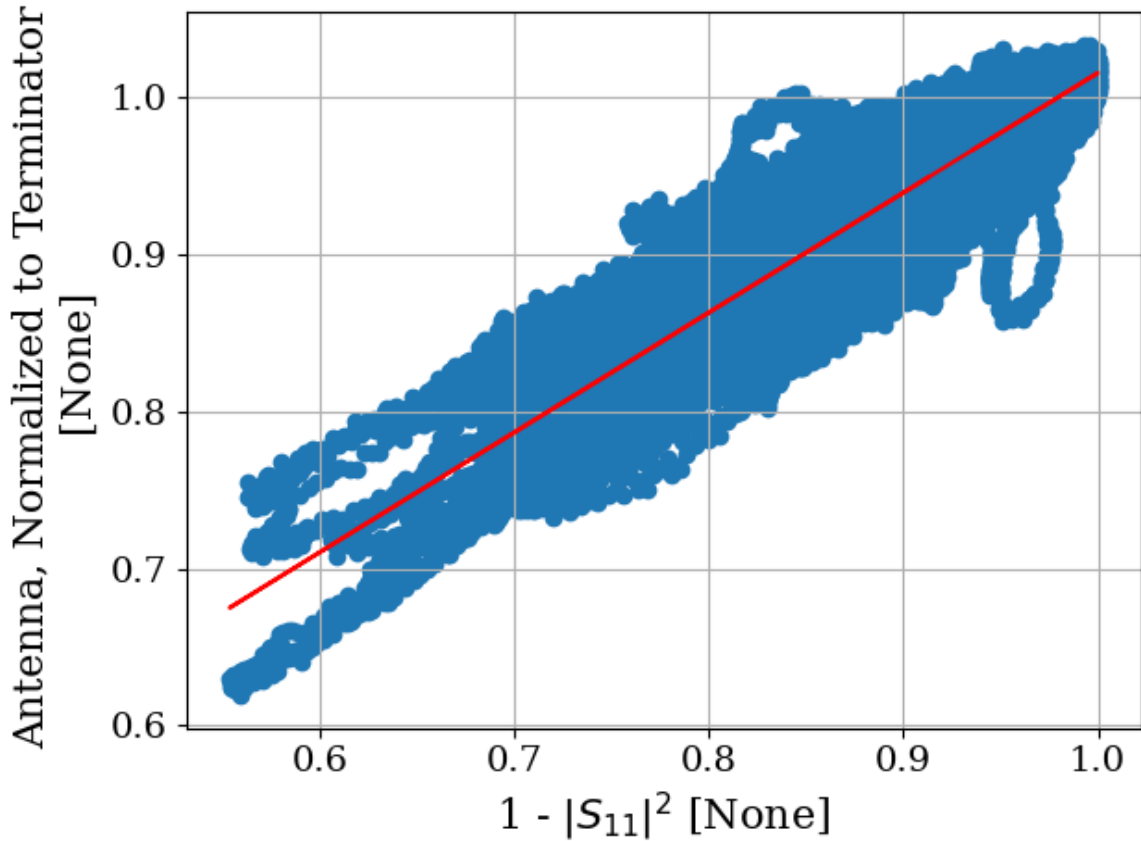


Figure 2.33: Correlation of  $1 - |S_{11}|^2$  and the normalized antenna spectrum without the circulator. The data are taken between 300 and 800 MHz, a much wider span than shown in Fig. 2.32. The antenna is connected directly to the low noise amplifier (LNA), i.e. with the circulator shown in Fig. 2.19 removed. The line of best fit is shown in red. The Pearson correlation coefficient is 0.92.

### 1113 2.3.9 Discussion of Thermal Wiggles

1114 Inspection of the output of the experiment ( $S_o$ , Fig. 2.16) reveals small variations in PSD  
1115 (power spectral density) over spans of tens of kHz. Given an antenna in a cavity in thermal  
1116 equilibrium with the input of an LNA, whose input is assumed to be real and matched,  
1117 one would expect an output PSD which is constant with respect to frequency (up to small  
1118 variations in system gain and noise temperature). The theory for this is outlined in Sec 2.3.1.  
1119 These observed variations are not noise; for a given antenna position, the same shape is  
1120 repeatedly measured (though the noise riding on these variations *is* random). The origin of  
1121 the observed small variations lies in the effective temperature difference between the room  
1122 and the LNA, causing a net power flow from the antenna into the LNA (Fig. 2.26). This  
1123 effective temperature difference partially excites modes of the antenna/cavity system, causing  
1124 the observed variations. This effect likely originates from a small reactive component of the  
1125 LNA's input causing the electronic cooling described originally by Radeka [19]. This effect  
1126 can be eliminated by adding a circulator between the antenna and LNA [47, 48] though for  
1127 this experiment, it is impractical to get an isolator that covers such a wide band at relatively  
1128 low frequency. Furthermore, the relatively wide (tens of kHz) variations can be handled by  
1129 fitting to them, which is discussed in Sec. 4.2. Finally, a topic which was not described here  
1130 but may be fruitful for future inquiry into this topic is the analysis of noise waves. See [49]  
1131 or Sec. 9.12 of [50].

1132 **2.4 Reverberation Chambers and Statistical**

1133 **Uniformity**

1134 The Dark E-Field Radio experiment consists of an antenna in a cavity. An averaged noise  
1135 power spectrum is measured and an exclusion limit is set on the amount of power excess  
1136 that would have been detected if it were there. In order to convert this limit on power into  
1137 a limit on kinetic mixing  $\epsilon$ , the antenna/cavity detector system must be calibrated.

1138 In many situations, an electromagnetic cavity can be treated with a "spherical cow"  
1139 approach; they contain one mode with a few simple properties that can be analytically  
1140 computed. This works well enough for a smooth, empty cavity that resonates near its  
1141 first mode, but for complex cavities, this treatment turns out to be insufficient. At high  
1142 frequencies (where the wavelength is much smaller than the cavity), many modes, each with  
1143 a finite spread in frequency, overlap. Each of these modes depends on very specific boundary  
1144 conditions of the cavity and everything within it. The configuration of the cavity and its  
1145 contents simply cannot be known to a level of precision that would allow for an analytic or  
1146 simulated solution. Qualitatively, placing a small conducting object<sup>21</sup> in a cavity greatly  
1147 impacts the cavity's resonances as measured by its S-parameters (Fig. 2.36).

---

<sup>21</sup>This is a point made by Hill [51], with the example of placing a soda can in a reverb chamber. Ben Godfrey and I independently discovered this by measuring  $S_{21}$  of an antenna in our shielding room with and without a small SMA terminator on the ground with surprisingly different results.

1148     The problem is summarized nicely by Price et al. [52];

1149     The solution cannot depend in detail on such things as whether a small metallic  
1150     can has been set down somewhere inside the test article, or the position of the  
1151     pilot's arms, or whether some mechanical widget has moved from position A  
1152     to position B, changing the mode structure. If the answer did depend on those  
1153     things, all of the measurements would be useless, defeated by the minutiae present  
1154     in all systems.

1155     The answer to this dilemma is found in the study of mode-stirred reverberation chambers,  
1156     such as those studied by Price, whose quote appears directly above. These are electromag-  
1157     netic or acoustic cavities in which a large volume is occupied by an object that is highly  
1158     reflective and designed to move, a so-called *mode stirrer*. Making the geometry more com-  
1159     plex seems counter-intuitive. However, the payoff is in the transition from a deterministic  
1160     theory to a statistical one. The fields in the cavity at any given configuration are complex  
1161     and are not known, but the statistics of the fields subject to the stirring can be rather simple.

1162     This section provides a mostly qualitative overview of the subject. The de facto reference  
1163     is David Hill's 2009 book [51] which consolidates his many papers spanning his  $\sim 30$ -year  
1164     career. There is little I can do to explain the theory of electromagnetic reverberation cham-  
1165     bers, which is not in this book, so I will focus on their application to the experiment and  
1166     cite Hill where appropriate. The reader is encouraged to consult this book and its references  
1167     for a more detailed exploration of the subject.

### 2.4.1 Deterministic solutions to electromagnetic waves in cavities

The electromagnetic fields within a cavity can be modeled by applying Maxwell's equations with the appropriate boundary conditions. In principle, with enough knowledge about the contents of the cavity, this treatment could calculate fields in any cavity. Unfortunately, it quickly becomes untenable for all but the simplest cases. Therefore, we will restrict ourselves to an empty cavity with perfectly conducting surfaces. The resulting fields have simple analytic solutions which vary sinusoidally in both space and time. They are derived in many places. See for example [51, 53]. While this treatment will not solve the problem at hand, it is a good starting point and will illustrate important features leading to the statistical treatment in the following subsection.

For a rectangular cavity of linear dimensions  $a$ ,  $b$  and  $d$ , the frequencies of resonance are given by

$$\nu_{mnp} = \frac{c}{2} \sqrt{\left(\frac{m}{a}\right)^2 + \left(\frac{n}{b}\right)^2 + \left(\frac{p}{d}\right)^2}, \quad (2.43)$$

for integer mode numbers  $m$ ,  $n$  and  $p \geq 0$  and wave speed  $c$ . The lowest frequency of resonance requires at least two non-zero mode numbers. Thus, for  $a < b < d$  the lowest frequency is at  $\text{TE}_{011}$ . For an ideal cavity with dimensions equal to that of the shielded room in this experiment ( $8 \times 10 \times 12$  feet), the lowest mode is 63.6 MHz. An important consideration is the degeneracy of electric and magnetic fields for any mode where all three mode numbers are non-zero. For example,  $\text{TE}_{111}$  and  $\text{TM}_{111}$  occur at the same frequency, and both of these modes must be counted in the following section. See page 28 of Hill [51] for a discussion.

1188 A quantity of interest is the functional form of the cumulative number of modes at  
 1189 frequencies below a given frequency  $N(\nu)$ . This is rather simple by brute force computer  
 1190 counting<sup>22</sup>, though an analytic solution can be computed by looking at the volume enclosed  
 1191 in a sphere of  $k$ -space [54], where  $k$  is the wave vector<sup>23</sup>. This analytic form is given by

$$N_s = \frac{8\pi}{3} abd \frac{\nu^3}{c^3} - (a + b + d) \frac{\nu}{c} + \frac{1}{2}. \quad (2.44)$$

1192 Differentiation of Eq. 2.44 results in a functional form for the mode density, i.e. the  
 1193 number of modes contained in a frequency band,

$$\frac{dN_s}{d\nu} = 8\pi abd \frac{\nu^2}{c^3} - \frac{a + b + d}{c}. \quad (2.45)$$

1194 Equations 2.44 and 2.45 are plotted in Fig. 2.34

1195 This is useful because as the mode density becomes high, modes in a cavity of finite  
 1196 conductivity begin to overlap. The modification of modal structure by conductors is demon-  
 1197 strated in Figs. 2.35 and 2.36 by placing different conductors in the room and measuring  
 1198  $S_{11}$ .

1199 From these measurements it can be seen that modes can be pulled around, even by  
 1200 conductors occupying a small percentage of room volume. This is especially true for high  
 1201 frequencies. However, by using a large volume of conductors such as a mode-stirrer (sim-  
 1202 ulated here with scrap metal), high-frequency modes are pulled around so much that they  
 1203 overlap. This is the intuition behind reverb chambers and the idea of statistical uniformity.

---

<sup>22</sup>As long as you don't forget the degeneracy!

<sup>23</sup>This whole business of mode counting is directly analogous to the calculation of density of states in statistical mechanics. It shouldn't come as a surprise that the calculation is carried out in the same way.

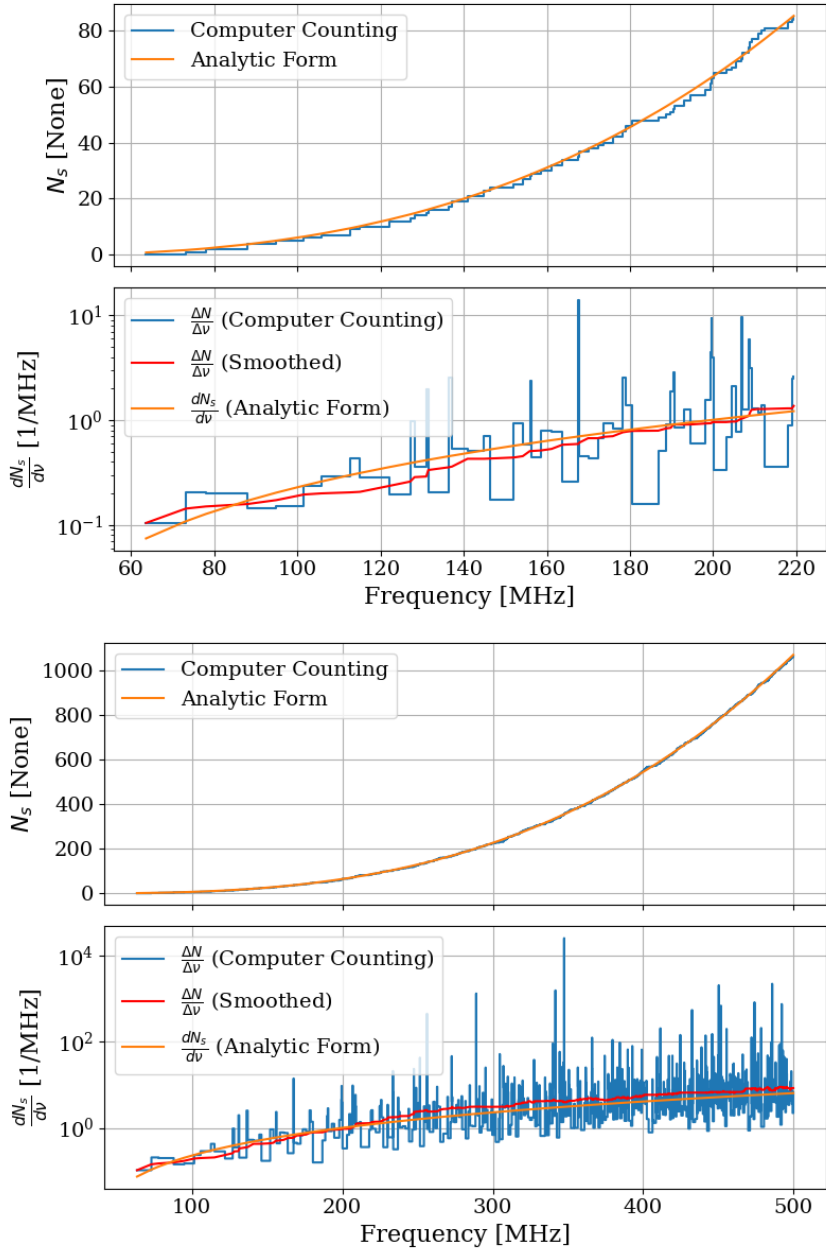


Figure 2.34: Modal density for an electromagnetic cavity with dimensions of the shielding room (nominally  $8 \times 10 \times 12$  ft, see table 2.2). The upper sub-plot shows  $N_s(\nu)$ , the cumulative number of modes below a given frequency. The lower sub-plot shows the derivative of  $N_s(\nu)$ . The upper and lower panels show the same data at two different frequency spans. These plots are a recreation of Figs. 3, 4 and 5 from [54] for a cavity with dimensions of the shielding room. Note that large spikes in  $\Delta N/\Delta\nu$  should be interpreted as binning artifacts and are only shown for reference. The analytic derivative is more useful.



Figure 2.35: Pictures of conductor configurations in the shielded room. The antenna is in the same position between photos. The left panel shows a tin foil hat, and the right shows a random placement of scrap metal. Hat and scrap metal courtesy of Tyler Erjavec.

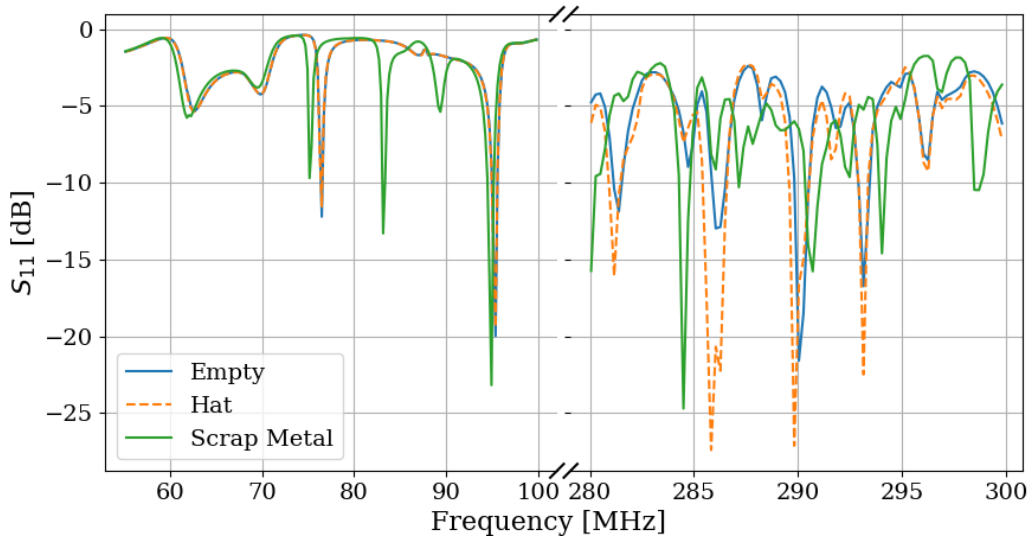


Figure 2.36: Measured  $S_{11}$  with different conductors in shielded room, as pictured in Fig. 2.35. Modes visible at low frequency agree nicely with the predictions of Eq. 2.43, though they are pulled around by the scrap metal. Note, the scale changes slightly after the X-axis break.

1204 **2.4.2 Statistical approach to electromagnetic waves in cavities**

1205 By using a mode stirrer, modes are intentionally pulled around in frequency, and the average  
1206 response of the cavity begins to converge to be relatively flat. The regime where this occurs is  
1207 known as being well-stirred. It requires the stirrer to be large enough and obey some design  
1208 principles and that the frequency to be above a threshold. This lowest usable frequency  
1209 (LUF) is determined by a minimum modal density since the modes must be close enough  
1210 together in order to overlap. For a room-sized reverberation chamber with a lowest resonance  
1211 of around 60 MHz ( $\sim 3$  or 4 meters per side), the rule of thumb cited by Hill, among others,  
1212 is the LUF is close to where the modal density is about 1 mode/MHz. Therefore, according  
1213 to Fig. 2.34, the LUF of our shielded room is about 200 MHz.

1214 A simple alternative to using a purpose-built mode stirrer is moving a receive antenna  
1215 around in the room. Instead of moving the spatial structure of the modes around the antenna,  
1216 the antenna is moved through the modes. While not as effective, it is simpler to implement,  
1217 so this was the method used in Run 1A. Note that Run 1A does not rely on statistical  
1218 uniformity. Simulations provide a means to calibrate the system as discussed in Sec. 4.3.  
1219 However, using these statistical ideas provides a much more stable simulation with a much  
1220 better agreement with measurement.

1221 One final remark that is relevant to the experiment is the concept of composite  $Q$ . This  
1222 parameter represents a resonant enhancement factor that corresponds to the antenna/room  
1223 system's tendency to “ring up” in the same way any resonator will. It is referred to as *com-*  
1224 *posite Q* and represented as  $\tilde{Q}$ . It is analogous to the standard quality factor of a resonator

1225 with one important modification; the experiment is operated across a wide frequency range,  
1226 so  $\tilde{Q}$  is defined across the continuum of these resonances, not only on classical eigenmodes  
1227 of the system.

## 1228 **2.5 System Design**

1229 This section outlines the subsystems which make up the experiment. While specifics and  
1230 basic calculations are provided as they apply to design choices of subsystems, testing and  
1231 characterization of the system as a whole is left to Ch. 3. A simplified schematic of the  
1232 entire experiment is shown in Fig. 2.37 and a photo of the lab is shown in Fig. 2.38.

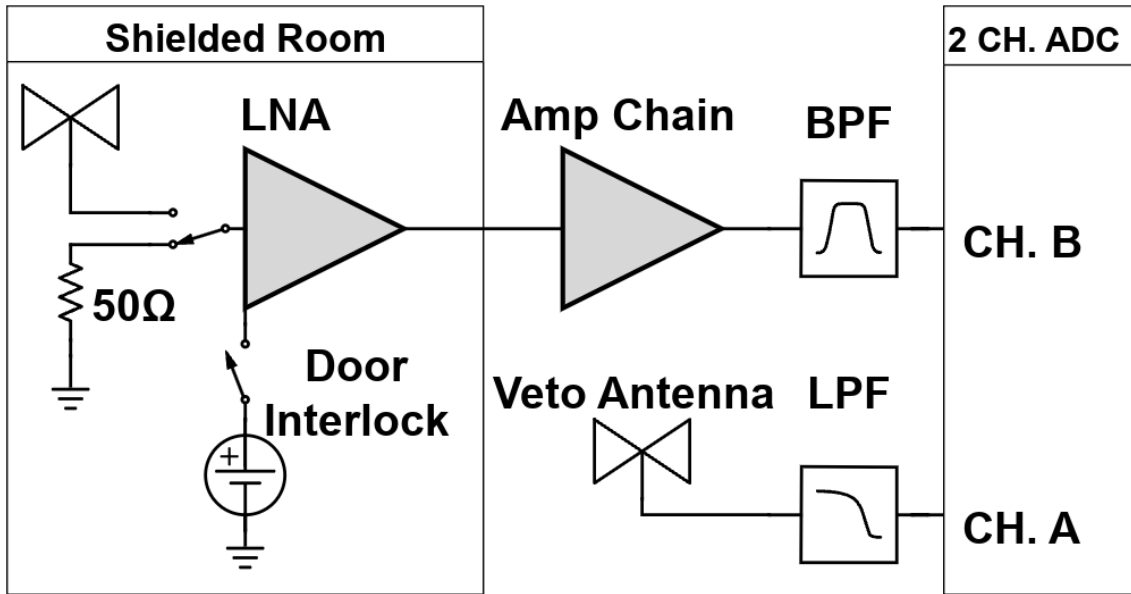


Figure 2.37: Schematic of the RF receiver system. An RF coax switch allows the PC to control the source (antenna or terminator). The amplifier chain is shown with more detail in Fig. 2.42. The switch is controlled by optical fiber to maintain the isolation of the room. The LNA (Pasternack PE15A1012) has a nominal gain and noise temperature of 40dB and 100K (measurements shown in Sec. 3.1.1). It is interlocked (Fig. 2.43) to the door to protect amp B and the ADC from large signals when the door is open. The secondary amplifier is a Mini-Circuits (MC) ZKL-1R5+ and has a nominal gain of 38dB. Not pictured after this amplifier is a fixed 4dB of attenuation. The band pass filter (BPF) defines the experiment's bandwidth,  $-3 \text{ dB} \approx 40 - 320 \text{ MHz}$  and is discussed in Sec. 2.5.4. The veto antenna is outside of the room and interference is not reduced by the  $\approx 100 \text{ dB}$  SE of the room, so no gain is required. The low pass filter (LPF) on the veto is for anti-aliasing.



Figure 2.38: Photo of dark radio lab. The shielded room contains the main antenna as well as the LNA and power supply (not visible). The veto antenna can be seen hanging outside of the shielded room. Photo taken looking south.

1233 **2.5.1 Shielded room**

1234 The shielding room [55] serves two purposes. The first is straightforward; to shield the  
1235 antenna, keeping radio frequency interference (RFI) *out*. The second purpose is a bit more  
1236 subtle; to keep any converted dark photons *in*. This second point is addressed further as an  
1237 aspect of system calibration in Ch. 4, but roughly can be described by the loaded quality  
1238 factor [56–58] of the antenna/room system. Namely, a more resonant system will be more  
1239 sensitive to coherent signals. This subsection will focus on the first point, keeping RFI out.

1240       Shielding effectiveness SE is a measurement of a shielding enclosure's ability to attenuate  
1241 electromagnetic waves from entering,

$$\text{SE} \equiv 10 \log_{10} \left( \frac{P_{\text{open}}}{P_{\text{closed}}} \right) = P_{\text{open}, \text{dB}} - P_{\text{closed}, \text{dB}} \quad (2.46)$$

1242 where  $P_{\text{open}}/P_{\text{closed}}$  are powers received with the door open/closed. The ratio of powers  
1243 allows all the specifics of antenna matching to cancel, allowing for a very simple differential  
1244 measurement. The results of this are described in Sec. 3.2.

1245       Another important measurement are the dimensions, shown in table 2.2. I carefully  
1246 measured the room with a laser range finder. I checked the rangefinder against a measuring  
1247 tape, and it gives good agreement to 1 mm<sup>24</sup>. The room is out of square by a few mm,  
1248 especially the height measured in the south-west corner compared to the height measured  
1249 everywhere else. This is the most extreme deviation and is about 5 mm.

---

<sup>24</sup>After a year, I dropped it and it now gives crazy readings which jump around by 10s of cm. Be careful!

Direction	Coordinate	Nominal Length [ft]	Measured Length [m]
West-East	x	10	3.070
Vertical	y	8	2.457
North-South	z	12	3.684

Table 2.2: Direction, coordinate, and length measurements of the shielded room in lab 314. Note that Fig. 2.38 is looking south, so x is right-left, and z is into the page. Note that these are the mean values of several measurements. The room was found to be about 5 mm out of square, so these should be interpreted as  $\pm$  5 mm.

## 1250 2.5.2 Antenna

1251 The antenna plays an important role in the experiment as the matching device between  
 1252 electromagnetic waves in the cavity and the  $50\Omega$  receiver system. For a broadband search  
 1253 such as the 50-300 MHz run (a 6:1 bandwidth), a broadband antenna must be used. The  
 1254 chosen antenna must provide a good impedance match and high efficiency since an inefficient  
 1255 antenna would convert a substantial amount of the converted dark photon's power into heat  
 1256 within the antenna's structure. The antenna is connected to the RF switch via a low loss  
 1257 (0.45dB at 300 MHz) 21 ft. LMR400 cable. This contributes about 31.6 K to the  $\approx$  400 K  
 1258 antenna noise, see Eq. 2.27. Note that the final limit on epsilon scales with the square root  
 1259 of system temperature, so this is only a few percent degradation in the final limit after a 9  
 1260 day run.

1261 For the 50-300 MHz run, a  $\approx$  131 cm biconical antenna (bicon) was chosen. The selected  
 1262 model is manufactured by COMPOWER, model AB-900A [59]. In a phone call with the  
 1263 manufacturer as well as testing of the isolated balun, it was determined that the balun used  
 1264 in the antenna was 1:1. This allows for simple simulation of a free-space aperture which

1265 agrees remarkably well with manufacturer data, Fig. 2.39. In COMSOL [60], the lumped  
1266 port option allows for a balanced drive of an antenna. A match to a  $50 \Omega$  transmission line  
1267 through a 1:1 balun is simply modeled as a lumped port, a very simple object in COMSOL  
1268 featured in nearly all of the antenna tutorials<sup>25</sup>. Additionally, there is good agreement  
1269 between simulated and measured antenna impedance. See the Smith Chart in Fig. 2.40.

---

<sup>25</sup>See for example the dipole antenna tutorial, available at <https://www.comsol.com/model/dipole-antenna-8715>

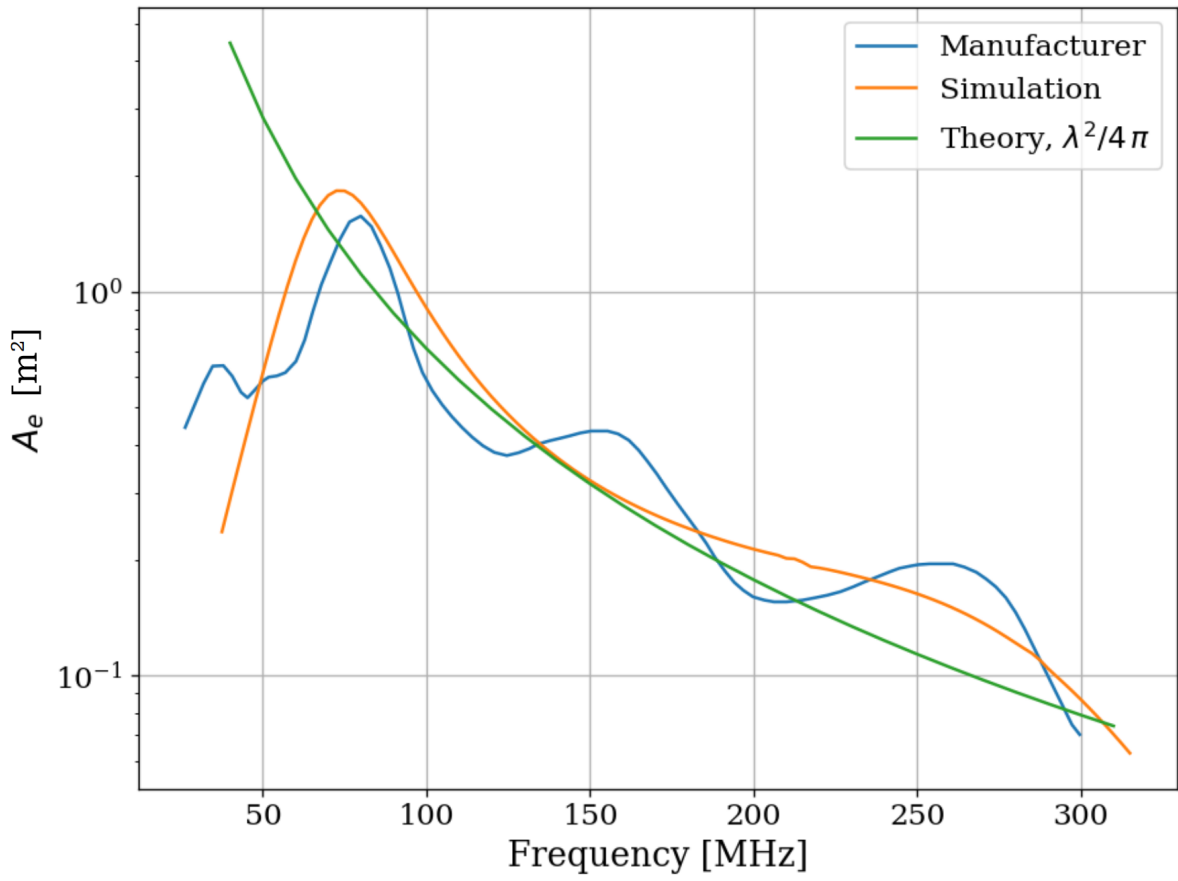


Figure 2.39: AB-900A biconical antenna effective aperture, simulated, measured and theoretical in free space. Simulation performed in COMSOL [60]. The measurement was provided by manufacture [59] as an antenna factor and was converted to aperture. Variations observed in the manufacturer's measured data are the result of testing over a ground plane and are a known discrepancy between simulations and measurements of “free space” antenna factor. See for example [61]

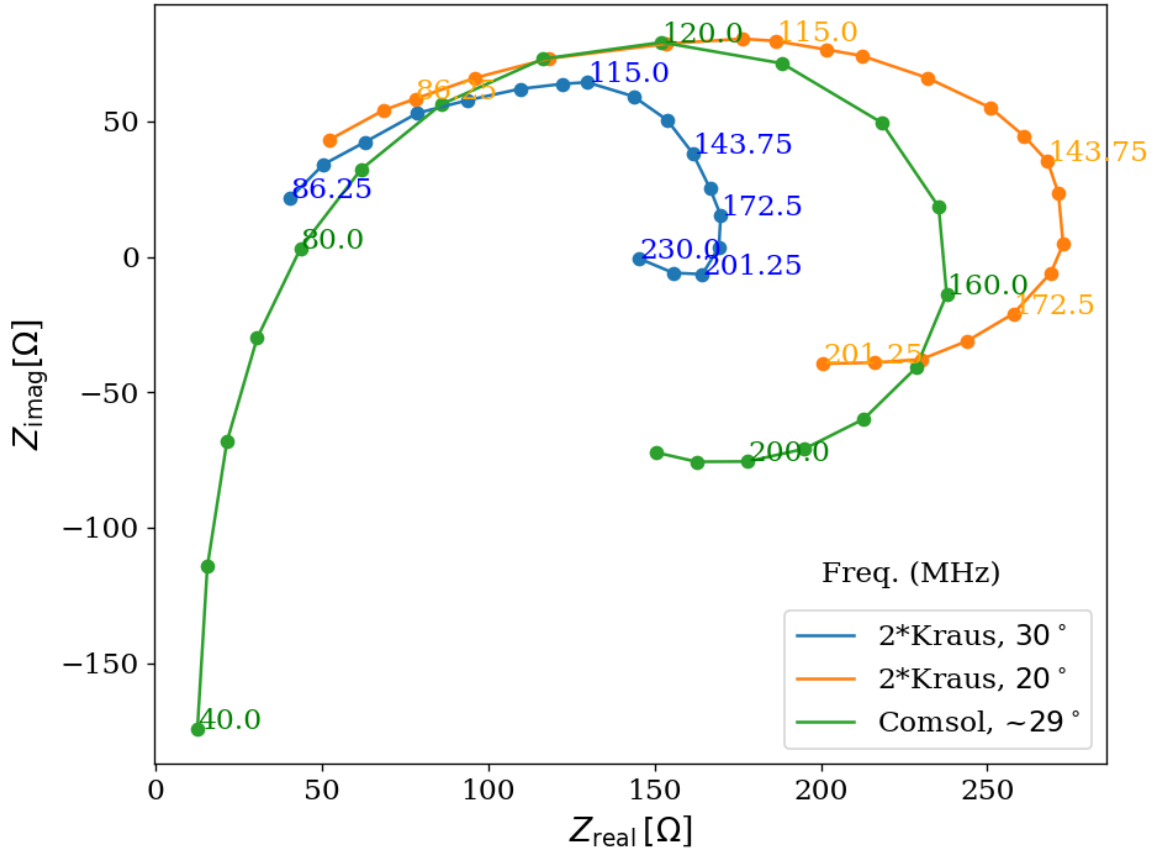


Figure 2.40: Simulated AB-900A biconical antenna free space complex input impedance shown in blue. The simulation was performed in COMSOL. The measurement is from Kraus' Antennas, second edition, Fig 8-13 [62]. Measured data is for a monoconical antenna and must be multiplied by 2 to compare to a biconical antenna, as discussed in Kraus. Numbers along the curve indicate the frequency in MHz.

1270 **2.5.3 Terminator and fiber-optic switch control**

1271 Experience has shown that it is advantageous to have a stable noise reference at the begin-  
1272 ning of the signal chain to monitor system performance. One may think the antenna can  
1273 provide this following Sec. 2.1.1.2, but in practice, the antenna is not that stable, Sec. 2.3.  
1274 Furthermore, while RFI was not significant in the actual run, it very well could have been,  
1275 introducing some uncontrolled, coherent power into the spectrum, which would have had  
1276 an unknown origin. A terminator will give a very constant noise power density  $S_{\text{term}} = kT$   
1277 regardless of RFI and antenna position. For this reason, one is included. It is at the same  
1278 temperature as the walls and is a nice passive solution. The RF switch shown in Fig. 2.37  
1279 is actuated periodically during the run to measure the terminator's noise power through the  
1280 same amplifier chain as the antenna. The terminator is connected to the switch via a 21-foot  
1281 cable (LMR 400) that is identical to the antenna's cable. The switch is controlled via a  
1282 fiber-optic link in order to reduce RFI. The fiber optic is an extremely important feature  
1283 that was overlooked for several years at the beginning of the experiment, leading to lots of  
1284 RFI.

1285 **2.5.4 Signal conditioning**

1286 As discussed in Sec. 2.1.5, the ADC has internal signals that are mitigated by introducing  
1287 gain before the ADC. The amount of gain must be carefully chosen since too much will  
1288 cause the ADC to clip. Additionally, high frequencies must be limited before digitizing to  
1289 prevent aliasing. To accomplish this, several RF components must be selected to condition

1290 the analog signal: an LNA, a secondary amplifier, band-pass filter and several attenuators.

1291 **2.5.4.1 Low noise amplifier**

1292 The important concepts of the LNA have been introduced in Sec. 2.1.4. The key takeaway  
1293 is that low noise gain helps to mitigate signal-to-noise degradation that occurs later in the  
1294 signal path. Relevant specifications for the Pasternack PE15A1012 [36] are summarized in  
1295 table 2.3.

Specification	Value	Uncertainty (50-300MHz)	Units
Frequency Range	50-1,000	-	MHz
Gain	40	$\pm 1$	dB
Noise Temperature	110	$\pm 10$	K
Input Return Loss	< -15	-	dB
Output Return Loss	< -15	-	dB
Price	500	-	USD
Voltage	9-15		V
Current	100	10	mA

Table 2.3: Specifications for the Pasternack PE15A1012-E. The voltage is regulated internally, so the exact voltage supplied is not critical, though there is a slight gain dependence on voltage since a higher voltage causes the amp to run warmer, see Fig 3.8.

1296 We have several identical amplifiers which are labeled with letters. At the time of writing,  
1297 amplifiers A-D are out of commission. Amplifier E was used for run 1.4.

1298 **2.5.4.2 Secondary amplifier**

1299 As discussed in 2.1.4, the noise temperature of a secondary amplifier has negligible impact  
1300 on the total system noise temperature. For this reason, a cheaper secondary amplifier is  
1301 used. The specifications for the Mini-Circuits ZKL-1R5+ [63] are outlined in Table 2.4.

1302 This amplifier has no internal regulator, so gain and noise temperature depend strongly on  
1303 the bias voltage. Voltage was set to 9.05 V for run 1.4 using an external regulator (built  
1304 around a TI LM317 [64]).

Specification	Value	Uncertainty (50-300MHz)	Units
Frequency Range	50-1,000	-	MHz
Gain	40.5	.3	dB
Noise Temperature	275	15	K
Input VSWR	<1.14	-	dB
Output VSWR	<1.37	-	dB
Price	235	-	USD
Voltage	9-15	-	V

Table 2.4: Specifications for the Mini-Circuits ZKL-1R5+ as measured with 9.05 V bias.  
There is no internal regulator, so the voltage is set using an external regulator (built  
around a TI LM317 [64]).

1305 **2.5.4.3 Band pass filter**

1306 The band-pass filter has two purposes. The first purpose is to minimize the bandwidth  
1307 entering the ADC. This allows for introducing as much gain as possible without wasting  
1308 power amplifying frequencies where the antenna doesn't offer a good match. This will be  
1309 computed below in Sec. 2.5.4.4. The second purpose is to prevent aliasing<sup>26</sup>. Aliasing occurs  
1310 when the analog signal contains frequency components at frequencies greater than half the  
1311 sample rate, in other words, when the signal and ADC don't obey a condition called the  
1312 Nyquist criterion,  $\nu_s/2 \geq \nu$ , where  $\nu_s$  is the sampling frequency and  $\nu$  is the frequency of  
1313 the analog signal.

---

<sup>26</sup>Aliasing is a rather complex topic that is greatly simplified here. Wikipedia's aliasing page is an excellent reference. For a more rigorous treatment, see Ch. 7 Sec. 3 of the second edition of Signals and Systems by Oppenheim et. al [65]

1314 When this criterion is not met, higher frequencies are mapped back down to a lower  
1315 frequency, described by the aliasing formula:

$$\nu_{\text{alias}} = |\nu_{\text{signal}} - n \times \nu_s|, \quad (2.47)$$

1316 where  $\nu_{\text{alias}}$  is the aliased frequency,  $\nu_{\text{signal}}$  is the original signal frequency,  $\nu_s$  is the  
1317 sampling rate, and  $n$  is an integer which specifies the Nyquist zone. In the simple case  
1318 with bandpass filters that roll off well within the first Nyquist zone, only  $n = 1$  must be  
1319 considered.

1320 As an example, a  $\nu_{\text{signal}} = 500$  MHz signal sampled at  $\nu_s = 800$  MHz (the run 1.4 sample  
1321 rate), it would alias to  $\nu_{\text{alias}} = 300$  MHz. This also means that 1,300 MHz (residing in the  
1322 second Nyquist zone) would alias down to 300 MHz, but again this and higher frequencies  
1323 won't be considered. This means that by choosing only to analyze frequencies less than 300  
1324 MHz, only frequencies greater than 500 MHz will alias into this analysis span.

1325 The Mini-Circuits ZX75LP-288-S+ low pass filter[66] serves as the anti-aliasing filter in  
1326 run 1.4. It has an insertion loss of 68 dB at 500 MHz, while being flat to within 2dB from  
1327 50 to 300 MHz. Additionally, the Mini-Circuits SHP-50+ [67] is used as the high pass filter.  
1328 When connected in series, these two filters constitute the band-pass filter shown in Fig. 2.37.

#### 1329 2.5.4.4 Putting together a signal conditioning chain

1330 The total gain required can be estimated by setting the output referred power of bandlimited,  
1331 400 K noise source times the gain equal to the maximum power the ADC can handle,

1332  $V_{\text{RMS}}^2/Z = 0.63 \text{ mW}$  for  $Z = 50 \Omega$ . Assuming a perfect filter from 50-300MHz (a 250 MHz  
1333 bandwidth), the gain required is

$$G = \frac{0.63 \text{ mW}}{k 400\text{K} 250 \text{ MHz}} = 4.5 \times 10^8 = 87\text{dB}. \quad (2.48)$$

1334 Noise is a Gaussian random process, however. This much gain ensures  $1\sigma$  of the time  
1335 domain samples are below clipping. Since many samples are collected ( $2^{24} \approx 1.6 \times 10^7$  in  
1336 run 1.4), and each has a probability of about 16% of clipping, many samples will clip with  
1337 87 dB of gain. However, it gives a good estimation for what to expect.

1338 The band-pass filter is not a brick wall from 50 - 300 MHz as was assumed in 2.48. The  
1339 effective bandwidth of a filter is defined here as the integral of the square magnitude of its  
1340 through gain,

$$B_{\text{eff}} \equiv \int_{-\infty}^{\infty} d\nu 10^{S_{21}/10}. \quad (2.49)$$

1341 Where  $S_{21}$  is measured in dB, and we are interested in integrating a quantity that is  
1342 proportional to linear power, so it is divided by 10 rather than 20. The linear S-parameters of  
1343 components connected in series multiply [43], but since dB are logarithmic, this is equivalent  
1344 to adding their S-parameters (in dB). Also note that  $S_{21} \equiv \text{IL}$ , the insertion loss. Insertion  
1345 loss is frequently given on data sheets.

1346 With all this in mind, we can compute  $B_{\text{eff}} = 237.06 \text{ Hz}$  for the actual filters (Mini-  
1347 Circuits SLP-50+ high pass filter and Mini-Circutis ZX75LP-288-S+ low pass filter) from  
1348 their data sheets. Curves of  $S_{21}$  for the real band pass filter and an ideal brick wall filter are

1349 shown in Fig. 2.41. Note that it is actually slightly less than the ideal 250 MHz bandwidth  
1350 since there is some loss in band.

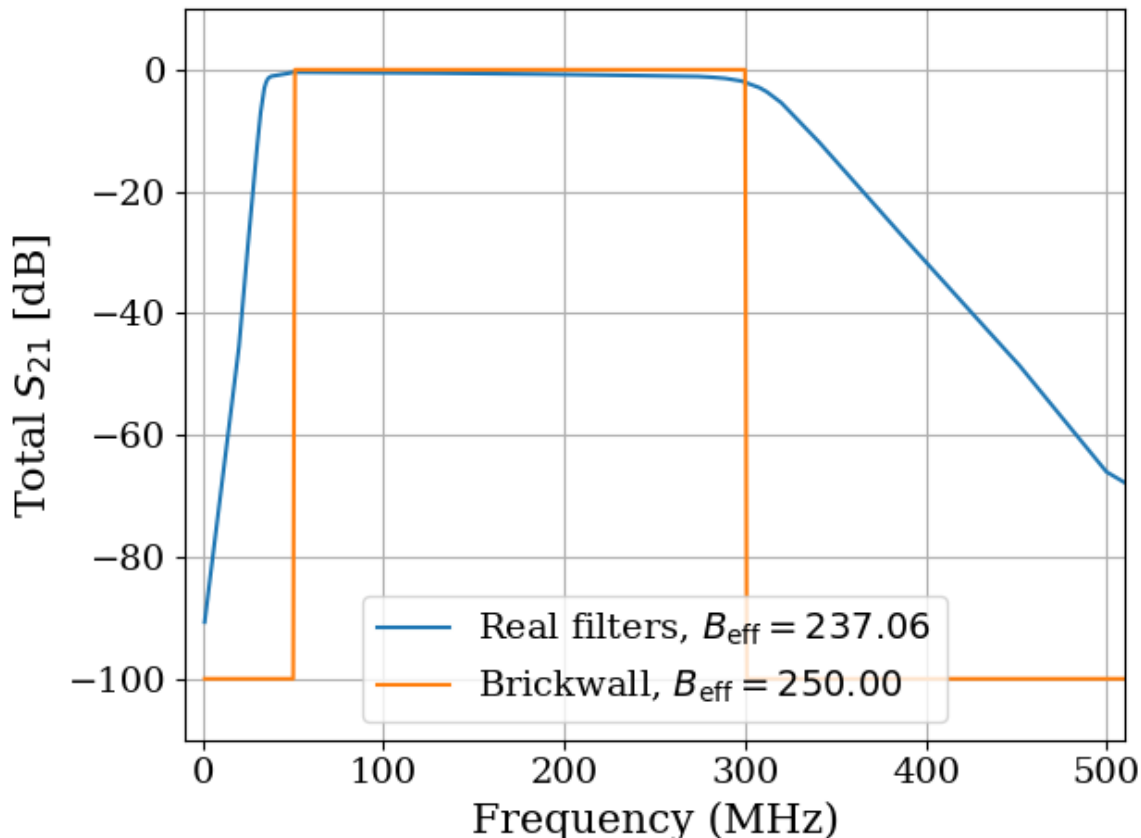


Figure 2.41: Through gain ( $S_{21}$ ) of bandpass filter. Shown in dB, however  $B_{\text{eff}}$  is computed with linear  $S_{21}$  as in Eq. 2.49. Ideal brickwall filter shown for reference.  
comment: Add Hz in legend

1351 Setting the gain is ultimately done by trial and error; taking a scan, adding some atten-  
1352 uation if it clips, taking a scan, etc. Experience and preliminary simulations have shown  
1353 that a few dB of clipping for a noise-dominated signal actually doesn't matter much, but  
1354 this was not fully explored. If future runs are to scan for longer, they may have significant  
1355 contamination from ADC spurs (see Sec. 2.1.5.1), so additional gain driving into clipping

1356 may be fruitfully explored. Every dB of gain added allows for  $10^{1dB/5} \approx 44\%$  more averaging  
 1357 before ADC effects are at the same relative level<sup>27</sup>, so a little extra gain goes a long way.

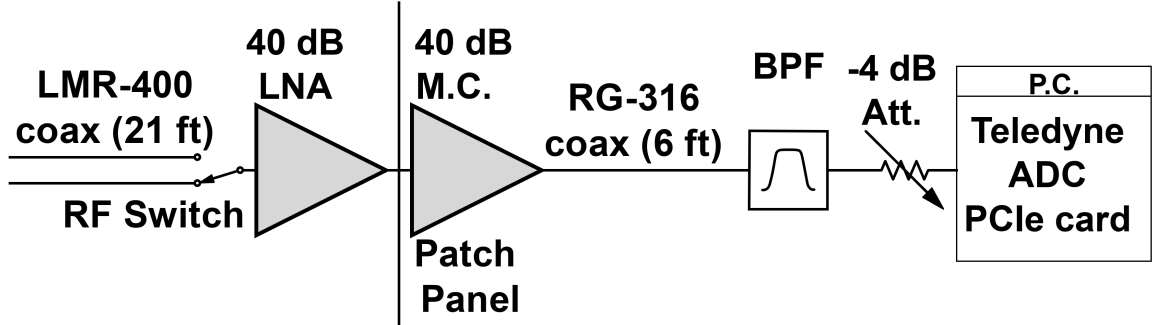


Figure 2.42: Schematic of Run 1A amplifier chain. Antenna (Sec. 2.5.2) and terminator (Sec. 2.5.3) are not part of the amplifier chain and, therefore, are not shown, but they would be at the far left of the schematic. All RF connectors are SMA, except the connection between the bicon antenna and its cable which is N type (though that cable has SMA on the switch-side). RF switch is Teledyne CR-33S8D-T. 40 dB LNA is Pasternack PE15A1012-E (Table 2.3). The patch panel uses an SMA bulkhead connector labeled “A” (far left-hand side when standing outside the shielding room, as shown in Fig. 2.38). 40 dB Mini-Circuits (M.C.) is Mini-Circuits ZKL-1R5+ (Table 2.4). Band-pass filter (BPF) is made up of Mini-Circuits SLP-50+ high pass filter and Mini-Circutis ZX75LP-288-S+ low pass filter. Note that filters and attenuator are directly connected to the SMA port of the Teledyne ADC (Sec. 2.5.7) to mitigate RFI received in the RG-316 cable run.

## 1358 2.5.5 Veto antenna

1359 The veto antenna is an identical Compower AB900 bicon antenna [68] as is used in the  
 1360 shielded room. It is connected to channel A of the ADC with no amplification. However, it  
 1361 has a Mini-Circuits ZX75LP-288-S+ low pass filter [66] to prevent aliasing. This is the same  
 1362 model low pass filter that is used for the main channel. The antenna is hung a few feet in

---

<sup>27</sup>Calculations in dB like this are handy once they are understood, but can seemingly come out of nowhere. This can be worked out by a careful reading of section 2.2, using properties of logarithms and definition of the dB.

1363 front of the door from some pipes on the ceiling. The proximity to these pipes likely gives  
1364 the antenna a strange response, but its purpose is simply to look for large RFI signals, so  
1365 this isn't that important.

1366 **2.5.6 12 V power system**

1367 The LNA and switch are active components that require power to operate. The experiment  
1368 is incredibly sensitive to RFI, so while there is 120 VAC in the room, it is simpler to provide  
1369 the power from a 12 V battery than to use an AC/DC regulator. Originally a 12 V lithium-  
1370 ion (LiFePO4) battery was used. Lithium-ion batteries contain several cells and a controller  
1371 to regulate charge/discharge between the cells. In order to remove the possibility of this  
1372 controller emitting RFI in the room (which would create candidates that would be extremely  
1373 difficult to veto), the lithium-ion was replaced with a 12 V lead acid golf cart battery <sup>28</sup>.

1374 The LNA is interlocked to the door such that power is cut when the door is opened.  
1375 This prevents the large radio signals from being amplified once they enter the room and  
1376 protects the ADC. The circuit that controls this is shown in Fig. 2.43. Note that it takes a  
1377 few seconds for the slow turn on circuit to discharge, so the door should be opened slowly

---

<sup>28</sup>This was done between run 1.2 and 1.3 due to interference resulting in many candidate detections. Most of these were likely external RFI, which were eliminated by cleaning the door (discussed in Sec. 3.2). Two variables were changed (cleaning of the door and replacement of the battery) so it's unclear if a lead acid is necessary. It works, however, and if it ain't broke, don't fix it.

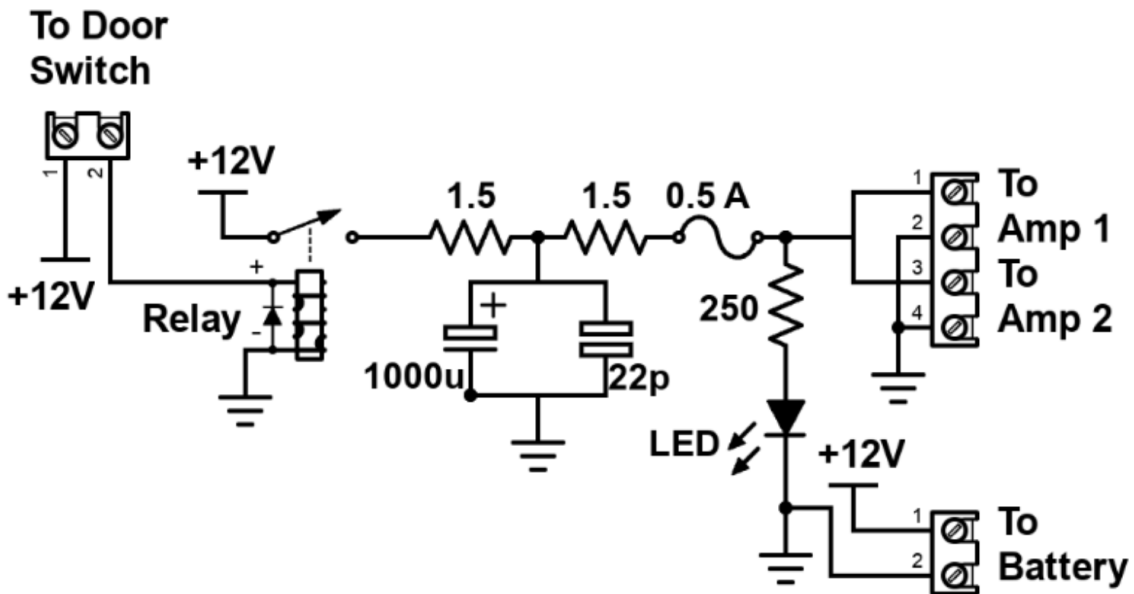


Figure 2.43: Schematic of Interlock board. No voltage regulation is provided because it is designed to work with amplifiers containing internal regulation (Pasternack PE15A1012 [36]). Not shown is a simple “slow turn on circuit” consisting of a  $0.68\text{ F}$  capacitor and an  $8\Omega$ ,  $10\text{ W}$  resistor (time constant = 5.4 seconds) which was installed to protect the amplifier from transient voltages when the door is closed. This circuit can be seen in Fig. 2.44. Experience has shown the liberal use of fuses to be prudent when working with car batteries in a metal room.

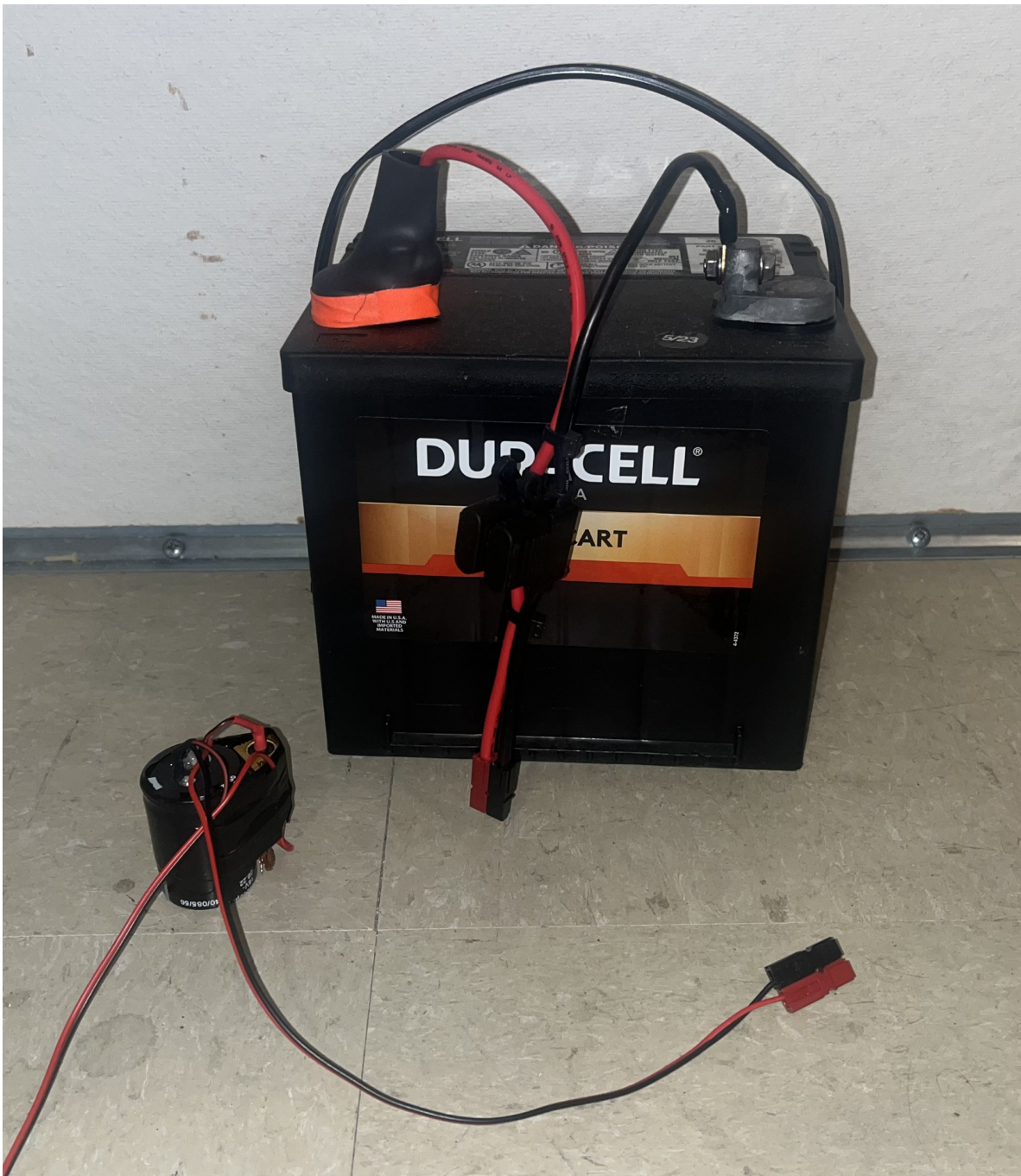


Figure 2.44: Photo of 12 V lead-acid battery and slow turn-on circuit. Both connect directly to the interlock board shown in Fig. 2.43. The slow turn-on circuit is connected between the interlock board and amplifier. The battery includes a 2A fast fuse installed in a commercial Anderson power pole assembly.

1378 **2.5.7 GPU-Based Real-Time Spectrum Analyzer**<sup>29</sup>

1379 The use of commercial Spectrum Analyzers (SAs) that feature so-called real-time spectrum  
1380 analyzer (RTSA) mode comes with several restrictions that limit the efficiency with which  
1381 they are able to perform wide-band scans with narrow frequency resolution, as pointed out  
1382 the dark radio pilot run [4]. The number of frequency bins output by a real discrete Fourier  
1383 transform (DFT) is equal to half of the number of time domain samples, while the bandwidth  
1384 is given by half of the sample rate. Furthermore, the ability to acquire data in real-time  
1385 requires a DFT algorithm (generally implemented as a fast Fourier transform, FFT) and  
1386 computational resources that can operate on time domain data at least as fast as it is  
1387 acquired. In practice, real-time DFTs with high-frequency resolution and wide bandwidth  
1388 require modest memory, transfer rates and processing resources. Commercial “real-time  
1389 spectrum analyzers” tend to cheat a bit to reduce hardware requirements. Frequency mixers  
1390 reduce the required sample rate (and therefore span), limits on FFT lengths reduce either  
1391 span or resolution, and limits on the rate of scans make it so that these SAs aren’t real-time  
1392 (at least in the sense that we require them to be).

1393 For this reason, I have constructed a custom SA based on the Teledyne ADQ32 PCIE  
1394 digitizer[37], which is wide-bandwidth (up to 1.25 GHz frequency span), high resolution  
1395 ( $2^{24}$  point FFT), and nearly 100% real-time (see Fig. 3.16). I have been unable to find a  
1396 commercial SA with comparable capabilities. Specifications are shown in table 2.5.

---

<sup>29</sup>Code for this section can be found at: <https://github.com/josephmlev/darkRadio/tree/master/daqAnalysisAndExperiments/teledyne>

Bit depth	12 bits
Sample rate	800MHz
DFT input length	$2^{24}$ samples
FFT compute time	2 ms
Channel count	2
Efficiency	99.765%

Table 2.5: Specifications for the custom, real-time spectrum analyzer used for run 1A.

1397 After passing through an amplifier and filter chain outlined in Sec. 2.5.4, both the main  
 1398 and veto antenna's RF signals are digitized by the ADQ32's two independent ADCs. This  
 1399 raw, digitized time series is sampled at the digitizer's clock rate. Since the discrete Fourier  
 1400 transform (DFT) of a perfect sinusoid sampled by an unstable clock will have a finite spectral  
 1401 width, clock stability must be better than the expected spectral width of candidate signals,  
 1402 which in our case is set by the expected  $Q_{DP} \approx 10^6$ . To achieve the required stability, we  
 1403 synchronize the sample clock (Valon 5009 RF synthesizer) of our ADC to a 10 MHz rubidium  
 1404 frequency standard (Stanford Research Systems FS725), which is further steered by the  
 1405 one pulse-per-second (PPS) signal from a GPS receiver. Clock performance is discussed in  
 1406 Sec. 3.3.3.

1407 This system utilizes a GPU direct write in order to minimize CPU-GPU copies tends to  
 1408 be significantly slower than the FFT itself. This GPU direct write is implemented by the digi-  
 1409 tizer's C++ API which is called from python. This happens in the `teledyneTemplate/drDaq.py`  
 1410 script (within the directory linked as a footnote at the beginning of this subsection). The  
 1411 GPU is a Nvidia A5000. The process is shown graphically in Fig. 2.45

1412 First, several buffers are allocated in GPU memory. A record is acquired ( $2^{24}$  time domain

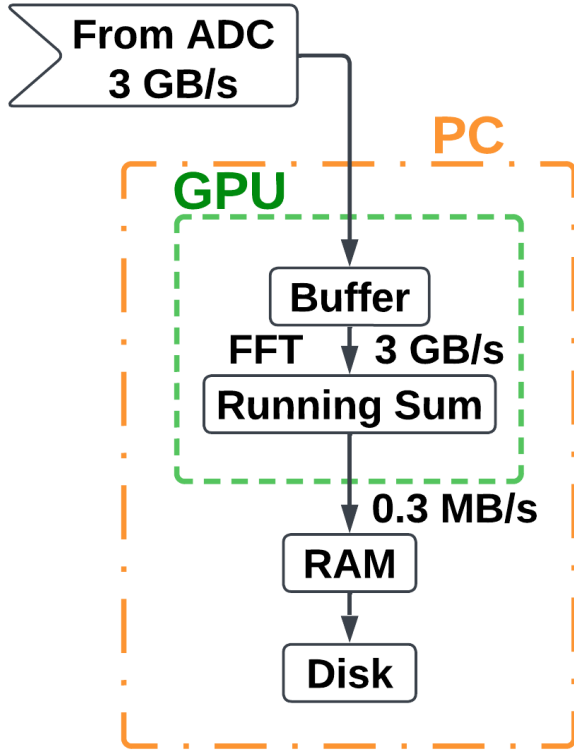


Figure 2.45: Real time DAQ data stream. Approximately  $10^4$  time series records (about 3 minutes of real-time data) are written from the ADC directly to GPU buffers. FFTs are performed on these records, resulting in a pre-averaged spectrum that can be saved to disk. This setup is duplicated for channels A and B, though the data rates indicate the sum of both channels.

samples for run 1.4). This record is written to a pre-allocated, time-domain buffer in the GPU's memory. Next, an FFT is performed using Pytorch, which I found to be the fastest algorithm, at least on a Nvidia GPU. 8,600 FFTs are performed and added to a cumulative sum on the GPU (representing about 3 minutes of real-time data). Dividing by the number of FFTs provides an averaged spectrum that is saved for offline processing. This *pre-averaging* reduces the raw  $\approx 1.5 \text{ GB/s}/\text{channel}$  data stream to  $\approx 0.15 \text{ MB/s}/\text{channel}$ , which greatly reduces storage requirements. However, this comes at the cost of temporal resolution of

1420 transient candidates. Since we are interested in constant (or at least very slowly varying)  
1421 signals, this is not a problem, but in other radio astronomy applications, this step should be  
1422 avoided. Pre-averaging is set using the NOF\_BUFFERS\_TO\_RECEIVE variable, see Appendix A .

<sup>1423</sup> **Chapter 3**

<sup>1424</sup> **System Characterization and Data**

<sup>1425</sup> **Acquisition System**

<sup>1426</sup>

“When you can measure what you are speaking about and express it in numbers you know something about it; but when you cannot measure it, when you cannot express it in numbers your knowledge is of meagre and unsatisfactory kind; it may be the beginning of knowledge but you have scarcely progressed in your thoughts to the stage of science whatever the matter may be.”

---

Lord Kelvin

1427 This chapter covers the characterization of the system as a whole, including the shielded  
1428 room (Introduced in Sec. 2.5.1), amplifier chain (Sec. 2.5.4) and real-time spectrum analyzer  
1429 system (RTSA, Sec. 2.5.7). This section provides data and information about how they  
1430 were collected from tests that were performed, but that distract from the narratives of the  
1431 preceding and following chapters. This chapter can be skimmed and referenced with further  
1432 care during the reading of Ch. 4.

## 1433 **3.1 Measurement of Amplifier Chain Performance**

1434 The amplifier chain conditions the analog signal (described in Sec. 2.5.4). The following data  
1435 show some measurements that are useful in confirming the system is operating as expected.  
1436 Similar data should be collected and inspected before, during and after a new data run so  
1437 that any performance degradation can be monitored. At the very least, one should take  
1438 note of the power spectrum from a room temperature terminator (Fig. 3.10) and monitor it  
1439 throughout the run for any changes. The heads-up display (Fig. A.1) makes this very easy.

### 1440 **3.1.1 Y-factor method<sup>1</sup>**

1441 The Y-factor method [69] [70] is a common technique for measuring the gain and noise  
1442 temperature of an amplifier chain (details in Sec. 2.1.4). A matched terminator is placed at  
1443 the end of a transmission line, which is connected to the input of an amplifier chain under  
1444 test. The output of the amplifier chain is measured with the terminator at two different

---

<sup>1</sup>Code for this section can be found at: <https://github.com/josephmlev/darkRadio/tree/master/daqAnalysisAndExperiments/run1p4/yFactorTest/yFactorTest.ipynb>

1445 temperatures<sup>2</sup>. These temperatures must be known, and the larger the difference the better  
1446 the measurement because it is easier to extrapolate the slope and intercept from these data  
1447 (see Fig. 3.1).

1448 There are a few different ways to handle the algebra, but the simplest is to fit a line of  
1449 the form

$$T_{\text{out}}(\nu) = G T_{\text{term}} + B, \quad (3.1)$$

1450 where all terms are dependent on frequency. The x-intercept (and therefore the negative  
1451 amplifier temperature) is simply  $G/B$ . This is shown as a cartoon for a single frequency in  
1452 Fig. 3.1.

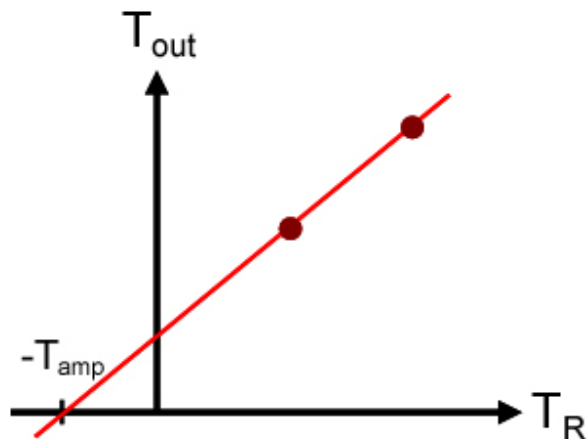


Figure 3.1: Cartoon showing Y-factor data. The (negative of) amplifier temperature is read off of the x-intercept. The gain is given by the slope. Figure from Wikipedia [71].

1453 To make this measurement, I wanted to use liquid nitrogen for the cold temperature

---

<sup>2</sup>Alternatively, a calibrated noise source can be used to simulate a very hot terminator, usually thousands of degrees Kelvin.

1454 (77 K) and a calibrated noise source for the hot temperature ( $\sim$ 12,000 K). The test was  
1455 conducted using the noise source and a 30 dB attenuator placed directly before the ADC.  
1456 This attenuation was later accounted for, yielding a calibrated measurement. However,  
1457 while the test was set up to use this noise source, it gave unreliable results. I was able  
1458 to confirm it became uncalibrated using a spectrum analyzer so I did not use that data  
1459 point. Additionally, I made the measurements with a much wider band-pass filter (0-1 GHz)  
1460 compared to the span of this Run 1.4 (0-0.3 GHz) so that the same data would also give the  
1461 gain and noise temperature up to 1 GHz (though this is not shown in this thesis). Both the  
1462 30 dB attenuator and the 0-1 GHz band-pass filter will be calibrated out. As a check this  
1463 is done correctly, the gain was measured again using a tracking generator with the actual  
1464 setup, avoiding corrections. This is shown in Fig 3.7. The two gain curves agree quite well.

1465 The test setup is nearly identical to the Run 1A amplifier chain (see Fig. 2.42). The  
1466 differences are the 30 dB attenuator and band-pass filter (discussed above) and the short,  
1467 semi-rigid, cryogenic-capable cable between the terminator and LMR 400 cable. The cryo-  
1468 genic setup is the same as shown in the right panel of Fig. 2.28. The raw data (including  
1469 only liquid nitrogen and room temperature) are shown in Fig. 3.2.

1470 The spectra of Fig. 3.2 contain hot and cold measurements at  $2^{18}$  frequency points. At  
1471 each point, a fit is performed according to Eq. 3.1. To demonstrate, this is shown for a single  
1472 frequency (625 MHz) in Fig. 3.3.

1473 Finally, fitting the raw spectra shown in Fig. 3.2 with Eq. 3.1 at each of the frequency  
1474 points, the frequency-dependent gain and noise temperature of the amplifier chain is ex-  
1475 tracted. These are shown (after correcting for the 30 dB attenuator) in Figs. 3.4 and 3.5.

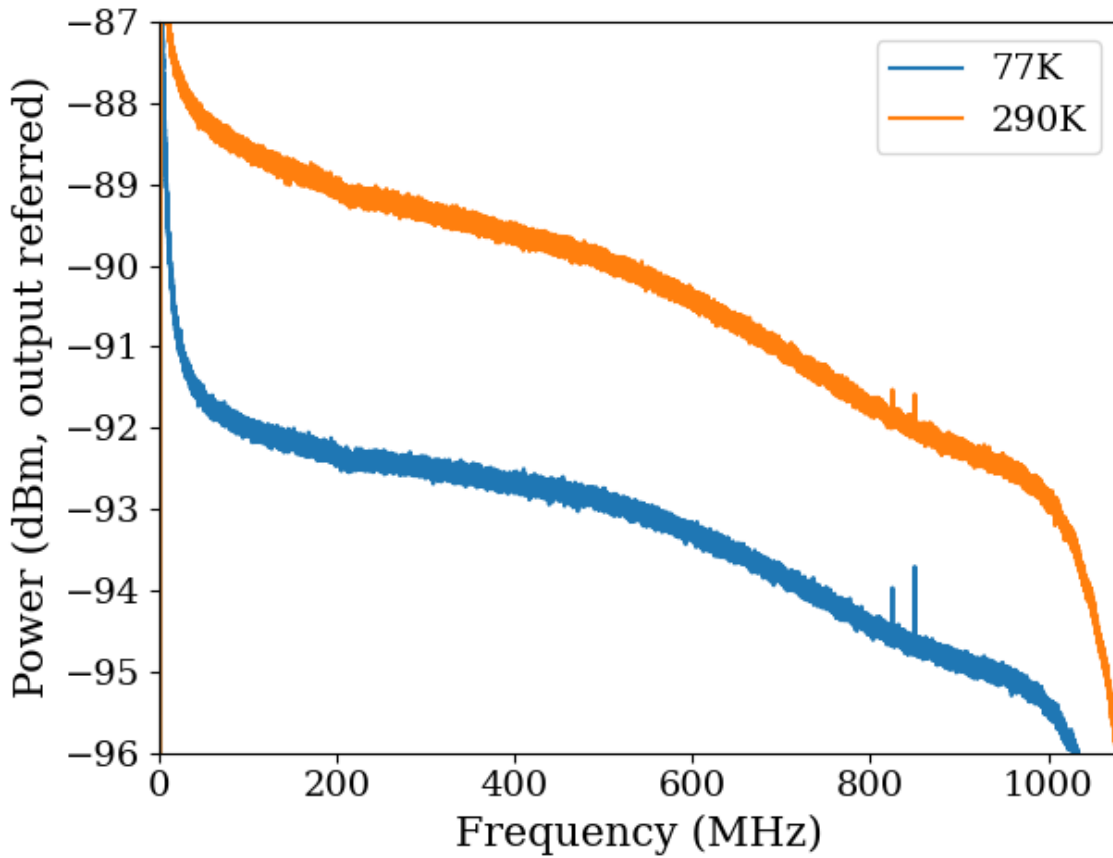


Figure 3.2: Raw output power spectra used to compute the gain and noise temperature for the Run 1.4 amplifier chain using the Y-factor method.  $\Delta\nu_{\text{RF}} \approx 9.5 \text{ kHz}$ , and 10,000 averages were taken. These data are only used to characterize the system between 50 and 300 MHz, so the low frequency ADC effects and RFI around 800 MHz do not affect the calculation. Note that the amplifier chain under test has a 30 dB attenuator directly before the ADC which is discussed in the text. This had an impact on the measured gain, and it is corrected for in the following analysis. It has negligible impact on the noise figure however, as shown in Eq. 2.29.

1476 As a final check, I took the Run 1.4 terminator data and corrected it for the gain and noise  
 1477 figure found using the Y-factor method of this section, expecting to recover the  $-174 \text{ dBm/Hz}$   
 1478 as predicted by Johnson's formula for a terminator at room temperature. The agreement is  
 1479 quite good as shown in Fig. 3.6.

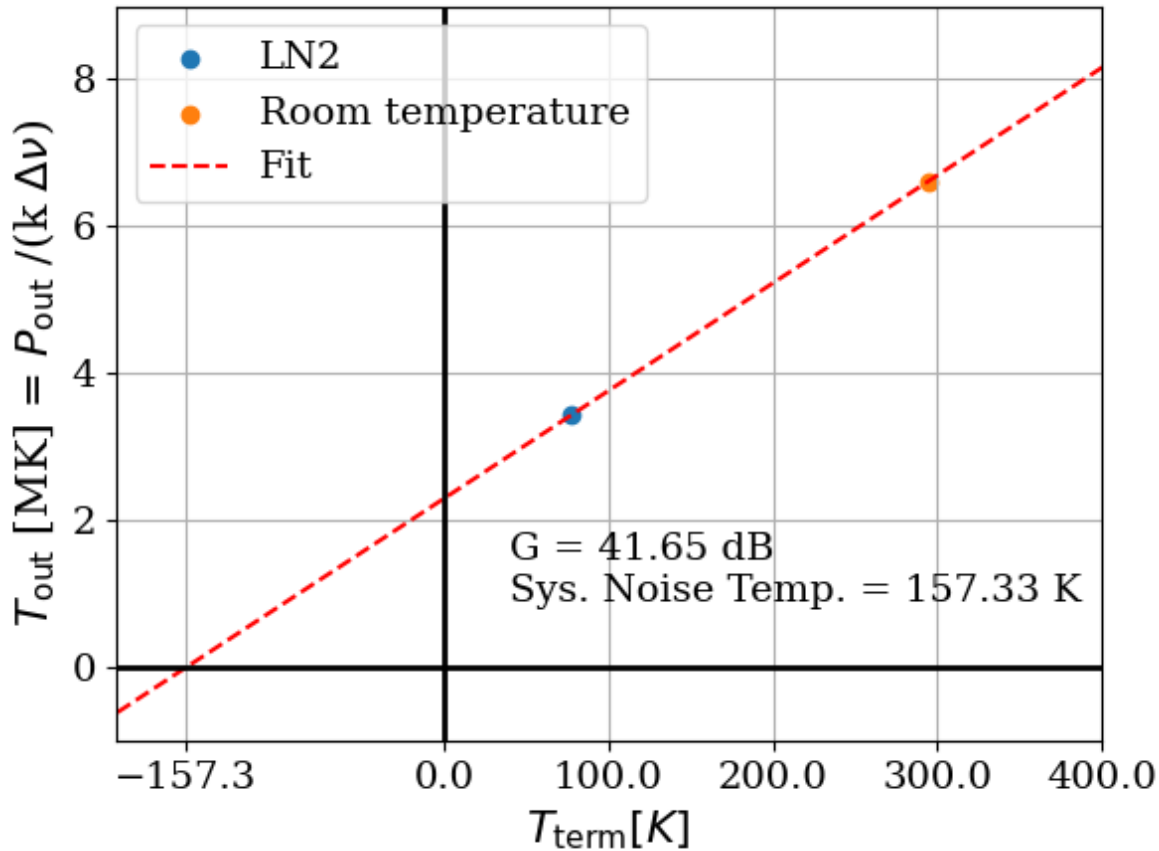


Figure 3.3: Y-factor data from Run 1.4 amplifier chain at a single frequency (625 MHz). Note that  $T_{\text{out}}$  is in MK or millions of degrees Kelvin. This is expected since there is approximately 41 dB of gain on an input temperature of a few hundred Kelvin. Reminder, there is a 30 dB attenuator which has not yet been corrected for.

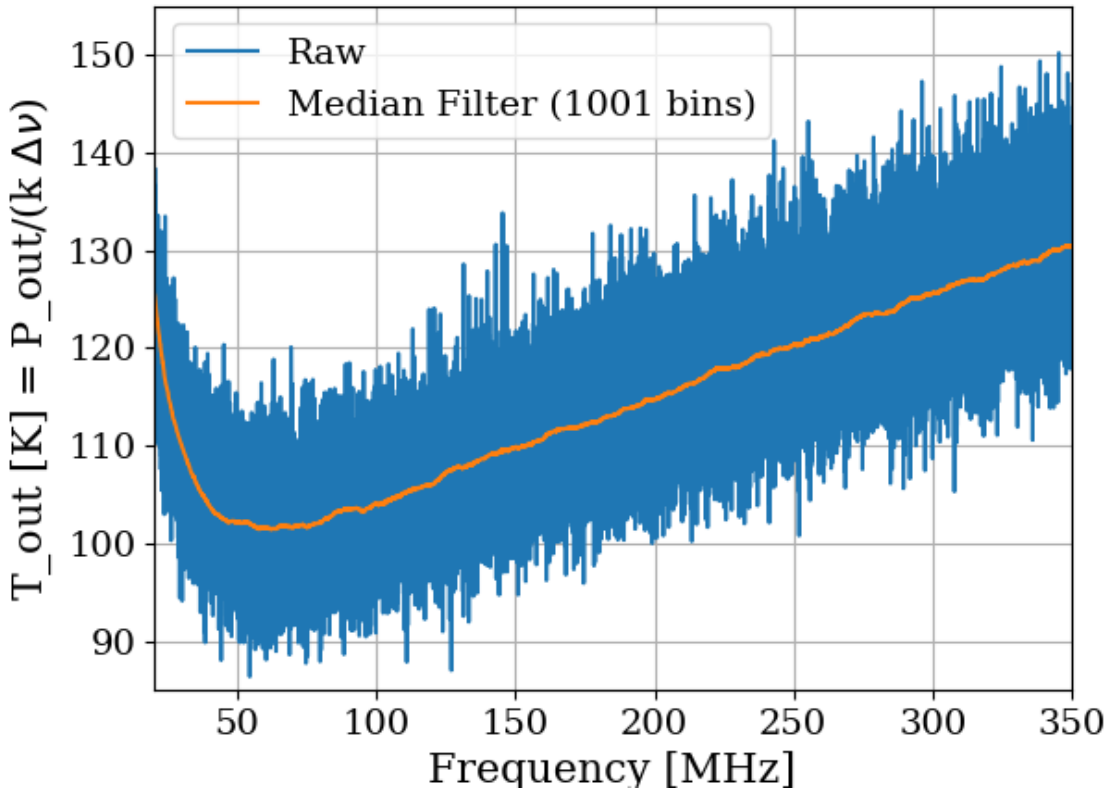


Figure 3.4: Frequency-dependent noise temperature of the Run 1.4 amplifier chain, measured using the Y-factor method. Low-frequency behavior is consistent with the data sheet of the LNA [36]. The increase at high frequency is due to the attenuation of the cable before the LNA. Future runs may place the LNA directly on the antenna to minimize this issue, though other complications will be introduced. The median filter is a simple rolling median to smooth out the noisy measurements.

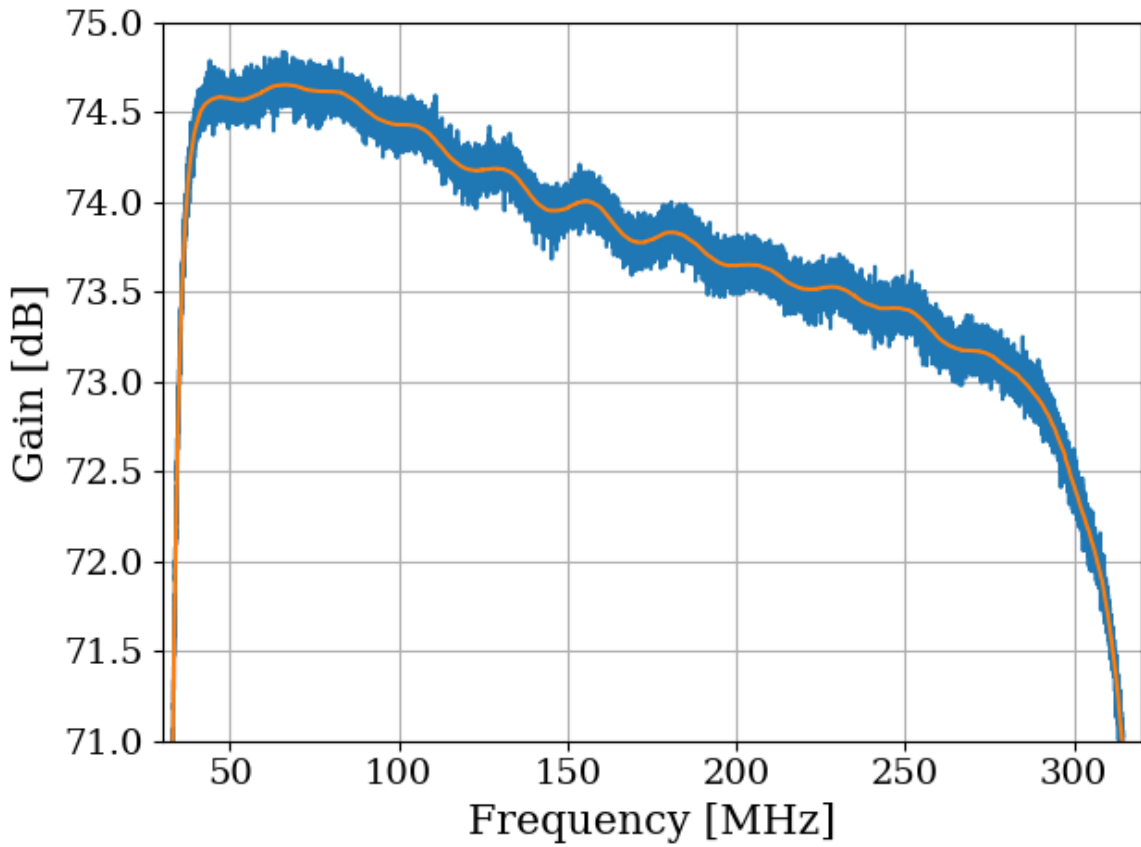


Figure 3.5: Frequency-dependant gain of the Run 1.4 amplifier chain, measured using the Y-factor method. The 30 dB attenuator and band-pass filter have been corrected for in this plot. The slow decrease of gain with frequency is consistent with the data sheets for the LNA [36] and secondary amplifier [63]. Roll-off at high and low frequencies is due to the band-pass filter (see 2.5.4.3). Bumpy behavior is due to the small impedance mismatch of the terminator to the  $50\Omega$  system.

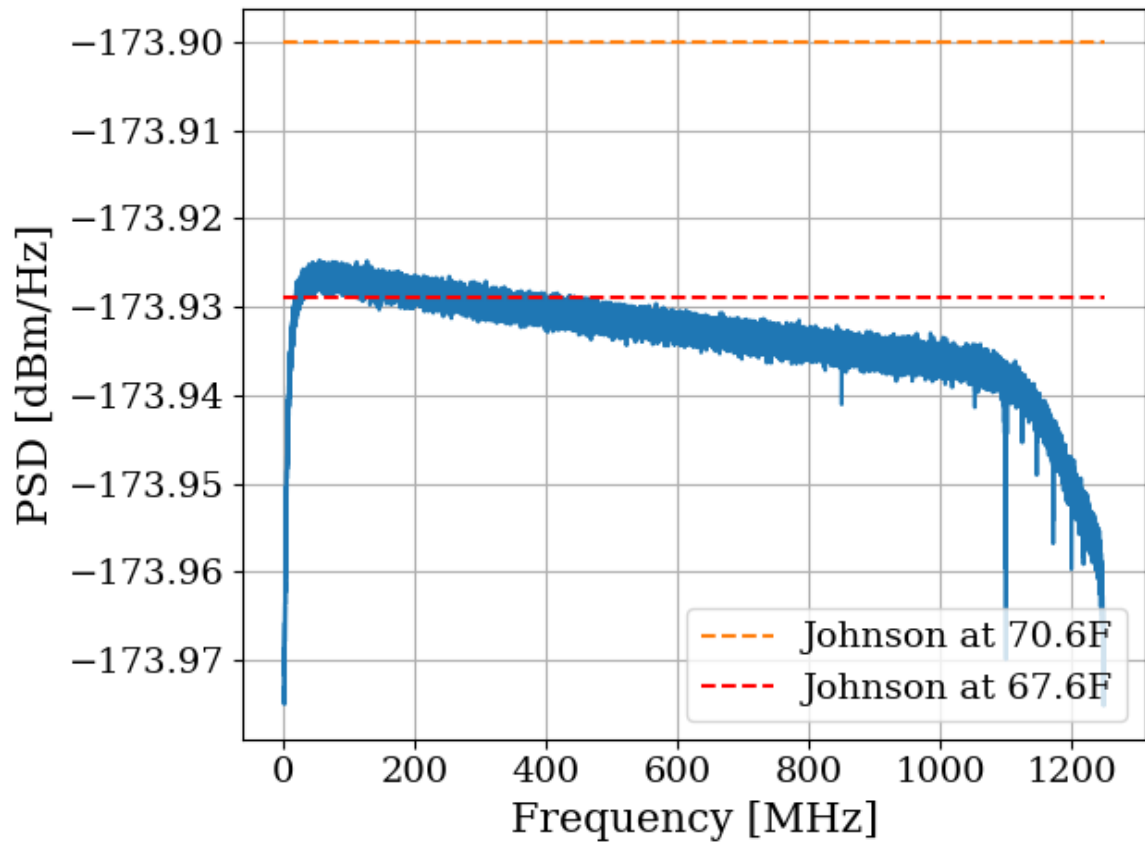


Figure 3.6: Run 1.4 terminator, input-referred power spectral density. Excellent agreement with the predicted value from the formula for Johnson noise at room temperature. Two reference temperatures are given with the dashed lines.

### 1480 3.1.2 Confirming gain with tracking generator measurement

1481 As a sanity check for the Y-factor method, the system gain was measured again using the  
1482 tracking generator on the Rigol RSA-5065-TG [72], with good agreement. This measurement  
1483 was useful since there were some corrections involved in the Y-factor measurement (the 30 dB  
1484 attenuator and band-pass filter).

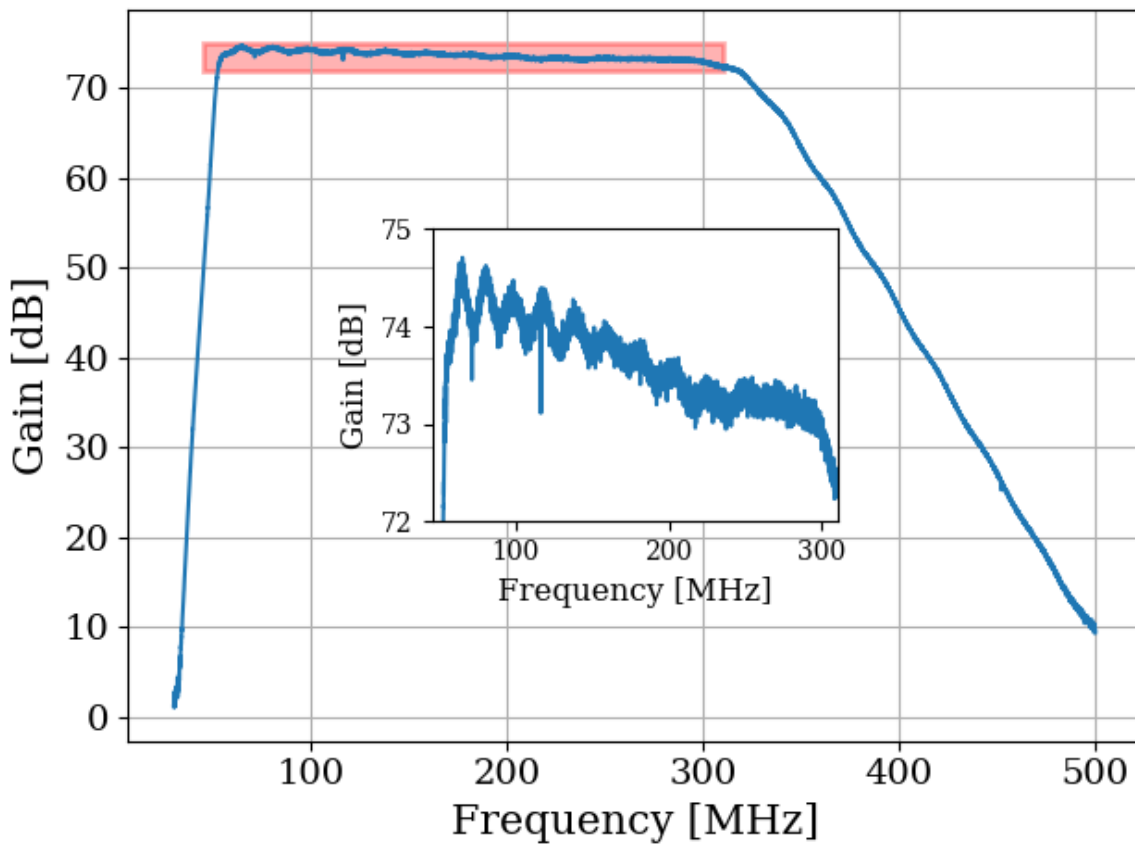


Figure 3.7: Gain vs. frequency of Run 1.4 amplifier chain, including LNA, secondary amplifier, band-pass filter and attenuators. Inset shows zoom of region enclosed in red box. This was measured using the tracking generator on Rigol RSA-5065-TG [72]. Wiggles visible in inset are a known artifact due to an impedance mismatch between the Rigol's tracking generator and the system under test. Gain was confirmed by comparing to Y-factor method (Sec. 3.1.1)

1485    **3.1.3 System stability over a run period** <sup>3</sup>

1486    The system's gain will vary slightly over the course of a run. An obvious culprit is the  
1487    battery voltage decreasing with time <sup>4</sup>. At first glance, one may conclude that since the  
1488    LNA is equipped with an internal voltage regulator, it is insensitive to the battery voltage  
1489    as long as it is above some minimum value. However, at higher voltage, the regulator must  
1490    dissipate more power which will make the LNA warmer. Temperature does have an effect  
1491    on the gain of the LNA. Tests of gain vs. LNA voltage show that this is a minor issue. This  
1492    is shown in Fig. 3.8.

1493        Knowing the gain vs voltage is only useful if it is understood how the battery voltage  
1494    will behave over the course of the run. These data are shown in Fig. 3.9.

1495        As a final check of system performance during the run, Fig. 3.10 shows the output-referred  
1496    power (averaged from 50-300 MHz) over the course of the 9-day Run 1.4. The gain varies by  
1497    about 0.7%, an insignificant amount given the other uncertainties involved (especially that  
1498    of simulation and calibration, Sec. 4.3).

---

<sup>3</sup>Code for this section can be found at: [https://github.com/josephmlev/darkRadio/tree/master/daqAnalysisAndExperiments/run1p4/run1p4\\_timeDependence.ipynb](https://github.com/josephmlev/darkRadio/tree/master/daqAnalysisAndExperiments/run1p4/run1p4_analysis/run1p4_timeDependence.ipynb)  
[https://github.com/josephmlev/darkRadio/tree/master/daqAnalysisAndExperiments/run1p4/gainAndNf/gainAndNF\\_analysis.ipynb](https://github.com/josephmlev/darkRadio/tree/master/daqAnalysisAndExperiments/run1p4/gainAndNf/gainAndNF_analysis.ipynb)

<sup>4</sup>The LNA is powered by a battery. The secondary amplifier is outside of the room and powered with a voltage regulator.

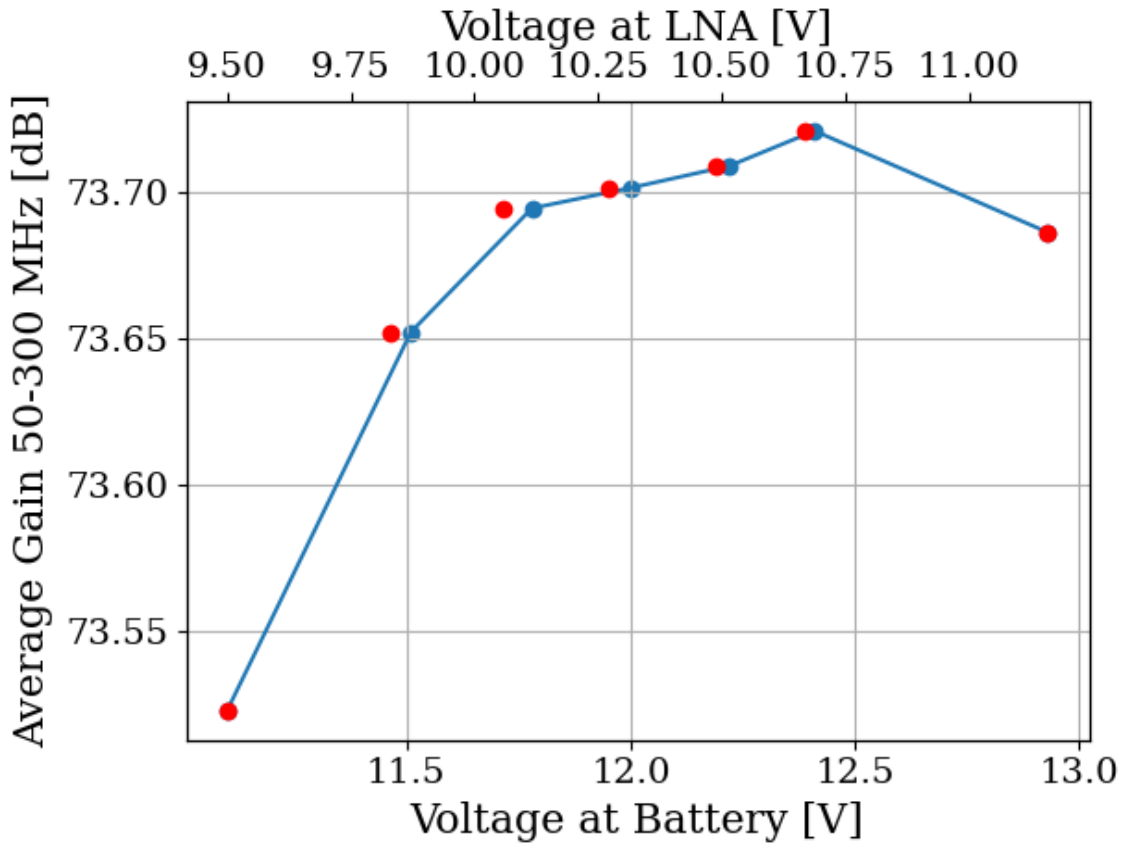


Figure 3.8: Gain vs. LNA voltage of Run 1.4 amplifier chain, including LNA, secondary amplifier, band-pass filter and attenuators. This was measured using the tracking generator on Rigol RSA 5065TG [72]. Gain is frequency dependent; its average value between 50 and 300 MHz is shown here. Voltage at the amplifier was measured directly at its terminals, after significant voltage drop due to interlock and slow turn-on circuits (described in Sec. 2.5.6). Gain is in good agreement with the previous two subsections, 3.1.1 and 3.1.2. The operating voltage range specified on LNA data sheet [36] is 10-15 V. The voltage at the LNA (red) does not exactly line up with voltage at battery (blue), so there is a slight offset. The scale of the x-axes scale has been set so that the maximum and minimum voltages line up.

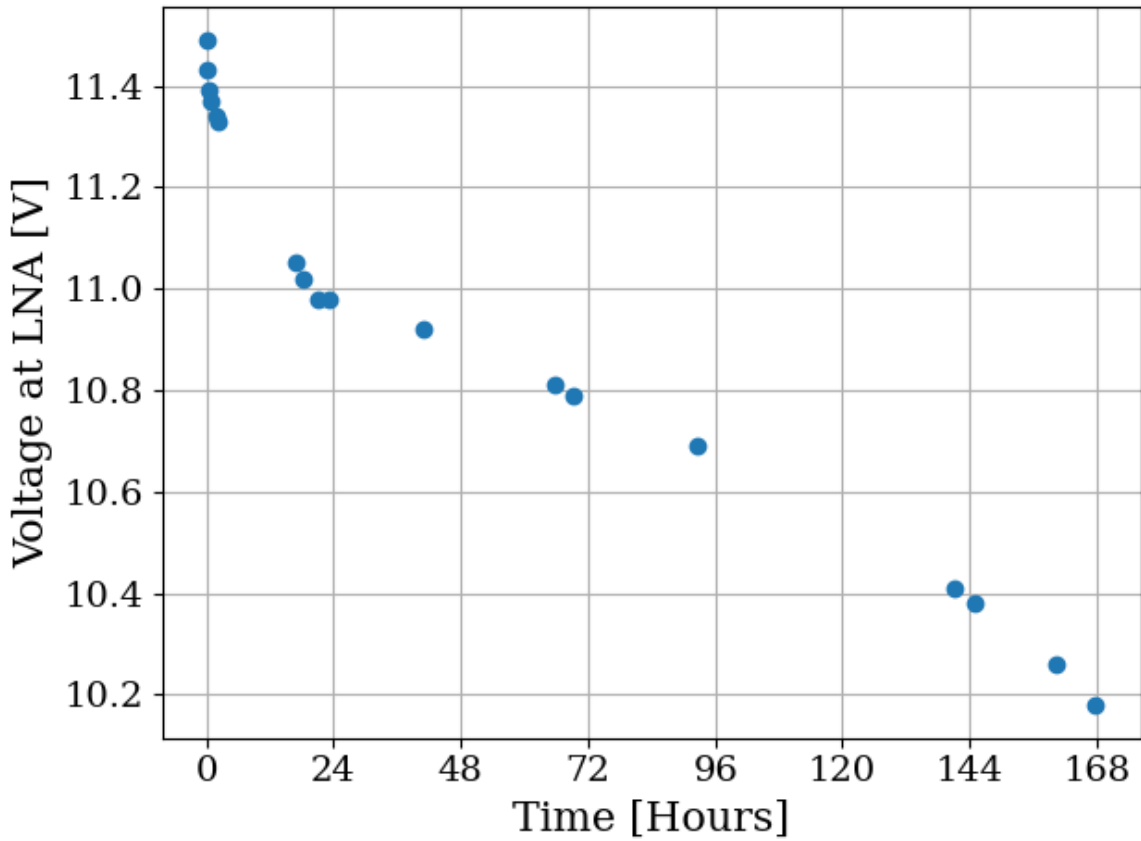


Figure 3.9: Voltage at LNA vs. time. Data were acquired 7/15/2024 through 7/22/2024 using battery number 2 immediately after being charged. The system was set up as it was for Run 1.4, including the switching cycle (on for 3 minutes, off for 45 minutes). The battery supplies 177 mA when the switch is off, and 370 mA when the switch is on. There is an additional data point (not shown) around 196 hours where the voltage has dropped to 6.2 V, well below the minimum required voltage. The battery had approximately 20 charge/recharge cycles at the time of this test and was about 14 months old. A repeat of this test may be required to use the battery for longer periods between charges.

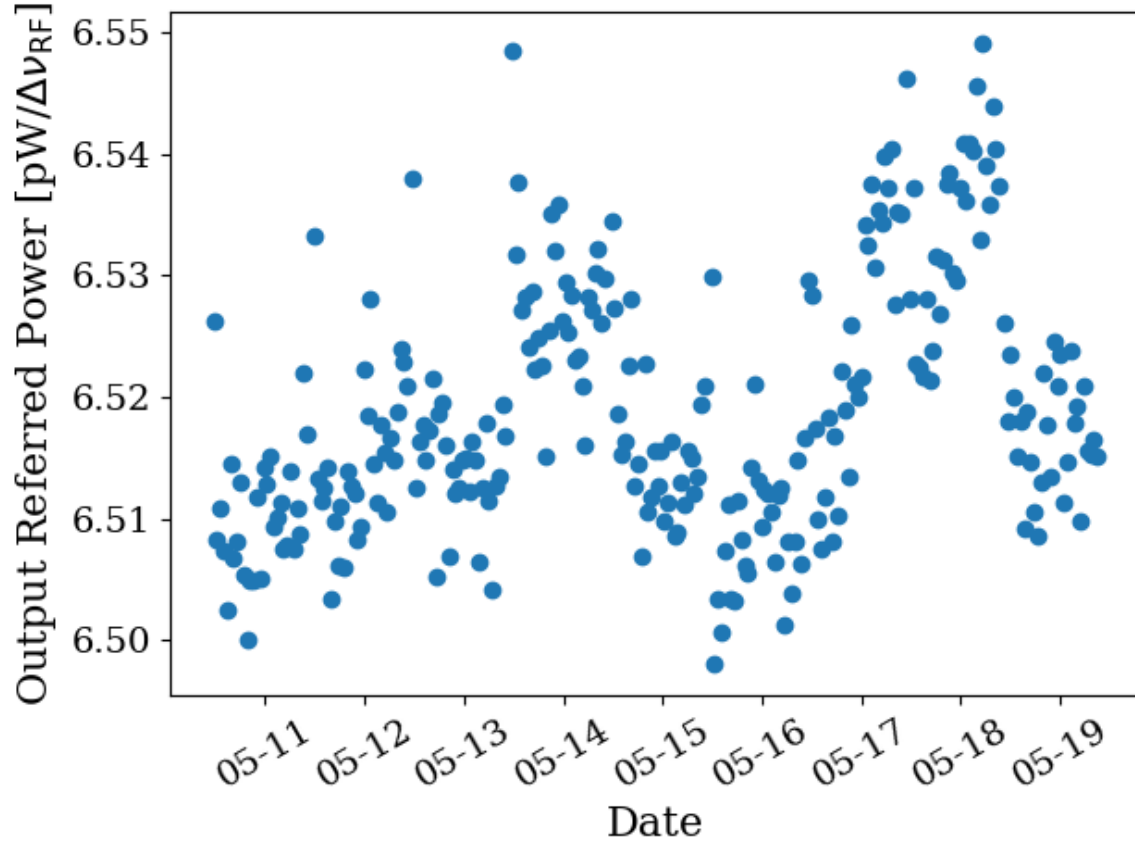


Figure 3.10: Frequency-averaged power spectral density vs. time of the terminator from Run 1.4 (schematically shown in Fig. 2.37). Each data point represents the mean power between 50 and 300 MHz of the terminator. In Run 1.4, a  $\sim$ 3 minute long scan of the terminator took place after  $\sim$ 45 minutes of antenna scans. Dates shown are all May 2023 (month-day format, year suppressed), and x-axis ticks are shown at midnight.

1499    **3.2 Measurement of shielding effectiveness and radio**  
1500                 **frequency interference**

1501   Shielding effectiveness (SE) and radio frequency interference (RFI) were introduced in Secs.

1502   2.1.3 and 2.5.1. Their measurement is introduced here.

1503      Similar to the warning given in the previous section, SE should be measured before  
1504   starting a data run or after entering a new frequency range/modifying anything on the  
1505   patch panel. In addition, it is best practice to clean the door's RF seal before beginning a  
1506   run (the procedure is described in the text of this section).

1507      Due to reciprocity between antennas, measuring the shielded room's ability to keep radi-  
1508   ation *out* is equivalent to measuring how well the room can keep it *in*. The latter method is  
1509   simpler and was performed. The IEEE standard prescribing a very detailed SE measurement  
1510   procedure [73] was used as a rough guideline, but the simple results presented here should  
1511   be viewed as an estimate. While simplified, the results do tend to agree with predictions of  
1512   when RFI should become detectable, based on comparisons to the veto antenna spectrum <sup>5</sup>.

1513      The SE was measured by placing a Rigol DSG830 signal generator and 25 Watt RF power  
1514   amplifier inside the room, both powered by the filtered 120 VAC Edison outlets inside the  
1515   room, shown in Fig. 3.11. An antenna was connected to the signal generator. Outside of  
1516   the room, an identical antenna was connected to a Rigol RSA-5065-TG spectrum analyzer  
1517   [72]. The spectrum is scanned to find a frequency without local interference which would

---

<sup>5</sup>Or at least they did agree before cleaning the door. With the excellent isolation values, no RFI was detected in Run 1.4.

1518 confuse the results. The spectrum analyzer was set to attenuate its input to prevent clipping  
1519<sup>6</sup>, and the signal generator was set to output a sine wave near the maximum power of the  
1520 RF amplifier ( $20\text{ W} = 43\text{ dBm}$ ). The power measured on the spectrum analyzer is  $P_{\text{open}}$  in  
1521 Eq. 2.46. The door was closed, attenuation removed and  $P_{\text{closed}}$  was measured. In some  
1522 cases the SE was so high a signal was buried below the noise floor of the spectrum analyzer.  
1523 These data are shown in red in Figs. 3.12 3.13 and should be interpreted as an upper limit  
1524 on isolation, since the true value is lower (better).

1525 SE can drop off to less than 80 dB if the RF gasket around the door is not clean. Previous  
1526 day-long test runs detected several hundred signals that originated from RFI emitted from  
1527 the PC and several local radio stations. Cleaning was performed by scrubbing the copper  
1528 finger stock and steel mating surfaces with red Scotch-Brite using denatured alcohol as a  
1529 lubricant<sup>7</sup>. After two passes of polishing were complete, a layer of DeoxIT D100L liquid  
1530 was added. Maintenance cleanings were performed using only DeoxIT D5 spray. These  
1531 signals were not detected after the gasket was cleaned, which is consistent with calculations  
1532 of Sec. 2.1.3

1533 The primary RFI in the 50-300 MHz span are from local radio broadcasts. The electric  
1534 field of the strongest signals is  $\sim 100\text{ }\mu\text{V/m}$  when measured in the lab. There are also many  
1535 lower level peaks which span the entire frequency range, though are more pronounced in a  
1536 few frequency bands (60-75 MHz, 130-140 MHz, and 270-290 MHz). These peaks come from

---

<sup>6</sup>The spectrum analyzer automatically calibrates the displayed spectrum to its internal attenuator and pre-amplifier. If external gain/attenuation are used, they must be accounted for manually. Since this is a relative measurement (i.e., a ratio of  $P_{\text{open}}/P_{\text{closed}}$ ), this calibration does not matter much.

<sup>7</sup>Alcohol fumes are nasty. Be careful to open the hallway door and use a fan to blow in air from the hall. Take frequent breaks. Don't get dizzy while standing on a chair!



Figure 3.11: Photo showing setup to measure SE of 314. Photo taken using Vivaldi antennas for data shown in Fig. 3.13. The same setup was used with bicon antennas for the 50-300 MHz data shown in Fig. 3.12. The bicon antenna shown in the background of this photo was not used for this test.

1537 the PC which is an integral part of the spectrum analyzer system, housing the ADC, so it  
1538 can not be removed. Before the door was cleaned, many of these signals were detectable  
1539 after a few hours of integration, but cleaning the door resulted in a clean spectrum for the  
1540 9-day data Run 1.4. The spectrum from the veto antenna (discussed in Sec. 2.5.5) is shown  
1541 in Fig. 3.14

### 314 Shielding Effectiveness

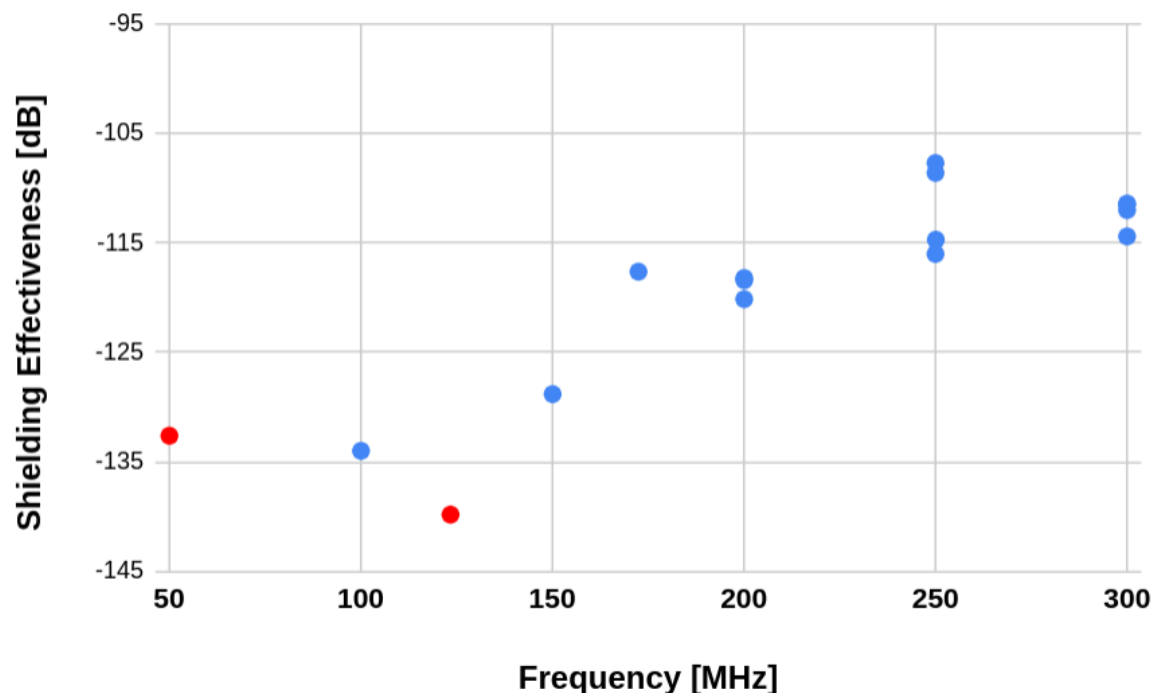


Figure 3.12: Shielding effectiveness of shielded room measured with bicon antenna. Red points indicate measurements limited by the noise floor of the spectrum analyzer located outside the shielded room and are an upper limit. The true SE is lower (better). To get the true SE for these points, measurement would require a higher gain amplifier inside the room. SE measurements are all better than required for Run 1.4, and no RFI candidates were detected. At a few frequencies, the antenna inside the room was moved to get a sense of the uncertainty of the measurement.

### 314 Shielding Effectiveness

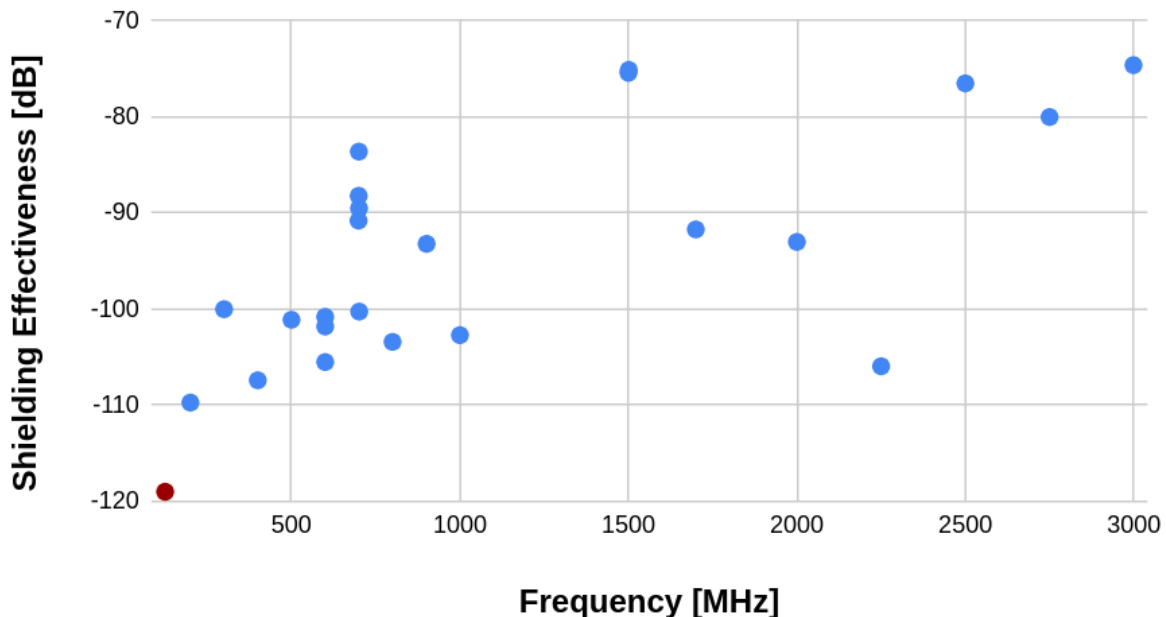


Figure 3.13: Shielding effectiveness of shielded room measured with Vivaldi antenna. Red points indicate measurements limited by the noise floor of the spectrum analyzer located outside and are an upper limit; true SE is lower (better). Measurement would require a higher gain amplifier inside the room. At a few frequencies, the antenna inside the room was moved to get a sense of the uncertainty of the measurement.

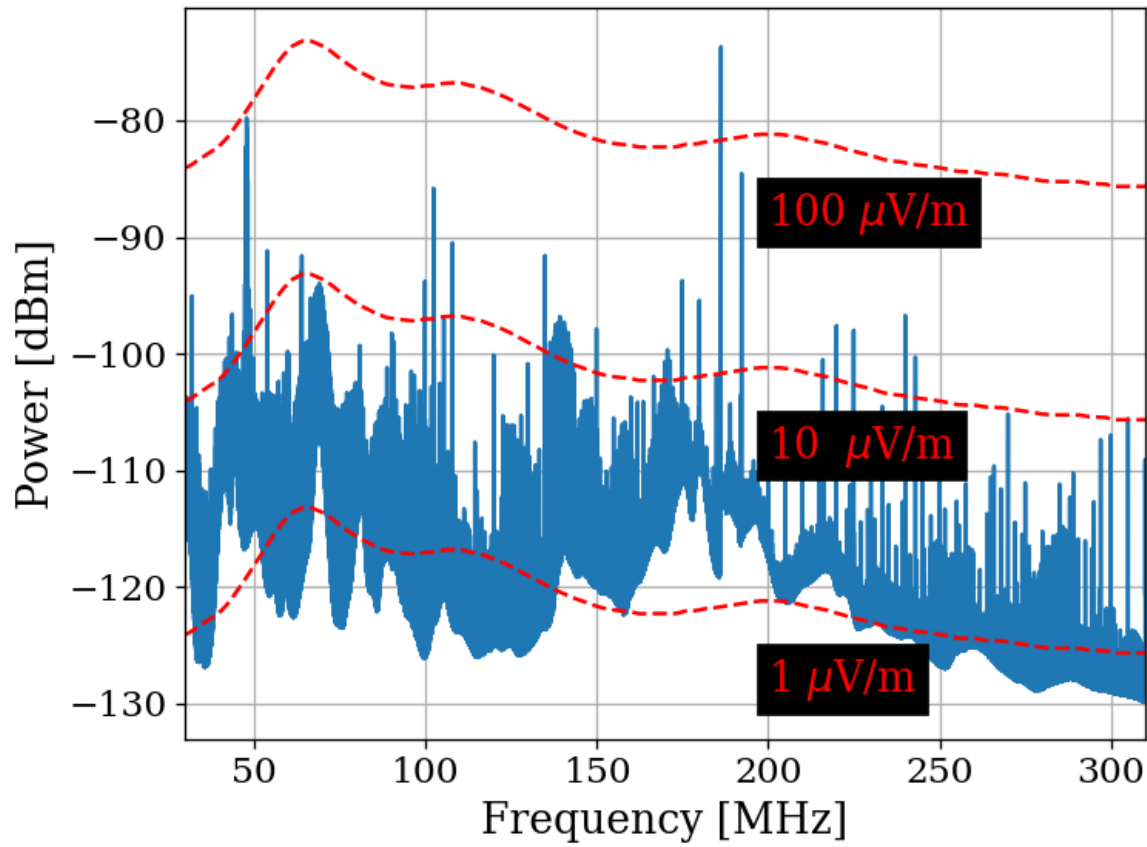


Figure 3.14: Spectrum from veto antenna during the 300 MHz data run. Spectrum plotted as measured power in dBm. Red curves indicate the equivalent field strength. These curves track the free-space antenna factor with frequency for the Com-Power AB900 [59] bicon. Two identical AB900-A antennas are used, one to search for dark photons in the shielded room, and a second to monitor the local RFI background.

### **1542 3.3 Spectrum Analyzer Characterization**

1543 This section outlines several tests performed to ensure the GPU-based real-time spectrum  
1544 analyzer (RTSA) system performs as expected. Background information that relates to  
1545 this system is described in Sec. 2.5.7.

#### **1546 3.3.1 Spectrum analyzer calibration**

1547 The first step in determining if the RTSA system is working adequately is to make sure  
1548 it is able to correctly identify known, injected signals and noise. This calibration step is  
1549 important since the FFT is normalized manually (see Eq. 2.15), and it is rather easy to  
1550 mess up. The test signals were generated with a Rigol DSG830 signal generator. The time-  
1551 domain peak-to-peak voltage measured by the RTSA system agreed with the injected voltage  
1552 to about 2 %. The signal generator's output frequency and power were verified in both the  
1553 frequency and time domain using a separate oscilloscope and spectrum analyzer. This is an  
1554 important step since cable losses are significant at this level of precision. They can be taken  
1555 into account by consulting the data sheet for the cable<sup>8</sup>.

1556 Next, it is important to understand how the system handles noise spectra, since this is the  
1557 primary use of the system. This is tested by amplifying the Johnson noise of a terminator (see  
1558 Sec. 2.1.1.2) and measuring the power spectral density. Knowing the gain and noise figure  
1559 of the amplifier chain allows for calibration using the procedure outlined in detail earlier in  
1560 this chapter, see Sec. 3.1, specifically Fig. 3.6. These results were confirmed several times

---

<sup>8</sup>There are several cheap black SMA cables which are great for testing, but not for calibration. They have more than 5 dB of loss above 1 GHz. Use a nice cable for these tests, and blow out the SMA connector with compressed air while you are at it.

1561 preceding the data run. Note that due to windowing, other spectrum analyzers will disagree  
1562 with the theoretical calculation by a few dB if the equivalent noise bandwidth (ENBW) of  
1563 the window function is not included. Also remember to take cable effects into account as  
1564 discussed in the previous paragraph.

### 1565 3.3.2 Spurious signal performance of the ADC

1566 Any practical spectrum analyzer will have small, coherent, signals that sneak into the analog  
1567 signal path and, after being digitized and Fourier transformed, manifesting as spurious signals  
1568 or *spurs* (see Sec. 2.1.5.1). These spurs likely come from clock signals within the same  
1569 enclosure as the ADC. They can also come from local oscillators bleeding through mixers in  
1570 a mixed, high-frequency system such as the Rigol RSA 5065TG [72] or the future, upgraded  
1571 dark radio system discussed in Ch. 6.

1572     Regardless of their origin, the spurs must be characterized such that if a known spur is  
1573 detected it can be classified as such and rejected quickly. Ideally, the system has enough  
1574 gain that any spurs are subdominant to the amplified thermal noise, as discussed in Eq. 2.1.  
1575 However, since there is a maximum amount of gain that can be added before clipping the  
1576 ADC (see Sec. 2.5.4.3), this is not always possible.

1577     Experience with the Teledyne RTSA system has shown that spurs are rather simple to  
1578 classify because they do not change much with time in either frequency or amplitude. Their  
1579 frequency drifts by  $\sim 1 \text{ kHz}$  and their amplitude changes by a few dB.

1580     To classify them, the input of the Teledyne is terminated and a scan is performed few

1581 minutes using the exact same system configuration as for the run (with the possible exception  
 1582 of the number of averages). See Appendix A for details. The averaged spectra of the  
 1583 terminated inputs are shown in Fig. 3.15.

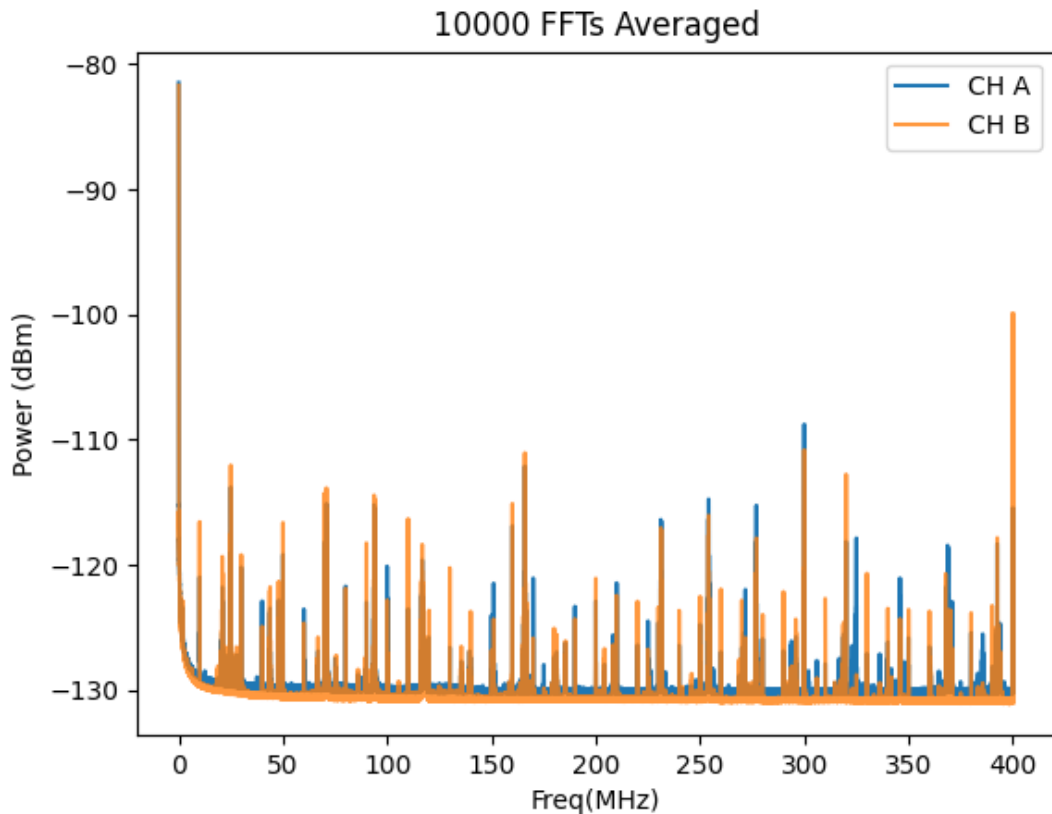


Figure 3.15: Scan of terminated input of Teledyne spectrum analyzer system to measure spur performance. The spectra were acquired with run 1A parameters ( $\Delta\nu_{RF} = 47.7$  Hz) with 10,000 averages ( $\sim 3.5$  minutes). This plot is taken directly from test mode of the system (not post-processed in any way). The largest spur in the 50-300 MHz range is at 299.97 MHz and is also the single significant signal in Run 1.4 (see Sec. 4.2.5).

1584 Once a test scan is acquired, comparing the largest spurs ( $\approx -110$  dB) to the expected  
 1585 output-referred background ([Johnson noise + LNA noise] \* Gain  $\approx -81$  dBm/ $\Delta\nu_{RF}$ ) allows  
 1586 the calculation of the number of averages which are required before the spurs are significant.

1587 Working this out is a good test of understanding of Sec. 2.2. This spur should be detectable  
1588 with 95% confidence after about 4 days, which is exactly what happened in Run 1.4. The  
1589 false positive candidate is described in Sec. 4.2.5.

1590 **3.3.3 ADC clock performance**

1591 Any ADC requires a clock that dictates the precise time at which a sample should be ac-  
1592 quired. This subsection deals with the evaluation of the performance of that clock.

1593 Determining the performance of a clock generally relies on having a better (read: more  
1594 expensive) clock known as a *standard* and measuring the clock under test against the stan-  
1595 dard. The Valon 5009 RF synthesizer was tested against a rubidium frequency standard and  
1596 was found to be just on the threshold of stable enough to work (this threshold is explained in  
1597 Sec. 2.5.7). To ensure the measurement is not limited by clock instability, the sample clock  
1598 of the ADC is synchronized to a 10 MHz rubidium frequency standard (Stanford Research  
1599 Systems FS725) which is further steered by the one pulse-per-second (pps) signal from a  
1600 GPS receiver. This system has medium and long term fractional frequency stability (Allan  
1601 deviation [74, 75]) of  $\sigma_y(\tau) < 3 \times 10^{-12}$  (where  $\tau$  is the averaging time) and phase noise of  
1602 less than -65 dBc/Hz at offset frequencies  $> 50$  Hz from the carrier [76]. This means that  
1603 over the course of a single acquisition, the power contained in a bin will spread to an adjacent  
1604 bin by less than 1 part in  $10^6$  which is more than sufficient for our experiment.

1605 This is a rare example of something in this experiment where we trust the data sheet.  
1606 We do not have access to a clock which is better than this, so confirming its performance

1607 is difficult. Furthermore, even if the specs are an order of magnitude worse than advertised  
1608 there is still more than enough stability for the experiment. This statement holds at higher  
1609 frequencies. Since the  $Q$  of the signal is fixed, higher frequencies have wider bins so the  
1610 relevant offset frequency at which the phase noise is measured increases with frequency. The  
1611 dimensionless Allan deviation is also not affected.

### 1612 **3.3.4 Real-time data collection efficiency**

1613 As a final test, one would like to know how efficiently data scans can be acquired and  
1614 averaged. We call a 100 % efficient system *real-time* as described in Sec. 2.5.7. Figure 3.16  
1615 illustrates this efficiency. For Run 1.4, it is  $\sim 99.765\%$ . However, in practice run logistics  
1616 such as moving the antenna prevent the full efficiency of the system from being realized.

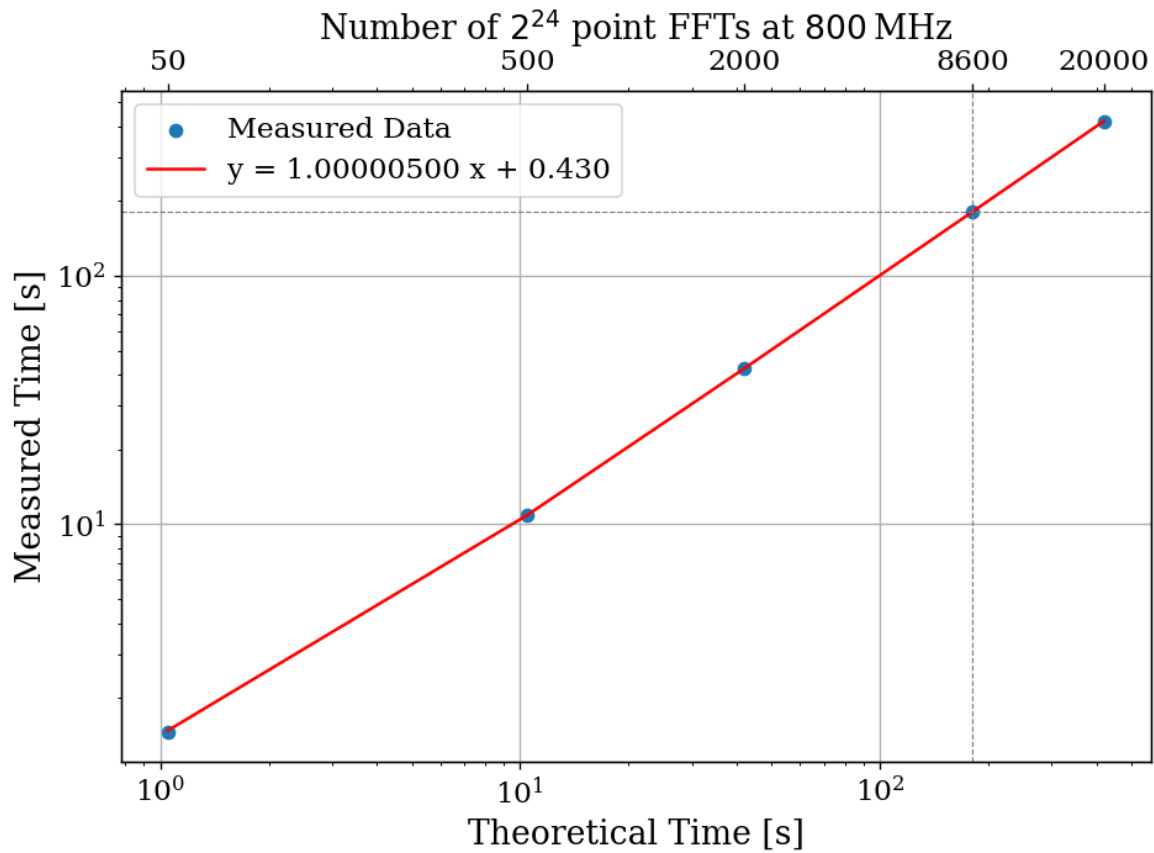


Figure 3.16: Acquisition efficiency for GPU-based real-time spectrum analyzer computed from measured vs. theoretical times. The constant offset of 0.43 s corresponds to a small set-up period when starting an acquisition containing, in the case of run 1A, 8600 FFTs. In the limit of an infinite length acquisition, the system's efficiency may be read off from the slope and is 99.9995%. The more realistic efficiency is a function of the number of FFTs per acquisition and for Run 1.4 =  $180.3551 \text{ [s]} / 180.7782 \text{ [s]} = 99.765\%$ .

<sub>1617</sub> Chapter 4

<sub>1618</sub> Data Acquisition, Data Analysis and  
<sub>1619</sub> Calibration

1620        Thus far this thesis has focused on building up a background on the dark radio technique  
1621      as well as the design and testing of the experiment and its sub-systems. This chapter outlines  
1622      the process of acquiring actual data, analyzing that data to search for a small power excess,  
1623      and, in the absence of that excess, converting the null result into an exclusion limit on the  
1624      dark photon mass/ $\epsilon$  parameter space. Section 4.4 describes an injection test that detects a  
1625      realistic, hardware-injected, dark photon proxy-signal. This chapter borrows heavily from  
1626      my paper, *New Limit on Dark Photon Kinetic Mixing in the 0.2-1.2  $\mu eV$  Mass Range From*  
1627      *the Dark E-Field Radio Experiment*[39], which was published in August 2024.

1628        The cleanest way to model the contents of this chapter is by compartmentalizing the  
1629      steps outlined above. For this reason, the chapter is organized as follows. In Sec. 4.1, the  
1630      procedure for a 9-day data run is outlined. Where appropriate, references to previous sections  
1631      are provided which are helpful in understanding how different procedures were developed.  
1632      This section concludes with the frequency-dependent, output-referred power spectral density  
1633       $S_o$ , which must be searched for a power excess. We call this search *analysis*, and it is covered  
1634      in Sec. 4.2. The task of analysis is to extract a dark photon signal from this spectrum if  
1635      it is present. Otherwise, in its absence, we set a limit on the amount of output-referred  
1636      power that would have been detectable *most of the time* were a narrow signal to be present  
1637      in this averaged dataset. We quantify the meaning of “most of the time” by conducting a  
1638      series of Monte Carlo *pseudo-experiments* on artificial signal-containing spectra for synthetic  
1639      signals of varying powers and frequencies. With a limit on dark photon power extracted,  
1640      Sec. 4.3 works back through the system to determine a limit on  $\epsilon$  above which we have some  
1641      confidence we would have observed a signal. This produces the exclusion limit, which is

1642 ultimately the deliverable of this experiment. This limit is shown in Sec. ??.

## 1643 4.1 Data Acquisition

1644 Data were collected during a 9-day run from May 10 to May 19, 2023. This data run is  
1645 referred to Run 1.4 in the code base since it was the fourth attempt at taking this data. It  
1646 was used for to publish the limit of Run 1A, so it is referred to as Run 1A throughout this  
1647 thesis. its details are shown in Table ??.

Specification	Value
Analysis span	50-300 MHz
Antenna	AB-900A biconical antenna
RTSA	Teledyne GPU system (Sec. 2.5.7)
Frequency resolution ( $\Delta\nu_{RF}$ )	47.7 Hz
Length of record	$2^{24}$ samples
Sample rate	800 MHz
Window type	None (rectangular)
Acquisition time per spectrum	20.96 ms
Run start time	2023-05-10 11:29:48
Total time of run	8 days, 21.13 hours
Efficiency (Time spent scanning antenna/total time)	92.03%

Table 4.1: Run 1.4 Details. Many specifications are related and can be computed from each other but are listed for reference. The efficiency differs from that calculated in Fig. 3.16 mainly because of switching to a terminator and brief daily pauses to move the antenna.

1648 Each day was subdivided into data-collection (23 hours 15 minutes) and setup (45 min-  
1649 utes) periods. The setup period includes moving the antenna, changing a 12 V battery for  
1650 the LNA (Sec. 2.5.6), file management and documentation. In order to reduce the data  
1651 rate and storage requirements, all data were pre-averaged into 3-minute chunks and then

1652 saved. This pre-averaging is shown in Fig. 2.45. Additionally, an RF switch (see Fig. 2.37)  
1653 is actuated for a 3-minute scan for every 15 antenna scans in order to monitor the status  
1654 of the amplifier chain. For the data analysis, all 9 days of data were averaged together to  
1655 create a single spectrum  $S_o$  (Fig. 4.1). If candidates are found, their time dependence are  
1656 observed by looking at the 3-minute pre-averages. All further analysis is performed on the  
1657 full 9-day  $S_o$  spectrum and is described below (Sec. 4.2).

### 1658 4.1.1 Raw data, $S_o$

1659 All 9 days of pre-averaged data from the run are averaged together. The stability of the  
1660 sample clock (Sec. 3.3.3) ensures that this is a simple process. Frequency bins ( $\Delta\nu_{RF} =$   
1661 47.7 Hz) corresponding to a given frequency are added and normalized by the total number  
1662 of pre-averaged spectra. This process produces the raw spectrum,  $S_o$  (Fig. 4.1), on which  
1663 we will perform a search for power excess.

1664 Inspection of  $S_o$  reveals small power variations over spans of tens of kHz. The origin of  
1665 these variations is explored in Sec. 2.3, but it is summarized here. Given an antenna in a  
1666 cavity in thermal equilibrium with the input of an amplifier, whose input is assumed to be real  
1667 and matched, one would expect an output PSD which is constant with respect to frequency  
1668 up to small variations in system gain. The theory for this is outlined by Dicke in [77]. These  
1669 variations are not noise; for a given antenna position, we repeatedly measure the same shape  
1670 (though the noise riding on these variations *is* random). The origin of the observed small  
1671 variations lies in the effective temperature difference between the room and LNA causing a

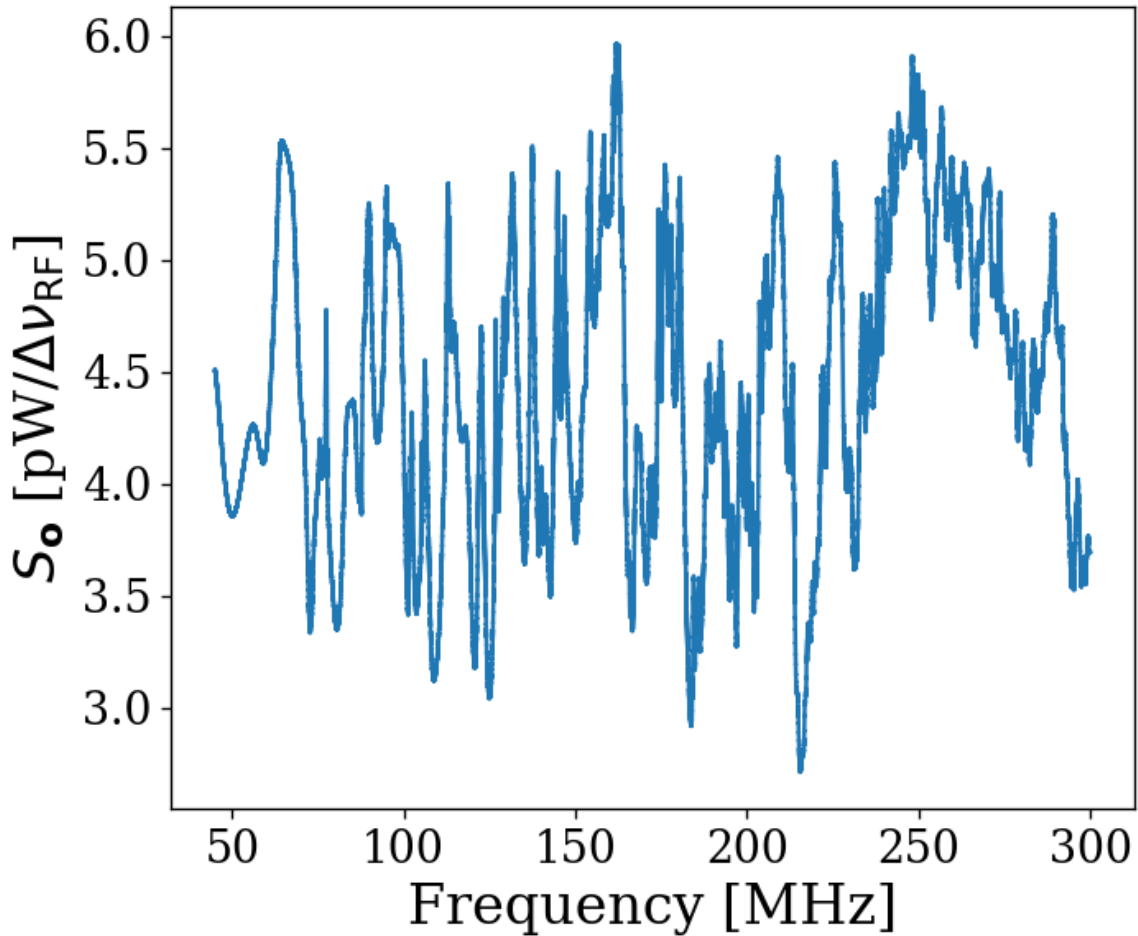


Figure 4.1: Run 1A averaged, output-referred antenna power spectrum  $S_o$ . Data were taken over a 9-day period at 9 antenna positions. For context, Fig. 4.2 shows these data plotted alongside the power spectrum of the terminator. The narrow variations are mainly due to the effective temperature difference between the room and LNA (Sec. 2.3), though there is a small contribution due to amplifier gain and noise temperature variations (Sec. 4.1.1). The variations seen here are not noise; their shape is repeatable for a given antenna position. The noise on this background is not visible at this level of zoom, but is seen in Fig. 4.4, which shows a zoomed-in view of the spectrum at 240 MHz. The noise is also seen nicely in Fig. 4.17

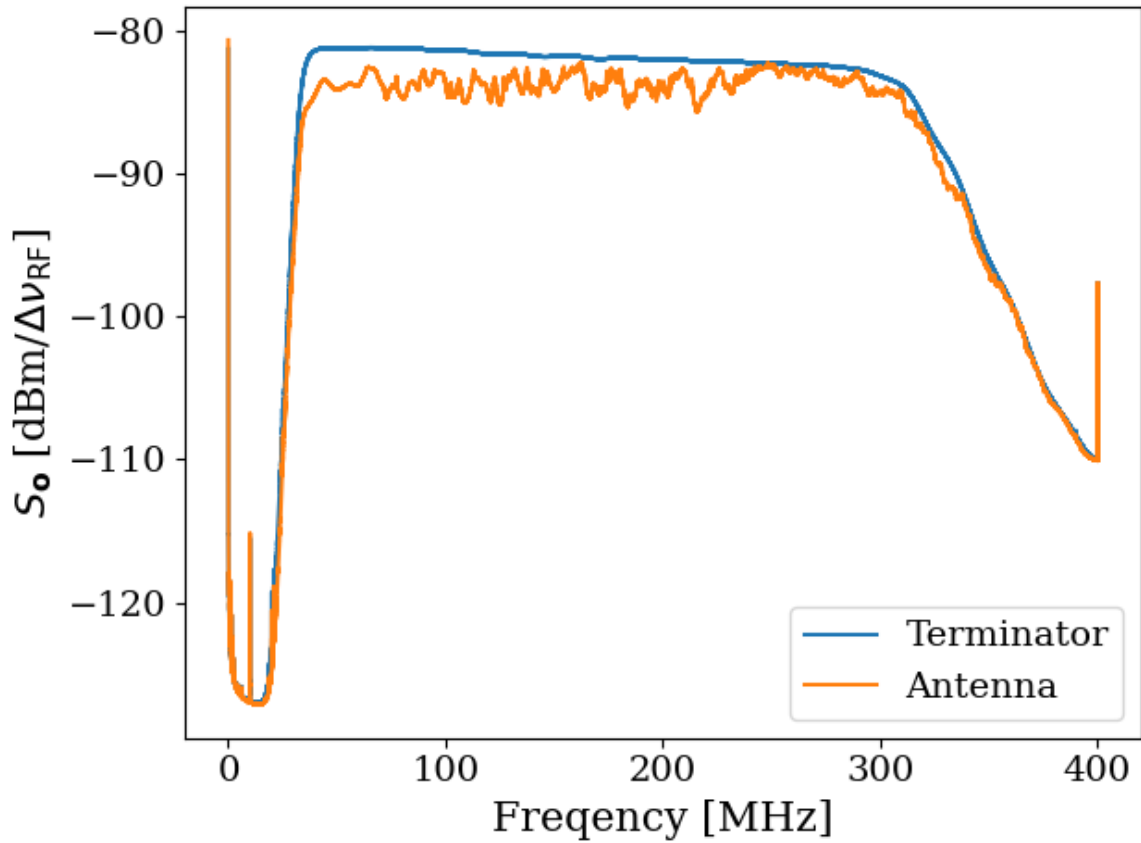


Figure 4.2: Logarithmic scaled Run 1A averaged, output-referred, antenna and terminator power spectra. Bandwidth is defined by hardware bandpass filters (Fig. 2.37). Spurious signals at 10 MHz, as well as low and high-frequency behavior, are ADC effects and are visible in Fig. 3.15.

1672 net power flow from the antenna into the LNA. This effective temperature difference partially  
 1673 excites modes of the antenna/cavity system, causing the observed variations. We suspect this  
 1674 effect originates from a small reactive component of the LNA's input causing the electronic  
 1675 cooling described originally by Radeka [19]. This effect can be eliminated by adding an  
 1676 isolator between the antenna and LNA [32, 78] though for our experiment, it is impractical  
 1677 to get an isolator that covers such a wide band at relatively low frequency. Furthermore, the

1678 relatively wide (tens of kHz) variations are handled by fitting to them, which is discussed in  
1679 Sec. 4.1.

1680 **4.2 Data Analysis**

1681 At this point, we have compiled a single, averaged, output-referred power spectrum,  $S_o$   
1682 (Fig. 4.1). The task of *analysis* is to extract a dark photon signal from this spectrum if  
1683 it is present. Otherwise, in its absence, we would like to set a limit on the amount of  
1684 output-referred power we would be able to detect *most of the time* were a narrow signal  
1685 to be present in this averaged dataset. We quantify the meaning of “most of the time”  
1686 by conducting a series of Monte Carlo “pseudo-experiments” on artificial, signal-containing  
1687 spectra for synthetic signals of varying powers and frequencies. The following subsections  
1688 are organized as follows:

1689 4.2.1: Fit  $S_o$  to extract an estimate of the background  $B$  (which we call  $\hat{B}$ ) whose origin was  
1690 discussed in Sec. 4.1.1. See Fig. 4.4.

1691 4.2.2 Divide the spectrum by  $\hat{B}$  to generate the *normalized spectrum*, which very nearly  
1692 follows a Gaussian distribution. Discuss statistics of the normalized spectrum and  
1693 choose a global significance level and its associated *significance threshold*. See Fig. 4.5.  
1694 Also note this was derived in Sec. 2.2.

1695 4.2.3 Apply a matched filter to the normalized spectrum and establish a significance thresh-  
1696 old on its output using the same method defined in the previous section. See Fig. 4.6.

1697        The previous three steps comprise our *detection algorithm* which is shown in Fig. 4.3.

1698 4.2.4 Perform a Monte Carlo analysis to simulate the required power of a signal that can be  
1699        detected above the significance threshold 95% of the time. We use this to recover a  
1700        95% exclusion limit on the output referred power spectrum.

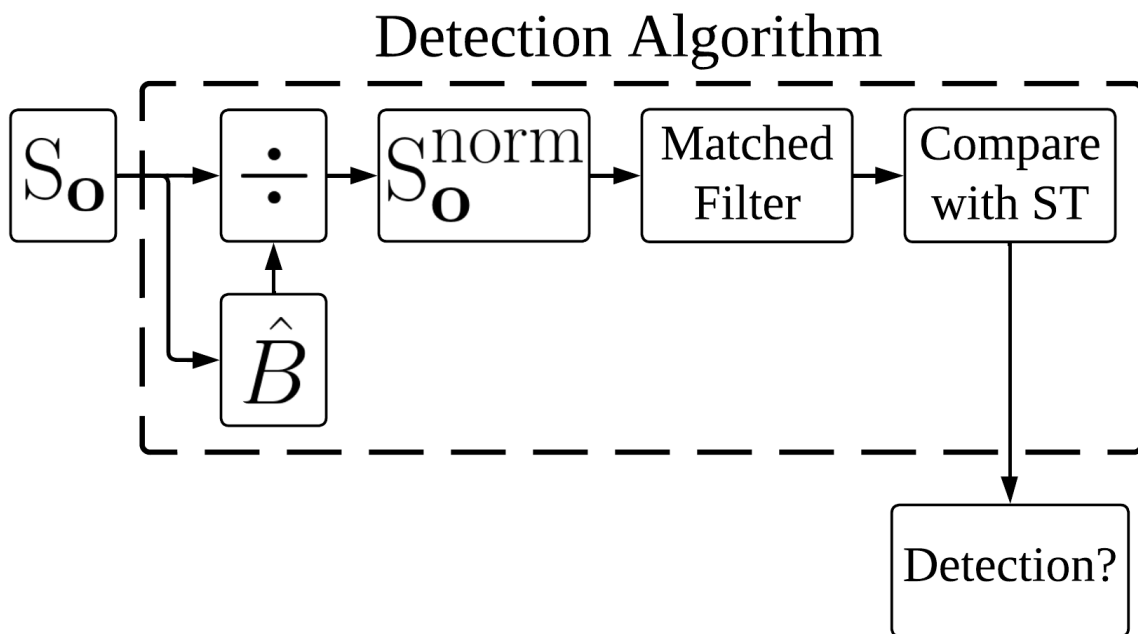


Figure 4.3: Flow chart outlining the logic of signal processing in the detection algorithm of sections 4.2.1 through 4.2.3.  $\hat{B}$  is the smoothed fit to  $S_o$  generated by low pass filtering. The output, *Detection?*, is a Boolean array which signifies a detection or lack thereof at each frequency bin. We detect a candidate if a bin contains more power than a significance threshold (ST) (Sec. 4.2.2).

1701        In Sec. 4.3 we convert this threshold on  $S_o$  into an actual limit on  $\epsilon$ .

1702        Throughout the figures of this section we will follow a relatively large (40 fW, output-  
1703        referred) software-injected, synthetic dark photon signal at 240 MHz to illustrate what a  
1704        candidate would look like as it passes through the analysis procedure. This signal is added

1705 to  $S_o$ . For clarity, a single interfering candidate has been removed. This is discussed in  
1706 Sec. 4.2.5.

1707 As a final note, at this point if you are unfamiliar with the data analysis, it would be  
1708 advantageous to spend a few minutes looking through Figs. 4.17 through 4.19 to get a sense  
1709 of the task at hand. It can be disorienting to deal with a spectrum that contains 8 million  
1710 frequency points. Zooming in on a signal is very informative.

### 1711 4.2.1 Fit background, $\hat{B}(\nu)$ <sup>1</sup>

1712 As shown in Fig. 4.1, the measured power spectrum looks like flat thermal noise *multiplied* by  
1713 some frequency-dependent background,  $B(\nu)$ <sup>2</sup>. However, for this section we will not concern  
1714 ourselves with the origin of  $B$  or any details of the experiment aside from two assumptions:

1715 1. The measured background is the product of a normally distributed spectrum and some  
1716 background. This is enforced by the central limit theorem due to the large number of  
1717 averaged spectra, independent of any experimental specifics.

1718 2. The line shape of the signal is known and the width of this signal is much narrower  
1719 than the width of features on the background, viz.  $\Delta\nu_{DP} \ll \Delta\nu_B$

1720 The first assumption (1) implies that if we were able to extract the background, dividing  
1721  $S_o$  by this extracted background would yield a *dimensionless*, normally distributed power

---

<sup>1</sup>Code for this section can be found at: [https://github.com/josephmlev/darkRadio/tree/master/daqAnalysisAndExperiments/run1p4/run1p4\\_analysis/analysisClass.ipynb](https://github.com/josephmlev/darkRadio/tree/master/daqAnalysisAndExperiments/run1p4/run1p4_analysis/analysisClass.ipynb)

<sup>2</sup>When I was first working on this, I used  $H(\nu)$  to represent this background. This naming convention persists in the analysis code.

1722 spectral density on which a search for a dimensionless signal is performed. The second  
1723 assumption (2) will be critical in both performing the fit to the background (this section),  
1724 and performing matched filtering (Sec. 4.2.3).

1725 In light of these assumptions, we attempt to fit the background power spectrum. Since  
1726 this fit estimates  $B$ , we use the symbol  $\hat{B}$  to refer to it. As discussed in [20], a particularly  
1727 effective fitting technique that can discriminate between the wide bumps of  $S_o$  and a narrow  
1728 signal is to use a low pass filter. We implement this filter in two stages:

- 1729 1. A median pre-filter (51 bins or about 2.4 kHz wide) attenuates any very narrow, very  
1730 large excursions which would interfere with any following filters, causing them to  
1731 “ring”<sup>3</sup>
- 1732 2. A 6<sup>th</sup>-order Butterworth low pass filter (corner frequency of 210 bins or 10 kHz)

1733 These bin widths/frequencies should be interpreted as the width of spectral features on  
1734  $S_o$  that are attenuated and will, therefore, not show up in the background fit. A narrow  
1735 zoom of this fit with a synthetic signal is shown in orange in Fig. 4.4.

---

<sup>3</sup>I recommend that this pre-filtering step is omitted if the spectrum analyzer in use does not produce large spurs. It is the slowest part of the analysis chain. It also causes the filtered spectrum to deviate slightly from Gaussian.

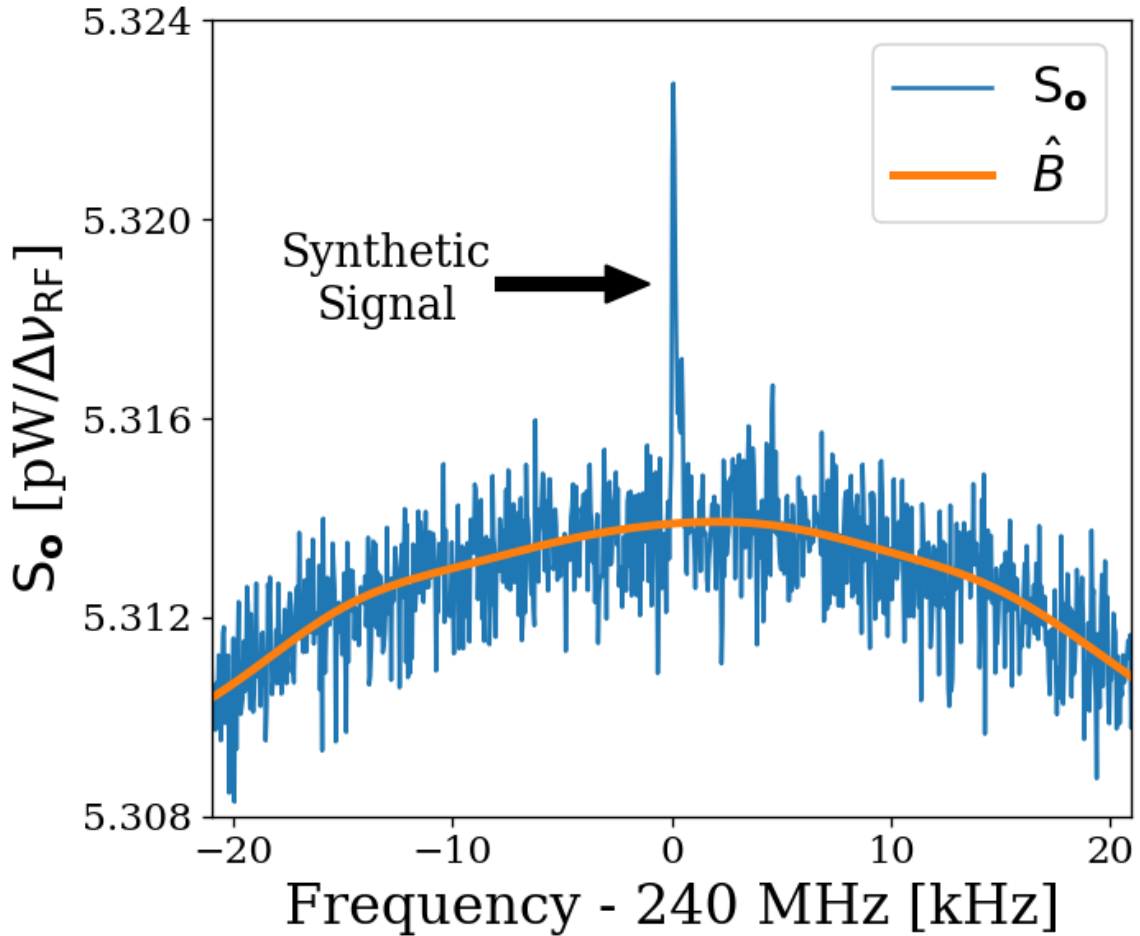


Figure 4.4: Fitting background  $\hat{B}$  in the presence of a synthetic signal injected at 240 MHz. Starting from the averaged, output-referred spectrum ( $S_o$ ), we fit the background using a series of filters (section 4.2.1, and Fig. 4.3). This figure is a highly zoomed-in view (240 MHz  $\pm$  20 kHz) in order to show the noisy Rayleigh signal shape.

<sub>1736</sub> **4.2.2 Normalized spectrum,  $S_o^{\text{norm}}$**

<sub>1737</sub> Once we have a fit to the background,  $\hat{B}$ , division of  $S_o$  by this fit yields a dimensionless,

<sub>1738</sub> Gaussian distributed spectrum

$$S_o^{\text{norm}} \equiv \frac{S_o}{\hat{B}}. \quad (4.1)$$

1739 As discussed in Sec. 2.1.1.3, this normalized spectrum (Fig. 4.5) should have a mean  $\mu_{\text{norm}} = 1$   
 1740 and a standard deviation given by the Dicke radiometer equation  $\sigma_{\text{norm}} = (\tau \Delta\nu_{\text{RF}})^{-1/2}$  where  
 1741  $\tau$  is the total integration time ( $\approx 9$  days) and  $\Delta\nu_{\text{RF}}$  is the width of a bin (47.7 Hz). This  
 1742 works out to a predicted  $\sigma_{\text{norm}}$  of  $1.727 \times 10^{-4}$ .  $\mu_{\text{norm}}$  and  $\sigma_{\text{norm}}$  calculated from the data  
 1743 are  $1 - 1.2 \times 10^{-5}$  and  $1.741 \times 10^{-4}$  respectively, which agree with the predicted values  
 1744 to better than 1%. Knowing the statistics of the background allow us to set a threshold  
 1745 above which we have some confidence that a candidate is not a random fluctuation. This  
 1746 significance threshold was derived in Sec. 2.2.1. As a reminder, the probability that all  $N$   
 1747 bins are less than  $z$  standard deviations,  $z\sigma$ , for a standard normal distribution is given  
 1748 by  $\left\{ \frac{1}{2} [1 + \text{erf}(z/\sqrt{2})] \right\}^N$ , where  $\text{erf}(z)$  is the standard error function and  $z$  is real. A 5%  
 1749 ST for  $5.2 \times 10^6$  bins (our 50-300 MHz analysis span) works out to  $5.6\sigma$ . This is shown in  
 1750 Fig. 4.5.

1751 It is possible to set a simple limit using this significance threshold on the normalized  
 1752 spectrum, which was our method in [4]. However, knowing the line shape of the dark photon  
 1753 signal provides additional information that improves sensitivity (up to a factor of  $\approx 2$ ) at  
 1754 the higher frequency end of the spectrum, as shown in Fig. 4.8.

### 1755 4.2.3 Signal-matched filter

1756 As discussed in 4.2.2, one simple method to set a limit is to look for single-bin excursions  
 1757 above some threshold. However, galactic dynamics impart a dark photon candidate with  
 1758 a Rayleigh-distributed, spectral signature, which has a dimensionless width  $Q_{\text{DP}} \approx 10^6$

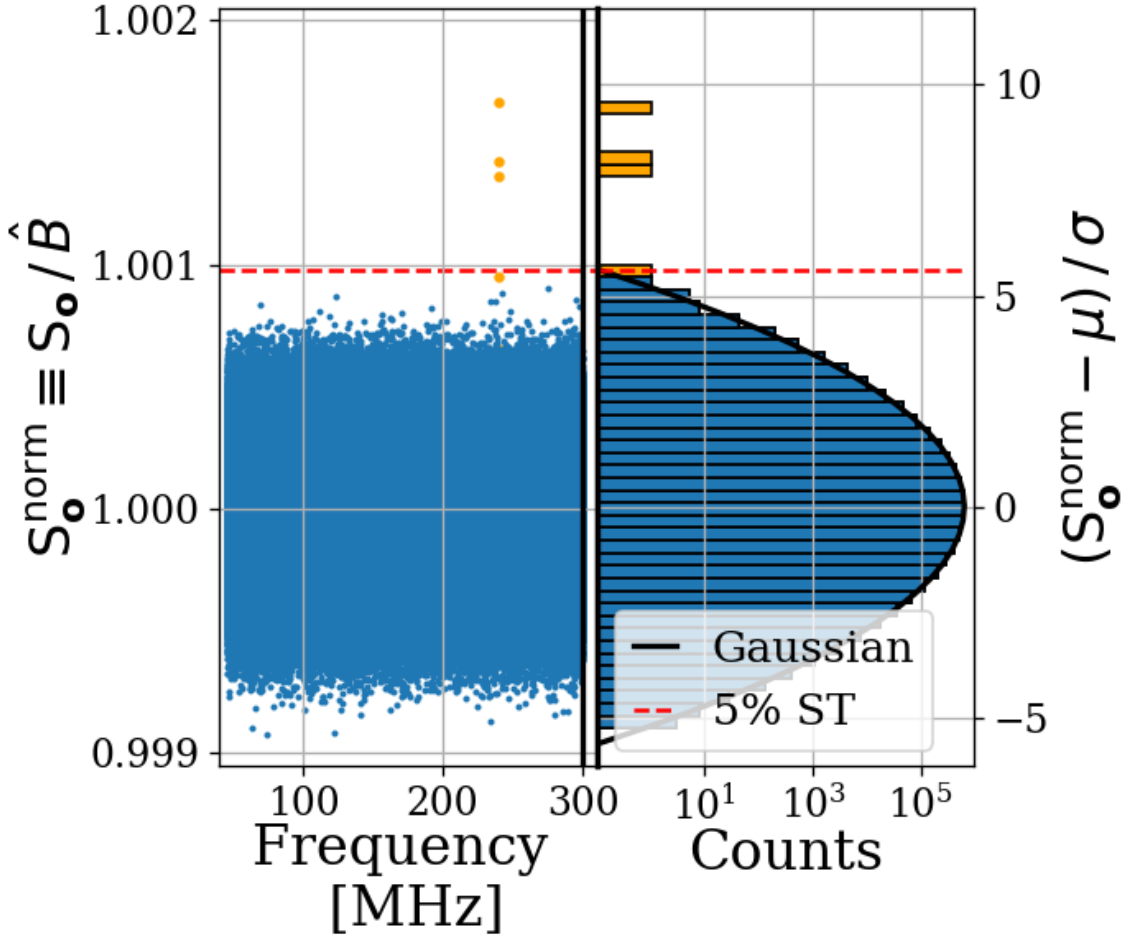


Figure 4.5: Dividing  $S_o$  by  $\hat{B}$  yields a dimensionless, normally distributed power spectrum that we define as  $S_o^{\text{norm}}$ . We show  $S_o^{\text{norm}}$  in two ways: a normalized power/frequency spectrum (*left*) and rescaled into Z-score units and collapsed into a histogram (*right*). The histogram shows power excess and Gaussian fit, but frequency information is lost. We compute a 5% significance threshold ST (*dashed red*), above which we will detect a candidate by chance 5% of the time. Bins adjacent to the 240 MHz synthetic signal show up in orange on both plots. A single interfering signal has been removed for clarity. We discuss this further in Sec. 4.2.5

1759 [33]. This means that the expected width of a candidate signal over our analysis span (50-  
1760 300 MHz) varies between 50-300 Hz. We set  $\Delta\nu_{\text{RF}} = 47.7$  Hz to maximize SNR for the lowest  
1761 expected signal width. However, this divides signal power between adjacent bins, an effect

1762 that becomes more pronounced at higher frequencies, leading to a decrease in sensitivity.  
1763 By using a signal processing technique known as *signal-matched filtering* [79, 80], we restore  
1764 some of the sensitivity lost due to the splitting of signal between the fixed-width frequency  
1765 bins of the FFT. A similar “optimal weighting” procedure has been well established in axion  
1766 haloscope experiments, notably by [20, 81]. Below, the signal-matched filter is referred to  
1767 simply as a *matched filter*.

1768 For a known signal shape, the detection technique that optimizes SNR is the matched  
1769 filter. This is implemented on the normalized power spectrum using the Rayleigh-distributed  
1770 spectral line shape of [33] as a template. Since we have a constant  $\Delta\nu_{\text{RF}}$  and expect the  
1771 width of the signal to vary across our span, we must calculate several templates of varying  
1772 width to match the expected line shape. Every 10% of fractional frequency change, a new  
1773 template is generated and used to search that small subspan of the normalized spectrum,  
1774 each of which is also normally distributed though with its own standard deviation. This  
1775 results in 20 subspans (50-55 MHz, 55-60.5 MHz etc.). The normalized spectra of all 20  
1776 subspans and the histogram of the 227-250 MHz subspan are shown in Fig. 4.6.

1777 As the width of the templates increase, the standard deviation of the output decreases,  
1778 resulting in the  $\nu^{-1/2}$  shape of the 5% significance threshold shown in Fig. 4.6. It should be  
1779 noted that since the total number of bins remains 5.2 million, the 5% significance threshold  
1780 still corresponds to  $5.6\sigma$ ; the shaping in Fig. 4.6 is due to the variation in  $\sigma$  for different  
1781 templates, not a change in the  $z = 5.6$  pre-factor.

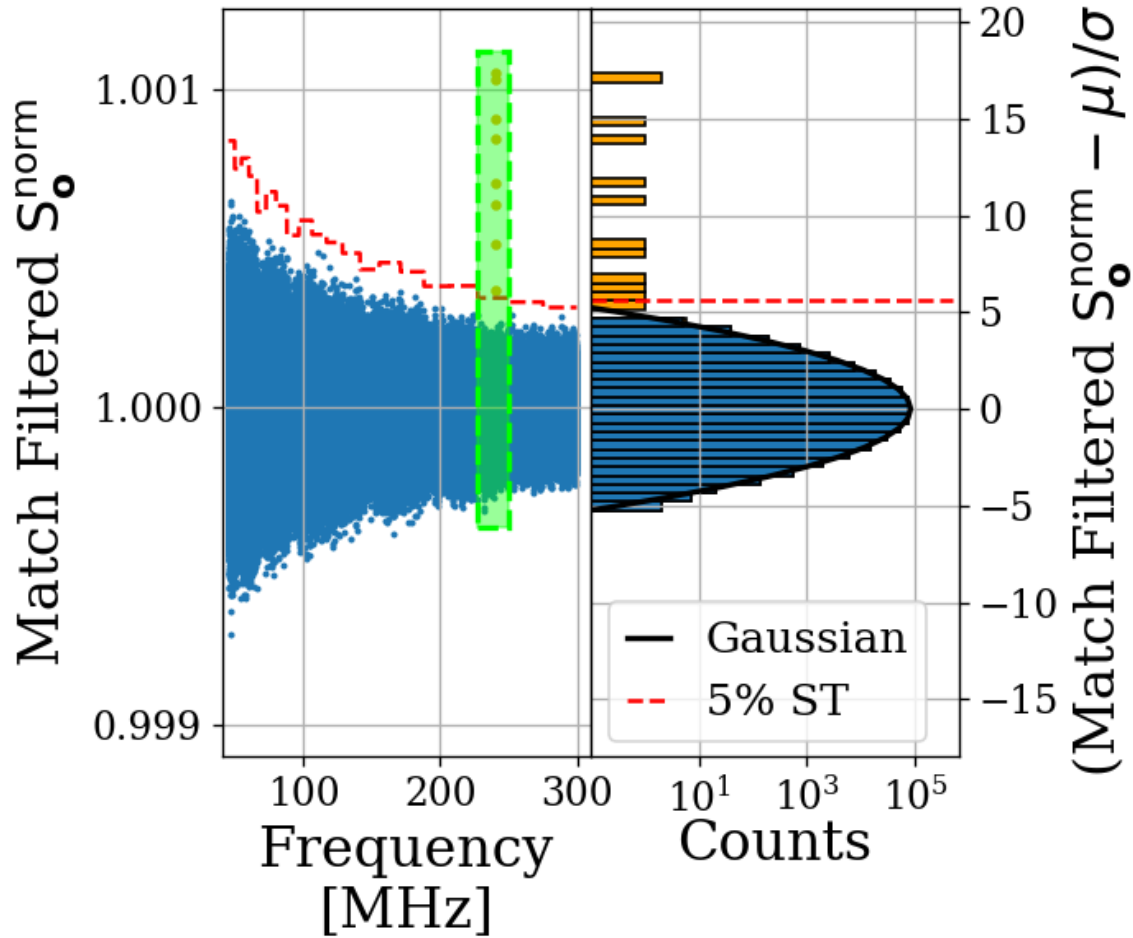


Figure 4.6:  $S_o^{\text{norm}}$  after it has been passed through a matched filter. The template varies in width throughout the frequency span resulting in 20 subspans, each with a constant 5% significance threshold ST (*dashed red*). This is discussed in the text of this section. The histogram only includes 227-250 MHz subspan (enclosed in the green box). The signal-to-threshold ratio of the synthetic signal (orange) improves by a factor of about 1.8 as compared to Fig. 4.5 without a matched filter. The frequency dependence of this effect is shown in Fig. 4.8. A single interfering signal has been removed for clarity.

#### <sup>1782</sup> 4.2.4 Monte Carlo: pseudo experiments

<sup>1783</sup> The previous three sub-sections outline the procedure for detecting the presence of a signal

<sup>1784</sup> of known spectral line shape embedded in wide-band noise. We refer to this procedure as a

1785 *detection algorithm* (see Fig. 4.3), which we now calibrate through a Monte Carlo method.  
1786 Synthetic background spectra are generated, and known signals are added to this background  
1787 to create a *test spectrum*. This test spectrum is passed to the detection algorithm, which  
1788 attempts to detect the signal. This process is repeated many thousands of times, and the  
1789 statistics of the detectability of a signal (as a function of its frequency and power) provide  
1790 insight into how much power could have been detected in the experiment.

1791 A synthetic, background spectrum is constructed by multiplying some background  $B(\nu)$   
1792 by randomly generated Gaussian white noise characterized by  $\mu_{\text{norm}}$  and  $\sigma_{\text{norm}}$ , as discussed  
1793 in section 4.2.2. A Rayleigh-distributed signal of known, total integrated, output-referred  
1794 power and frequency,  $\lambda(p, \nu)$ , can now be added to this spectrum to create a *test spectrum*  
1795 that can be passed through the detection algorithm (see Sec. 2.1.2 for a discussion of signal  
1796 line-shape). The frequencies of the synthetic signals are evenly spaced (approximately every  
1797 10 MHz). However, because the signal spans a small number of bins (one to six), the shape  
1798 of the discretized signal is very sensitive to the frequency at which its peak lands relative to  
1799 the bins. To compensate for the unknown dark photon frequency relative to a given bin, the  
1800 frequency of the synthetic signal is randomly jittered by  $\pm\Delta\nu_{\text{RF}}/2$ , which is drawn from a  
1801 uniform probability distribution at each iteration of the Monte Carlo. By repeatedly running  
1802 these synthetic, signal-containing, test spectra through the detection algorithm, statistics are  
1803 built up about how much total integrated power is required to detect a signal as a function  
1804 of frequency *most of the time*. We quantify this as the statistical power of the detection  
1805 algorithm and denote it  $100\% - Y = 95\%$  following the standard convention of hypothesis  
1806 testing.

	Only Noise	Noise + Signal
Detection	X	100% – Y
No Detection	100% – X	Y

Table 4.2: Threshold parameters that are part of the detection algorithm and Monte Carlo. X is the significance of the analysis. It is a parameter passed to the detection algorithm which specifies the significance threshold. The quantity 100% – Y is the statistical power of the analysis. It is a parameter in the MC, which specifies a threshold on signal power where a given signal is detected in 100% – Y of the MC iterations. We choose both X and Y = 5%.

1807 This Monte Carlo allows us to treat the detection algorithm as a black box that can  
 1808 be calibrated by passing it a known input (a test spectrum, i.e. a synthetic  $S_o$  containing  
 1809 a synthetic signal, both software-generated) and looking at its output; a Boolean array of  
 1810 frequency bins representing signal detection. These data, along with a simple linear fit to  
 1811 the 95% confidence interval, are shown in Fig. 4.7.

1812 The Monte Carlo’s output  $MC_{lim}(\nu, Y)$ , is a normalized limit on signal power required  
 1813 for detection. It is a function of frequency  $\nu$  and statistical power  $1-Y$ .  $MC_{lim}$  can simply be  
 1814 converted back to the limit on the total output-referred power contained in injected signals  
 1815 which can be detected 95% of the time,

$$P_o^{lim} = MC_{lim}\sigma_{norm}\hat{B}. \quad (4.2)$$

1816  $P_o^{lim}$  is shown in Fig. 4.8 in blue. Also shown in Fig. 4.8 is a limit that does not include  
 1817 any matched filtering (orange) to highlight the frequency-dependent improvement of the  
 1818 matched filter. This limit is only for illustration and not used in the following sections.

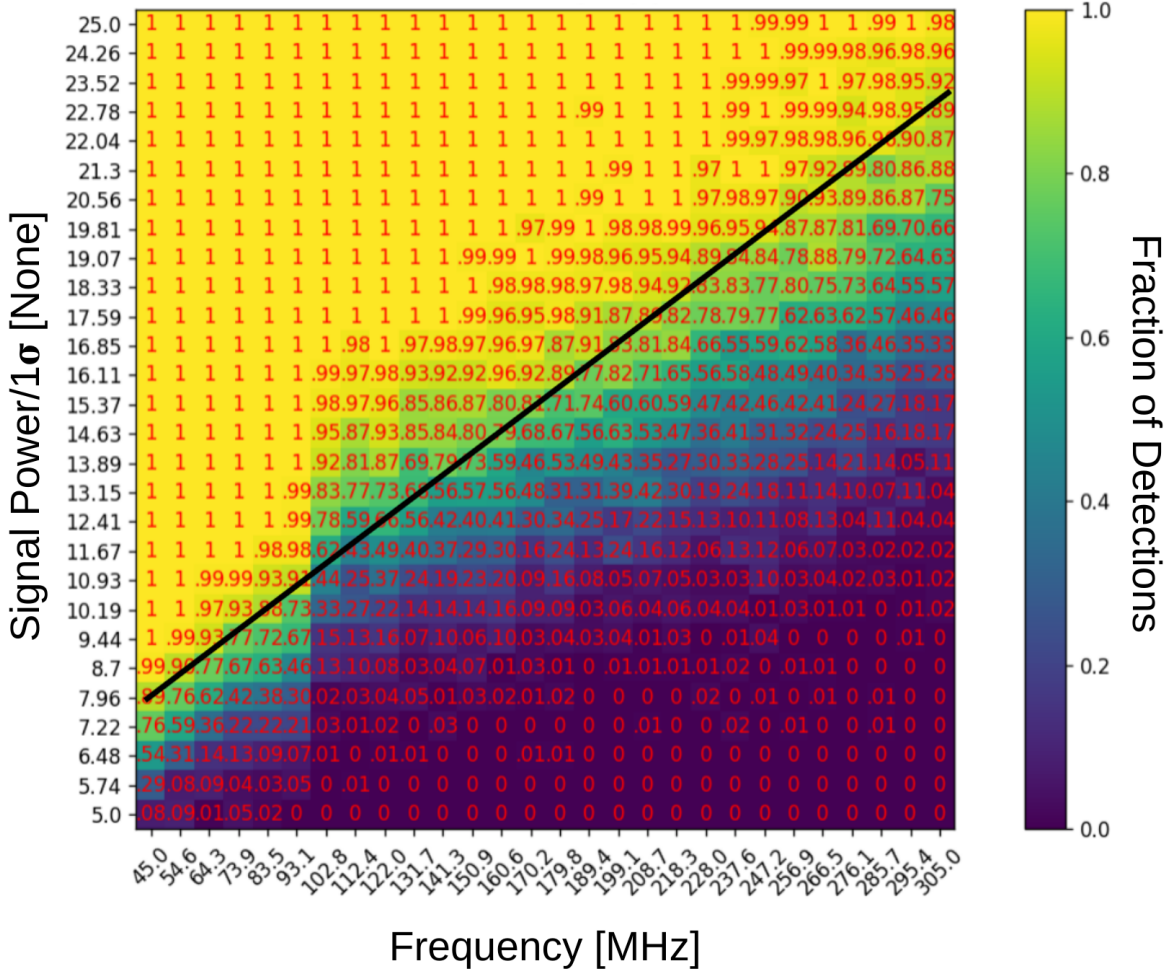


Figure 4.7: Result of Monte Carlo pseudo experiments on signal detection. Color and red numbering show the fraction of detections for each frequency/injected signal power of the 784 combinations tested. The signal power is shown in units of noise standard deviation  $\sigma$ . MC<sub>lim</sub> is shown as a black line. This line was inserted by eye and gives an approximate fit to the frequency vs. injected signal power which results in a detection 95% of the time. The approximate form of this line is MC<sub>lim</sub>( $\nu$ , Y = 5%) = 0.0686[P<sub>norm</sub>/MHz] + 2.411[P<sub>norm</sub>] where P<sub>norm</sub> is the normalized injected signal power shown on the Y-axis.

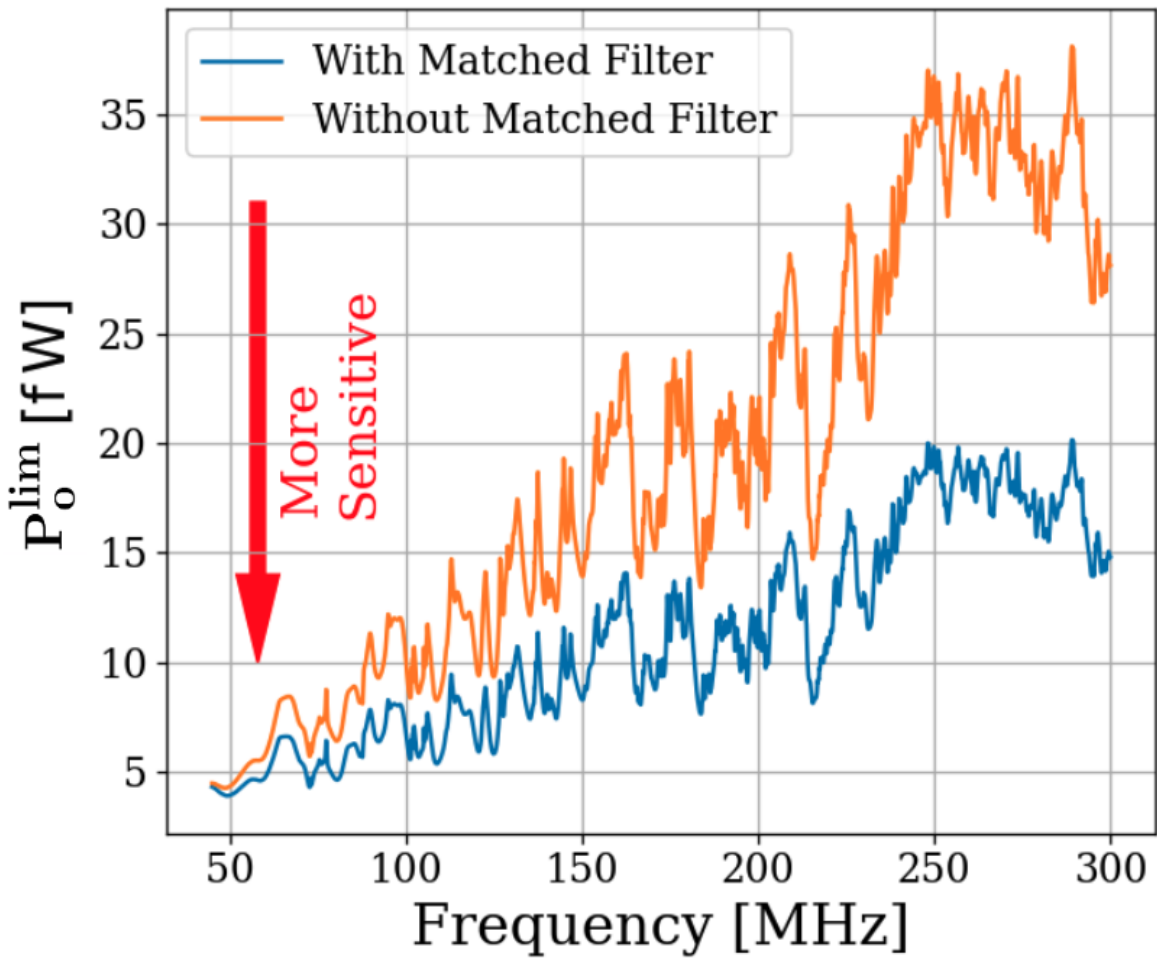


Figure 4.8: Limit on output-referred total integrated signal power,  $P_o^{\text{lim}}$ . Limits computed with (blue) and without (orange) a matched filter (Sec. 4.2.3). The limits are similar at lower frequencies, but the matched filter improves sensitivity at higher frequencies where the signal power is split among more bins. The blue curve is used in the following sections.

1819 **4.2.5 Rejection of a single candidate**

1820 Passing  $S_o$  through the detection algorithm diagrammed in Fig. 4.3 yields a single candidate  
1821 at 299.97 MHz which is approximately 1 kHz wide. This candidate first became detectable  
1822 above the noise after about 4 days of averaging, indicating it is just on the threshold of  
1823 detectability. Four factors allow for the conclusion that the candidate is an interfering signal  
1824 originating from within the PC or ADC, and not a signal in the shielded room (either a dark  
1825 photon or RFI):

1826 • The candidate is present not only in the main spectrum, but also in the veto and  
1827 terminator spectrum.

1828 • Inspection of the time evolution of this signal shows a narrow signal (about two bins,  
1829 or  $\sim$ 100 Hz wide) which seems to wander in frequency periodically over the course of a  
1830 day and, therefore, with temperature. This is expected behavior for a quartz oscillator.

1831 • Reducing the gain of the system causes the SNR of the candidate to *increase*, indicating  
1832 it enters the signal path after the gain stages.

1833 • Changing the clock rate causes the frequency of the candidate to change.

1834 The limit set in this section is referred to the output of the amplifier chain. A single  
1835 significant candidate was found, but the method of determining that it was not due to a  
1836 dark photon was outlined above. The topic of the next section will be to work back through  
1837 the amplifier chain, to an E-field limit in the cavity and ultimately to a limit on  $\epsilon$ .

## 1838 4.3 Calibration

1839 In this section, we describe the calibration of the experiment and estimate its uncertainty.

1840 The previous section concluded with a frequency-dependent limit on the output-referred

1841 power  $P_o^{\lim}$  (Fig. 4.8), which we now must convert into a frequency-dependent limit on  $\epsilon$ .

1842 We begin by inverting Eq. 1.7,

$$\epsilon(\nu) < \sqrt{\frac{|\mathbf{E}_{\text{ant}}^{\lim}|^2 \varepsilon_0}{2 \rho_{DM}}}, \quad (4.3)$$

1843 where the *lim* superscript indicates a limit, below which a detectable electric field may be

1844 hiding. The  $<$  should be taken to mean that in setting a limit on  $|\mathbf{E}_{\text{ant}}^{\lim}|$ ,  $\epsilon$  is constrained to

1845 be less than the right-hand side (if it exists at all).

1846 The first step of calibration is to convert from output-referred power to *antenna-referred*

1847 *power*. This represents the signal power presented to the LNA by the antenna via a matched

1848 transmission line and is given by

$$P_{\text{ant}}(\nu) = \frac{P_o}{G} - T_{\text{amp}} k_B \Delta\nu_{\text{RF}}, \quad (4.4)$$

1849 where  $G$  and  $T_{\text{amp}}$  are the frequency-dependent system gain and noise temperature (74–75 dB

1850 and 100–120 K respectively, measured via the Y-factor method, see Sec. 3.1.1) and  $k_B$  is

1851 Boltzmann’s constant.

1852 Ultimately, the exclusion limit is set by fluctuations on this baseline described by

$$\begin{aligned}
P_{\text{ant}}^{\lim}(\nu) &= \frac{P_{\text{o}}^{\lim}}{G} - \left( \frac{2}{n} \right)^{1/2} T_{\text{amp}} k_B \Delta\nu_{\text{RF}} \\
&= \frac{P_{\text{o}}^{\lim}}{G} - \left( \frac{2 \Delta\nu_{\text{RF}}}{\tau} \right)^{1/2} T_{\text{amp}} k_B,
\end{aligned} \tag{4.5}$$

1853 where the *lim* superscript indicates an exclusion limit,  $n$  is the total number of spectra  
 1854 averaged together, and  $\tau$  is the total integration time. In the second line, we have used  
 1855  $n = \Delta\nu_{\text{RF}} \tau$ . In practice, the LNA correction is small; the first term divided by the second  
 1856 varies with frequency between 7 and 50. The  $\tau^{-1/2}$  dependence of  $P_{\text{o}}^{\lim}$  is implicit because it  
 1857 was calculated from  $S_{\text{o}}$  which is itself an averaged spectrum. As mentioned above, this  $\tau^{-1/2}$   
 1858 dependence implies that the limit on  $\epsilon$  scales as  $\tau^{-1/4}$ .

1859 In the remainder of this section we explore the relationship between  $P_{\text{ant}}^{\lim}$  and  $|\mathbf{E}_{\text{ant}}^{\lim}|$  so  
 1860 that we can use our experimental data to set a constraining limit on  $\epsilon$  by employing Eq. 4.3.

### 1861 4.3.1 Average effective aperture, $\langle A_e(\nu) \rangle$

1862 An antenna's effective aperture,  $A_e$  [ $\text{m}^2$ ], represents the effective area that it has to collect  
 1863 power density or irradiance [ $\text{W/m}^2$ ] from an incident Poynting vector. It was defined in  
 1864 Eq. 2.9. Notably, it assumes a polarization match between the wave and the antenna (see  
 1865 Sec 2.1.1.2).

1866  $A_e$  is useful for an antenna in free space, however some modifications must be made to  
 1867 construct an analogous quantity for an antenna in a cavity.

1868 The first modification is to average over many configurations of the system. The back-  
 1869 ground for this is given in Sec. 2.4. As discussed, we denote this averaging with  $\langle \rangle$  so that the

average, effective aperture is denoted  $\langle A_e \rangle$ . It is interesting to note that by averaging over configurations (namely antenna direction),  $\langle A_e \rangle$  simplifies since  $\langle D(\Omega) \rangle = 1$  by construction [23].

The second modification is to introduce a resonant enhancement factor that corresponds to the system's tendency to "ring up" in the same way any resonator will. We refer to this as *composite Q* and represent it as  $\tilde{Q}$ . It is analogous to the standard quality factor of a resonator with one important modification; we operate our experiment across a wide frequency range so we define  $\tilde{Q}$  across the continuum of these resonances, not only on classical eigenmodes of the system.

These modifications provide a relationship between an observable E-field ( $\mathbf{E}_{\text{ant}}$  in Eq. 4.3) and the power available at the port of an antenna for a given aperture

$$\langle P_{\text{ant}} \rangle = \frac{|\mathbf{E}_{\text{ant}}|^2}{\eta_0} \langle \tilde{Q} A_e \rangle, \quad (4.6)$$

where  $\eta_0$  is the impedance of free space. With this in mind, we perform an RF simulation to compute  $\langle \tilde{Q} A_e \rangle$ .

### 4.3.2 Simulation of $\langle \tilde{Q} A_e \rangle$

It is difficult to make claims about statistical uniformity in the "undermoded" regime where modes are not sufficiently mixed [82], so we have employed a commercial, electromagnetic, finite-element modeling software package (COMSOL Multiphysics RF module [60]). Within the simulation, a model of the antenna (with a  $50 \Omega$  feed) is placed in a simplified room with

1888 wall features removed. Spot testing at various frequencies has shown that averaging results  
1889 from various antenna positions using this simplified simulation behaves very similarly to one  
1890 with the room features included at a fraction of computational complexity.

1891 Two similar simulations are run; driving an E-field while measuring the antenna's re-  
1892 sponse and driving a second small monopole antenna and measuring the response of the  
1893 primary antenna.

1894 In the first simulation, we drive currents on the walls which correspond to a surface E-  
1895 field magnitude of 1 V/m (made up of equal components in the x, y and z directions) using  
1896 COMSOL's source electric field option. This field takes the place of  $\mathbf{E}_{\text{ant}}$  in Eq. 4.6. The  
1897 antenna/cavity system resonates and causes an enhancement by  $\tilde{Q}$ . The power received at  
1898 the antenna's port is measured, allowing the calculation of  $\tilde{Q} A_e$ , again from Eq. 4.6. By  
1899 repeating this simulation for several positions, averaging allows us to compute  $\langle \tilde{Q} A_e \rangle$ .

1900 The second simulation shares the same geometry, but is used to compute a correction  
1901 factor to account for differences between simulation and measurement and to estimate un-  
1902 certainty on the first simulation through comparison to physical measurement. Rather than  
1903 driving the system through currents on the walls, power is injected into the system with a  
1904 40 cm monopole. From this simulation, two-port scattering parameters (S-parameters, de-  
1905 fined in 4.3.3) are computed. A similar test is performed on the physical system using a  
1906 vector network analyzer (VNA) which provides a physical measurement of the S-parameters  
1907 to compare with the simulation. The processing of the simulated and measured S-parameter  
1908 datasets is discussed in the following sub-section. A screenshot of the COMSOL model GUI  
1909 is shown in Fig. 4.9. The resulting S-parameters from the simulation are plotted against the

1910 measured S-parameters in Fig. 4.10

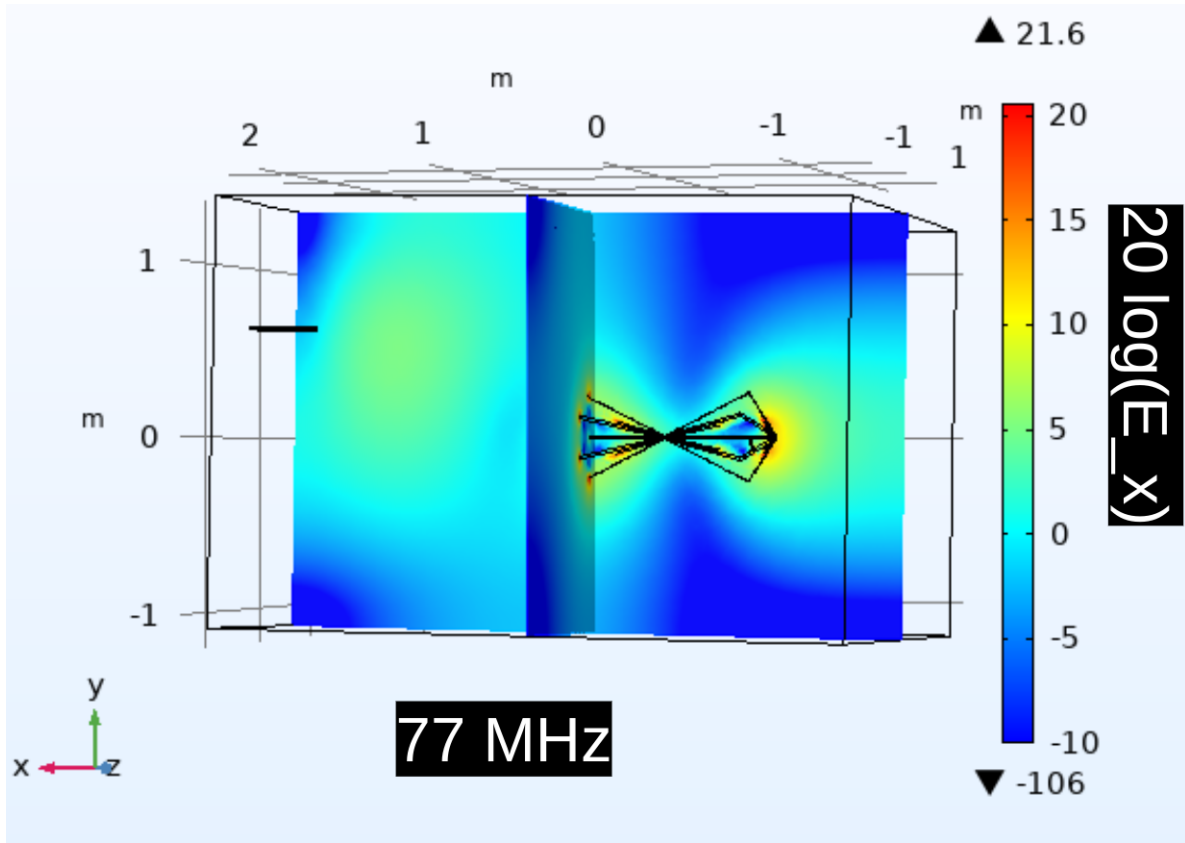


Figure 4.9: Screenshot of COMSOL simulation GUI for two-antenna validation. Shown only at a single position and single frequency (77 MHz). There are 18 antenna positions, 3 E-field components, and  $\sim 1000$  frequency points, so there are many similar figures to this one. The x-component of the electric field is shown in color compared to 1 V/m.

1911 Both simulations are run at the same 18 positions; 9 of which are approximately equiva-  
1912 lent to the physical antenna positions while the other 9 are different in order to estimate how  
1913 many positions are required for decent convergence of  $\langle \tilde{Q} A_e \rangle$ . Repeatedly averaging 9 differ-  
1914 ent, random positions (with replacement) results in about 20% variation on their averaged  
1915  $\langle S_{21} \rangle$  coefficients at each frequency, allowing us to conclude 9 positions and polarizations  
1916 provide acceptable convergence. This is a bootstrap method[83].

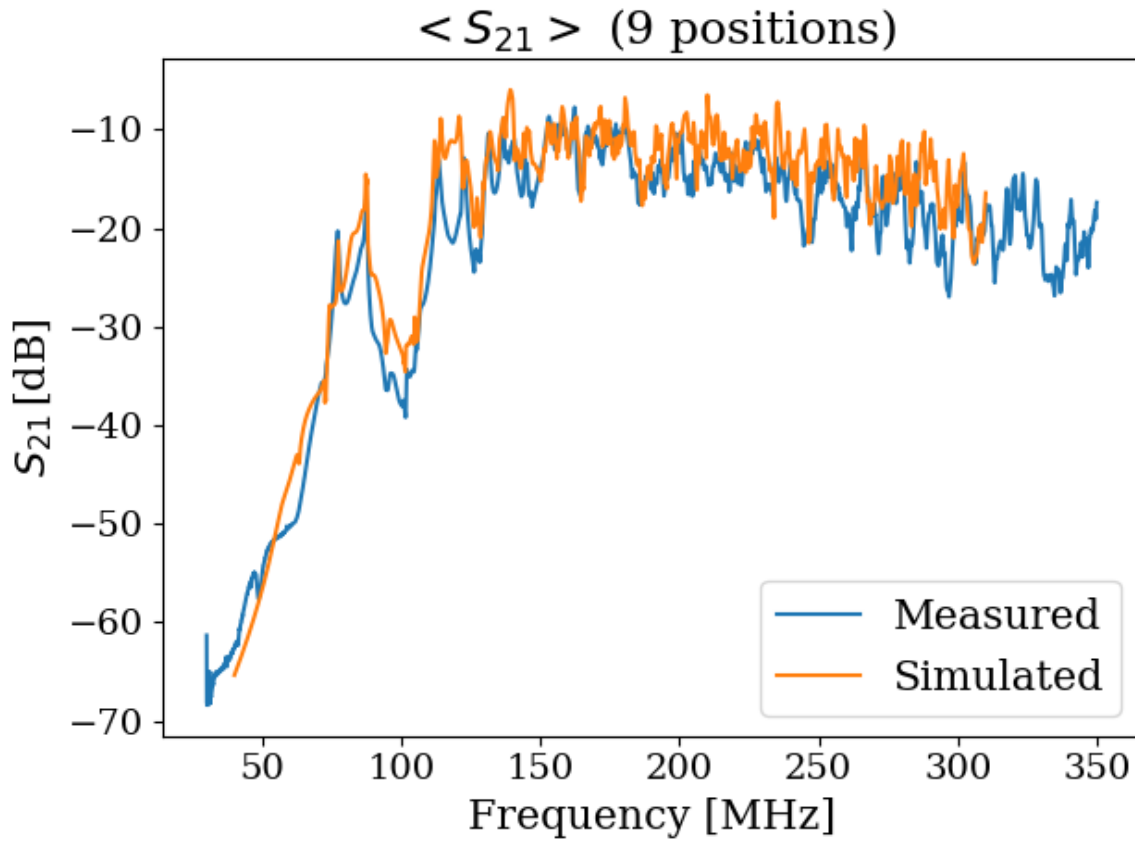


Figure 4.10: Simulated vs. measured  $\langle S_{21} \rangle$ . Averaged over 9 antenna positions. The procedures for generating these data are described in the text of this section.

<sup>1917</sup> **4.3.3 Correction and uncertainty of  $\langle \tilde{Q} A_e \rangle$**

<sup>1918</sup> As outlined above, we approximate the uncertainty of the simulation by injecting power into

<sup>1919</sup> the system via a second antenna and comparing the results to simulation.

<sup>1920</sup> For a two-port microwave device, the ratio between the voltage presented at port one and

<sup>1921</sup> the voltage measured at port two is known as  $S_{21}$  [43, 44]. For our system,  $S_{21}$  is a measurable

<sup>1922</sup> quantity that is similar to a dark photon detection in that it requires the antenna to convert

<sup>1923</sup> an electric field (which has interacted with the room) into a port voltage. Having frequency-

1924 dependent measurements of  $S_{21}$  for simulation and measurement gives us a correction to  
 1925 the simulation (to account for discrepancies in geometry) and estimate the uncertainty on  
 1926  $\langle \tilde{Q} A_e \rangle$ .

1927 The difference between the measured and simulated values of  $\langle |S_{21}| \rangle$  is described by

$$\langle |S_{21}^{\text{meas}}|^2 \rangle = \alpha \langle |S_{21}^{\text{sim}}|^2 \rangle, \quad (4.7)$$

1928 where meas/sim indicates measured/simulated and the average is over all 18 measured/sim-  
 1929 ulated positions and orientations of the antenna. We have taken the square since we are  
 1930 interested in the aperture, which is proportional to the square of the voltage. This equa-  
 1931 tion implies  $\alpha$  is a frequency-dependent, multiplicative correction factor which results in a  
 1932 corrected  $\langle |S_{21}^{\text{sim}}|^2 \rangle$ . We find  $\alpha$  to have a mean of 0.6, a minimum of 0.1 and a maximum of  
 1933 2.

1934 To determine uncertainty on effective aperture, we define the following test statistic

$$\Delta = \frac{\langle |S_{21,n}^{\text{meas}}|^2 \rangle - \alpha \langle |S_{21,n}^{\text{sim}}|^2 \rangle}{\langle |S_{21}^{\text{meas}}|^2 \rangle}, \quad (4.8)$$

1935 where  $n$  refers to the subset of  $n$  measured/simulated positions sampled randomly with re-  
 1936 placement.  $\Delta$  defines the fractional difference between corrected, simulated  $S_{21}$  and measured  
 1937  $S_{21}$ . The test statistic,  $\Delta$ , is calculated 1000 times, providing a distribution of frequency  
 1938 dependent  $\Delta$ s. The curves bounding 63% of these curves are taken to be the uncertainty  
 1939 on  $\Delta$ . Thus we calculate the corrected  $\langle \tilde{Q} A_e \rangle$  as well as its uncertainty. This is shown as a  
 1940 function of frequency in Fig. 4.11. The uncertainty on it is shown in gray and is simply

$$\delta \langle \tilde{Q} A_e \rangle = \langle \tilde{Q} A_e \rangle \delta \Delta. \quad (4.9)$$

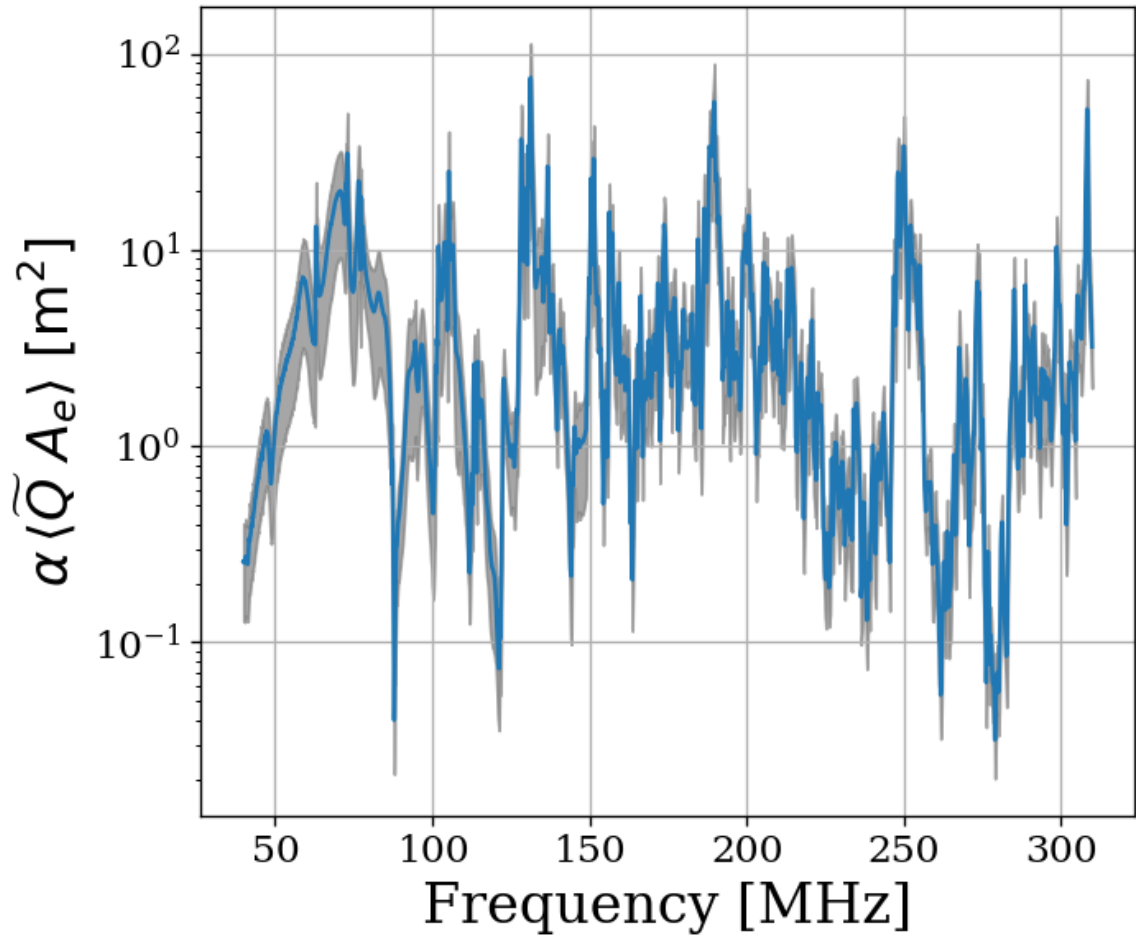


Figure 4.11: Corrected average effective aperture. Calculated with COMSOL RF. The aperture correction  $\alpha$  (Eq. 4.7) and its uncertainty (gray) are estimated by comparing simulations to measured  $S$  parameters.

1941        A brief summary of the system's aperture is in order. In free space an antenna's ability  
 1942        to couple an incoming wave's power density into a transmission line is given by its effective  
 1943        aperture, Eq. 2.9. An antenna in a cavity acts as a coupled oscillator that exhibits very

1944 complex resonances above the first few modes ( $\sim 100$  MHz for our system). Attempts to  
 1945 simulate an aperture for the antenna-cavity system are difficult because of the system's  
 1946 extreme dependence on the placement of any conductor in the room, especially the antenna.  
 1947 Averaging over system configurations (antenna positions and polarizations in our case) allows  
 1948 for a significantly more repeatable *statistical* treatment of the aperture/quality factor, which  
 1949 we call  $\langle \tilde{Q} A_e \rangle$ . Comparison of simulated and measured  $S_{21}$  gives a small, dimensionless  
 1950 correction factor  $\alpha$ , Eq. 4.7.

1951 Armed with  $\alpha \langle \tilde{Q} A_e \rangle$  we now compute a limit on  $\epsilon$  using the measured and simulated  
 1952 quantities via Eqs. 4.5 and 4.6,

$$\epsilon(\nu) < \sqrt{\frac{1}{2c\rho_{\text{DM}}} \frac{P_{\text{ant}}^{\text{lim}}}{\alpha \langle \tilde{Q} A_e \rangle}}, \quad (4.10)$$

1953 where  $c$  is the speed of light,  $\rho_{\text{DM}}$  is the local dark matter density and  $P_{\text{ant}}^{\text{lim}}$  is defined in  
 1954 Eq. 4.5. We have separated the equation into constants (or, in the case of  $\rho_{\text{DM}}$ , values that  
 1955 we fix) and values that we measure or simulate.

1956 In order to validate our entire detection system, we inject sub-threshold signals into the  
 1957 shielded room to verify we are able to detect them.

## 1958 4.4 Hardware Injection Test <sup>4</sup>

1959 To validate the detection methodology, a separate proof-of-concept run with a proxy dark  
 1960 photon signal injected into the shielded room was performed. Apart from the injection

---

<sup>4</sup>Code for this section can be found at: <https://github.com/josephmlev/darkRadio/tree/master/daqAnalysisAndExperiments/run1p4/injectionTesting/injectionTesting.ipynb>

1961 antenna (a 40 cm monopole, see Sec. 4.3.2), the setup was equivalent to run 1.4, including  
1962 the data analysis. The proxy dark photon signal (detailed in Sec. 4.4.1.2) was injected at a  
1963 frequency set by a colleague and was unknown to me at the time of analysis, constituting a  
1964 blind analysis.

### 1965 4.4.1 Injection test prerequisites

#### 1966 4.4.1.1 Determination of required injected power

1967 To accomplish the test, a minimum detectable power required for injection  $P_{\text{inject}}$  must be  
1968 computed.  $P_{\text{inject}}$  should correspond to a signal that can be detected in a predictable amount  
1969 of time (with some uncertainty, discussed in detail in Sec. 2.2.2). A simple way to begin  
1970 is to read off the detectable, total integrated, power from Fig. 4.8. In other words the  
1971 power contained in a dark photon line, integrated over the few bins spanned by the line  
1972 ( $Q_{\text{DP}} \approx 10^6$ , discussed in Sec. 2.1.2). This gives the amount of output-referred power that  
1973 would be detectable 95% of the time after 9 days of integration. Since we do not want to  
1974 wait 9 days for this test, it is simple to convert this detection limit into one that would be  
1975 produced in a shorter time using the Dicke radiometer equation, Eq. 2.16. Namely, the limit  
1976 on power scales like the square root of time<sup>5</sup>, so a one-hour integration will require a factor  
1977  $\sqrt{9 \text{ days}/1 \text{ hour}} = 14.7$  more power than is shown in Fig. 4.8.

1978 At this point, the simplest way to proceed is to measure the average through-power of the

---

<sup>5</sup>It is important to point out that one needs to test whether or not the system in question actually behaves as predicted by the Dicke equation for the amount of averaging in question. After lots of averaging, one may encounter non-thermal backgrounds that do not scale properly. It is shown in Fig. 4.16 that the dark radio system follows the Dicke radiometer equation at least for 9 days.

1979 monopole to the bicon in several antenna positions. This power is proportional to  $\langle |S_{21}|^2 \rangle$ .

1980 This is the same as the set up described in Sec. 4.3.2. The bicon was moved to 9 positions

1981 and the resulting S-parameters were measured at the reference planes shown in Fig. 4.12.

1982 They are shown in Fig. 4.13 after being averaged together.

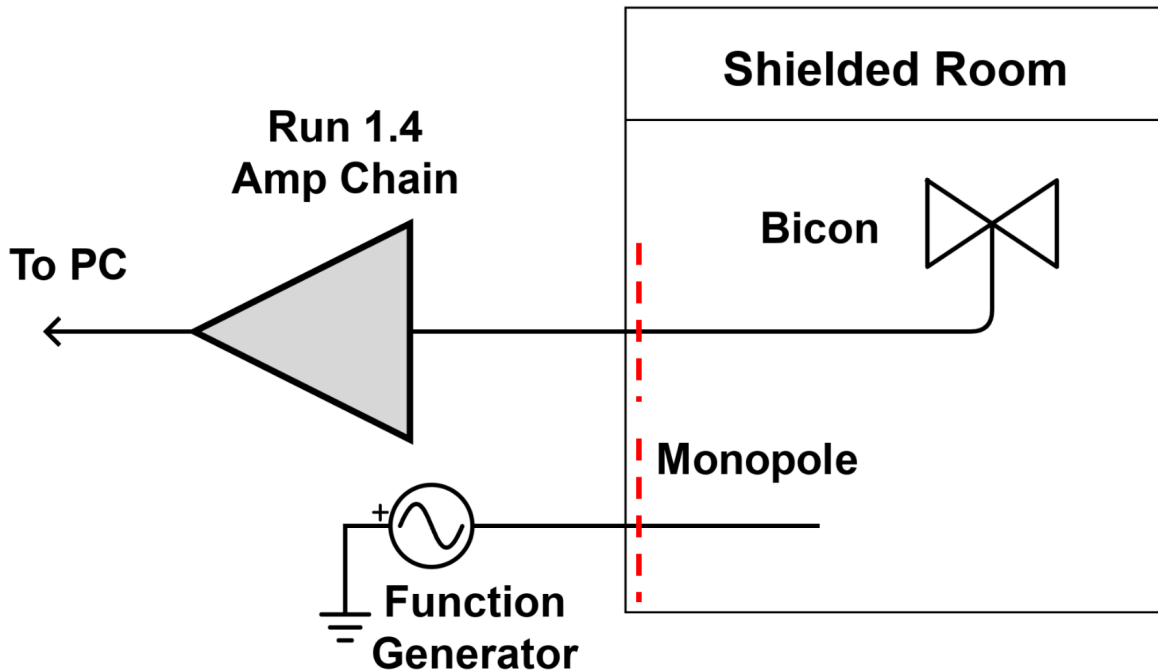


Figure 4.12: Schematic of hardware injection test. Dashed red lines indicate reference planes used to measure S-parameters, shown in Fig. 4.13. “Amp Chain” includes amplifiers, attenuators and filters as described in Sec. 2.5.4.

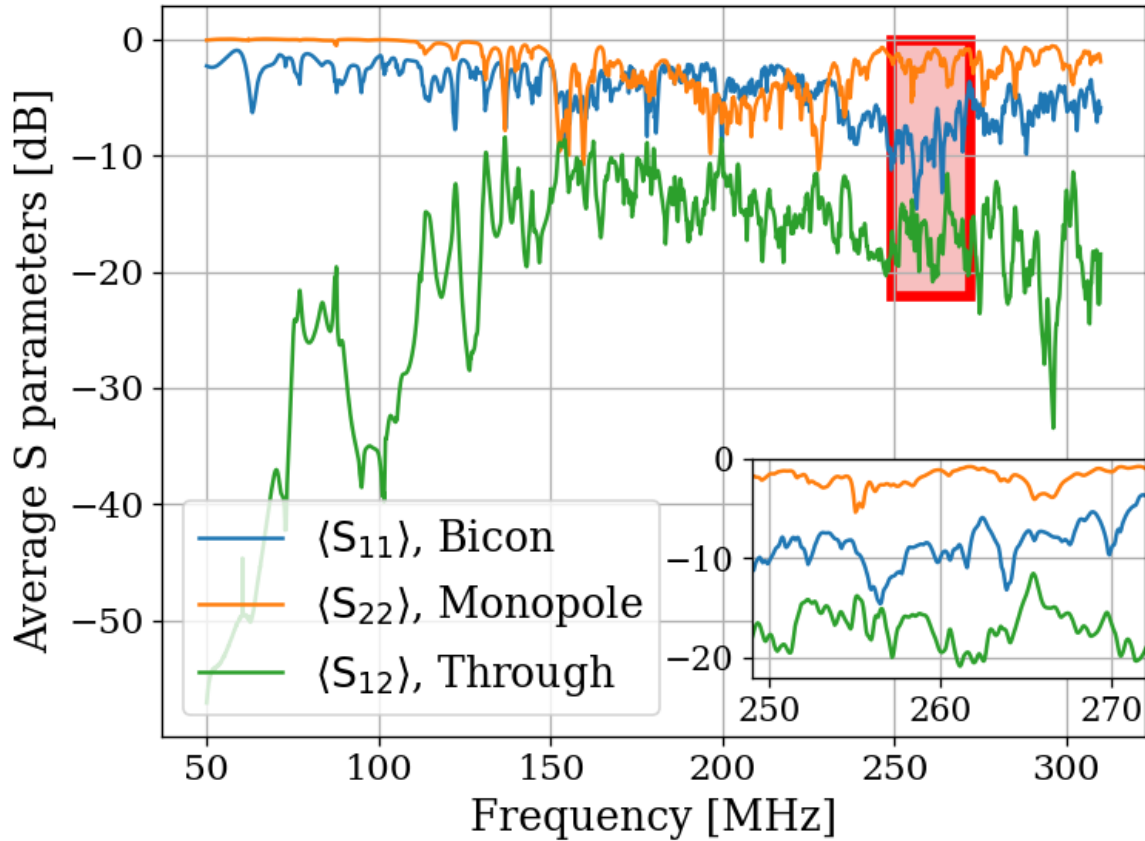


Figure 4.13: Average S-parameters of hardware injection test. Taken at 9 positions of the bicon antenna and averaged together (linearly). Ports 1 and 2 are defined to be for the bicon and monopole respectively. Note that  $\langle S_{12} \rangle = \langle S_{21} \rangle$  so only  $\langle S_{12} \rangle$  is shown. The inset shows a zoom-in of the area enclosed by the red box. Also note that dB is implicitly proportional to power.

1983 Knowing the output-referred power limit, the system's average  $\langle |S_{21}|^2 \rangle$ , and the gain G,  
 1984 allows for a calculation of the required signal strength (as a function of frequency) which  
 1985 will become detectable after a known amount of time. In order to simplify the test, a  
 1986 smaller 1 MHz band is chosen between 268 and 269 MHz for the blind injection, where  
 1987  $\langle |S_{21}|^2 \rangle$  is constant to about 1 dB. At first glance, this seems like cheating. However, there  
 1988 are still  $\sim 21,000$  frequency bins in this span, so a detection is very unlikely to be random.

1989 Furthermore, the entire 50-300 MHz span is sent to the detection algorithm (Discussed in  
1990 Sec. 4.2 and illustrated in Fig. 4.3), which produces an output without knowing about this  
1991 frequency restriction.

With all this in mind, the signal power required is simply

$$P_{\text{inject}} = \frac{P_o^{\text{lim}}}{G \langle |S_{21}|^2 \rangle},$$

1992 where each term is a function of frequency. For the parameters described in this section  
1993 (including the increase in the power limit  $\sqrt{9 \text{ days}/1 \text{ hour}} = 14.7$ ), this works out to  
1994  $\approx 6 \times 10^{-19} W$  or -152.5 dBm. The Rigol DSG830 signal generator is not calibrated  
1995 to such low levels, so this was achieved through attenuation<sup>6</sup>.

#### 1996 4.4.1.2 Proxy dark photon signal injection

1997 Now that the power for signal injection has been established, the finite-width proxy-signal  
1998 ( $Q_{\text{DP}} \approx 10^6$ ) is generated. The signal's line-shape is discussed in Sec. 2.1.2. An intuitive way  
1999 to accomplish this would be with an arbitrary waveform generator injecting a time domain  
2000 signal which is the Fourier transform of the the expected Rayleigh line shape, Eq. 2.24. This  
2001 is the method employed by the ADMX experiment (see, for example, [84]). Another option  
2002 would be to frequency-modulate a sine wave such that it slowly sweeps out the line shape,  
2003 spending an amount of time at each frequency weighted by Eq. 2.24. While intuitive, I was  
2004 unable to get this to work. Zhu et al.'s method of frequency hopping [85] is the discretized  
2005 version of this, and it was very simple to implement. The signal generator is set to change

---

<sup>6</sup>Experience with this signal generator has shown it exhibits the best performance is when it is set around -30 dBm. Higher than this, large non-harmonic distortions appear, contaminating the run. Smaller, and the signal-to-spurious-noise-floor of the generator is poor, also contaminating the run.

2006 frequencies at some interval (discussed below). The frequency is randomly drawn from the  
2007 PDF of Eq. 2.24.

2008 There are three considerations that determine the frequency hop period  $\tau_{\text{FH}}$  that the  
2009 frequency is changed<sup>7</sup>. First,  $\tau_{\text{FH}}$  should be much longer than the acquisition time of a single  
2010 buffer  $\tau_{\text{FFT}}$ <sup>8</sup>. On the Rigol signal generator, the power is briefly shut off while the frequency  
2011 is changed.  $\tau_{\text{FFT}} \ll \tau_{\text{FH}}$  ensures that most FFTs of data do not contain a frequency-hop.  
2012 Second,  $\tau_{\text{FH}}$  should be small compared to the total time of integration  $\tau$ , so that there are  
2013 many frequencies represented in the entire run. In the limiting case,  $\tau_{\text{FH}} = \tau$  will yield an  
2014 averaged spectrum containing a single injected frequency. In this case, the proxy-signal will  
2015 be a delta function in the frequency domain. Third,  $\tau_{\text{FFT}}$  should be longer than the ring-up  
2016 time of the room,  $\tau_{\text{FFT}} \gg Q/\nu$ . For  $Q = 100$  and  $\nu = 260$  MHz, the right-hand side of this  
2017 inequality is  $\approx 0.3$   $\mu$ s.

2018 Testing has shown that  $\tau_{\text{FH}}/\tau_{\text{FFT}} \approx 10$  is more than adequate to address the first con-  
2019 sideration. For Run 1A (and therefore, this test, which shares settings with Run 1A),  
2020  $\tau_{\text{FFT}} = 2^{24}/800$  MHz = 21 ms, so  $\tau_{\text{FH}}$  was set to 250 ms. This means that over 1 hour, the  
2021 frequency will be set to  $\approx 1.4 \times 10^4$  values, which addresses the second and third concerns.  
2022 A histogram of this signal is shown in Fig. 4.14.

---

<sup>7</sup>Zhu et al. randomized this period to prevent any unintentional periodic signals entering. I did not find this to be necessary.

<sup>8</sup>One can likely bypass this restriction by coordinating the signal generator and ADC such that there is some dead time between collection of buffers, in which the frequency is set. Testing has shown that this restriction is adequate to avoid this extra programming step

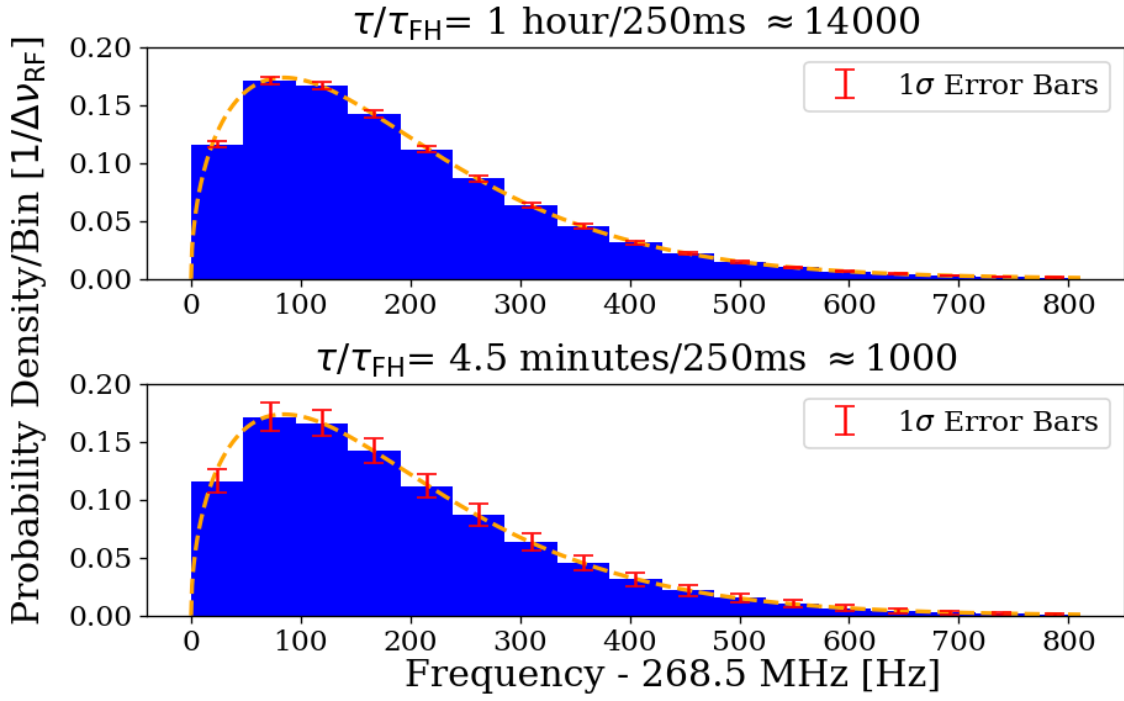


Figure 4.14: Histogram of frequencies used for hardware injection test, with realistic  $\Delta\nu_{\text{RF}} = 47.7 \text{ Hz}$ . The Orange dashed curve is the expected line shape from 2.24, and is the PDF frequencies are drawn from. The blue histogram and error bars are generated from the Monte Carlo simulation. They show the mean value per bin, with  $1\sigma$  error bars in red. This involves generating 1000 lists of random frequencies (each of length  $\tau/\tau_{\text{FH}}$ ), binning the data and calculating the standard deviation of each bin.  $\tau$  is the total acquisition time and  $\tau_{\text{FH}}$  is the amount of time spent on each frequency before “hopping” to the next. Their ratio,  $\tau/\tau_{\text{FH}}$ , is the number of frequencies that are injected in a given injection test, and was approximately  $1.4 \times 10^4$  for the one-hour test outlined in this section. Two plots give an idea of how error scales with  $\tau/\tau_{\text{FH}}$ .

#### 2023 4.4.2 Performing the injection test

2024 Due to the uncertainties involved, more data were taken than the required 1 hour. This also  
 2025 helped produce the pretty plot in Fig. 4 of Levine et al. [39]. 3.6 hr of data were collected  
 2026 and saved in 30 s pre-averages so that progressively more data could be averaged if the signal  
 2027 was not detected at the predicted time. As mentioned above, the signal was injected at a

2028 relatively high frequency within the span so that it would be split up into 5 or 6 bins, testing  
2029 the matched filter's effectiveness. The bicon was moved to 9 positions. Spectra resulting from  
2030 9 antenna positions and 30 seconds of pre-averaging at each position were averaged together  
2031 giving 4.5 m time resolution. Three of these spectra are shown in Fig. 4.15. The standard  
2032 deviation of these spectra average down with the square root of time, closely following the  
2033 Dicke radiometer equation (discussed in Sec. 2.1.1.3). This scaling is shown in Fig. 4.16.

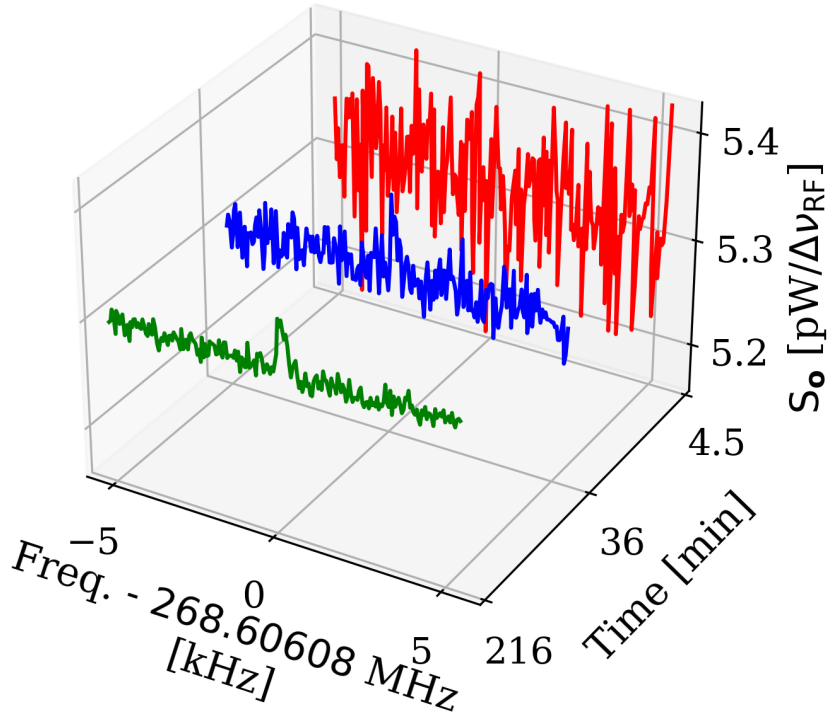


Figure 4.15: Output-referred power spectral density from the hardware injection test illustrating noise averaging down to reveal a persistent, hardware-injected, dark photon proxy signal. Spectra shown are highly zoomed around the injected frequency, 268.60608 MHz. The red, blue and green spectra represent 4.5, 36 and 216 minutes of integration time, respectively. The standard deviation of these spectra (excluding the bins containing the injected signal) averages down with the square root of time as expected. The blue spectrum shows the amount of averaging required for the signal to be detected by the detection algorithm (including the matched filter) at 5% significance. The tight zoom shown here is less than 1 part in  $10^4$  of the full 50-300 MHz spectrum analyzed.

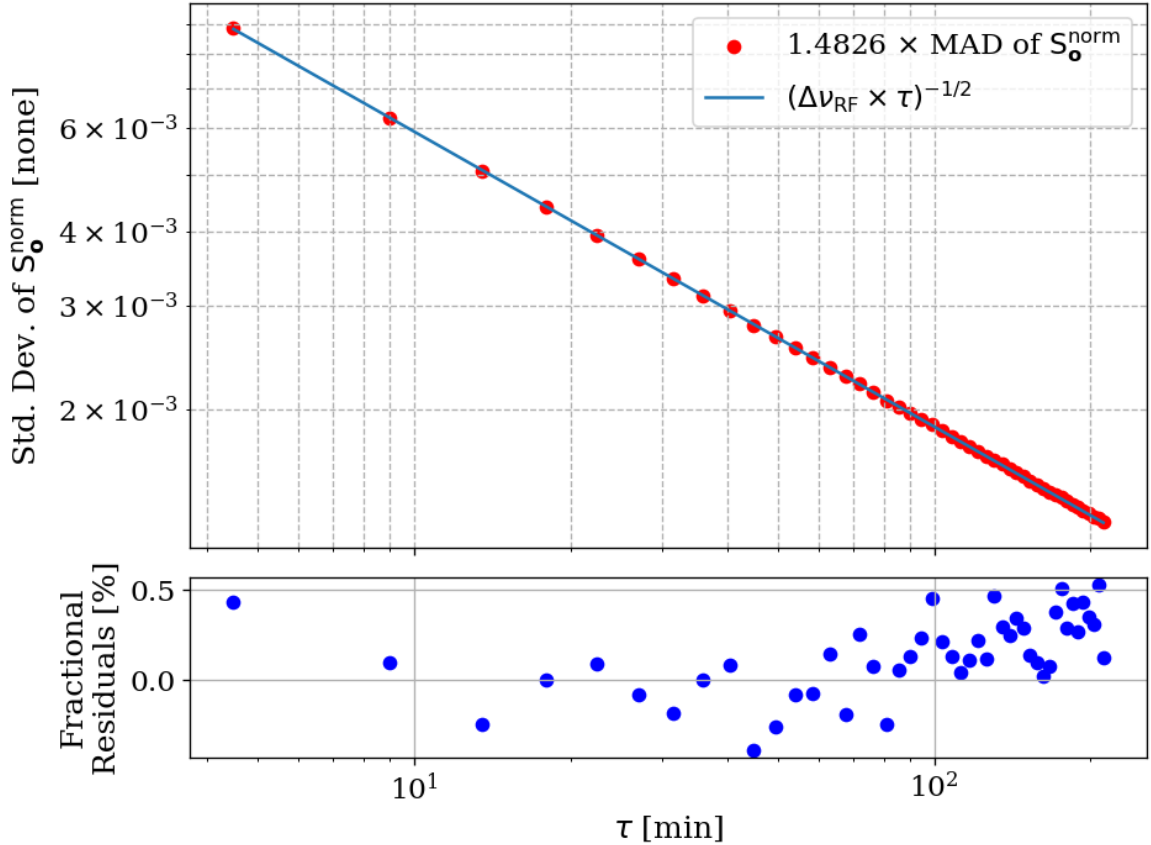


Figure 4.16: Standard deviation of output-referred power spectral density from the hardware injection test, computed with median absolute deviation (MAD). The blue curve represents the predicted standard deviation from the Dicke radiometer equation, Eq. 2.16. Each point corresponds to 9 antenna positions with an additional 4.5 minutes of data averaged (see Sec. 4.4.2). MAD provides a more robust measure of variability, reducing the influence of outliers and offering a better fit than direct standard deviation calculations. Note that the factor of 1.4826 is required to convert between MAD and standard deviation and assumes normally distributed data. It is derived in Sec. 2.3 of [86].

2034 These spectra were generated one at a time and passed through the detection algorithm.  
2035 The first spectrum where a signal was detected was at 36 minutes, shown in blue in Fig. 4.15.  
2036 Although hardly detectable to the eye, the matched filter detects the signal with 5% signifi-  
2037 cance. At the point the signal was detected (i.e. before all data were averaged together), the  
2038 injection frequency was confirmed to have been correctly identified, resulting in a success-  
2039 ful, blind, hardware injection test. Only after this confirmation were all the data averaged  
2040 together to make Fig. 4.15.

#### 2041 **4.4.3 Inspection of Data**

2042 This final subsection simply contains some full-page figures which show data from the injec-  
2043 tion test. They are all from the same 34 minutes of data but at different stages of processing,  
2044 closely following the three main steps of Analysis, Sec. 4.2. They are meant to simulate the  
2045 experience of inspecting a  $2^{24}$ -point FFT's power spectrum in a matplotlib widget window.  
2046 The zoom is seemingly unending, a feature that is difficult to appreciate in a printed docu-  
2047 ment. These figures should provide some context for how futile a manual search of unfiltered  
2048 data would be. Try and pick out the signal in the top left panel of Fig. 4.17!

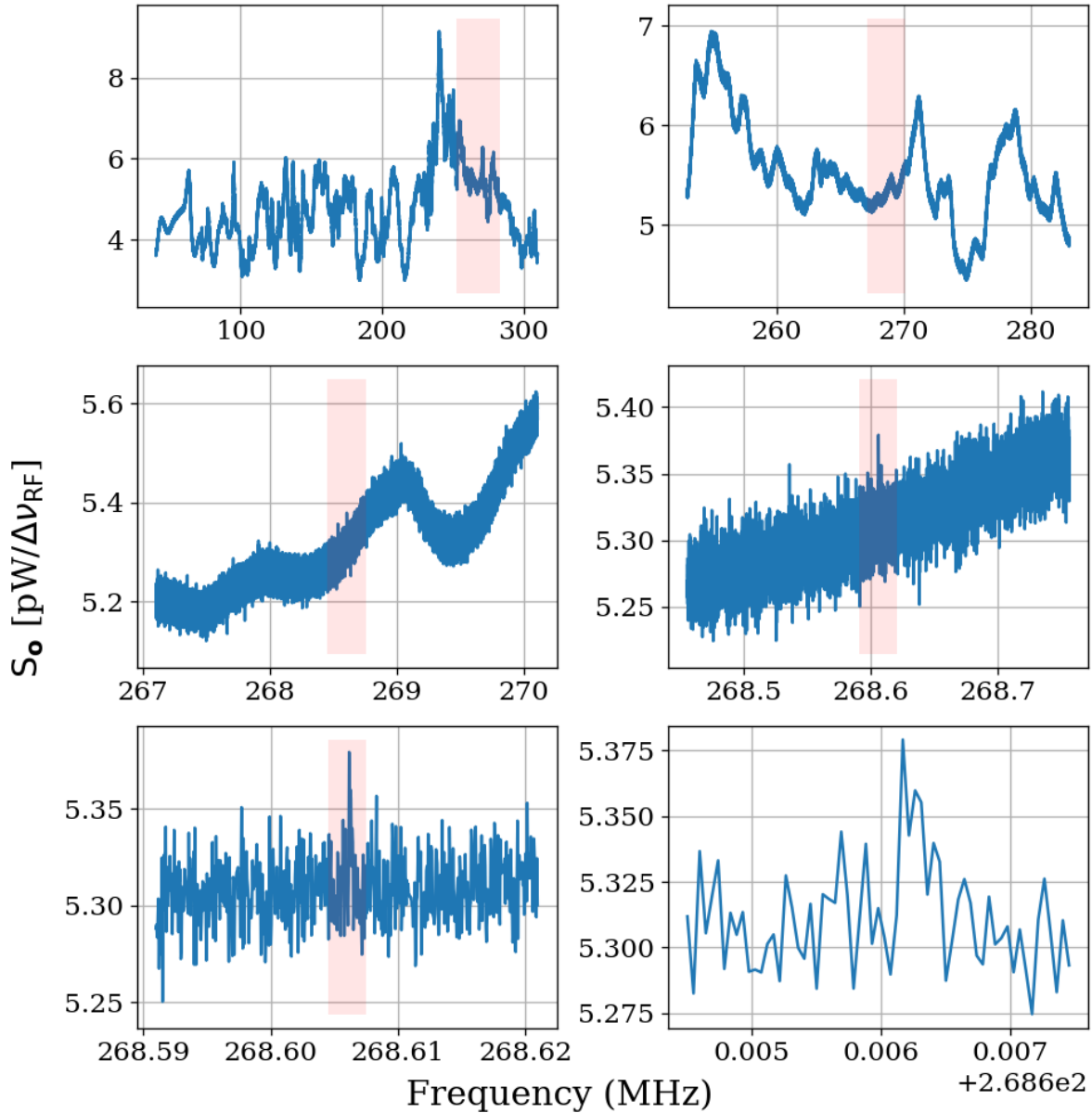


Figure 4.17: Output-referred power spectrum from hardware injection test. Injected signal at 268.60608 MHz. All spectra correspond to a total of 36 minutes of averaging, split evenly between 9 antenna positions. The full 50-300 MHz span contains  $\approx 5.2 \times 10^6$  bins. Light pink boxes show the zoom level on the following plot.

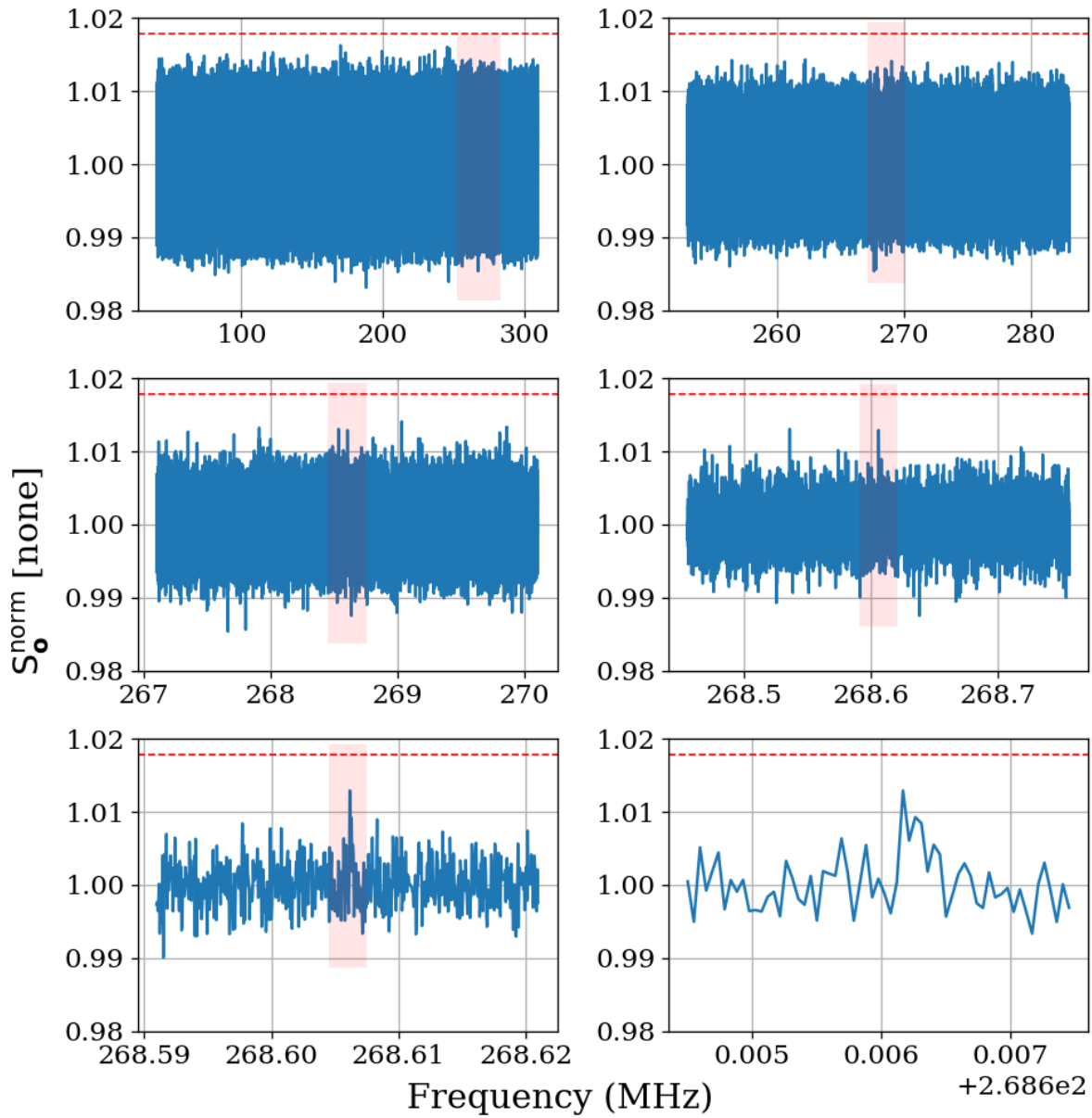


Figure 4.18: Normalized, output-referred power spectrum from hardware injection test. Injected signal at 268.60608MHz. Light pink boxes show the zoom level on the following plot. The red dashed line indicates the 5% significance threshold, derived in Sec. 2.2.1. A signal was not detectable above this threshold.

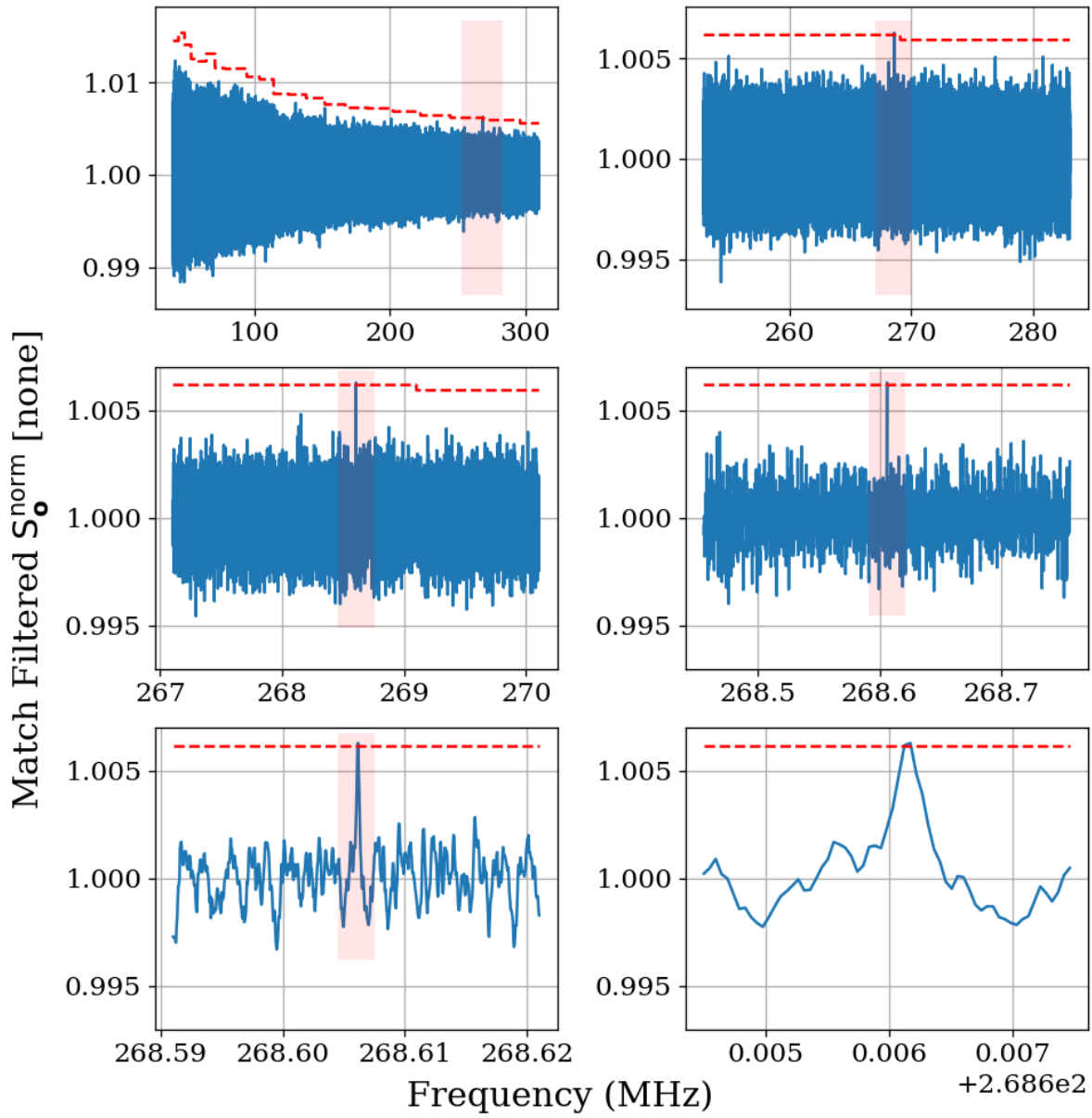


Figure 4.19: Matched filtered, output-referred power spectrum from hardware injection test. Injected signal at 268.60608MHz. Light pink boxes show zoom level on following plot. Red dashed line indicates the 5% significance threshold, derived in Sec. 2.2.1. Introducing the matched filter pushed signal above detectable above threshold compared to Fig. 4.18.

<sub>2049</sub> Chapter 5

<sub>2050</sub> Results

XXXXXX

<sub>2051</sub>

---

XXXXXX

2052 In this chapter, we report a 95%, frequency-dependent, exclusion limit on the kinetic  
2053 mixing strength  $\epsilon$  of the dark photon (Fig. 5.1). We discuss uncertainties in measured  
2054 data, the identification of a candidate signal and our process of excluding it. Finally, we  
2055 display our results in context by plotting these new limits on top of an aggregation of  
2056 existing limits in Fig. 5.2. Future runs of this experiment from 0.3-14 GHz in similar room-  
2057 temperature RF enclosures and 100 K noise temperature LNAs are indicated (the foundation  
2058 for such a system is outlined in Sec. 6.2). We have only indicated planned runs, however  
2059 at microwave frequencies, highly resonant cryogenic cavities and cryogenic LNAs as well as  
2060 sub-THz instrumentation are feasible and could result in an order of magnitude improvement  
2061 in the limit over the indicated frequency range and beyond. The design principles of such a  
2062 system are outlined in Sec. 6.3.

## 2063 5.1 Discussion of uncertainties

2064 The systematic uncertainty in this experiment comes primarily from three sources, listed in  
2065 order of their contribution from greatest to least:

- 2066 1. Fractional uncertainty on the simulated antenna aperture, which is discussed in Sec. 4.3.3,  
2067  $\approx 60\%$
- 2068 2. Fractional uncertainty on the first-stage amplifier noise temperature,  $\approx 10\%$
- 2069 3. Fractional uncertainty on the gain of the amplifier chain,  $\approx 5\%$

2070        The uncertainty on the simulated antenna aperture is significantly larger than the other  
2071        two, and so we neglect them in the reported uncertainty on the  $\epsilon$  limit.

2072        We follow the convention of similar experiments where we fix the value of  $\rho_{\text{DM}}$  and  
2073        solve for an  $\epsilon$  limit given this value. Therefore we treat  $\rho_{\text{DM}}$  as a known constant with no  
2074        uncertainty.

2075        **5.2 Exclusion Limit<sup>1</sup>**

2076        This section incorporates the exclusion limit on output-referred power (Fig. 4.8) and Eq. 4.10  
2077        to report a 95%, frequency-dependent, exclusion limit on the kinetic mixing strength  $\epsilon$  of  
2078        the dark photon. This limit is presented in Fig. 5.1, as well as in context by plotting it with  
2079        other, similar experiments in Fig. 5.2.

---

<sup>1</sup>Code for this section can be found at: <https://github.com/josephmlev/darkRadio/tree/master/Computelimit>

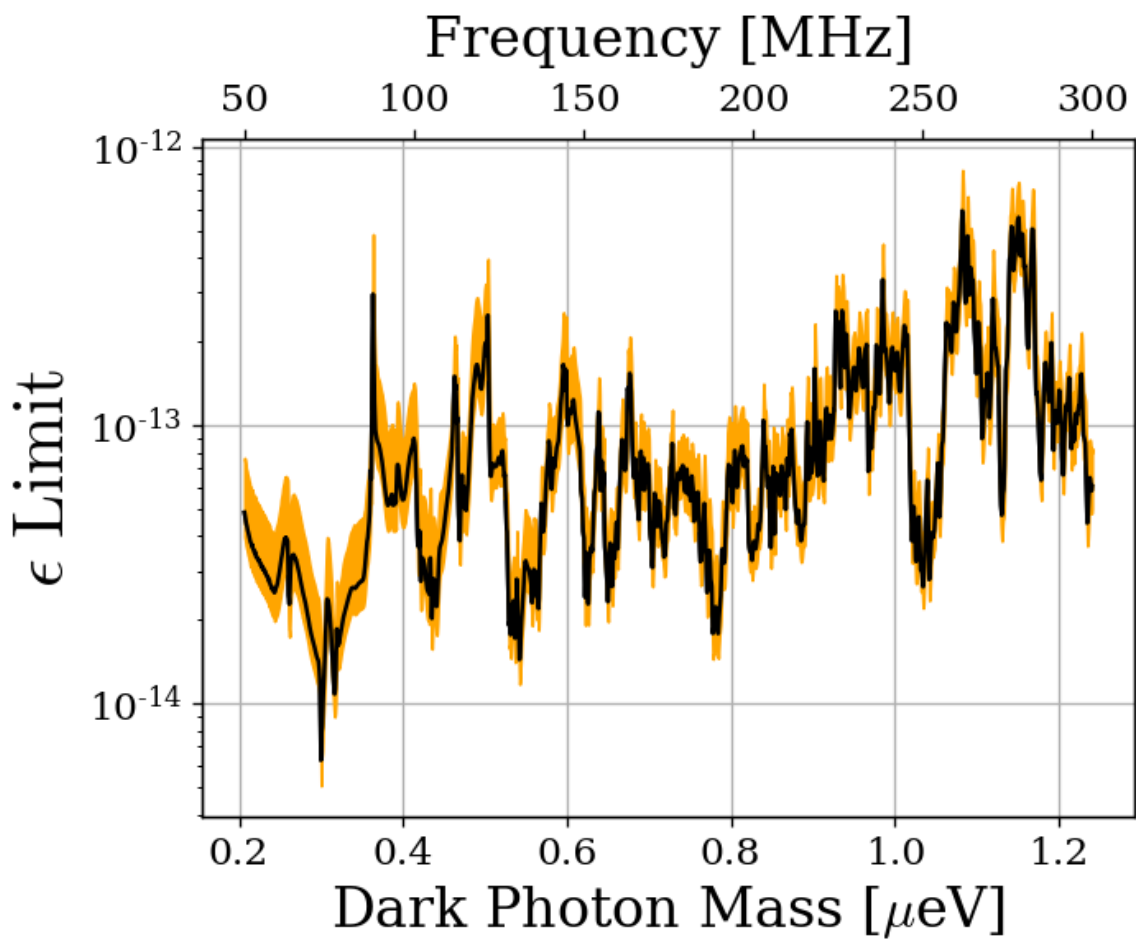


Figure 5.1: 95% exclusion limit on  $\epsilon$  with uncertainty shown in the orange shaded region. This is based on a local dark matter density of  $\rho_{\text{DM}} = 0.45 \text{ GeV/cm}^3$ . The error estimate does not take the comparatively small gain and amplifier noise temperature errors into account.

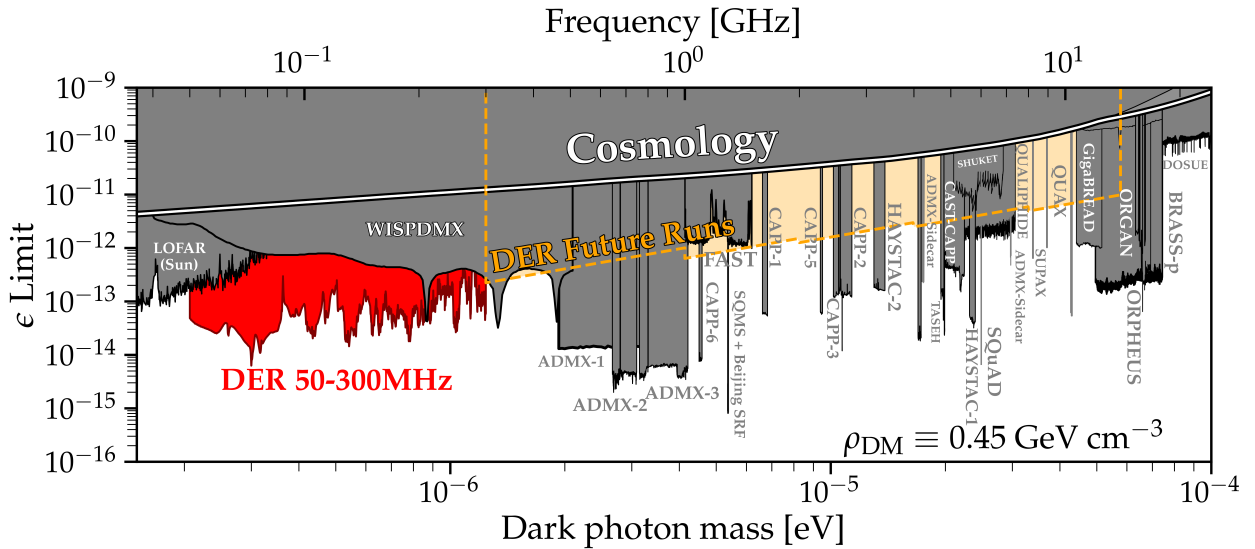


Figure 5.2: Dark photon limits of various experiments circa August 2024, with this work shown in red. The ragged lower bound is due to the complex structure of the resonant modes of the shielded room. Plot adapted by Ben Godfrey from [87] using code found at [88] and includes limit projections of various axion experiments. Astrophysical limits such as CMB interactions with the dark photon are in the region labeled *Cosmology*. Planned wideband extensions of our experiment search from 0.3-14 GHz in similar room temperature RF enclosures are indicated (*orange*). These planned runs are summarized in Table 6.1.

2080 Chapter 6

2081 Beyond 300 MHz

To infinity and beyond!

2082

---

Buzz Lightyear

2083        As discussed in previous chapters, there is a wide parameter space available for explo-  
2084    ration. This chapter details how the Dark E-Field Radio Experiment is poised to clear out  
2085    additional parameter space.

2086        Since the parameter space consists of two variables (namely mass, AKA frequency  $\nu$  and  
2087    kinetic mixing  $\epsilon$ ), the “area” of this space must be considered. The advantage of this exper-  
2088    iment is not absolute sensitivity; many experiments are orders of magnitude more sensitive  
2089    due to extremely high Q superconducting cavities or lumped-element circuits. Rather, the  
2090    advantage lies in the ability to clear out large frequency spans efficiently. The aforemen-  
2091    tioned high-Q experiments are only capable of searching a single, narrow frequency span at  
2092    a given time and must slowly step through the total required frequency span, waiting for  
2093     $\approx Q/\nu$  at each step for the system to ring up. Limitations on tuning require swapping out  
2094    hardware, slowing down the process. See, for example, DMRadio m<sup>3</sup>[89].

2095        The four completed or planned phases are outlined in Table 6.1. These phases are  
2096    projected to exclude the orange shaded region shown in Fig. 5.2.

2097        The remainder of this chapter is arranged XXXXXXXXXXXXXXXX

Run Name	Frequency Range	Antenna	LNA	Mixer	Status	Statistical Uniformity	Comments
1A	50-300 MHz	Compower Bicon, 50-300 MHz	Pasternack PE15A-1012	N/A	Complete, published	Below lowest usable frequency.	N/A
1B	300-1000 MHz	RF Space UWB-5 Vivaldi, 0.3-6 GHz	Pasternack PE15A-1012	N/A	Preliminary run complete by moving antenna. 21 candidates detected.	Mode stirrer	50% dead time to allow for 2 GHz sampling rate on Teledyne
2A	1-8 GHz	Small Vivaldi, model TBD	Low noise factory LNC0.3_14B	Miteq TB0440LW1	Waiting on mode stirrer and mixer system commissioning	Use mode stirrer to ensure uniformity	N/A
2B	8-14 GHz	TBD	Low noise factory LNC0.3_14B	Miteq TB0440LW1	Waiting on mode stirrer and mixer system commissioning	Mode stirrer	N/A

Table 6.1: Overview of future runs including hardware (antenna, LNA, mixer), status, how/if statistical uniformity will be ensured, and any comments

2098 **6.1 A first attempt at Run 1B<sup>1</sup>**

2099 A preliminary attempt at Run 1B (300-1000 MHz) has been completed. This attempt had  
2100 a few issues which are discussed here and will be addressed in the future, but are beyond  
2101 the scope of this thesis. In this section, upgrades and data acquisition are discussed. The  
2102 projected  $\epsilon$  limit from this run (along with Runs 2A and 2B) is shown in Yellow in Fig. 5.2,  
2103 however this projection is independent of the data shown here.

2104 **6.1.1 Run 1B upgrades**

2105 There are three main upgrades to consider before beginning Run 1B: software upgrades of  
2106 the GPU-based spectrum analyzer, modifying the current antenna stand to accept a Vivaldi  
2107 antenna, and building a mode stirrer to ensure statistical uniformity. The remainder of this  
2108 subsection will detail these upgrades.

2109 **6.1.1.1 Run 1B spectrum analyzer**

2110 The GPU-based spectrum analyzer (Sec. 2.5.7) is capable of sampling at up to 2.5 GHz,  
2111 easily allowing for a run up to 1 GHz. However, the PCIe-based ADC has a maximum data  
2112 transfer rate of 7GB/s. To accommodate two channels (main experiment and veto), the  
2113 system was set up with 50% dead time to allow for data to transfer. The limit on  $\epsilon$  scales  
2114 with the quarter root of time, so this is only a 16% reduction in sensitivity. This is purely a  
2115 software upgrade and has been completed

---

<sup>1</sup>Code for this section can be found at: <https://github.com/josephmlev/darkRadio/tree/master/daqAnalysisAndExperiments/run1B/analysis>

2116 **6.1.1.2 Vivaldi antenna stand**

2117 The COMPOWER bicon antenna stand was modified to accommodate the RFSpace UWB-5  
2118 Vivaldi antenna. This was completed and pictures of the modifications are shown in Figs. 6.1  
2119 and 6.2.



Figure 6.1: Picture of modified COMPOWER antenna stand holding Vivaldi antenna for Run 1B.

2120 **6.1.1.3 Mode stirrer and statistical uniformity**

2121 Run 1A relied on moving the antenna to improve the statistical uniformity (Sec.2.4) but still  
2122 required simulation to calibrate it (Sec.4.3.2). Run 1B, however, benefits from its frequency

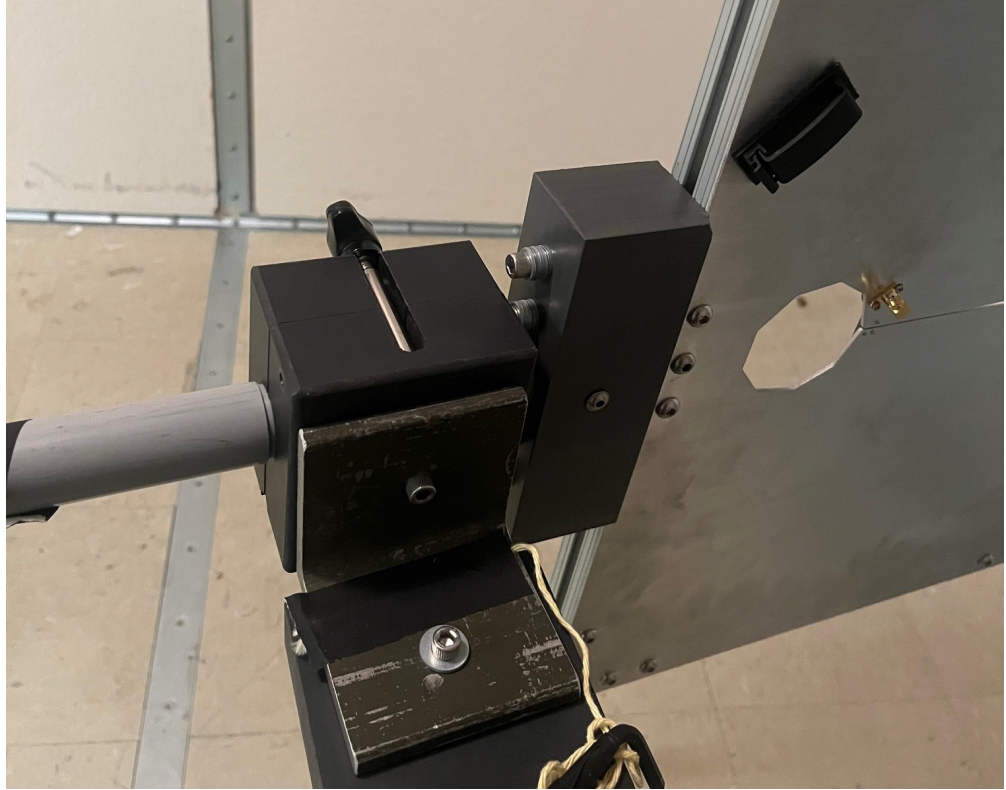


Figure 6.2: Closeup of modified COMPOWER antenna stand holding Vivaldi antenna for Run 1B

2123 range beginning above the lowest usable frequency of the shielded room ( $\sim 200$  MHz, see  
2124 Sec. 2.34). To take advantage of this, a proper mode stirrer (Sec. 2.4) must be employed. A  
2125 lack of mode stirrer is the main limitation of this attempt at Run 1B. At the time of writing,  
2126 work is ongoing to construct a mode stirrer. **comment:** Since this is ongoing, I will circle  
2127 back and add photos with current progress right before submitting a final draft

2128 **6.1.2 Run 1B data run and analysis**

2129 The first attempt at Run 1B, (Run 1B.1) was taken between September 13 and 22, 2023.  
2130 At the time of writing, this has been the only attempt at this run. The raw data are shown  
2131 in Fig. 6.3. The normalized standard deviation  $\sigma_{\text{norm}}$  (defined in Sec. 4.2.2 from the Dicke  
2132 radiometer equation) is predicted to be  $0.9885 \times 10^{-3}$ , and is calculated from the data to be  
2133  $1.001 \times 10^{-3}$ .

2134 Processing this data through the detection algorithm (Fig. 4.3) of Run 1A, yields the  
2135 normalized, signal-matched-filtered spectrum and 5% significance threshold which are shown  
2136 in Fig. 6.4.

2137 Comparison of the spectrum and threshold pictured in Fig. 6.4 reveal 21 candidates<sup>2</sup>.  
2138 Furthermore, 13 of these are clustered between 758 and 768 MHz. This frequency span is  
2139 reserved for the First Responder Network Authority (FirstNet) and is likely in use locally  
2140 by emergency services.

2141 All of these candidates are almost certainly RFI with enough energy (i.e. signal power  
2142 integrated over the 9-day run) to overcome the isolation of the shielded room (Fig. 3.13).  
2143 These signals are visible in the veto spectrum (Fig. 6.5 ), but further investigation is required  
2144 to conclusively exclude them as dark photons.

2145 Since simulations of this run are extremely difficult to calculate (wavelength at 1GHz <<  
2146 room dimensions), it will have to be revisited when statistical uniformity can be established,  
2147 i.e. with a mode stirrer. For this reason, further time domain analysis of these candidates is

---

<sup>2</sup>There are a total of 60 bins over the threshold, but many bins are adjacent. Combining adjacent bins results in 21 independent candidates

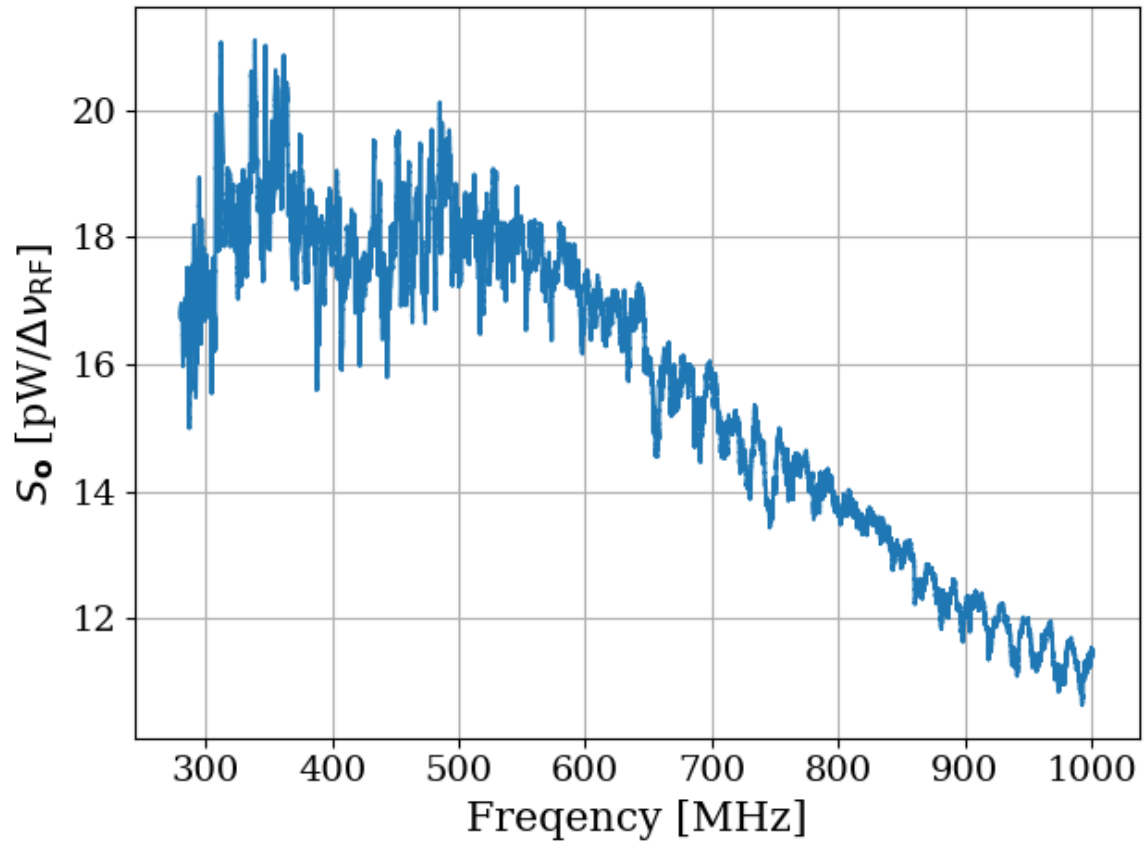


Figure 6.3: Run 1B averaged, output-referred antenna power spectrum  $S_o$ . Data were taken over a 9-day period at 9 antenna positions. The narrow variations are mainly due to the effective temperature difference between the room and LNA (Sec. 2.3), though there is a contribution due to amplifier gain and noise temperature variations (Sec. 4.1.1). The variations seen here are not noise; their shape is repeatable for a given antenna position. The noise on this background is not visible at this level of zoom.

2148 not explored here.

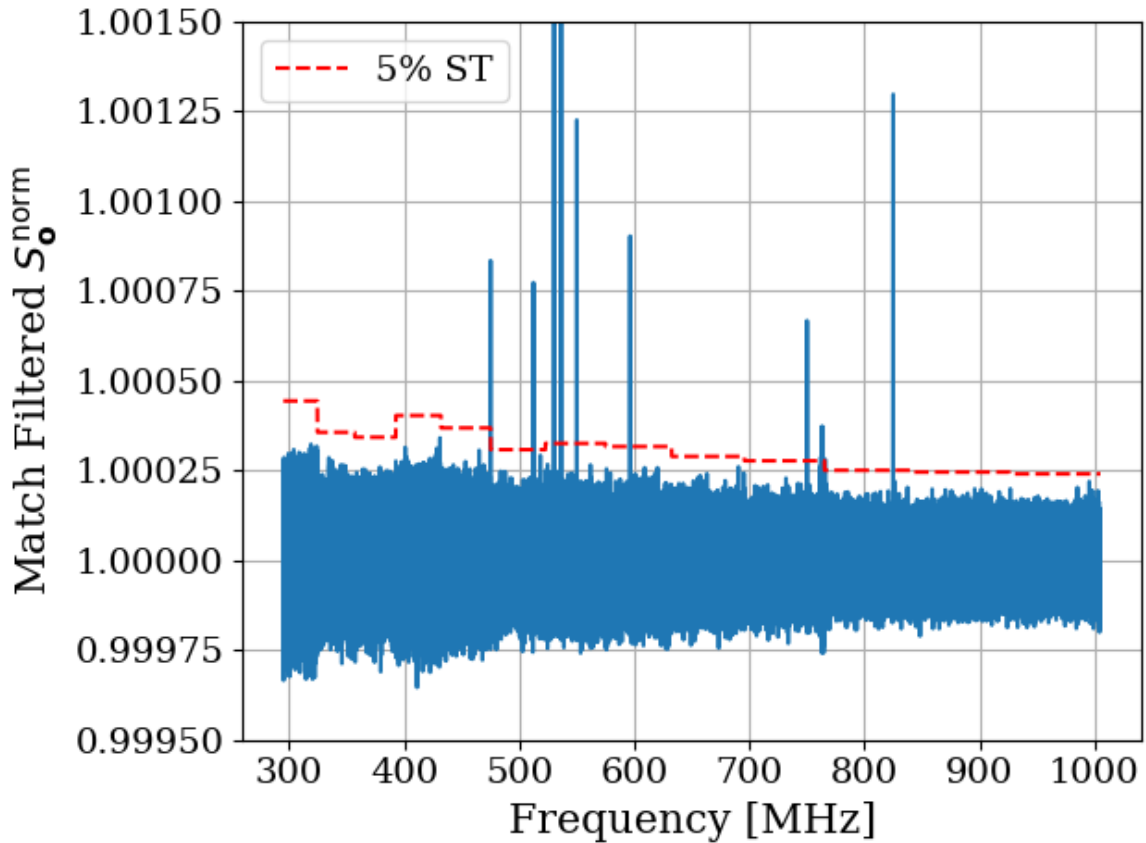


Figure 6.4: Run 1B  $S_o^{\text{norm}}$  after it has been passed through a matched filter. The template varies in width throughout the frequency span resulting in 13 subspans, each with a constant 5% significance threshold ST (*dashed red*), see Secs. 2.2.1 and 4.2.3. This plot is to Run 1B as Fig. 4.6 was to Run 1A. In contrast to Fig. 4.6, however, the narrow signals are not injected. They are almost certainly RFI with enough power to overcome the isolation of the shielded room (Fig. 3.13). These signals are visible in the veto spectrum, but further investigation is required to conclusively exclude them as dark photons. The vertical scale has been set such that the tops of some of the signals are cut off.

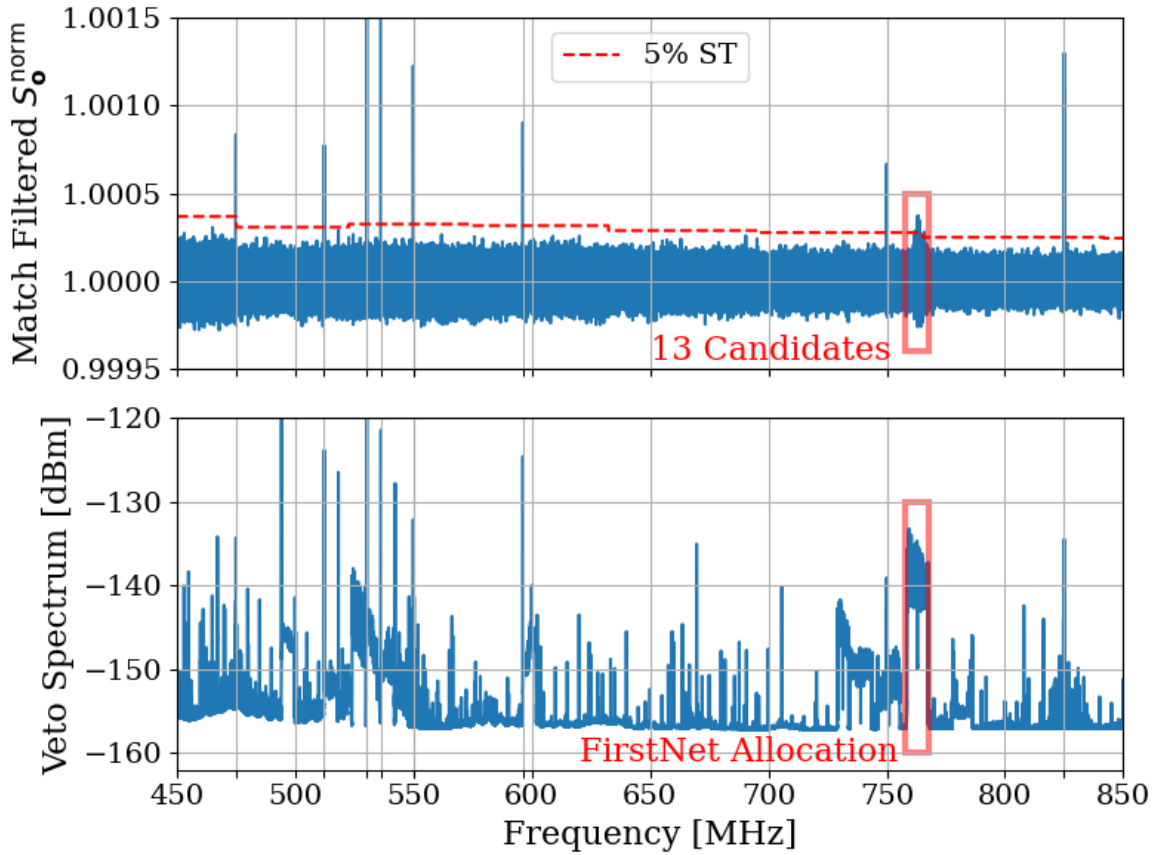


Figure 6.5: 9-day averaged veto spectrum and Run 1B  $S_0^{\text{norm}}$  after it has been passed through a matched filter. The 5% significance threshold ST (Sects. 2.2.1 and 4.2.3) is shown as a dashed red line. There are 21 independent candidates, however 13 of them are found in the FirstNet frequency span (758–768 MHz) which is discussed in the text of this subsection. This frequency span is shown in both the veto and experimental spectra with a red box. The remaining 8 candidates have ticks added to the x-axis to guide the eye between candidates in the upper panel and RFI in the lower panel. The vertical scale has been set such that the tops of some of the signals are cut off.

## 2149 6.2 Mixer System: Run 2

2150 Run 1 relied on an ADC with a sample rate of up to 2.5 GHz, allowing for direct RF sampling  
2151 of Run 1A/B. This system is a flexible platform, allowing for future upgrades to extend its  
2152 maximum frequency through the use of a mixer system which is described in this chapter.

### 2153 6.2.1 Frequency mixing

2154 Frequency mixing is a technique in RF and microwave systems used to shift the frequency  
2155 of a signal to another frequency range which is more useful for a given task. For example,  
2156 electronics are simpler at kHz frequencies, but antennas operate at MHz. After processing a  
2157 kHz signal for transmission, it can be mixed up to MHz for transmission over the air. Once  
2158 it is received, it can be mixed back down to kHz. Mixer engineering is a rather complex  
2159 topic, and many details will be omitted here. The reader is encouraged to reference the  
2160 Marki Microwave mixer primer [90] for a tutorial on mixers and Ch. 13 Pozar's *Microwave*  
2161 *Engineering* [91] for a more thorough treatment.

2162 In a mixer system, an input signal (RF) is combined with another signal, typically from a  
2163 local oscillator (LO), such that the two frequencies mix, producing an intermediate frequency  
2164 (IF). This RF signal  $\cos(2\pi f_{\text{signal}}t)$  is multiplied by a local oscillator signal  $\cos(2\pi f_{\text{LO}}t)$ <sup>3</sup>.  
2165 Using the trigonometric identity

---

<sup>3</sup>The multiplication of CW signals outlined here is a simplification. In reality, the LO should have higher harmonics and approximate a square wave to overcome the transition region of the voltage-current curve of a real diode. See the Marki Microwave mixer primer for more details [90].

$$\cos(A)\cos(B) = \frac{1}{2}(\cos(A+B) + \cos(A-B)), \quad (6.1)$$

2166 it can be seen that this multiplication produces two new components: one at the sum  
2167 frequency  $f_{\text{signal}} + f_{\text{LO}}$  and one at the difference frequency  $|f_{\text{signal}} - f_{\text{LO}}|$ .

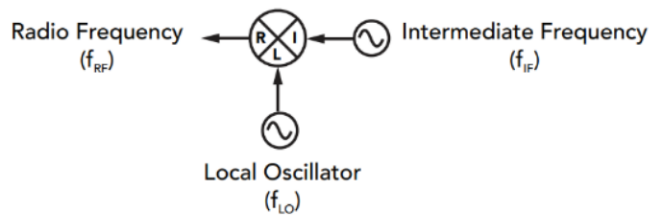
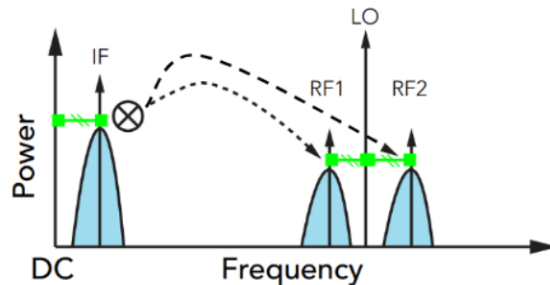
2168 A mixer is a 3-port device that has two inputs and one output. The LO port is almost  
2169 always an input, while the RF and IF ports can be used as either an input or an output  
2170 (as long as they are opposite)<sup>4</sup>. Such a system can be used for upconversion (where the RF  
2171 is shifted to a higher frequency) or downconversion, as shown in Fig. 6.6. The remainder  
2172 of this subsection will focus on downconversion, but both downconversion and upconversion  
2173 are important in the system that is presented later in this section.

---

<sup>4</sup>Again, this is simplified. All three ports actually behave as a load and a source. See the first footnote of the Marki Microwave mixer primer [90].

## UPCONVERSION

$$f_{RF1} = f_{LO} - f_{IF} \quad f_{RF2} = f_{LO} + f_{IF}$$



## DOWNCONVERSION

$$f_{IF} = |f_{LO} - f_{RF}|$$

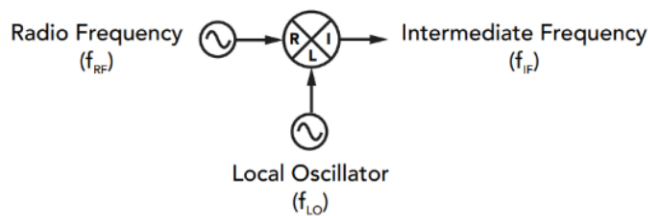
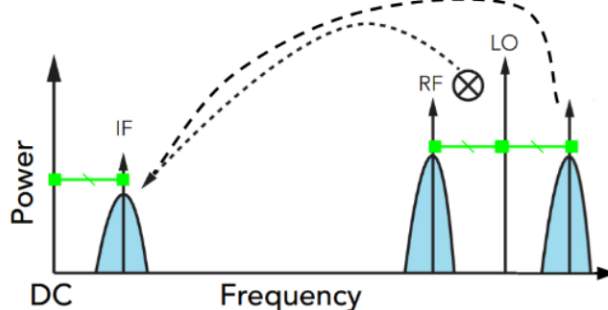


Figure 6.6: Overview of basic mixer operation in both upconversion and downconversion mode. The green lines with hash marks represent the IF frequency. Image modified from Marki Microwave's mixer primer [90].

2174 6.2.1.1 The superheterodyne receiver

2175 The presence of both a sum and difference frequency in Eq. 6.1 creates a challenge when  
2176 employing mixers. A mixer performing downconversion will present the sum of both the  
2177 sum-frequency and difference-frequency at its IF port. Usually one of these signals will be  
2178 desirable and will not. The latter is known as an image. This situation is shown in frequency  
2179 space in Fig. 6.7.

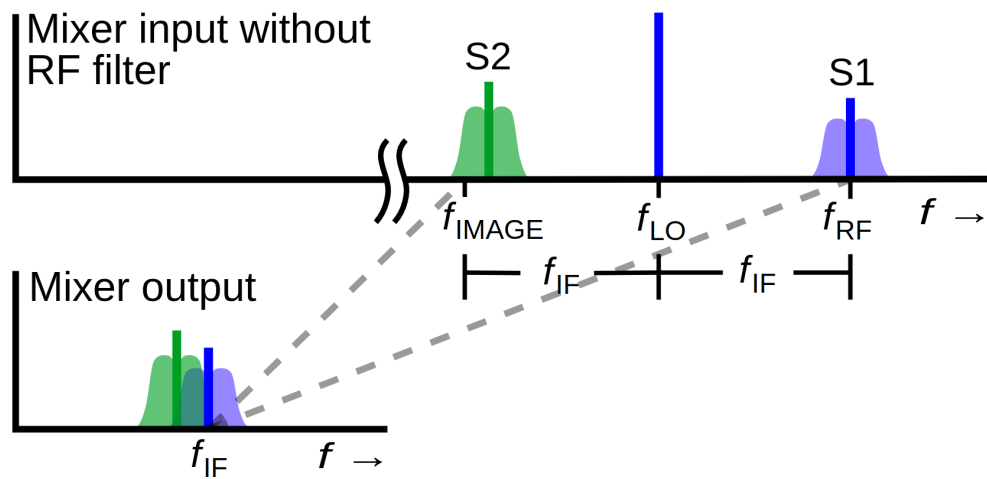


Figure 6.7: Illustration of the problem of images in frequency mixing. Both  $S_1$  and  $S_2$  are overlapping at the mixer's output as predicted by Eq. 6.1. The image must be filtered before mixing to avoid this problem. Image from Wikipedia[92]

2180 Note that the situation when the signal above the LO is desired, and the signal below the  
2181 LO is the image is known as low-side injection downconversion. To rephrase the previous  
2182 sentence,

Low-Side Injection:  $f_{LO} < f_{RF}$  (desired signal is above the LO)

High-Side Injection:  $f_{LO} > f_{RF}$  (desired signal is below the LO).

2183        The solution to this image problem is to filter the image out of the RF before mixing.  
2184   Furthermore, in a realistic mixer, the LO will bleed through to the IF port and will also  
2185   need to be filtered. These points motivate including both an RF and IF filter in the design  
2186   of a mixer-based receiver system (sometimes known as a superheterodyne receiver). The  
2187   schematic of this type of system is shown in Fig. 6.8. Figure 6.9 shows the result of filtering  
2188   the RF and IF in frequency space; the signal S1 is available for further processing at the  
2189   desired frequency.

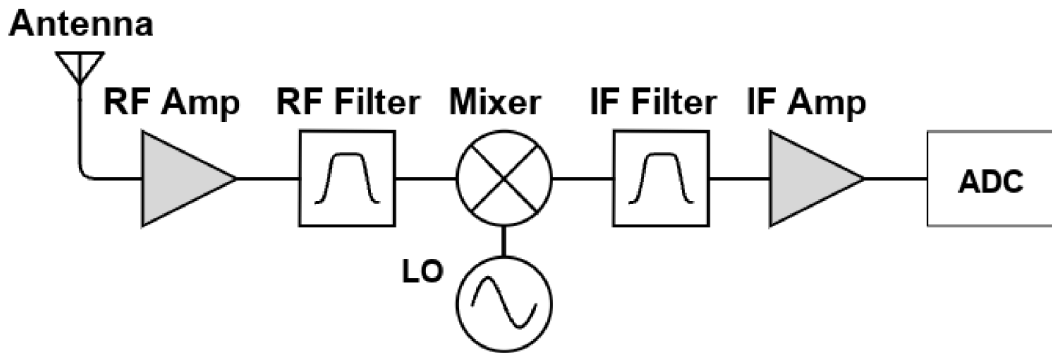


Figure 6.8: Schematic of a basic superheterodyne receiver system. The introduction of the RF filter before the mixer removes the image. The IF filter separates interfering signals that were nearby S1. This is an example of low-side injection down conversion, as described in the text of this subsection. Image from Wikipedia[92]

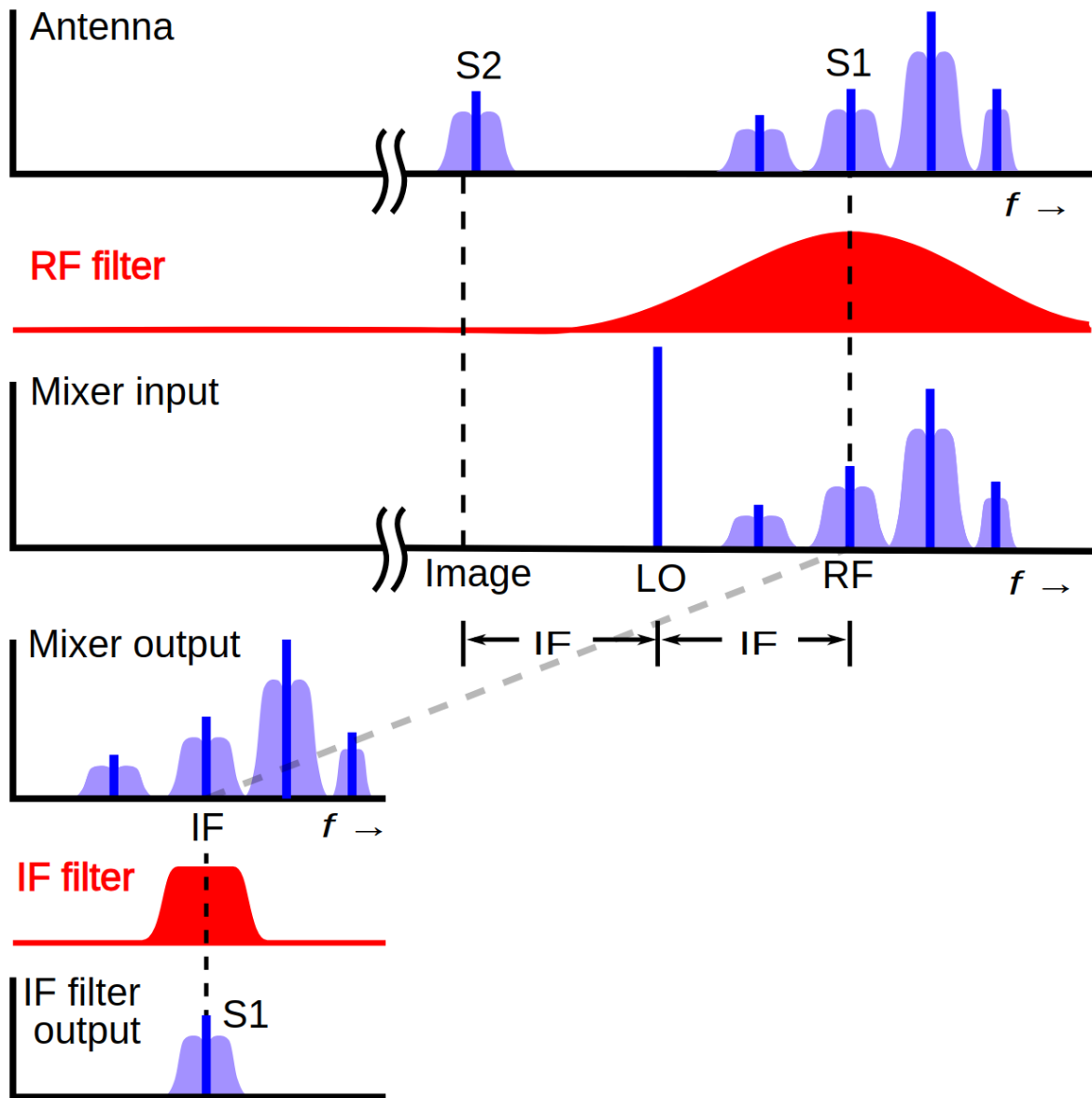


Figure 6.9: Image from Wikipedia[92]

### 2190 6.2.2 A mixer system for DER

2191 The maximum sampling rate of the ADC (2.5 GHz) sets a limit as to how high of frequencies  
 2192 it can scan. Introducing a mixer system between the front end of the experiment (anten-

2193 na/LNA) and the DAQ (ADC/GPU/PC) allows for previously inaccessible frequencies to be  
 2194 mixed down into the so-called *baseband* of the ADC,  $\lesssim 1$  GHz. The block diagram of such a  
 2195 system is shown in Fig. 6.10.

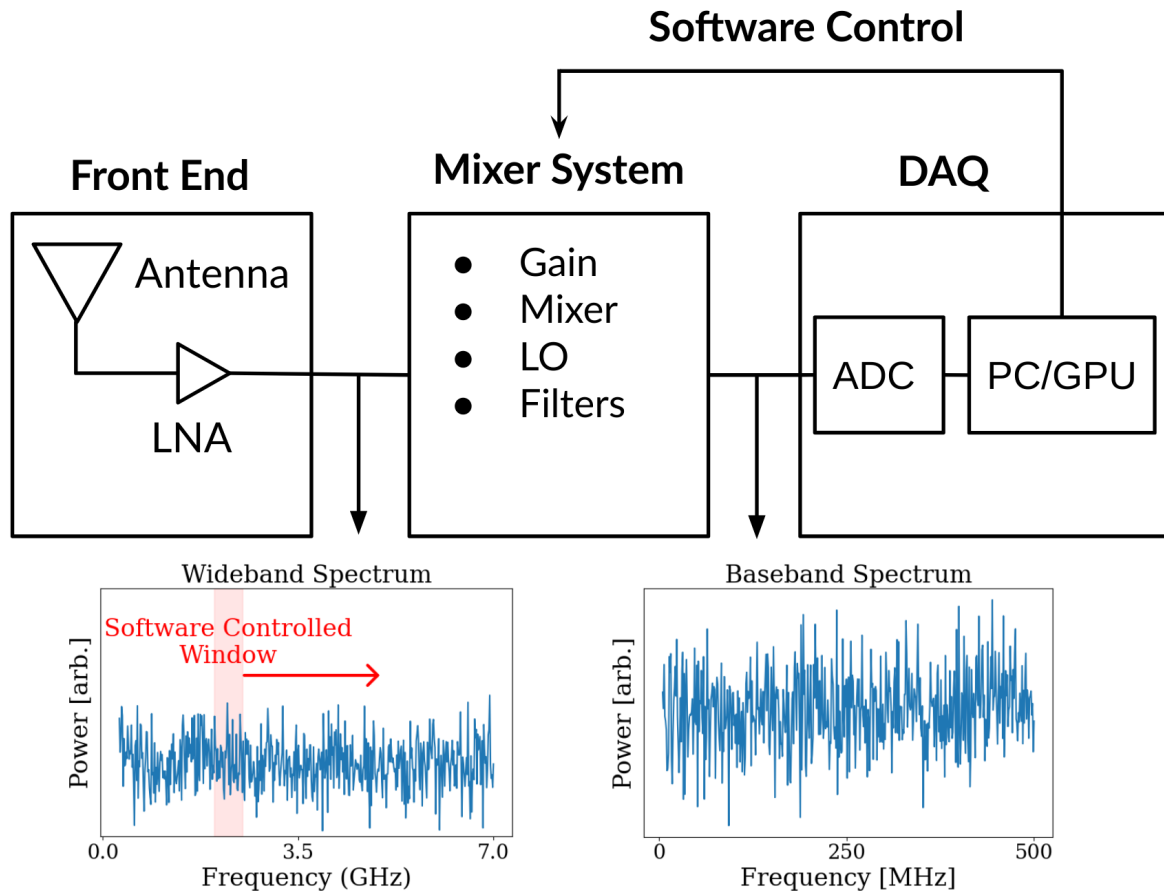


Figure 6.10: Block diagram of the mixer system to be used in Run 2. The PC provides control of the mixer system to sweep the frequency span (shown as a red box on the wideband spectrum) that is mixed down to the baseband and digitized. Frequencies are based on Run 2A, but are nominal and shown only for illustration.

2196 The ability to control the mixer system via software greatly boosts efficiency since it  
 2197 means the experiment can be set up and stepped through a large frequency span (several  
 2198 GHz) without human intervention. The span of a given step will be limited by the hardware

2199 of the front end, e.g. antenna, LNA. The bandwidth of the baseband (1.25 GHz) sets the  
2200 maximum span that may be scanned at each step, though to reduce the data transfer rate,  
2201 a smaller span closer to 500 MHz will likely be used for Run 2.

## 2202 6.3 Possible Future Upgrades

2203 The previous sections in this chapter addressed the progress towards the planned Run 1B  
2204 (Sec. 6.1) and Runs 2A/B (Sec. 6.2). This section gives an outline for experiments beyond  
2205 this. This section will be rather vague compared to the previous sections of this chapter. It  
2206 is not as much a road map as a broad vision for the next steps and potential directions to  
2207 explore based on the findings and challenges encountered in the earlier runs.

2208 Two principles should guide the design of future experiments

2209 1. Cold

2210 2. Resonant

2211 3. Broadband

2212 4. Optimally-coupled

2213 It is likely that pursuing these principles will result in reinventing HAYSTAC or DMRa-  
2214 dio.

2215 The DER experiment operates at room temperature, using a low noise amplifier (LNA).

2216 Compared to cryogenic experiments, this represents an advantage in terms of reduced ex-  
2217 perimental complexity, but it means the dominant background is classical thermal noise

2218 ( $\sim 300$  K, Sec. 2.1.1), followed closely by amplifier noise ( $\sim 100$  K, Sec. 2.1.4). These noises  
2219 add to form the total system temperature  $T_s \approx 400$  K. However, the limit in sensitivity scales  
2220 with  $T_s^{-1/2}$  (at least in the classical regime,  $h\nu << k_b T$ ). For this reason, most haloscope  
2221 experiments choose to forgo experimental simplicity and operate at extremely cold temper-  
2222 atures (100s of mK, sometimes lower). At these temperatures, quantum effects begin to  
2223 dominate the noise budget and simple linear amplifiers must be replaced by read-out tech-  
2224 nologies such as superconducting quantum interference devices (SQUIDs) or single photon  
2225 counting.

## 2226 Appendix A

### 2227 Overview of RTSA code base

2228 A basic overview of the code which are used to acquire and process data are outlined here.

2229 The version control is very simple and each experiment has it's own directory containing  
2230 several key files. The general usage template from which other experiments can be developed  
2231 is in the `teledyneTemplate` directory. The important files, in order of importance, are

2232 • `settings.py`: Settings are controlled from this file. If the DAQ code isn't to be  
2233 modified, this is all the user must interact with in normal usage. While it is a python  
2234 script, it functions more like a text file. Descriptions and notes about allowed values  
2235 are included as comments. Read them carefully, settings can conflict.

2236 • `drDaq*.py`: Main script which calls all the helper functions. To take data, run this  
2237 script after modifying (and saving) `settings.py`. There is usually a suffix indicating  
2238 the date and information about version.

2239 • `avgFftModule.py`: This is modified code from teledyne. It handles all the heavy

2240 lifting: Interfacing with the C++ API, pinning GPU memory, transfer of data from  
2241 PCIE card to the GPU, computation of the FFT on the GPU. This is all wrapped in  
2242 a class called `avgFft`. An instance of this class is called `avgSpec` and is the workhorse  
2243 of `drDaq.py`

2244 • `daqHelpers.py`: Lots of helper functions which are separated here to keep other code  
2245 clean. It is imported as a module in other files. Lots of useful code lives in here,  
2246 including the code that converts time series to power spectra (normalization is non-  
2247 trivial, see Eq. 2.15), writes info to `database.txt`, saves the pre-averaged spectra  
2248 including metadata in an HDF5 file.

2249 • `plotTesting.py`: This uses `dash` to host a web app which allows interactive `plotly`  
2250 graphs for simple visualisation of run data. This is extremely useful as it can tell you  
2251 if amplifiers die. Without this, all data would have to be averaged and more fully  
2252 analyzed, but this is a good light-weight option. There is some creative use of data  
2253 down sampling so it runs quickly while not removing any candidates. An example  
2254 window is shown in Fig. A.1.

2255 • `backup.sh`: Simple shell script which backs up run data to locations of your choosing.  
2256 In the `teledyneTemplate` directory, it is set up to back up to the secondary hard disk  
2257 drive in the DR2 machine, and to peloton, but this can be easily modified. When taking  
2258 real data, this script should not be run at the same time as `drDaq.py`. `backup.sh`  
2259 should be run first, so it completes while the antenna is moved and batteries changed.  
2260 This ensures there is not a heavy load on the hard drive due to back ups while data

2261 acquisition is ongoing. `valonInit.py`: sets up the valon signal generator to work as a  
2262 clock. This should probably be a function inside of `daqHelpers.py`, but there may have  
2263 been a reason I kept it separate.

2264 • `gdrapi.py` Comes from Teledyne. Defines functions for the api. I have not modified  
2265 it at all.

2266 • `helperCupy.py` Comes from Teledyne. Defines functions for the GPU. I have not  
2267 modified it at all.

2268 • `streamingHelpers.py` comes from Teledyne. Defines functions for streaming from  
2269 PCIE card to GPU. I have not modified it at all.

## 2270 A Tips for using the RTSA system

2271 • As of September 2024, you must boot into kernel version 5.15.

2272 • Make sure to run `insmod.sh` in the `teledyneInstall/gdrcopy` directory after restart-  
2273 ing the machine.

2274 – look at `teledyneInstall/installGuide.txt` on how to handle common errors  
2275 involving this process.

2276 • Read through the `settings.txt` file carefully! Some settings will conflict with others,  
2277 but they are mostly noted. There are also some notes about possible upgrades which  
2278 could be made, some of which without much effort.

2279 **B Data structure and processing**

2280 Figure 2.45 shows the handling of data as it comes in as an RF time series and is converted  
2281 to pre-averaged spectra. While significantly less cumbersome than the raw data, processing  
2282 these spectra still represents a challenge. This subsection outlines how I have attempted to  
2283 handle it. While it is a little convoluted, this is the third iteration of how to handle this  
2284 data processing and is likely simpler than it seems on first blush. In other words, there is  
2285 probably a better way to do this, but don't knock it til you try it.

2286 **B.1 Writing data**

2287 Once a pre-averaged spectrum is computed by dividing the running sum by `NOF_BUFFERS_TO_RECEIVE`,  
2288 this can be written to an HDF5 file. Whether or not it is, can be controlled by the `SAVE_H5`  
2289 boolean variable<sup>1</sup>. Each pre-averaged spectrum is uniquely specified by `ACQ_NUM` in a given  
2290 data run. In order to simplify backups and avoid placing all our eggs in one HDF5 basket,  
2291 `NUM_SPEC_PER_FILE`<sup>2</sup> pre-averaged spectra are saved into a single HDF5 file, before starting  
2292 a new file. These files are simply named as a zero-indexed number followed by their `.hdf5`  
2293 extension. These files are saved in `SAVE_DIRECTORY`<sup>3</sup>. I usually make this save directory in  
2294 a secondary SSD named `drBiggerBoy` in order to preserve the main drive. I think the stress

---

<sup>1</sup>This variable exists because when testing things or taking miscellaneous measurements, you will frequently want to acquire a single spectrum without engaging the complex machinery of the HDF5 saving procedure.

<sup>2</sup>I have kept this around 16 and not experimented much outside of this range, but it's probably fine. This keeps the files around 1 GB. For run 1.4, this is about 45 minutes of antenna data and 3 minutes of terminator data per file, so if a file is corrupted it's not a big deal. I have never had a problem, this is paranoia inherited from Ben.

<sup>3</sup>A reminder that this is specified, like all other variables, in `settings.py`. Note you must create this directory ahead of time and include a sub-directory called `data`. It says this in the comments of `settings.py` which you are reading, right?

2295 of continuous reads and writes will probably kill this drive, so I prefer to keep it separate  
2296 from the main boot drive, drBigBoy.

2297 When `SAVE_H5 == 1`, a `database.txt` file is created in `SAVE_DIRECTORY`, shown in Table  
2298 A.1.

Attribute	Pre-averaged spectrum 0	Pre-averaged spectrum 1
ACQ_NUM	0	1
DATETIME	2023-05-10 11:32:48.365	2023-05-10 11:35:49.193
SWITCH POS	0	1
ANT POS IDX	0	0
TEMP	295.64	295.54
LEN FFT LOG2	24	24
SAMPLE RATE MHZ	800.0	800.0
NOF BUFFERS	8600	8600
AMP1	1012_E_PbAcid	1012_E_PbAcid
AMP2	ZKL_9p05VReg	ZKL_9p05VReg
LPF	HSP50+	HSP50+
HPF	288S+	288S+
ATTENUATOR	4dB_FIXED	4dB_FIXED
ADC	ADQ32	ADQ32
CLOCK	SRS_VIA_VALON	SRS_VIA_VALON
File Number	0	0

Table A.1: Example database file from run 1.4. In this run, `ACQ_NUM` counts up to 4175, and these spectra are saved between 261 HDF5 files. Some of the values are auto-generated (`temp`, `DATETIME`, etc.) while others are manually entered into `settings.txt` (`AMP1`, `LPF`, etc.) Note that this table has been transposed in order to fit on the page.

2299 When setting up a data run, you must test that the data are saved how you expect. I have  
2300 had success by reducing `NOF_BUFFERS_TO_RECEIVE` to a small number<sup>4</sup>, and taking a simu-  
2301 lated data run. The process of switching is hacked together and can give you unpredictable

<sup>4</sup>`NOF_BUFFERS_TO_RECEIVE` times the time per buffer must be larger than around 2 seconds or it will crash

2302 results. Did I mention to read the comments in `settings.py`?

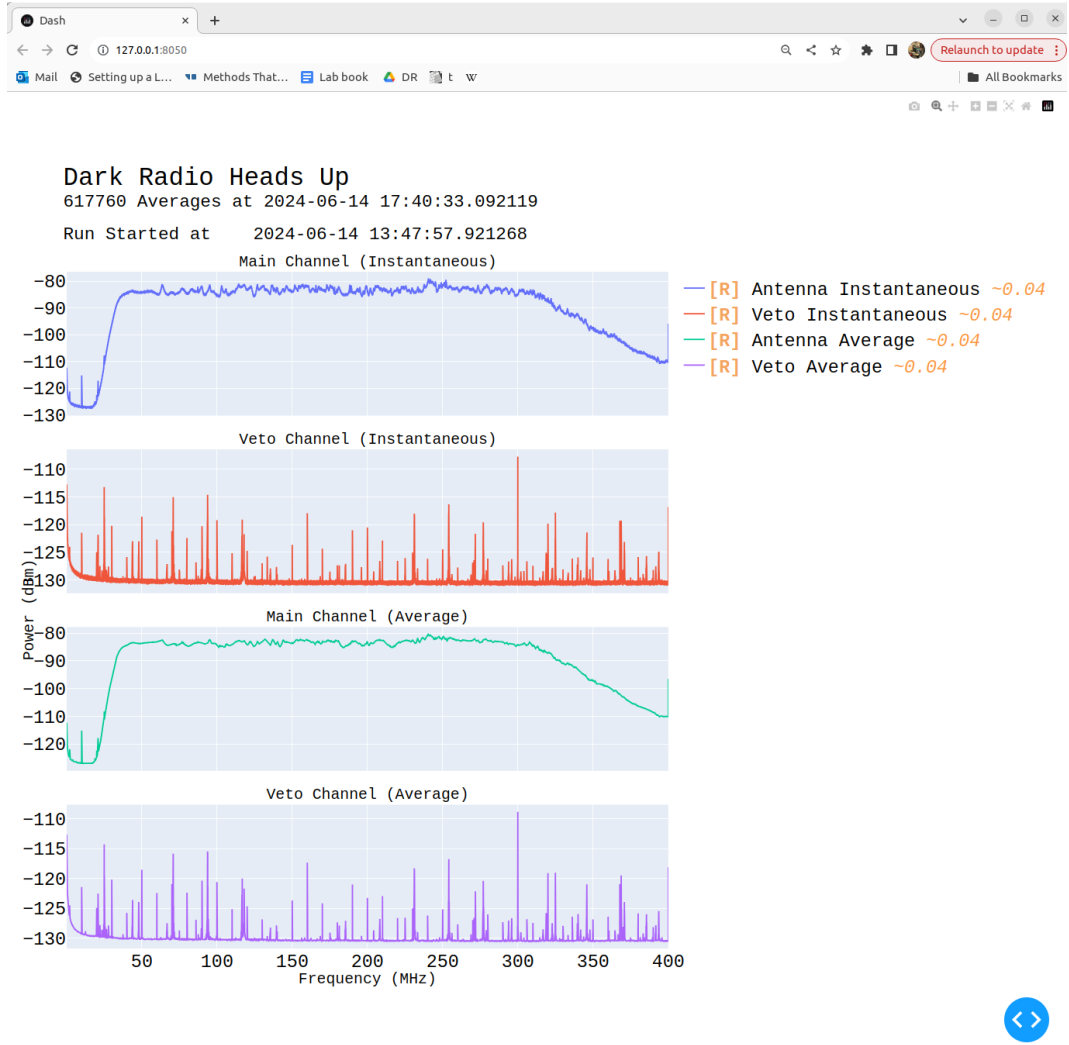


Figure A.1: Real time heads up window for data acquisition. Built with Plotly and Dash, and displays in web browser, in this case Google Chrome. Spectra contain  $2^{23}$  frequency bins, so are down-sampled so as to display  $10^4$  bins at any given level of zoom. This allows for interaction with the plot in real time with very little lag. The resolution currently displayed (in MHz) is shown in yellow next to the legend (right of first plot). This down-sampling is "smart" in that it will show any excursions, and is implemented with the `plotlyResampler` package in `MinMaxAggregator` mode. Mousing over a curve causes a "Tooltip" to appear, indicating the frequency and power at that point in the curve. The frequency axes are all linked, so zooming on one plot will cause all plots to display the same frequency range. Icons on upper right allow for navigation of plot. Frustratingly there is no back button, so be careful when zooming on a very narrow feature; a wrong move means you have to go all the way back out and start over.

2303 **B.2 Reading and averaging data**<sup>5</sup>

2304 After taking a data run, you should have a `SAVE_DIRECTORY` containing a directory full of  
2305 many HDF5 files and a `database.txt` file (and possibly a directory of plotting spectra if  
2306 that is chosen in `settings.txt`. The basic idea is to “pre-process” the HDF5 files into a  
2307 single, large HDF5 file which can be more quickly accessed to compute a single, averaged  
2308  $S_o$  spectrum for further analysis (see next chapter). The `database.txt` file is loaded into  
2309 python as a pandas dataframe in order to find specific spectra in this large data structure.

2310 I tried (for a while) to keep the files separate to allow for multi-processing to speed up  
2311 the averaging, but I ran into issues. The most serious issue is that all the files live on the  
2312 same drive, so you can’t get much of a speed up since the drive is read-limited to around  
2313 500 MB/s. I found multiprocessing is more effort than it’s worth. It takes about 20 minutes  
2314 to pre-average run 1.4 (9 days of data, 3 minute pre-averages yields 4175 spectra which take  
2315 about 280 GB), and you only have to do this once after a run.

2316 Following the example of `run1p4_packAvgAllAnalysis.ipynb`, the first step is to load  
2317 `database.txt` as a pandas dataframe which can be used to index the pre-processed file.  
2318 Next, a list of which `ACQ_NUMs` correspond to an antenna and terminator must be computed,  
2319 after removing any which are known to be contaminated<sup>6</sup>. The list of indices which are  
2320 to be averaged together is called either `antIdx` or `termIdx`. Note that you can devise any  
2321 number of ways to generate these lists, or even hard code them. The code given is just an

---

<sup>5</sup>Code for this section can be found at: [https://github.com/josephmlev/darkRadio/tree/master/daqAnalysisAndExperiments/run1p4/run1p4\\_analysis/run1p4\\_packAvgAllAnalysis.ipynb](https://github.com/josephmlev/darkRadio/tree/master/daqAnalysisAndExperiments/run1p4/run1p4_analysis/run1p4_packAvgAllAnalysis.ipynb)

<sup>6</sup>In run 1.4, the first antenna and terminator spectra are thrown out, since the computer monitor was on to verify the run started successfully. This was out of paranoia and probably didn’t do anything.

2322 example.

2323 Next, info in the dataframe (no power spectra data yet) are analyzed as a sanity check.

2324 These are not super important but a good check.

2325 The cell beginning with the comment `#pack pre proc dataset` is where the heavy lifting

2326 happens. A large HDF5 file is initialized. It contains two datasets, one for each channel

2327 (main experiment and veto in run 1.4). Note that in this example, it is hard coded to expect

2328 8388609 frequency bins ( $2^{23} + 1$ ), and this must be changed if doing something other than a

2329  $2^{24}$ -point FFT. The HDF5 sub-files are iterated over, their data is read, and written into the

2330 pre-processed HDF5 file. Make sure not to remove the error handling for closing the HDF5

2331 file, or you will corrupt it and have to rerun the pre-processing.

2332 Now that the pre-processed HDF5 file has been packed with data and a list of indices

2333 to be averaged has been generated, averaging is trivial (though still takes a few minutes, so

2334 maybe test it with a sub set of `antIdx`. The code is provided below:

```
2335
23361 def avgSpecFromPacked(avgIdxs, specStr):
23372     sum = np.zeros(2**23+1)
23383     for i in avgIdxs:
23394         sum += f[specStr][:,i]
23405     avgSpec = sum/(len(avgIdxs))
23416     return avgSpec
2342
```

Listing A.1: Python function for averaging spectra from pre-processed data

2343 Note that this assumes a single HDF5 file, `f`, is in scope. `specStr` is a string which

2344 specifies which channel to average, for example `spec_W_chA`.

2345        The output of this function is  $S_o$  which can be passed to following functions for further  
2346        analysis.

# <sup>2347</sup> Bibliography

- 2348 [1] Fritz Zwicky. “The Redshift of Extragalactic Nebulae”. In: (1933).
- 2349 [2] Vera C. Rubin and Jr. Ford W. Kent. “Rotation of the Andromeda Nebula from a  
2350 Spectroscopic Survey of Emission Regions”. In: (1970).
- 2351 [3] Marco Battaglieri *et al.* *US Cosmic Visions: New Ideas in Dark Matter 2017: Com-*  
2352 *munity Report*. 2017. DOI: 10.48550/ARXIV.1707.04591. URL: <https://arxiv.org/abs/1707.04591>.
- 2353
- 2354 [4] Benjamin Godfrey et al. “Search for dark photon dark matter: Dark  $E$  field radio pilot  
2355 experiment”. In: *Phys. Rev. D* 104 (1 July 2021), p. 012013. DOI: 10.1103/PhysRevD.  
2356 104.012013. URL: <https://link.aps.org/doi/10.1103/PhysRevD.104.012013>.
- 2357 [5] E. E. Barnard and A. C. Ranyard. “Structure of the Milky Way”. In: *Knowledge: An*  
2358 *Illustrated Magazine of Science* 17 (Nov. 1894), p. 253.
- 2359 [6] Kelvin, William Thomson, Baron. *Baltimore Lectures on Molecular Dynamics and the*  
2360 *Wave Theory of Light*. English. Collection: University of California Libraries. London,  
2361 Baltimore: C. J. Clay and sons; Publication agency of the Johns Hopkins University,  
2362 1904, pp. xxi, 703. URL: <https://archive.org/details/baltimorelecture00kelvrich>.

- 2363 [7] Richard H. Maurer. “The Idea Man”. In: *SLAC Beam Line* 31.1 (2001). Accessed:  
2364 2024-06-23. URL: <https://www.slac.stanford.edu/pubs/beamline/31/1/31-1-maurer.pdf>.
- 2365
- 2366 [8] Anthony Tyson. “Mapping Dark Matter with Gravitational Lenses”. In: *Physics Today*  
2367 45.6 (June 1992), pp. 24–32. ISSN: 0031-9228. DOI: 10.1063/1.881309. eprint: <https://pubs.aip.org/physicstoday/article/45/6/24/407200/Mapping-Dark-Matter-with-Gravitational-LensesMost>. URL: <https://doi.org/10.1063/1.881309>.
- 2368
- 2369
- 2370
- 2371 [9] R. Clausius. “XVI. On a mechanical theorem applicable to heat”. In: *The London, Edinburgh, and Dublin Philosophical Magazine and Journal of Science* 40.265 (1870),  
2372 pp. 122–127. DOI: 10.1080/14786447008640370. eprint: <https://doi.org/10.1080/14786447008640370>. URL: <https://doi.org/10.1080/14786447008640370>.
- 2373
- 2374
- 2375 [10] Herbert Goldstein, Charles P. Poole, and John L. Safko. *Classical Mechanics*. 3rd. San  
2376 Francisco: Addison-Wesley, 2002. ISBN: 9780201657029.
- 2377
- 2378 [11] A. S. Eddington. “The Kinetic Energy of a Star Clusters”. In: *Monthly Notices of the Royal Astronomical Society* 76.6 (Apr. 1916), pp. 525–528. ISSN: 0035-8711. DOI:  
2379 10.1093/mnras/76.6.525. eprint: <https://academic.oup.com/mnras/article-pdf/76/6/525/18494199/mnras76-0525.pdf>. URL: <https://doi.org/10.1093/mnras/76.6.525>.
- 2380
- 2381
- 2382 [12] Gianfranco Bertone and Dan Hooper. “History of dark matter”. In: *Reviews of Modern Physics* 90.4 (2018), p. 045002.
- 2383

- 2384 [13] F. D. Kahn and L. Woltjer. “Intergalactic Matter and the Galaxy.” In: *American*  
2385 *Journal of Physics* 130 (Nov. 1959), p. 705. DOI: 10.1086/146762.
- 2386 [14] Hugo van Woerden and Richard G. Strom. “The beginnings of radio astronomy in  
2387 the Netherlands”. In: *Journal of Astronomical History and Heritage* 9.1 (June 2006),  
2388 pp. 3–20.
- 2389 [15] J.I. Read. “The Local Dark Matter Density”. In: *J. Phys.* G41 (2014), p. 063101. URL:  
2390 <https://arxiv.org/abs/1404.1938>.
- 2391 [16] S Sivertsson et al. “Estimating the local dark matter density in a non-axisymmetric  
2392 wobbling disc”. In: *Monthly Notices of the Royal Astronomical Society* 511.2 (Apr.  
2393 2022), pp. 1977–1991. ISSN: 0035-8711. DOI: 10.1093/mnras/stac094.
- 2394 [17] Sung Hak Lim et al. *Mapping Dark Matter in the Milky Way using Normalizing Flows*  
2395 and *Gaia DR3*. 2023. arXiv: 2305.13358 [astro-ph.GA]. URL: <https://arxiv.org/abs/2305.13358>.
- 2397 [18] Virginia Trimble. “History of Dark Matter in Galaxies”. In: *Planets, Stars and Stel-*  
2398 *lar Systems: Volume 5: Galactic Structure*. Ed. by Gerard Gilmore. New York, NY:  
2399 Springer, 2013, pp. 1093–1116.
- 2400 [19] V. Radeka. “Signal, Noise and Resolution in Position-Sensitive Detectors”. In: *IEEE*  
2401 *Transactions on Nuclear Science* 21.1 (1974), pp. 51–64. DOI: 10.1109/TNS.1974.  
2402 4327444.

- 2403 [20] B. M. Brubaker et al. “HAYSTAC axion search analysis procedure”. In: *Physical Re-*  
2404 *view D* 96.12 (Dec. 2017). DOI: 10.1103/physrevd.96.123008. URL: <https://doi.org/10.1103%2Fphysrevd.96.123008>.
- 2405
- 2406 [21] C. Boutan et al. *Axion Dark Matter eXperiment: Run 1A Analysis Details*. 2023. arXiv:  
2407 2312.16668.
- 2408 [22] Maximiliano Silva-Feaver et al. “Design Overview of DM Radio Pathfinder Experi-  
2409 *ment*”. In: *IEEE Transactions on Applied Superconductivity* 27.4, 2631425 (June 2017),  
2410 p. 2631425. DOI: 10.1109/TASC.2016.2631425.
- 2411 [23] David Hill. “Plane Wave Integral Representation for Fields in Reverberation Cham-  
2412 bers”. en. In: 40 (1998-08-01 00:08:00 1998).
- 2413 [24] W. L. Stutzman and G. A. Thiele. *Antenna Theory and Design*. John Wiley Sons,  
2414 1998.
- 2415 [25] J.D. Kraus. *Antennas*. McGraw-Hill, 1950. ISBN: 07-035410-3.
- 2416 [26] H. Nyquist. “Thermal Agitation of Electric Charge in Conductors”. In: *Phys. Rev.* 32  
2417 (1 July 1928), pp. 110–113. DOI: 10.1103/PhysRev.32.110. URL: <https://link.aps.org/doi/10.1103/PhysRev.32.110>.
- 2418
- 2419 [27] J. B. Johnson. “Thermal Agitation of Electricity in Conductors”. In: *Phys. Rev.* 32 (1  
2420 July 1928), pp. 97–109. DOI: 10.1103/PhysRev.32.97. URL: <https://link.aps.org/doi/10.1103/PhysRev.32.97>.
- 2421

- 2422 [28] Robert H Dicke. “The measurement of thermal radiation at microwave frequencies”.  
2423 In: *Review of Scientific Instruments* 17.7 (1946), pp. 268–275.
- 2424 [29] Albert Einstein. “Über die von der molekularkinetischen Theorie der Wärme geforderte  
2425 Bewegung von in ruhenden Flüssigkeiten suspendierten Teilchen”. In: *Annalen der  
2426 Physik* 322.8 (1905), pp. 549–560.
- 2427 [30] Herbert B. Callen and Theodore A. Welton. “Irreversibility and Generalized Noise”.  
2428 In: *Phys. Rev.* 83 (1 July 1951), pp. 34–40. DOI: 10.1103/PhysRev.83.34. URL:  
2429 <https://link.aps.org/doi/10.1103/PhysRev.83.34>.
- 2430 [31] C. L. Mehta. “Coherence-time and effective bandwidth of blackbody radiation”. In:  
2431 *Il Nuovo Cimento (1955-1965)* 28.2 (1963), pp. 401–408. DOI: 10.1007/BF02828589.  
2432 URL: <https://doi.org/10.1007/BF02828589>.
- 2433 [32] Raphael Cervantes et al. *Deepest Sensitivity to Wavelike Dark Photon Dark Matter  
2434 with SRF Cavities*. 2022. arXiv: 2208.03183 [hep-ex].
- 2435 [33] Alexander V. Gramolin et al. “Spectral signatures of axionlike dark matter”. In: *Physi-  
2436 cal Review D* 105.3 (Feb. 2022). ISSN: 2470-0029. DOI: 10.1103/physrevd.105.035029.  
2437 URL: <http://dx.doi.org/10.1103/PhysRevD.105.035029>.
- 2438 [34] Michael S. Turner. “Periodic signatures for the detection of cosmic axions”. In: *Phys.  
2439 Rev. D* 42 (10 Nov. 1990), pp. 3572–3575. DOI: 10.1103/PhysRevD.42.3572. URL:  
2440 <https://link.aps.org/doi/10.1103/PhysRevD.42.3572>.
- 2441 [35] Greg Durgin. *Lecture on Noise Figure*. Accessed: 2024-06-23. 2017. URL: [https://www.youtube.com/watch?v=M\\_SRUF4TQgA](https://www.youtube.com/watch?v=M_SRUF4TQgA).

- 2443 [36] Pasternack Enterprises. *PE15A1012: 1 Watt Amplifier Operating From 0.01 GHz to*  
2444 *6 GHz*. Accessed: 2024-05-17. 2024. URL: <https://www.pasternack.com/images/ProductPDF/PE15A1012.pdf>.
- 2445
- 2446 [37] SP Devices. *ADQ32 Datasheet*. Accessed: 2024-06-23. 2024. URL: [https://www.spdevices.com/en-us/Products\\_/Documents/ADQ32/20-2378%20ADQ32%20datasheet.pdf](https://www.spdevices.com/en-us/Products_/Documents/ADQ32/20-2378%20ADQ32%20datasheet.pdf).
- 2447
- 2448
- 2449 [38] Benjamin Godfrey. “A Novel Search for Dark Photons”. Ph.D. dissertation. UC Davis,  
2450 2022. URL: <https://escholarship.org/uc/item/72b776v4>.
- 2451 [39] Joseph Levine et al. *New Limit on Dark Photon Kinetic Mixing in the 0.2-1.2 μeV*  
2452 *Mass Range From the Dark E-Field Radio Experiment*. 2024. arXiv: 2405.20444  
2453 [hep-ex]. URL: <https://arxiv.org/abs/2405.20444>.
- 2454 [40] L.A. Wainstein and V.D. Zubakov. *Extraction of Signals from Noise*. Englewood Cliffs,  
2455 NJ: Prentice-Hall, 1962. ISBN: 9780132981330.
- 2456 [41] Andy Marvin and Simon Jonathan Bale. “Thermal Noise Measurements in a Rever-  
2457 beration Chamber”. English. In: *IEEE Transactions on Electromagnetic Compatibility*  
2458 64.3 (June 2022). © 2022 IEEE. This is an author-produced version of the published  
2459 paper. Uploaded in accordance with the publisher’s self-archiving policy. Further copy-  
2460 ing may not be permitted; contact the publisher for details, pp. 893–896. ISSN: 0018-  
2461 9375. DOI: [10.1109/TEMC.2022.3142937](https://doi.org/10.1109/TEMC.2022.3142937).
- 2462 [42] F. Reif. *Fundamentals of Statistical and Thermal Physics*. Long Grove, IL: Waveland  
2463 Press, 2009. ISBN: 9781577666127.

- 2464 [43] R. H. Dicke. “A Computational Method Applicable to Microwave Networks”. In: *Jour-*  
2465 *nal of Applied Physics* 18.10 (Oct. 1947), pp. 873–878. ISSN: 0021-8979. DOI: 10.1063/  
2466 1.1697561. eprint: <https://pubs.aip.org/aip/jap/article-pdf/18/10/873/18307533/873\1\online.pdf>. URL: <https://doi.org/10.1063/1.1697561>.
- 2467
- 2468 [44] Hewlett-Packard. *S-Parameter Design*. Application Note 154. 1990. URL: [https://www.hpmemoryproject.org/an/pdf/an\\_154.pdf](https://www.hpmemoryproject.org/an/pdf/an_154.pdf).
- 2469
- 2470 [45] NoiseWave. *NoiseWave FAQ Document*. Accessed: 2024-06-23. 2024. URL: <https://noisewave.com/faq.pdf>.
- 2471
- 2472 [46] Whitham D. Reeve. *Noise Tutorial Part III: Attenuator and Amplifier Noise*. Revision  
2473 0.1, Updated: July 7, 2014. Reeve Engineers. 2014. URL: [https://www.reeve.com/Documents/Noise/Reeve\\_Noise\\_3\\_AttenAmpNoise.pdf](https://www.reeve.com/Documents/Noise/Reeve_Noise_3_AttenAmpNoise.pdf).
- 2474
- 2475 [47] S. Al Kenany et al. “Design and operational experience of a microwave cavity axion  
2476 detector for the 20-100  $\mu$ eV range”. In: *Nuclear Instruments and Methods in Physics*  
2477 *Research Section A: Accelerators, Spectrometers, Detectors and Associated Equipment*  
2478 854 (May 2017), pp. 11–24. ISSN: 0168-9002. DOI: 10.1016/j.nima.2017.02.012.  
2479 URL: <http://dx.doi.org/10.1016/j.nima.2017.02.012>.
- 2480 [48] Raphael Cervantes et al. *Deepest Sensitivity to Wavelike Dark Photon Dark Matter*  
2481 *with SRF Cavities*. 2022. arXiv: 2208.03183 [hep-ex].
- 2482 [49] Maurio B. Grando, Christian R. Boutan, and Jihee Yang. *A Multiport Approach to*  
2483 *Thermal Noise and Scattering Parameter Simulation of Cryogenic Experiments*. 2022.  
2484 arXiv: 2209.04008 [physics.ins-det]. URL: <https://arxiv.org/abs/2209.04008>.

- 2485 [50] G.H. Bryant. *Principles of Microwave Measurements*. London, United Kingdom: Pe-  
2486 ter Peregrinus Ltd., on behalf of the Institution of Electrical Engineers, 1993. ISBN:  
2487 0863412963.
- 2488 [51] David A. Hill. “Wall Losses and Cavity Q”. In: *Electromagnetic fields in cavities: De-*  
2489 *terministic and statistical theories*. John Wiley & Sons Inc., 2009, pp. 31–33.
- 2490 [52] R.H. Price, H.T. Davis, and E.P. Wenaas. “Determination of the statistical distribution  
2491 of electromagnetic-field amplitudes in complex cavities”. In: *Physical Review E* 48  
2492 (1993), pp. 4716–4729. DOI: 10.1103/PhysRevE.48.4716.
- 2493 [53] John David Jackson. *Classical Electrodynamics*. 3rd. New York: Wiley, 1998. ISBN:  
2494 9780471309321.
- 2495 [54] Bing-Hope Liu, David C. Chang, and Mark T. Ma. *Eigenmodes and the Composite Q*  
2496 *Factor of a Reverberating Chamber*. Tech. rep. Aug. 1983.
- 2497 [55] *Series 83 RF Shielded Enclosure*. Lindgren R.F. Enclosures, Inc. 2021. URL: <https://www.ets-lindgren.com/datasheet/shielding/rf-shielding-and-accessories/11003/1100307>.
- 2500 [56] David A. Hill. *Electromagnetic Theory of Reverberation Chambers*. Technical Note  
2501 1506. Gaithersburg, MD: National Institute of Standards and Technology, 1998. URL:  
2502 [https://tsapps.nist.gov/publication/get\\_pdf.cfm?pub\\_id=24427](https://tsapps.nist.gov/publication/get_pdf.cfm?pub_id=24427).
- 2503 [57] D.A. Hill. “A reflection coefficient derivation for the Q of a reverberation chamber”. In:  
2504 *IEEE Transactions on Electromagnetic Compatibility* 38.4 (1996), pp. 591–592. DOI:  
2505 10.1109/15.544314.

- 2506 [58] Lawrence Krauss et al. “Calculations for cosmic axion detection”. In: *Physical Review*  
2507 *Letters* 55.17 (1985), pp. 1797–1800. DOI: 10.1103/PhysRevLett.55.1797. URL:  
2508 <https://doi.org/10.1103/PhysRevLett.55.1797>.
- 2509 [59] *Biconical Antenna AB-900A*. Rev. D05.19. Com-Power Corporation. May 2019. URL:  
2510 <https://documentation.com-power.com/pdf/AB-900A-1.pdf>.
- 2511 [60] *COMSOL Multiphysics*. 5.4. Available at <https://www.comsol.com/>. COMSOL, Inc.  
2512 One First Street, Suite 4 Los Altos, CA 94022.
- 2513 [61] Zhong Chen and Michael D. Foegelle. “A numeric investigation of ground plane effects  
2514 on biconical antenna factor”. In: *Electromagnetic Compatibility, 1998. 1998 IEEE In-*  
2515 *ternational Symposium on*. Vol. 2. IEEE. IEEE, 1998, pp. 802–806. DOI: 10.1109/  
2516 ISEMC.1998.750302. URL: <https://ieeexplore.ieee.org/document/750302>.
- 2517 [62] John D. Kraus. *Antennas*. 2nd. New York: McGraw-Hill, 1988, p. 892. ISBN: 9780070354227.
- 2518 [63] Mini-Circuits. *ZKL-1R5: 50 Ω Gain Block Amplifier*. Accessed: 2024-06-23. 2024. URL:  
2519 <https://www.minicircuits.com/pdfs/ZKL-1R5.pdf>.
- 2520 [64] Texas Instruments. *LM317: 3-Terminal Adjustable Regulator*. Accessed: 2024-06-23.  
2521 2024. URL: <https://www.ti.com/lit/ds/symlink/lm317.pdf?ts=1720749307506>.
- 2522 [65] Alan V. Oppenheim, Alan S. Willsky, and S. Hamid Nawab. *Signals and Systems*. 2nd.  
2523 Upper Saddle River, NJ: Prentice Hall, 1996. ISBN: 978-0138147570.
- 2524 [66] Mini-Circuits. *ZX75LP-288-S+: Low Pass Filter*. Accessed: 2024-06-23. 2024. URL:  
2525 <https://www.minicircuits.com/pdfs/ZX75LP-288-S+.pdf>.

- 2526 [67] Mini-Circuits. *SHP-50+: High Pass Filter*. Accessed: 2024-06-23. 2024. URL: <https://www.minicircuits.com/pdfs/SHP-50+.pdf>.
- 2527
- 2528 [68] *Biconical Antenna*. AB-900A. Rev. D. Com-Power Corporation. May 2019.
- 2529 [69] *The Y Factor Technique For Noise Figure Measurements*. 1MA178. Version 5e. Rhode
- 2530 & Schwarz. Oct. 2021.
- 2531 [70] *Noise Figure Measurement Accuracy: The Y-Factor Method*. 1MA178. Version 5e.
- 2532 Keysight Technologies. Oct. 2021.
- 2533 [71] Wikipedia contributors. *Y-factor Sketch*. Accessed: 2024-06-23. 2024. URL: [https://en.wikipedia.org/wiki/Y-factor#/media/File:Y-factor\\_sketch.jpg](https://en.wikipedia.org/wiki/Y-factor#/media/File:Y-factor_sketch.jpg).
- 2534
- 2535 [72] Rigol Technologies. *RSA5000 Series: Real-Time Spectrum Analyzer Datasheet*. Ac-
- 2536 cessed: 2024-06-23. 2024. URL: [https://beyondmeasure.rigoltech.com/acton/attachment/1579/f-0816/1/-/-/-/RSA5\\_datasheet.pdf](https://beyondmeasure.rigoltech.com/acton/attachment/1579/f-0816/1/-/-/-/RSA5_datasheet.pdf).
- 2537
- 2538 [73] “IEEE Standard Method for Measuring the Effectiveness of Electromagnetic Shielding
- 2539 Enclosures”. In: *IEEE Std 299-1997* (1998), pp. 1–48. DOI: [10.1109/IEEESTD.1998.88115](https://doi.org/10.1109/IEEESTD.1998.88115).
- 2540
- 2541 [74] David W. Allan. “Statistics of atomic frequency standards”. In: *Proceedings of the*
- 2542 *IEEE 54.2* (1966), pp. 221–230.
- 2543 [75] Keysight Technologies. *Analyzing Frequency Stability in the Frequency and Time Do-*
- 2544 *mains*. Tech. rep. 5991-4797EN, August 11, 2014. USA: Keysight Technologies, 2014.

- 2545 [76] Stanford Research Systems. *FS725 Rubidium Frequency Standard Manual*. Accessed:  
2546 2024-06-23. 2024. URL: <https://www.thinksrs.com/downloads/PDFs/Manuals/FS725m.pdf>.
- 2547
- 2548 [77] R. H. Dicke. “The Measurement of Thermal Radiation at Microwave Frequencies”.  
2549 In: *Rev. Sci. Instrum.* 17 (1946), p. 268. DOI: 10.1063/1.1770483. URL: <https://aip.scitation.org/doi/10.1063/1.1770483>.
- 2550
- 2551 [78] S. Al Kenany et al. “Design and operational experience of a microwave cavity axion de-  
2552 tector for the 20-100 micro-eV Range”. In: *Nuclear Instruments and Methods in Physics*  
2553 *Research Section A: Accelerators, Spectrometers, Detectors and Associated Equipment*  
2554 854 (May 2017), pp. 11–24. ISSN: 0168-9002. DOI: 10.1016/j.nima.2017.02.012.  
2555 URL: <http://dx.doi.org/10.1016/j.nima.2017.02.012>.
- 2556 [79] G. Turin. “An introduction to matched filters”. In: *IRE Transactions on Information*  
2557 *Theory* 6.3 (1960), pp. 311–329. DOI: 10.1109/TIT.1960.1057571.
- 2558 [80] Robert N McDonough and Anthony D Whalen. *Detection of signals in noise*. Academic  
2559 Press, 1995.
- 2560 [81] S. Asztalos et al. “Large-scale microwave cavity search for dark-matter axions”. In:  
2561 *Phys. Rev. D* 64 (9 Oct. 2001), p. 092003. DOI: 10.1103/PhysRevD.64.092003. URL:  
2562 <https://link.aps.org/doi/10.1103/PhysRevD.64.092003>.
- 2563 [82] G. Orjubin et al. “Statistical model of an undermoded reverberation chamber”. In:  
2564 *IEEE Transactions on Electromagnetic Compatibility* 48.1 (2006), pp. 248–251. DOI:  
2565 10.1109/TEMC.2006.870705.

- 2566 [83] B. Efron. “Bootstrap Methods: Another Look at the Jackknife”. In: *The Annals of*  
2567 *Statistics* 7.1 (1979), pp. 1–26. DOI: 10.1214/aos/1176344552. URL: <https://doi.org/10.1214/aos/1176344552>.
- 2568
- 2569 [84] R. Khatiwada et al. “Axion Dark Matter Experiment: Detailed design and operations”.  
2570 In: *Review of Scientific Instruments* 92.12 (Dec. 2021), p. 124502. ISSN: 0034-6748.  
2571 DOI: 10.1063/5.0037857. eprint: [https://pubs.aip.org/aip/rsi/article-pdf/doi/10.1063/5.0037857/16136265/124502/\\_1/\\_online.pdf](https://pubs.aip.org/aip/rsi/article-pdf/doi/10.1063/5.0037857/16136265/124502/_1/_online.pdf). URL: <https://doi.org/10.1063/5.0037857>.
- 2572
- 2573
- 2574 [85] Yuqi Zhu et al. “An improved synthetic signal injection routine for the Haloscope  
2575 At Yale Sensitive To Axion Cold dark matter (HAYSTAC)”. In: *Review of Scientific*  
2576 *Instruments* 94.5 (May 2023). ISSN: 1089-7623. DOI: 10.1063/5.0137870. URL: <http://dx.doi.org/10.1063/5.0137870>.
- 2577
- 2578 [86] Frank Hampel et al. *Robust Statistics: The Approach Based on Influence Functions*.  
2579 John Wiley & Sons, Mar. 1986. ISBN: 9780471735779. DOI: 10.1002/9781118186435.
- 2580 [87] Andrea Caputo et al. “Dark photon limits: A handbook”. In: *Phys. Rev. D* 104 (9  
2581 Nov. 2021), p. 095029. DOI: 10.1103/PhysRevD.104.095029. URL: <https://link.aps.org/doi/10.1103/PhysRevD.104.095029>.
- 2582
- 2583 [88] Ciaran O’Hare. *cajohare/AxionLimits: AxionLimits*. <https://cajohare.github.io/AxionLimits/>. Version v1.0. July 2020. DOI: 10.5281/zenodo.3932430.
- 2584
- 2585 [89] DM Radio Collaboration et al. *Electromagnetic modeling and science reach of DM Radio-*  
2586 *m<sup>3</sup>*. 2023. arXiv: 2302.14084 [hep-ex]. URL: <https://arxiv.org/abs/2302.14084>.

- 2587 [90] Ferenc Marki and Christopher Marki. *Mixer Basics Primer: A Tutorial for RF &*  
2588 *Microwave Mixers*. Marki Microwave, Inc. Morgan Hill, CA, 2010. URL: [https://markimicrowave.com/assets/c2c4688b-15c7-4421-a703-254cb238f9fb/Mixer\\_Basics\\_Primer.pdf](https://markimicrowave.com/assets/c2c4688b-15c7-4421-a703-254cb238f9fb/Mixer_Basics_Primer.pdf).
- 2590  
2591 [91] David M. Pozar. *Microwave Engineering*. 4th ed. Hoboken, NJ: Wiley, 2011. ISBN:  
2592 978-0470631553.
- 2593 [92] Wikipedia contributors. *Superheterodyne receiver*. Accessed: 2024-06-23. 2024. URL:  
2594 [https://en.wikipedia.org/wiki/Superheterodyne\\_receiver](https://en.wikipedia.org/wiki/Superheterodyne_receiver).